Universidade Federal de Santa Catarina
Programa de Pós-Graduação em Engenharia Mecânica

Controle ativo de vibrações de baixas e altas freqüências e ruído radiado de estruturas complexas

Tese submetida à

Universidade Federal de Santa Catarina

para obtenção do grau de

DOUTOR EM ENGENHARIA MECÂNICA

Guillaume François Gilbert Barrault

Florianópolis, 21 de agosto de 2006

Universidade Federal de Santa Catarina
Programa de Pós-Graduação em Engenharia Mecânica

Controle ativo de vibrações de baixas e altas freqüências e ruído radiado de estruturas complexas

Guillaume François Gilbert Barrault

Esta Tese foi julgada adequada para a obtenção do título de
Doutor em Engenharia Mecânica

Especialidade Engenharia Mecânica
sendo aprovada em sua forma final.

Prof. **Arcanjo Lenzi**, Ph.D.
Orientador

Prof. **Fernando Cabral**, Ph.D.
Coordenador do Curso

Prof. **José Carlos Moreira Bermudez**, Ph.D. – Co-Orientador

Banca Examinadora

Prof. **Arcanjo Lenzi**, Ph.D. – Presidente

Prof. **Roberto Jordan**, Dr.Eng.

Prof. **Colin Hansen**, Ph.D.

Prof. **Valder Steffen Junior**, Dr.Eng.

Prof. **Alexandre Trofino Neto**, Dr.Eng.

AGRADECIMENTO

Ao professor **Arcanjo Lenzi** que está me dando a oportunidade de poder efetuar esse trabalho de pesquisa e pela confiança. Ao CNPq, Embraco e RT-LAB pelo apoio financeiro.

Thanks to **Colin Hansen** who received me at Adelaide University and help me.

Special Thanks to **Dunant Halim** who advised me for all the vibration control part.

Ao professor **José C. Bermudez** que está me dando a maior força em processamento de sinal e que está me ajudando também a me superar para esse trabalho.

Um agradecimento muito especial ao professor **Valder Steffen** que está sempre disposto a ajudar e a dar muito dicas valiosas.

Ao **Gustavo Abreu** pelo precioso apoio e seu trabalho que está servindo de referencia nesse trabalho.

Ao **Marcio H. Costa** e ao **Alexandre Trofino Neto** que generosamente estão sempre presentes quando eu preciso.

Thanks to **Angela Yeoh**, this thesis is much easier to read.

DÉDICACES

Que serais-je sans vous, mes parents? merci d'être là pour moi.

De l'Australie au Brésil en passant par la France il y a un monde, le notre... Angela.

Mes Soeurs, Edwige et Audrey, de croire en moi vous m'avez allégé et permit d'aller toujours plus loin, merci.

Se eu não tivesse conhecido Humberto, minha vida não teria sido a mesma, obrigado.

Arcanjo não apena um orientador mas amigo com uma familia "show de bola".

Amir e sua Naraiana que bela familia, obrigado pela sua amizade.

Willy Bolly, you have the entire world open to you, my friend.

Colin and Dunant, thanks for your friendship and your tips.

Thanks Dick and Rohin for having supported me for a year and your advises.

Obrigado para as pessoas que me ajudaram de uma forma ou de uma outra. Merci aux personnes que m'ont aidé d'une forme ou d'une autre. Thanks to anyone who helped me in a way or an other.

RESUMO

Equipamentos industriais geramente são sujetos a vibrações mecânicas não desejadas que comprometem sua operação e integridade. Além disso, causam incômodo para o operador na forma de ruído. Desta observação surge a necessidade de controlar as vibrações e o ruído radiado. Atualmente existem várias abordagens de atenuação de ruído e vibrações as quais podem ser divididas em dois grupos: atenuação utilizando o controle passivo e o controle ativo. Quando o controle passivo não chega a ser possível ou eficiente, o controle ativo se torna necessário. Um sistema de controle ativo atenua a vibração ou ruído acústico medindo e contra-atuando a perturbação não desejada. O primeiro foco desta tese é prever a atenuação da perturbação, dependando do algorítmo de controle utilizado. A possibilidade de atenuar a radiação sonora de uma estrutura fechada é investigada nesse trabalho. O controle ativo é geralmente focalizado na região de baixas freqüências, porém este trabalho de pesquisa propõe uma solução para controlar globalmente a vibração de uma estrutura complexa em qualquer faixa de freqüência desejada. Todas as teorias desenvolvidas nesse trabalho foram comprovadas com experimentos.

Palvras-chave: controle ativo de ruído e vibrações, algoritmos adaptativos, identificação de sistemas, otimização, controle spatial, controle robusto.

ABSTRACT

The concept of active control is used in a range of disciplines, including signal processing and vibration theory. This thesis examines aspects of active vibration and noise control, contributing a number of new theories to advance available techniques for building real-world active control systems. A key contribution of this work is the proposal of a new model for analysing the behaviour of the Filtered-x LMS adaptive algorithm, in this case as applied to active noise control in a finite duct. The model was derived using a stochastic differential equation approach. This thesis also presents a new way of optimising both the analytical and experimental models (truncated to focus on a specified frequency bandwidth) upon which most active control systems are based. Finally, a methodology is set out, using subspace model identification and the theories of robust control and spatial input/spatial output control, for designing a controller to globally attenuate vibration in a complex structure within a specified frequency bandwidth.

Keywords: active control, adaptive algorithms, system identification, spatial control, optimisation, robust control.

SUMARÍO

LISTA DE FIGURAS

LISTA DE TABELAS

LISTA DE SIGLA E SÍMBOLOS

Sigla/Símbolo	**Descrição**
A/D	*Analogue to Digital*
ANC	*Active Noise Control*
APPA	*Adaptive Pole Placement Approach*
ARMA	*AutoRegressive Moving Average*
D/A	*Digital to Analogue*
DSP	*Digital Signal Processor*
FFT	*Fast Fourier Transform*
FIR	*Finite Impulse Response*
FPGA	*Field Programmable Gate Array*
FTF	*Fast Transversal Filter*
FxLMS	*Filtered-x Least Mean Square*
IIR	*Infinite Impulse Response*
IMSC	*Independent Modal Space Control*
I/O	*Input/Output*
LFT	*Linear Fractional Transformation*
LMS	*Least Mean Square*
LQG	*Linear Quadratic Gaussian*
LQR	*Linear Quadratic Regulator*
MIMO	*Multiple Inputs Multiple Outputs*
MSE	*Mean Square Error*
NP	*Nominal Performance*
ODE	*Ordinary Differential Equation*
PVDF	*PolyVinyliDene Fluoride*
PZT	*Lead Zirconate Titanate (lead=plomb in french)*
RLS	*Recursive Least Square*
RP	*Robust Performance*
RS	*Robust Stability*
SISO	*Single Input Single Output*

SDE	*Stochastic Differential Equation*
SDV	*Singular Value Decomposition*
S/N	*Signal to Noise*
$\boldsymbol{A}$	System dynamic matrix
$\boldsymbol{B}$	Input matrix
$\boldsymbol{C}$	Output matrix
$\mathcal{C}$	Damping operator
$\boldsymbol{D}$	Feedthrough matrix
$\boldsymbol{\mathcal{E}}$	Hankel error matrix
$\boldsymbol{F}$	External forces or secondary path
$\boldsymbol{G}$	MIMO transfer function
$\boldsymbol{I}$	Identity matrix
$\boldsymbol{K}$	Controller matrix
$\boldsymbol{\Lambda}$	Eigenvalue matrix
$\mathcal{L}$	Linear homogeneous differential operators
$\boldsymbol{N}$	Matrix inverse of $s\boldsymbol{I} - \boldsymbol{A}$
$\boldsymbol{P}$	Lyapunov inequality matrix solution
$\boldsymbol{Q}$	Weighting matrix
$\boldsymbol{R}$	Autocorrelation matrix
$\mathcal{R}$	Structure domain
$\boldsymbol{S}$	Primary path filter matrix
$\boldsymbol{T}$	Transformation matrix
$\boldsymbol{U}$	Input data matrix
$\boldsymbol{X}$	State variable matrix
$\boldsymbol{Y}$	Output data matrix
$\mathcal{Y}$	General output matrix
$\boldsymbol{V}$	Right singular Matrix
$\boldsymbol{W}$	Filter matrix
$\boldsymbol{0}$	Zero matrix
$\boldsymbol{\Omega}$	Spatial input matrix
$\boldsymbol{\Delta}$	Uncertainty matrix
$\boldsymbol{\Gamma}$	Observability or output spatial matrix
$\boldsymbol{e}$	Noise vector
$\boldsymbol{f}$	Force vector
$\boldsymbol{p}$	Cross-correlation vector
$\boldsymbol{q}$	State-space vector
$\boldsymbol{r}$	Reflection effect vector
$\boldsymbol{s}$	Primary path filter vector

$\boldsymbol{u}$	Input vector
$\boldsymbol{v}$	Weight-error or voltage input/output vector
$\boldsymbol{w}$	Adaptive filter
$\boldsymbol{w}_{opt}$	Optimal filter
$\boldsymbol{x}$	State-space vector
$\boldsymbol{y}$	Output vector
$\boldsymbol{\beta}$	Equivalent spatial distribution vector
λ	Wavelength
ω	System noise, period or natural frequency
ϵ	Strain
μ	Step-size
δ	Kronecker delta function
ρ	Density
ϕ	Structural eigenfunction
σ	Variance
ζ	Damping ratio
Γ	Brownian motion
p	Air pressure
t	Time
e	Estimation error
e_o	Minimum estimated error
E	Mean operator or Young's modulus
tr	Trace operator
I	Inertial moment
$^{a}\quad{}^{s}$	Parameter related to actuator and sensor
$\widetilde{\bullet}$	Estimation of $\bullet$
*	Transposed conjugate
$\otimes$	Kronecker product

INTRODUCTION

A wide range of modern commercial and industrial machines continue to be afflicted by problems of unwanted mechanical vibration and acoustic noise. In machine-driven equipment, incidental mechanical vibration may often compromise the behaviour and integrity of the equipment, while incidental acoustic noise can cause discomfort for the user ranging from the mildly irritating to the intolerable. The undesirability of such vibration and/or noise has led to the search for more effective ways of controlling them.

Various methods of noise and vibration attenuation have been developed over the years, and can be classified into one of two approaches: passive control or active control. Passive vibration control is commonly used because it is more intuitive and generally cheaper and more manageable to implement for a range of machine-driven systems. However, if passive control is found to be ineffective or infeasible, then an active control solution may need to be sought. This thesis will focus on active vibration control theory, looking at existing techniques and how they could be improved to provide even better ways of attenuating unwanted vibration and noise in real-world applications.

An active control system works by sensing the vibration to be controlled, then deliberately producing out-of-phase oscillations to counteract the undesired disturbance force(s). Generally, such a system consists of four main parts: the signal control system, one or more sensors, some form of actuation, and the structure itself.

According to control theory, there are two ways of defining the coefficients of

a controller. The first is known as adaptive control, and works by updating the coefficients on-line according to information obtained in real-time. In the second, an off-line modelling of the system in question must be performed, to enable optimal pre-defined coefficients to be determined that can then be assigned to the controller. This thesis will employ both of these techniques, according to which was judged the most appropriate for the control problem defined.

Chapter 1 will give an overview of key active control theory and techniques to date, particularly those used and developed in this thesis. In the last decade important breakthroughs have been made for active noise control (ANC) through the use of adaptive feedforward structures. Chapters 2 and 3 will both test the effectiveness of using the feedforward approach in designing active control systems.

The performance of a given ANC system depends primarily on the signal processing algorithm that is chosen. In Chapter 2, a new model will be presented for analysing the behaviour of the Filtered-x LMS adaptive algorithm when used for ANC inside a finite duct. The new analytical model was derived using a stochastic differential equation (SDE) approach, and the experiment setup automated to allow the use of Monte Carlo techniques to evaluate the model's performance. Experimental results verified that the model made accurate theoretical predictions about the stochastic behaviour of the adaptive algorithm.

Chapter 3 will then present an unconventional ANC approach, also based on adaptive control, that uses structural sensors and actuators to actively attenuate sound radiation from an irregular enclosure. The approach was tested for its effectiveness in minimising the enclosure's radiated sound field.

Chapter 4 will give an overview of some classic analytical modelling techniques for flexible structures, and will then introduce a new optimisation method for any given analytical model that has been truncated to focus on a specified frequency bandwidth.

Chapter 5 explains the recent theory of spatial input/spatial output control,

and will introduce a new way in which the theory can be extended, while Chapter 6 will set out the key ideas of robust control theory. An awareness of both robust control and spacial input/spatial output control is necessary for appreciating the new control theory put forward in the final two chapters.

Chapter 7 will present the new idea of achieving high frequency spatial vibration control for a given complex structure using an experimental model. This was achieved by bringing together three techniques that are normally used separately: subspace model identification (or SMI, to obtain a system's dynamics via experiment), spatial input/output control (to obtain a conceptualisation of the structure's global displacement and the contribution of unknown external disturbance(s) on the system), and $\mathcal{H}_\infty$ robust control (to concentrate the control energy within a chosen frequency bandwidth).

Chapter 8 will then validate the theories set out in Chapters 4, 5 and 7 through three experiments. The first experiment will show, for the first time, a real-life demonstration of spatial input/spatial output control theory. The second and third will validate Chapter 7 high frequency global vibration control theory, based on an analytical and an experimental model respectively.

It is the intention that each chapter can be read as a self-contained study.

Chapter 1

LITERATURE REVIEW

This work investigates active vibration and noise control; more specifically, active noise control (ANC) in a duct, and noise radiation through an enclosure for the acoustic part and model-based vibration attenuation for the structural part. This chapter provides an overview of existing techniques of vibration control, and also looks briefly at piezoelectric sensors and actuators as they can be used in vibration control systems.

1.1 Active noise control (ANC)

Noise reduction remains a primary concern in many industries, both to improve the work environment and to reach for whom customers where noise is a deciding factor between two products providing the same services. Although passive noise control is widely used in industry, there have been relatively few industrial applications of active control, mainly due to its unreliability, both in terms of control stability and in terms of embedded electronic devices (it will be shown in the following chapters how these problems can be overcome) and also because it is usually difficult and time consuming to implement. However ANC, where additional secondary sources are used to cancel noise from the original primary source, has shown increasing promise and is receiving growing interest.

ANC involves an electroacoustic or electromechanical system that cancels the

unwanted noise based on the principle of superposition; more specifically, an anti-noise of equal amplitude and opposite phase is generated and combined with the original noise, resulting in the effective cancelation of both noises [11]. However ANC systems are problematic in that they require highly precise control, temporal stability, and reliability. To produce a high degree of attenuation, the amplitude and phase of both the primary and the secondary noises must match with close precision. In order for an ANC system to execute the necessary sophisticated mathematical functions in real-time, it is desirable for the noise canceler to be digital [12, 13], so that signals from an electroacoustic or electromechanical transducer are sampled and processed using digital signal processing systems with sufficient speed and precision. And while nonadaptive active control of dynamic systems has been developed for stationary systems (from an approach based on forming a model of the system and computing the optimal controller for the desired response) the properties of the noise field in ANC application are typically non-stationary; for example, the speed and load of an engine or blower are continually changing, which results in varying frequency and amplitude of the undesired noise. Another example would be temperature and flow changes inside a duct, which result in sound velocity variations. In order to track and respond to such changes in real-time, the ANC system must be adaptive one [11].

Ioannou and Sun [7] present some common schemes for adaptive control. They first consider robust control. This consists of a constant feedback controller designed to cope with plant parameter changes, provided that such changes are within certain bounds. However, robust control is not considered as adaptive control even though it can handle certain classes of parameter and dynamic instabilities. This is because gain scheduling is based on a look-up table which assigns the controller parameters to the operating point. A second scheme is Model Reference Adaptive Control (MRAC), where the desired input/output properties of the closed-loop plant are given by a model. The transfer function matching is achieved by cancelling the zeros of the plant transfer function and replacing them with those of the model transfer function. The two principal approaches in MRAC are direct and indirect controls. Direct and indirect adaptive controllers combine on-line parameter estimation and the control law. The way in which this combination occurs

differentiates the system as direct or indirect control. The indirect adaptive control law uses an explicit plant model for the design of the controller, while for direct adaptive control, the plant is parameterised in terms of the controller parameters that are estimated directly without any intermediate calculations that involve the plant parameter estimates. A third type of adaptive control is the Adaptive Pole Placement Approach (APPA), also referred to as self-tuning regulators, where the performance requirements are translated into desired locations of the poles of the closed-loop plant. A feedback control law is developed that places the poles of the closed-loop plant at the desired locations. When the true parameter vector of the plant is unknown, the certainty equivalence can be used to replace the unknown vector with its estimate.

Ioannou and Sun also discuss three basic methods for online estimation: the sensitivity method, the Lyapunov design, and the gradient and least-squares methods. The problem with using the sensitivity method for adaptive control lies in its implementation, as the sensitivity function cannot be generated on-line in most instances. A popular method for coping with this problem is to approximate a sensitivity function with the MIT (Massachusetts Institute of Technology) rule. The MIT rule is based on the minimisation of a performance index, which is the integral of the square of the error between the desired input and the actual output of the plant. In the Lyapunov design, the problem of designing an adaptive law is formulated as a stability problem where the differential equation of the adaptive law is chosen so that certain stability conditions based on the Lyapunov theory are satisfied. Gradient and least-squares methods are based on estimation error cost criteria leading to sensitivity functions that are available for measurement [14].

Adaptive algorithms used in control scheme can be classified into either time domain methods or frequency domain methods. Time domain methods identify the coefficients of the transfer function polynomials, whereas frequency domain methods identify the zeros and poles of the transfer function. Time domain and frequency domain methods are discussed in [15], while [16] studies three widely used time domain algorithms: Recursive Least Squares (RLS), Least Mean Squares (LMS) and Fast Transversal Filter (FTF). The RLS algorithm has a computational

complexity that increases with the square of the order of the system. One of the main drawbacks of the time domain method is that the covariance matrix update diverges if the plant input is not continuously excited. Furthermore, time domain methods are sensitive to under- or over-parameterised problems: under-parametrisation leads to ignored modes while an over parameterised model loses accuracy. From the parametrisation of the transfer function, the frequency domain characteristics are converted to an AutoRegressive Moving Average (ARMA) model appropriate for controller implementation. The computation can be restricted to the expected frequency range of the system pole and zero locations. The presence of a transfer function in the auxiliary path following the adaptive filter and/or in the error-path, as in the case of ANC, has been shown to generally degrade the performance of the LMS algorithm. Thus, the convergence rate is lowered, the residual power is increased, and the algorithm can even become unstable.

To ensure convergence of the algorithm, the input to the correlator has to be filtered by a copy of the auxiliary-error-path transfer function. Such algorithms are referred to as Filtered-x LMS (FxLMS) algorithms, the most popular algorithm used for control experiments; this algorithm will be further discussed in Chapter 2. [17, 18] analyse the FxLMS algorithm, which was introduced in 1981 by Widrow et al [19]. In the FxLMS, the error sensor signal is computed using past coefficient vectors. The resulting delay between the coefficient updates leads to slower convergence, a restricted step size range for stability, and overall reduced performance. Effective algorithm design requires reasonable knowledge of algorithm behaviour for the desired operating conditions. Frequently, this knowledge is obtained from analytical models as opposed to evaluating simulations.

[20] discusses the distinction between two control approaches: feedforward or feedback. It is important to note that even when a feedforward structure is adopted, the overall scheme generally uses feedback through adaptation of the parameters. The distinction is therefore mostly in the inner structure of the control algorithm, rather than its overall feedforward or feedback nature. [21] assessed the performance of both feedforward and feedback systems, particularly with respect to plant delays. The main factor limiting the performance of the feedforward con-

troller is the fact that the multiple coherence between the reference signals and the disturbance signal is less than unity. For a feedback control system, this is not a limiting factor as no reference signal is used, and the disturbance is cancelled by a filtered version of the disturbance; here, the main performance limiting factors are the delay in the plant and how much the model differs from real system. The performance of the feedback controller is better if the plant delay is very small, while a feedforward controller is more robust to plant delays. It should also be emphasised that the variation of attenuation with delay is very dependent on the statistical properties of the disturbance. It will be shown in Chapter 3 how a simple robust active noise control system, based on the above consideration, can attenuate noise radiated from an irregular enclosure at frequencies below the first enclosure structural resonance frequency. The robustness of the control system comes from two properties: the use of only structural sensors/actuators, and the choice of an adaptive feedforward controller using a simple FxLMS control algorithm.

As ANC is a very large subject, the most common ANC example, ANC in a duct, is used to illustrate what complexity is involved in one of the simplest existing systems. The ANC approach in a duct depends on the reference signal characteristics and also how this signal is obtained. In other words, if the reference signal is measured directly from the source (see Fig. 2.20), it does not suffer any acoustic interferences. However, if the reference signal is measured by an acoustic sensor, interference occurs and the signal measurement no longer gives the desired signal (see Fig. 1.1 to observe the acoustic path inside a finite duct).

The *ANC in a duct* example has been widely examined, considering the number of books [11, 22, 23] and papers published on the subject; however, in general they only consider an infinite duct. Fewer publications deal with a finite duct system and even fewer with a finite duct where the reference signal is evaluated by an acoustic sensor. Considering a finite duct involves the concept of stationary waves which interfere with the cancelling of the signal measurements and can introduce instability in classic ANC systems [22]. Various solutions have already been proposed (for example [1, 24–26]) to overcome this issue. The biggest prob-

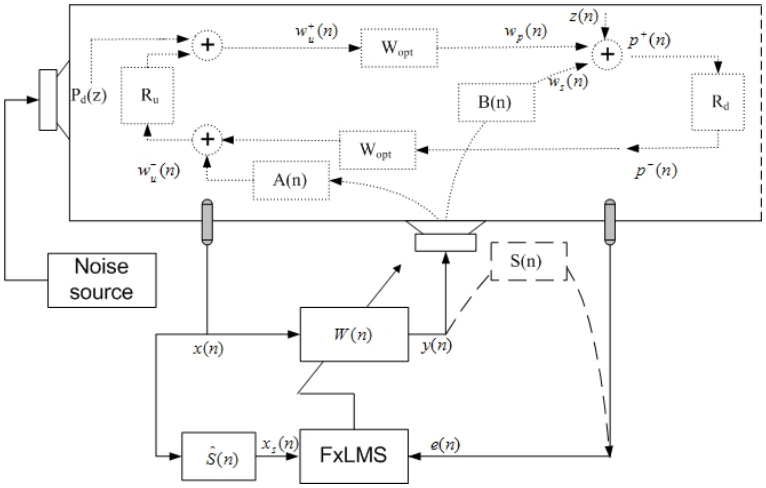

Figure 1.1: Wave propagation in a finite duct [1].

lem is being able to isolate the desired signal, even with a unidirectional sensor, because the return wave reflects itself against the noise source interferes with the reference signal measurement and generates poles within the control system.

Today, a standard method to isolate the desired periodic signal in a duct is the separation wave technique [27, 28]. This technique requires two sensors (which do not need to be unidirectional) and is based on the plane wave propagation theory. Several papers have already demonstrated importance of sensor location in obtaining the best desired signal performance [29, 30]. The wave separation theory is mostly used in post-processing in the frequency domain. Reference signal characteristics become important for real-time applications. For a known frequency range, it is possible to use the wave separation theory in the frequency domain in real-time but the algorithm has a high computational weight due to the real-time Fast Fourier Transform (FFT) [31]. Another solution is to find a recursive relationship to separate the desired signal in the time domain based on the wave separation theory. [32] gives a time domain recursive relationship for a signal with only one frequency, and can be extended to a narrow frequency range. [1] describes the acoustic phenomenon inside the duct caused by an acoustic source and defines a new approach to the ANC in a finite duct using the classical FxLMS algorithm in the robust form as shown in Fig. 1.1.

1.2 Piezoelectrics

Piezoelectric materials are a family of materials that demonstrate electromechanical coupling: when the material is mechanically strained, the material produces a corresponding electric charge, and when an electric field is applied across the material, it mechanically strains. The literature indicates that researchers have studied piezoelectric materials since their discovery by Pierre and Jacques Curie in 1880. The piezoelectric discovery directly resulted from Pierre Curie's research between crystal symmetry and so-called pyroelectricity [33]. The term piezoelectricity, proposed by Hankel, describes the well-known interaction between electrical and mechanical systems. Mathematically, this relationship is governed by two constitutive equations [34]:

$$\{\sigma\} = [C^E]\{\varepsilon\} - [e]\{E\} \tag{1.1a}$$

$$\{D\} = [e]^T\{\varepsilon\} - [\zeta^S]\{E\} \tag{1.1b}$$

where the superscript S means that the values are measured at constant strain and the superscript E means that the values are measured at constant electric field, $\{\sigma\}$ is the stress tensor, $\{D\}$ the electric displacement vector, $\{\varepsilon\}$ the strain tensor, E the electric field, $[C^E]$ the elastic constants at constant electric field, $[e]$ denotes the piezoelectric stress coefficients, and $[\zeta^S]$ the dielectric tensor at constant mechanical strain.

The above equations help to explain the possibility of employing piezoelectric materials as both actuators and sensors. If the piezoelectric materials are bonded properly to a structure, structural deformations can be induced by applying a voltage to the materials, employing them as actuators. On the other hand, they can be employed as sensors since deformations of a structure would cause the deformed piezoelectric materials to produce an electric charge. Measuring the electrical voltage the materials produce can give an indication of the extent of structural deformation. Two commonly used piezoelectric materials are polyvinylidene fluoride (PVDF), a semicrystalline polymer film, and lead zirconate titanate (PZT), a piezoelectric ceramic material. PZT has larger electromechani-

cal coupling coefficients than PVDF, so it can induce larger forces or moments on structures. However, PZT is also relatively brittle, while PVDF is flexible and can be easily cut into any desired shape. PVDF also has good sensing properties so it is commonly used for sensors. [35] gives a description of the dielectric polarisation concept. A dielectric, or insulator, describes material that does not support electrical conduction and restricts or completely impedes charge motion within the material when subjected to an external electric field. This class of materials can be contrasted against electrical conductors where charges migrate freely when exposed to a similar electric field yielding electric current. An important distinction between these two materials is the presence of an internal electric field within the dielectric and the absence of an electric field within the conductor. The presence of this internal electric field results in an electrical polarisation of the dielectric. The phenomenon of polarisation describes the net, or macroscopic, electric field resulting from deformed or altered microscopic electric fields of individual atoms or molecules. Dielectric polarisation results from the formation of dipoles; however, various mechanisms are responsible for several types of polarisation: electronic polarisation results from the formation of dipoles due to an electron cloud and molecular polarisation stems from dipoles resulting from the deformation of ionic molecular bonds, while polar fluids exhibit orientational polarisation when the polar molecules align in a field.

The coupled electro-mechanical properties of piezoelectric materials put it in the smart materials family. By definition, smart materials are both sensors and actuators, because they can perform both functions. They may or may not have control systems. At a more sophisticated level, smart materials become intelligent when they have the ability to respond intelligently and autonomously to dynamically-changing environmental conditions: they analyse the sensed signal, perhaps for its frequency components, and then decide what kind of response to make. This capability has led to an increase in the development of light-weight smart piezoelectric structures for several engineering applications that create structures and systems coupled with suitable control strategies and circuits exhibiting self-monitoring and self-controlling capabilities for vibration control [36, 37].

1.3 Active vibration control

To understand and control the vibration of a structure, first it is necessary to characterise the vibrational properties of the structure; that is to have certain knowledge of how the parts of the structure vibrate. Vibration characterisation is essential in anticipating the vibration levels or determining what actions can be taken to control the vibration. While passive noise control has been the predominant method used in industry, the quest for the ultimate control of vibration has advanced to the extent that using active forces would be preferable for counteracting vibration. This relatively new vibration control method is called active control of vibration, and requires sensing of the vibration in real-time. Regardless of the active control strategy, either feedback or feedforward, real-time sensing would be required [38].

Vibration of a multi-degree-of-freedom system can be expressed in terms of the motion of the system along several coordinates. The equations governing the motion of the system can be relatively simple or complex depending on the choice of the coordinate system. Some coordinate systems result in coupled equations of motion, which means that individual equations cannot be solved without involving others. The choice of coordinate system determines the degree of coupling among the equations. As a rule, the more coupling exists among the equations, the more complicated are their solutions. In controlling the vibration of a multi-degree-of-freedom system, a coordinate system that leads to no coupling among the equations allows more simple control schemes. In many cases, it is possible to choose a coordinate system that results in no coupling among the equations of motion. The coordinates in such a coordinate system are called the principal coordinates, also known as the natural coordinates. The natural coordinates provide a basis on which to mathematically express the vibration of a structure. On this basis, the vibration of a structure can be viewed as a summation of the products of a spatial function and a temporal function:

$$w(x,t) = \sum_{m=1}^{\infty} z_m(t)\psi_m(x) \tag{1.2}$$

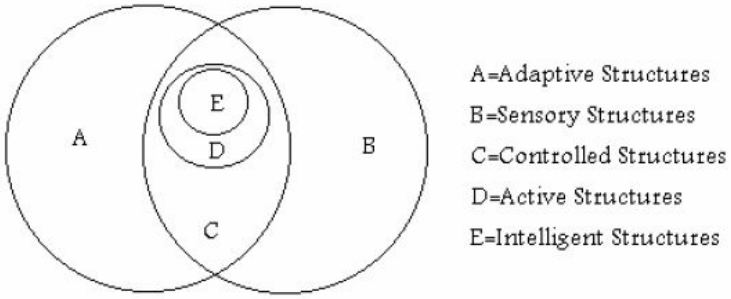

Figure 1.2: Adaptive structures framework defined by [2].

where x is position and t is time. The spatial function ψ_m is the mode shape of the structure, which is a characteristic of the structure. The temporal function z_m is called the modal coordinate[38].

[2] presents a classification of adaptive structures dividing these structures into five groups as shown in Fig. 1.2. These groups include sensory structures incorporating sensors to monitor the dynamics or health of structures; adaptive structures with attached or embedded actuator elements that influence the dynamics or the shape of the structure; controlled structures involving both sensors and actuators together with a controller; active structures with control elements acting as structural elements; and finally, intelligent structures which are active structures with learning elements.

Vibration control laws have followed the evolution of techniques coming from automatic control laws. In the early 1980s, the two principal control families used in active vibration control (Independent Modal Space Control (IMSC) and the coupled control) were opposed. The IMSC approach works by eliminating extensive cross-coupling between the modes. If the independence of the modal equations could be maintained during implementation of a feedback control system, then the control law would be derived as a set of independent control laws, one for each mode [39]. On the other hand, the coupled control approach allows mode dependance. This approach has the advantage of requiring less sensors and actuators since the system is controllable and observable.

[40] compares and contrasts the two main control families. The techniques used during the early 1980s are the pole placement, Linear Quadratic Regulator (LQR) or the Linear Quadratic Gaussian (LQG) control law. The pole placement design technique first selects n desired pole locations, from the desired characteristic polynomial, then calculates the closed-loop characteristic polynomial of the state feedback regulator $\boldsymbol{K}$ given by Eq. 1.3

$$\det\left[\boldsymbol{\Lambda I} - (\boldsymbol{A} - \boldsymbol{BK})\right] = 0 \,\text{for the state equation}\, \dot{\boldsymbol{x}} = \boldsymbol{Ax} + \boldsymbol{Bu} \,\text{and}\, \boldsymbol{u} = \boldsymbol{Kx} \quad (1.3)$$

and finally computes the elements of $\boldsymbol{K}$ by equating the coefficients of like powers of the first and second steps. The optimal control or LQR design determines the gain matrix $\boldsymbol{K}$ to minimise the performance index J detailed in Eq. 1.4.

$$J = \int_0^\infty \left[\boldsymbol{x}^T(\tau)\,\boldsymbol{Q}\boldsymbol{x}(\tau) + \boldsymbol{u}^T(\tau)\boldsymbol{R}\boldsymbol{u}(\tau)\right] d\tau = \int_0^\infty \left[\boldsymbol{x}^T(\tau)(\boldsymbol{Q} + \boldsymbol{K}^T\boldsymbol{R}\boldsymbol{K})\boldsymbol{x}(\tau)\right] d\tau \quad (1.4)$$

where $\boldsymbol{Q}$ and $\boldsymbol{R}$ are positive definite Hermitian or real symmetric referred to as the state weighting and control weighting matrices, respectively. They weight the relative importance of attenuating the response of certain states and limit the control effort. Hence, they have a great influence upon the control gain matrix $\boldsymbol{K}$ [22]. The LQG design combines LQR design and Kalman filter which attempt to minimise the estimation error variance where the state equation is increased by an external noise $\boldsymbol{w}$: the state-space equation thus becomes $\dot{\boldsymbol{x}} = \boldsymbol{Ax} + \boldsymbol{Bu} + \boldsymbol{w}$ and the measurement has a noise $\boldsymbol{v}$ $\boldsymbol{y} = \boldsymbol{Cx} + \boldsymbol{v}$.

Unfortunately, this strategy may cause spillovers, due to the structure's higher-frequency modes, and thereby lower stability of the control system due the inability to treat such uncertainties as model errors and external disturbances. Therefore, it seems that the robust control strategy should be considered in the controllable constrained damping layer technique to improve the stability of the control system. The past two decades have witnessed the development of the $\mathcal{H}_\infty$ robust control theory, which can not only deal with various model uncertainties but also carry

out conveniently the tradeoff between robust stability and control performance. It thus provides a powerful design tool for robust vibration control of engineering structures. With the $\mathcal{H}_\infty$ robust control theory, the uncertainties between the theoretical model and the actual structure can be analysed by means of numerical computation and experimentation, which lays the foundation of robust control design [41].

As discussed earlier, modern control theory provides tools that help to more reliably deal with uncertainty problems that arise due to the truncation or inaccuracy of a given model. Modern control theory also provides a framework for reducing the influence of undesired perturbation and, as will be shown in this work, can be used to develop a controller design to concentrate the controller energy in a selected frequency bandwidth. By extending modern control theory using $\mathcal{H}_\infty$ robust control theory, the uncertainties between the theoretical model and the actual structure can be analysed by means of numerical computation and experimentation, which lays the foundation of robust control design [41–44].

Another issue with traditional vibration attenuation control design is that the controller has only a local effect and global structural vibration control therefore requires a large number of actuators. Recently, with the introduction of the spatial norm concept [45], vibration reduction over an entire structure has been shown to be possible with just a few control actuators. Although the underlying theory describing this approach is well documented, the control approach mainly targets the first few structural resonances within a particular bandwidth. However, in some practical cases, it may be necessary to target resonances at higher frequencies such as for reducing the sound radiation from a structure. This work will later demonstrate how higher frequency vibration can be controlled based on the theories mention in this chapter.

Chapter 2

ANC IN A DUCT USING FEEDFORWARD CONTROL SYSTEMS

As indicated through references in the previous chapter the subject of the ANC system in a duct has already been widely researched. This particular setup allows the illustration of active control at its most elementary level. This chapter details a series of experiments to further demonstrate the idea of ANC and its complexity. A new analytical model is presented for the behaviour of the Filtered-x LMS adaptive algorithm when applied to active noise control in a finite duct. This new model is derived using a Stochastic Differential Equation (SDE) approach. Theoretical predictions are verified through experimental results. The real-time system has been implemented using only I/O cards and a general purpose computer. Automation of the experimental setup allowed the practical verification of the theoretical statistical model using Monte Carlo techniques. It is verified in this chapter that the behaviour of the algorithm is accurately predicted by the theoretical model.

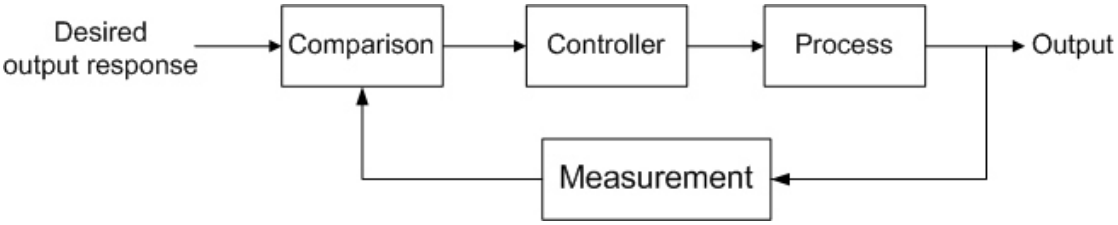

Figure 2.1: Closed-loop feedback control system [3].

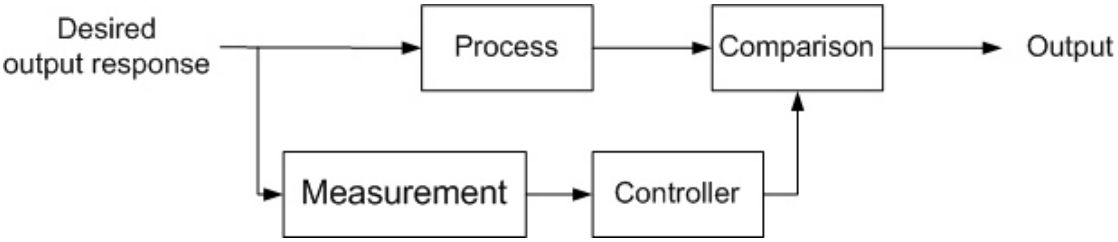

Figure 2.2: Closed-loop feedforward control system.

2.1 Basic ideas of active and adaptive control

A control system is a combination of components that form a system configuration which will provide a desired system response. Linear system theory provides the basis for analysing the system, and assumes a cause-effect relationship for the components of a system.

A feedback control system is a control system that tends to maintain a prescribed relationship of one system variable to another by comparing functions of these variables and using the difference as a means of control [3]. The feedback approach has been a key idea for control system analysis and design. A closed-loop feedback control system is shown in Fig. 2.1 and is further investigated in Chapter 4.

A control system may also employ the feedforward approach. A closed-loop feedforward control system is shown in Fig. 2.2. Modern control theory assumes that the systems engineer can quantitatively specify the required system performance. Whether the aim is to improve the design of a system or to design an adaptive control system, a performance index must be chosen and measured. When

the system parameters are adjusted so that the index reaches an extreme value, commonly a minimum value, the system is then considered an optimum control system. A performance index, in order to be useful, must be a number that is always positive or zero; thus the best system is defined as the system which minimises this index. A suitable performance can be the integral of the square of the error, which is defined as:

$$I = \int_0^T e^2(t)dt \tag{2.1}$$

This work chooses the ANC in a duct case to illustrate a concrete example of active control through a closed-loop feedforward control system. To understand how this basically works, picture a sound signal propagating in the tube, referenced with a first path, and a second sound source called the secondary path which is added in opposition to the phase of the first source in such a way that the addition of the two waves cancel out. This is based on the superposition wave principle, also known as anti-noise. In other words, the objective of ANC is to identify the filter, $\boldsymbol{w}(n)$, using a reference signal, $u(n)$, which will build a signal, aiming to cancel the desired signal, $d(n)$. The efficiency of the algorithm is evaluated for an objective function, generally the error criterion, mentioned above, which allows the updating of the filter coefficients, $\boldsymbol{W}(n)$ (see Fig. 2.3), where $z(n)$ is an undesired noise. This whole process has to be carried out under real-time imperatives. The error criterion can be minimised by using various approaches depending on the characteristics of the reference signal. Differences in outcomes depend on the quality of the cancelling out, computational load, convergence velocity, number of coefficients and stability of the algorithm.

For finding the objective function of the feedforward control algorithm, following is a quick summary of the equations that describes acoustic wave propagation inside a duct. The resonance frequency is related to λ, the wavelength. In our case study, the wavelength is much longer that the longest side dimension of the duct profile. This wave is a plane wave; that is, the phase in the perpendicular plane of a specific coordinate is constant. The propagation equation can be written as

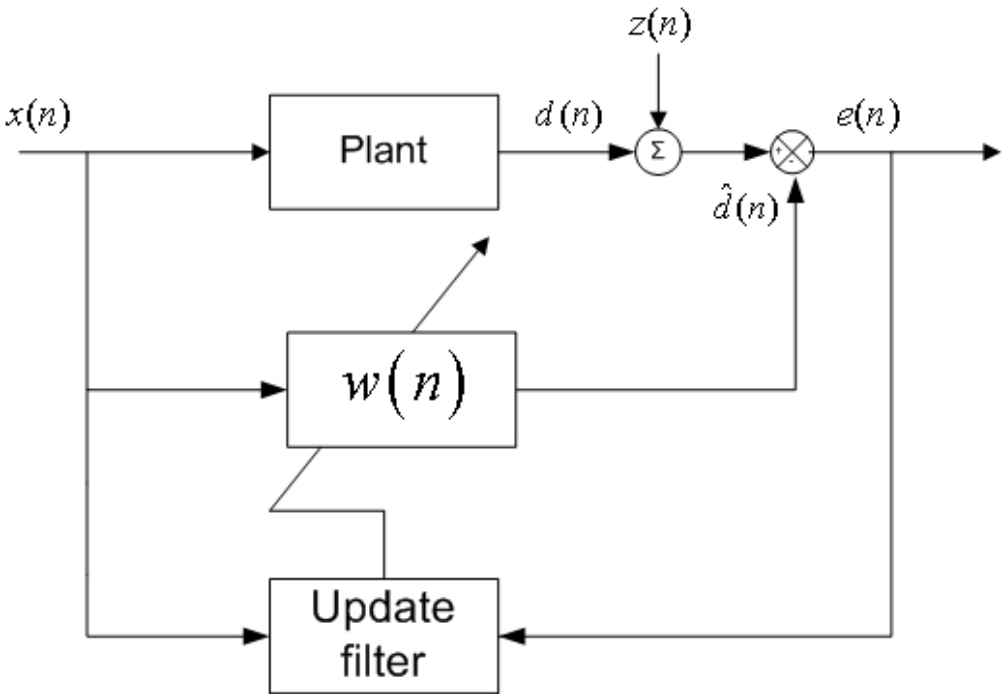

Figure 2.3: Adaptive feedforward control system.

follows:

$$\frac{\partial^2 p(x,t)}{\partial x^2} = \frac{1}{c^2}\frac{\partial^2 p(x,t)}{\partial t^2} \tag{2.2}$$

with $c = \lambda f$. All variables are assumed to be a function of a single spatial coordinate. The pressure $p(x,t)$ is written $p(x,t) = Ae^{j(wt+kx)} + Be^{j(wt-kx)} = p^+(x,t) + p^-(x,t)$, with $p^+(x,t)$ and $p^-(x,t)$ the pressure which propagates in the $+x$ and $-x$ directions respectively. The speed of the particle is related to the pressure expressed in the relationship: $\rho_0 \frac{\partial^2 u(x,t)}{\partial x^2} = -\nabla p(x,t)$, thus:

$$u(x,t) = \frac{1}{\rho_0 c}\left[p^+(x,t) - p^-(x,t)\right] \tag{2.3}$$

Control laws in the ANC, dictate that two functions be presented. The first is the energy density function for a stationary wave: $E = \frac{p^2(x,t)}{2\rho_0 c^2} + \frac{\rho_0 u^2(x,t)}{2} = \frac{p^2(x,t)}{\rho_0 c^2}$. The second is that for the acoustic intensity: $I(x,t) = p(x,t)u(x,t) = \frac{p^2(x,t)}{\rho_0 c}$. These two functions for plane waves are equal. As they are square functions, the per-

formance function therefore has a single minimum, which is helpful in terms of stability convergence.

In general, there are two digital filter structures used for adaptive or active filters: the Finite Impulse Response (FIR) and the Infinite Impulse Response (IIR). The selection of the filter model for the noise control depends on the system in question. FIR filters only contain feedforward paths, while IIR filters contain some feedback paths. The feedback paths of IIR filters have infinite duration. This makes them extremely practical for modelling systems with a long impulse response. However, the presence of feedback with IIR filter structures can cause filters to become unstable. By contrast, FIR filters are inherently stable, which explains their popularity in industrial use.

The equation formulation of Fig. 2.3 is expressed by an FIR structure:

$$\hat{d} = \sum_{l=0}^{n} w_l(n)\ x(n-l) = \boldsymbol{w}^T(n)\boldsymbol{x}(n) \tag{2.4}$$

The resulting error from the generating signal $\hat{d}$ and the desired signal is:

$$e(n) = d(n) + z(n) - \hat{d}(n) = d(n) + z(n) - \boldsymbol{w}^T(n)\boldsymbol{x}(n) \tag{2.5}$$

where $z(n)$ expresses the noise due to the system conditions; to simplify, it assumes zero-mean, stationary, white Gaussian noise with variance σ_z^2. When one deals with stochastic systems, the objective function evaluation is made through the study of means for feedforward control using the Mean Square Error (MSE) function:

$$\begin{aligned} \xi(n) &= E[e^2(n)] = E\left[\left(d(n) + z(n) - \boldsymbol{w}^T(n)\boldsymbol{x}(n)\right)^2\right] \\ &= E[d^2(n)] - 2\boldsymbol{p}^T(n)\boldsymbol{w}(n) + \boldsymbol{w}(n)^T\boldsymbol{R}(n)\boldsymbol{w}(n) + \sigma_z^2 \end{aligned} \tag{2.6}$$

with $\boldsymbol{p}(n)$ the cross-correlation vector between the input and the desired output, and $\boldsymbol{R}(n)$ the autocorrelation matrix of the input signal $\boldsymbol{x}(n)$.

The plant can be defined as $\boldsymbol{w}_{opt}$, the optimal filter to reach. To simplify, $\boldsymbol{w}(n)$

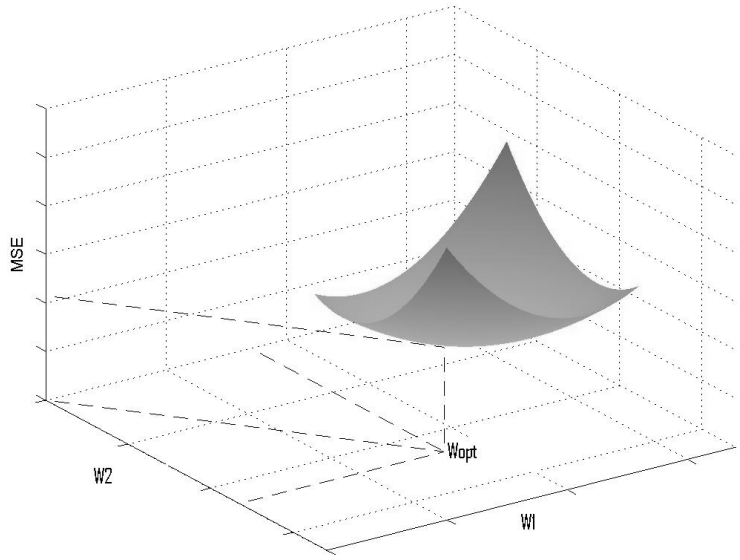

Figure 2.4: MSE plot for $\boldsymbol{w}(n)$ with two coefficients.

is assumed to have the same number of coefficients, and $\boldsymbol{w}_{opt}$ is then the solution which minimises the $\xi(n)$ in Eq. (2.1).

$$\begin{aligned} \frac{d\xi(n)}{d\boldsymbol{w}(n)} &= -2\boldsymbol{p}(n) + 2\boldsymbol{R}(n)\boldsymbol{w}(n) \\ \implies \boldsymbol{w}_{opt} &= \boldsymbol{R}^{-1}\boldsymbol{p}(n) \end{aligned} \tag{2.7}$$

assuming $\boldsymbol{R}(n)$ invertible. The MSE becomes, in this case:

$$\xi(n) = E\left[\left(\boldsymbol{w}_{opt}^T\boldsymbol{x}(n) - \boldsymbol{w}_{opt}^T\boldsymbol{x}(n) + z(n)\right)^2\right] = \sigma_z^2 \tag{2.8}$$

As the MSE is a quadratic function there is only one minimum. Fig. 2.4 shows the MSE curve of the Eq. (2.1) for $\boldsymbol{w}(n)$ with two coefficients. The idea in adaptive control is to update the weight coefficient to reach the $\boldsymbol{w}_{opt}$, whereas active control pre-defines the $\boldsymbol{w}$ vector to be optimal for a pre-defined model.

For adaptive control, the weight vector $\boldsymbol{w}(n)$ is updated through an iterative

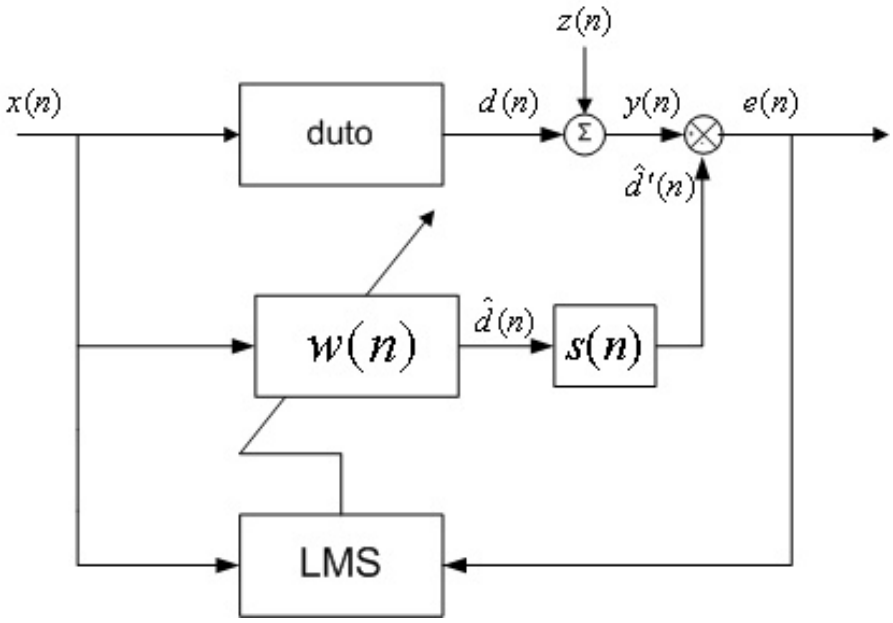

Figure 2.5: Adaptive algorithm with system transfer function $\boldsymbol{s}(n)$.

process. The LMS (Least Mean Square) algorithm, the adaptive algorithm most popular for its simplicity, is taken as an example to illustrate the philosophy of adaptive control. The LMS algorithm belongs to the algorithm family based on the objective gradient function of the MSE that has, as previously mentioned, only one minimum (see [11, 16] for more details):

$$\begin{aligned} \boldsymbol{w}(n+1) &= \boldsymbol{w}(n) - \frac{\mu}{2}\nabla\left[\xi(n)\right] = \boldsymbol{w}(n) - \frac{\mu}{2}2\nabla\left[e(n)\right]e(n) \\ &= \boldsymbol{w}(n) + \mu e(n)\boldsymbol{x}(n) \end{aligned} \tag{2.9}$$

with $\nabla\left[e(n)\right] = -\boldsymbol{x}(n)$ and μ is the step-size.

In the case of ANC, the filter is more complex than shown above because the error signal is obtained through an acoustical sensor as described in [11] and also because the system needs D/A (Digital to Analogue) converters, power amplifiers and speakers. All these can be characterised by a transfer function $\boldsymbol{s}(n)$ coupled with the adaptive filter as shown in Fig. 2.5. As a consequence $\boldsymbol{s}(n)$ modifies the

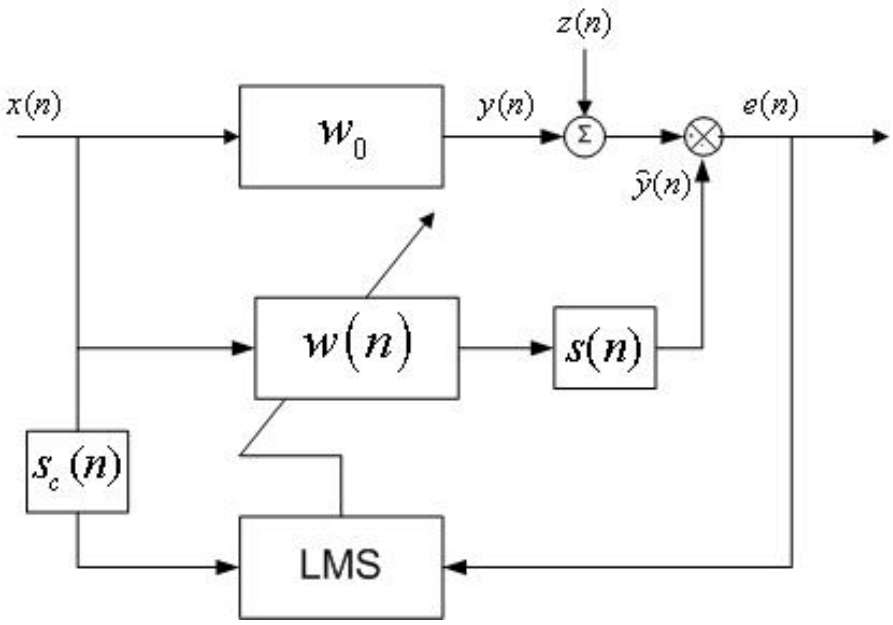

Figure 2.6: Adaptive algorithm with system transfer function approximation $\boldsymbol{s}_c(n)$: block diagram of FxLMS system.

objective function defined by Eq. (2.5). The objective function becomes then:

$$\begin{aligned} e'(n) &= d(n) + z(n) - \hat{d}'(n) = d(n) + z(n) - \boldsymbol{s}(n) * \hat{d}(n) \\ &= d(n) + z(n) - \boldsymbol{s}(n) * (\boldsymbol{s}(n)^T \boldsymbol{x}(n)) \end{aligned} \tag{2.10}$$

The transfer function $\boldsymbol{s}(n)$ has to be approximated by $\hat{\boldsymbol{s}}(n)$ to calculate the new $\nabla[e'(n)]$ in Eq. (2.9): $\nabla[e'(n)] = -\boldsymbol{s}(n) * \boldsymbol{x}(n) \approx -\boldsymbol{s}_c(n) * \boldsymbol{x}(n)$, as shown in Fig. 2.6.

The adaptive filter described in Fig. 2.6 is the FxLMS algorithm, used in most of real-world applications. The FxLMS algorithm's behaviour has been studied by several authors [18, 46] from a statistical point of view. [18] successfully modelled the statistical behaviour of the FxLMS algorithm, but because of the transfer function the model cannot compute systems for a transfer function more than three or four coefficients. There will be a new statistical analysis of the FxLMS algorithm behaviour proposed in this chapter, where the analysis is based on the stochastic differential equation approach introduced in [47] to study the behaviour

of recursive stochastic algorithms through the associated Ordinary Differential Equation (ODE) [48]. This approach has been successfully employed in [49] to study the behaviour of finite precision implementations of adaptive IIR filters. [50] uses this approach to model the NLMS algorithm behaviour and yields very promising results.

2.2 FxLMS model - the SDE method

The updated equation of the FxLMS algorithm is given by Eq. (2.11).

$$\boldsymbol{w}(n+1) = \boldsymbol{w}(n) + \mu e(n) \boldsymbol{S}_c^T \dot{\boldsymbol{x}} \tag{2.11}$$

where $\boldsymbol{w} = [w_0(n) \cdots w_N(n)]^T$ is the adaptive weight vector (it is assumed that $\boldsymbol{w}$ and $\boldsymbol{w}_o$ have the same length N), $\dot{\boldsymbol{x}} = [x(n) \cdots x(n-N-L_c+1)]^T$ is the input data vector, L_c is the estimator filter length of $\boldsymbol{s}_c$, μ is the step-size, and $\boldsymbol{S}_c$ is given by the following approximation matrix:

$$\boldsymbol{S}_{1c}_{[N+L_c,N]} = \begin{bmatrix} s_{c_0} & 0 & \cdots & 0 \\ \vdots & s_{c_0} & \ddots & \vdots \\ \vdots & \vdots & & 0 \\ \vdots & \vdots & & s_{c_0} \\ s_{c_{L_c-1}} & \vdots & & \vdots \\ 0 & s_{c_{L_c-1}} & & \vdots \\ \vdots & \ddots & \ddots & \vdots \\ 0 & \cdots & 0 & s_{c_{L_c-1}} \end{bmatrix} \tag{2.12}$$

and $e(n)$ is the estimation error, which can be written as:

$$\begin{aligned} e(n) &= y(n) + z(n) - \hat{y}(n) \\ &= \boldsymbol{w}_o^T \boldsymbol{x}(x) + z(n) - \sum_{i=0}^{L-1} s_i \boldsymbol{x}^T(n-i) \boldsymbol{w}(n-i) \end{aligned} \tag{2.13}$$

where $\boldsymbol{x}(n) = [x(n) \cdots x(n-N+1)]^T$ is the $N \times 1$ input vector. According to [51], the optimal weight vector is given by:

$$\boldsymbol{w}_{opt} = \boldsymbol{R}_{ss}^{-1} \boldsymbol{R}_s \boldsymbol{w}_o \tag{2.14}$$

with

$$\boldsymbol{R}_{ss} = \sum_{i=0}^{L-1} \sum_{j=0}^{L-1} s_i s_j, \quad \boldsymbol{R}_{i-j} = \boldsymbol{S}^T E\left[\bar{\boldsymbol{x}}(n) \bar{\boldsymbol{x}}^T(n)\right] \boldsymbol{S}$$

$$\boldsymbol{R}_{i-j} = E\left[\boldsymbol{x}^T(n-j) \boldsymbol{x}(n-i)\right],$$

$$\boldsymbol{R}_s = \sum_{i=0}^{L-1} s_i \ \boldsymbol{R}_{-i}, \quad \boldsymbol{R}_{-i} = E\left[\boldsymbol{x}^T(n-i) \boldsymbol{x}(n)\right]$$

where $\bar{\boldsymbol{x}} = [x(n) \cdots x(n-N-L+1)]^T$ and $\boldsymbol{S}$ is the $(N+L-1) \times N$ filtering matrix with coefficients s_i (similar to $\boldsymbol{S}_c$). The steady-state mean adaptive weight vector is given by

$$\boldsymbol{w}_\infty = \lim_{n \to \infty} E[\boldsymbol{w}(n)] = \boldsymbol{R}_{ss_c}^{-T} \boldsymbol{R}_{s_c} \boldsymbol{w}_o \tag{2.15}$$

with

$$\boldsymbol{R}_{ss_c} = \sum_{i=0}^{L-1} \sum_{j=0}^{L_c-1} s_i s_{c_j} \boldsymbol{R}_{i-j} = \boldsymbol{S}^T E\left[\bar{\boldsymbol{x}}(n) \dot{\boldsymbol{x}}^T(n)\right] \boldsymbol{S}_c$$

$$\boldsymbol{R}_{s_c} = \sum_{i=0}^{L_c-1} s_{c_i} \boldsymbol{R}_{-i}$$

Note that $\boldsymbol{w}_\infty = \boldsymbol{w}_{opt}$ for $\boldsymbol{s} = \boldsymbol{s}_c$, as expected. Defining the weight-error vector $\boldsymbol{v}(n) = \boldsymbol{w}(n) - \boldsymbol{w}_\infty$, Eq. (2.11) and Eq. (2.13) become

$$\boldsymbol{v}(n+1) = \boldsymbol{v}(n) + \mu e(n) \boldsymbol{S}_c^T \dot{\boldsymbol{x}}(n) \tag{2.16}$$

$$e(n) = e_0(n) - \sum_{i=0}^{L-1} s_i \boldsymbol{x}^T(n-i) \boldsymbol{v}(n-i) \tag{2.17}$$

2.3 Analysis

To determine an analytical model for the MSE behaviour, some approximations are required. For sufficiently small μ (slow adaptation) it is assumed that $\boldsymbol{v}(n) \approx \cdots \approx \boldsymbol{v}(n-L+1)$. Therefore, Eq. (2.17) can be approximated as

$$e(n) \approx e_0(n) - \boldsymbol{v}^T(n)\boldsymbol{S}^T\bar{\boldsymbol{x}}(n) \tag{2.18}$$

with

$$e_0(n) = z(n) + \boldsymbol{w}_o^T\boldsymbol{x}(n) - \boldsymbol{w}_\infty^T\boldsymbol{S}^T\bar{\boldsymbol{x}}(n) \tag{2.19}$$

The MSE is determined as follows:

$$\begin{aligned} E\left[e^2(n)\right] &= E\left[(e_0(n) - \boldsymbol{v}^T(n)\boldsymbol{S}^T\bar{\boldsymbol{x}}(n))^2\right] \\ = E\left[e_0^2(n) - 2\, e_0\boldsymbol{v}^T(n)\boldsymbol{S}^T\bar{\boldsymbol{x}}(n) + \boldsymbol{v}^T(n)\boldsymbol{S}^T\bar{\boldsymbol{x}}(n)\bar{\boldsymbol{x}}^T(n)\boldsymbol{S}\ \boldsymbol{v}(n)\right] \end{aligned} \tag{2.20}$$

Neglecting the correlation between $\boldsymbol{v}(n)$ and $\bar{\boldsymbol{x}}(n)$ [51], direct calculation of the expected value yields:

$$\begin{aligned} E\left[e^2(n)\right] &\approx \sigma_z^2 + \boldsymbol{w}_o^T\boldsymbol{R}\ \boldsymbol{w}_o + \boldsymbol{w}_\infty^T\boldsymbol{R}_{ss}\boldsymbol{w}_\infty \\ -2\boldsymbol{w}_\infty^T\boldsymbol{S}^T\widehat{\boldsymbol{R}}\ \boldsymbol{w}_o - 2\left[\boldsymbol{w}_o^T\widehat{\boldsymbol{R}}^T\boldsymbol{S} - \boldsymbol{w}_\infty^T\boldsymbol{R}_{ss}\right]\boldsymbol{v}(n) &\quad + \mathrm{tr}\left\{\boldsymbol{R}_{ss}\boldsymbol{K}(n)\right\} \\ = e_0^2 - 2H^T\boldsymbol{v}(n) + \mathrm{tr}\left\{\boldsymbol{R}_{ss}\boldsymbol{K}(n)\right\} \end{aligned} \tag{2.21}$$

with $\boldsymbol{R} = E\left[\bar{\boldsymbol{x}}^T(n)\bar{\boldsymbol{x}}(n)\right]$, $\widehat{\boldsymbol{R}} = E\left[\bar{\boldsymbol{x}}^T(n)\boldsymbol{x}(n)\right]$, $\boldsymbol{K}(n) = E\left[\boldsymbol{v}(n)\boldsymbol{v}^T(n)\right]$ and $H = \boldsymbol{w}_o^T\widehat{\boldsymbol{R}}^T\boldsymbol{S} - \boldsymbol{w}_\infty^T\boldsymbol{R}_{ss}$. In Eq. (2.21), $\mathrm{tr}\{\boldsymbol{A}\}$ is the trace of matrix $\boldsymbol{A}$. The first term

of Eq. (2.21) is equal to:

$$\begin{aligned} & E\left[e_0^2(n)\right] \\ = & E\left[z^2(n)+2\ z(n)\left(\boldsymbol{w}_o^T\boldsymbol{x}(n)-\boldsymbol{w}_\infty^T\boldsymbol{S}^T\bar{\boldsymbol{x}}(n)\right)+\left(\boldsymbol{w}_o^T\boldsymbol{x}(n)-\boldsymbol{w}_\infty^T\boldsymbol{S}^T\bar{\boldsymbol{x}}(n)\right)^2\right] \\ = & \sigma_z^2+E\left[\boldsymbol{w}_o^T\boldsymbol{x}(n)\boldsymbol{x}^T(n)\boldsymbol{w}_o\right] \\ & +E\left[\boldsymbol{w}_\infty^T\boldsymbol{S}^T\bar{\boldsymbol{x}}(n)\bar{\boldsymbol{x}}^T(n)\boldsymbol{S}\ \boldsymbol{w}_\infty\right]-2E\left[\boldsymbol{w}_\infty^T\boldsymbol{S}^T\bar{\boldsymbol{x}}(n)\boldsymbol{x}^T(n)\boldsymbol{w}_o\right] \\ = & \sigma_z^2+\boldsymbol{w}_o^T\boldsymbol{R}\ \boldsymbol{w}_o+\boldsymbol{w}_\infty^T\boldsymbol{S}^T\bar{\boldsymbol{R}}\boldsymbol{S}\ \boldsymbol{w}_\infty-2\boldsymbol{w}_\infty^T\boldsymbol{S}^T\widehat{\boldsymbol{R}}\ \boldsymbol{w}_o=e_0^2 \end{aligned} \tag{2.22}$$

In the following, $\boldsymbol{K}(n)$ and $\boldsymbol{v}(n)$ will be evaluated using the SDE method [47]. To this end, the ordinary differential equation (ODE) associated with Eq. (2.16) is first determined. Following the development done in [52], it can be shown that the associated ODE is given by Eq. (2.23).

$$\frac{d\boldsymbol{v}^D(t)}{dt}=E\left[e(k)\boldsymbol{S}_c^T\dot{\boldsymbol{x}}(t)|\boldsymbol{v}^D(t)\right]=-\frac{1}{2}\frac{d}{d\boldsymbol{v}^D(t)}E\left[e^2(t)\right] \tag{2.23}$$

with $t=\mu n$ a continuous variable. The ODE theory shows that $\boldsymbol{v}(n)$ in Eq. (2.16) converges in probability to the stationary point $\boldsymbol{v}^*$ of Eq. (2.23). It is shown in [47] that the process $\boldsymbol{\chi}_\mu(\tau)=\left(\boldsymbol{v}(\tau)-\boldsymbol{v}^D(t)\right)/\sqrt{\mu}$ converges weakly as $\mu\to 0$ to the continuous Gaussian process $\boldsymbol{\chi}(t)$ which is the solution of the linear SDE described by Eq. (2.24).

$$d\boldsymbol{\chi}(t)=\mu\boldsymbol{F}(\boldsymbol{v}^D(t))\boldsymbol{\chi}(t)dt+\mu\boldsymbol{P}^{1/2}(\boldsymbol{v}^D(t))d\Gamma(t) \tag{2.24}$$

where $\Gamma(t)$ is a Brownian motion, and $\boldsymbol{F}(\boldsymbol{v}^D(t))$ and $\boldsymbol{P}(\boldsymbol{v}^D(t))$ are defined in Eqs. (2.25) and (2.26).

$$\boldsymbol{F}(\boldsymbol{v}^D(t))=\frac{d}{d\boldsymbol{v}^D(t)}E\left[e(t)\boldsymbol{S}_c^T\dot{\boldsymbol{x}}(t)\middle|\boldsymbol{v}^D(t)\right] \tag{2.25}$$

$$\boldsymbol{P}(\boldsymbol{v}^D(t))=\sum_{n\ \in\ \mathbb{Z}}\operatorname{cov}\left[e(n)\boldsymbol{S}_c^T\dot{\boldsymbol{x}}(n),e(0)\boldsymbol{S}_c^T\dot{\boldsymbol{x}}(0)\middle|\boldsymbol{v}(n)=\boldsymbol{v}^D(t)\right] \tag{2.26}$$

To analyse $\boldsymbol{\chi}(t)$ near the equilibrium point $\boldsymbol{v}^*$, the time-variant Eq. (2.24) can be replaced by the time-invariant Eq. (2.27) [47].

$$d\boldsymbol{\chi}(s) = \mu \boldsymbol{F}(\boldsymbol{v}^*)\boldsymbol{\chi}(s)dt + \mu \boldsymbol{P}^{1/2}(\boldsymbol{v}^*)d\Gamma(s) \tag{2.27}$$

where $\boldsymbol{\chi}(s) \approx \boldsymbol{v}(n) - \boldsymbol{v}^*$ for $s = n$. If $\boldsymbol{F}(\boldsymbol{v})$ is independent of $\boldsymbol{v}$, then the SDE is a linear time-invariant even away from $\boldsymbol{v}^*$ [49]. It will be shown that this is the case in the present analysis. Integrating Eq. (2.27), one obtains Eq. (2.28).

$$\boldsymbol{\chi}(s) - \boldsymbol{\chi}(0) = \mu \boldsymbol{F}(\boldsymbol{v}^*) \int_0^s \boldsymbol{\chi}(k)dk + \mu \boldsymbol{P}^{1/2}(\boldsymbol{v}^*) \int_0^s d\Gamma(k) \tag{2.28}$$

The above equation has the following solution:

$$\boldsymbol{\chi}(s) = e^{\mu \boldsymbol{F}(\boldsymbol{v}^*)s}\boldsymbol{\chi}(0) + \boldsymbol{\chi}(\infty) + \mu \boldsymbol{P}^{1/2}(\boldsymbol{v}^*) \int_0^s e^{\mu \boldsymbol{F}(\boldsymbol{v}^*)(s-k)}\Gamma(k)dk \tag{2.29}$$

As $\Gamma(k)$ is an independent Brownian motion with $E[\Gamma(k)] = 0$, the mean solution of Eq. (2.29) is:

$$\begin{aligned} E[\boldsymbol{\chi}(s)] &= E[e^{\mu \boldsymbol{F}(\boldsymbol{v}^*)s}\boldsymbol{\chi}(0) + \boldsymbol{\chi}(\infty)] + E[\mu \boldsymbol{P}^{1/2}(\boldsymbol{v}^*) \int_0^s e^{\mu \boldsymbol{F}(\boldsymbol{v}^*)(s-k)}\Gamma(k)dk] \\ &= e^{\mu \boldsymbol{F}(\boldsymbol{v}^*)s}\boldsymbol{\chi}(0) + \boldsymbol{\chi}(\infty) \end{aligned} \tag{2.30}$$

and then $E[\boldsymbol{\chi}(s)] = E[\boldsymbol{v}(n)]$ for $s = n$ is given by Eq. (2.31).

$$E[\boldsymbol{v}(n)] = e^{\mu \boldsymbol{F}(\boldsymbol{v}^*)n}\boldsymbol{v}(0) \tag{2.31}$$

because $\boldsymbol{v}(\infty)$ is equal to 0 by definition.

It is now necessary to study the fluctuations of $\boldsymbol{v}(n)$, $E\left[\boldsymbol{\chi}(s)\boldsymbol{\chi}^T(s)\right]$. Use of

Itô calculus yields [47] to Eq. (2.32).

$$\frac{d}{ds}E\left[\boldsymbol{\chi}(s)\boldsymbol{\chi}^T(s)\right] = \mu\boldsymbol{F}(\boldsymbol{v}^*)E\left[\boldsymbol{\chi}(s)\boldsymbol{\chi}^T(s)\right] + \mu E\left[\boldsymbol{\chi}(s)\boldsymbol{\chi}^T(s)\right]\boldsymbol{F}^T(\boldsymbol{v}^*) + \mu^2\boldsymbol{P}(\boldsymbol{v}^*) \tag{2.32}$$

In our case, $\boldsymbol{v}^* = 0$ by definition of the weight-error vector. It is then possible to do the approximation shown in Eq. (2.33).

$$\begin{aligned} E\left[\boldsymbol{\chi}(s)\boldsymbol{\chi}^T(s)\right] &= E\left[(\boldsymbol{v}^D(s) - \boldsymbol{v}^*)(\boldsymbol{v}^D(s) - \boldsymbol{v}^*)^T\right] = E\left[\boldsymbol{v}^D(s)\boldsymbol{v}^D(s)^T\right] \\ &= \boldsymbol{K}(s) \approx \boldsymbol{K}(n) \end{aligned} \tag{2.33}$$

Eq. (2.32) can now be rewritten as Eq. (2.34).

$$\frac{d}{ds}\boldsymbol{K}(s) = \mu\boldsymbol{F}(\boldsymbol{v}^*)\boldsymbol{K}(s) + \mu\boldsymbol{K}(s)\boldsymbol{F}^T(\boldsymbol{v}^*) + \mu^2\boldsymbol{P}(\boldsymbol{v}^*) \tag{2.34}$$

To determine the solution of Eq. (2.34), $\boldsymbol{F}(\boldsymbol{v}^*)$ must be evaluated. From Eq. (2.25), the equality of Eq. (2.35) can easily be shown:

$$\begin{aligned} E\left[e(t)\boldsymbol{S}_c^T\dot{\boldsymbol{x}}(t)|\boldsymbol{v}^D(t)\right] &= E\left[\boldsymbol{S}_c^T\dot{\boldsymbol{x}}(t)(e_0(t) - \bar{\boldsymbol{x}}^T\boldsymbol{S}\ \boldsymbol{v}^D(t))|\boldsymbol{v}^D(t)\right] \\ &= E\left[\boldsymbol{S}_c^T\dot{\boldsymbol{x}}(t)e_0(t)\right] - \boldsymbol{R}_{ss_c}^T\boldsymbol{v}^D(t) \end{aligned} \tag{2.35}$$

$\boldsymbol{F}(\boldsymbol{v}^*)$ is then equal to:

$$\boldsymbol{F}(\boldsymbol{v}^*) = \boldsymbol{F}(\boldsymbol{v}^D(t)) = \frac{d}{d\boldsymbol{v}^D(t)}\left[-\boldsymbol{R}_{ss_c}^T\boldsymbol{v}^D(t)\right] = -\boldsymbol{R}_{ss_c} \tag{2.36}$$

since the first term of Eq. (2.35) is not a function of $\boldsymbol{v}^D(t)$. Also, Eq. (2.36) confirms that $\boldsymbol{F}(\boldsymbol{v}^D(t))$ is independent of $\boldsymbol{v}(t)$. Thus, Eq. (2.27) is valid, regardless of the value of $\boldsymbol{v}^*$.

Assuming that all eigenvalues of $\boldsymbol{R}_{ss_c}$ have negative real parts, the solution of Eq. (2.34) is expressed in Eq. (2.37).

$$\boldsymbol{K}(s) = e^{\mu\boldsymbol{F}(\boldsymbol{v}^*)s}\left[\boldsymbol{K}(0) - \boldsymbol{K}(\infty)\right]e^{\mu\boldsymbol{F}^T(\boldsymbol{v}^*)s} + \boldsymbol{K}(\infty) \tag{2.37}$$

where $\boldsymbol{K}(\infty)$ is the solution to the Lyapunov Eq. (2.38).

$$\boldsymbol{F}(\boldsymbol{v}^*)\boldsymbol{K}(\infty) + \boldsymbol{K}(\infty)\boldsymbol{F}^T(\boldsymbol{v}^*) = -\mu\boldsymbol{P}(\boldsymbol{v}^*) \tag{2.38}$$

$\boldsymbol{P}(\boldsymbol{v}^*)$ is evaluated in the following subsection.

2.3.1 Evaluation of $\boldsymbol{P}(\boldsymbol{v}^*)$

From Eq. (2.26), $\boldsymbol{P}(\boldsymbol{v}^D(t))$ can be detailed as follows:

$$\boldsymbol{P}(\boldsymbol{v}^D(t)) = \sum_{n\,\in\,\mathbb{Z}} E\left\{ \begin{array}{c} \left(e(n)\boldsymbol{S}_c^T\dot{\boldsymbol{x}}(n) - E\left[e(n)\boldsymbol{S}_c^T\dot{\boldsymbol{x}}(n)\right]\right) \\ \times \left(e(0)\boldsymbol{S}_c^T\dot{\boldsymbol{x}}(0) - E\left[e(0)\boldsymbol{S}_c^T\dot{\boldsymbol{x}}(0)\right]\right)^T \end{array} \Bigg|_{\boldsymbol{v}(n)=\boldsymbol{v}^D(t)} \right\}$$

$$\begin{aligned}
&= \sum_{n\,\in\,\mathbb{Z}} \Big\{ E\left[\boldsymbol{S}_c^T\dot{\boldsymbol{x}}(n)\bar{\boldsymbol{x}}^T(n)\boldsymbol{S}\;\boldsymbol{v}^D(t)\boldsymbol{v}^T(0)\boldsymbol{S}^T\bar{\boldsymbol{x}}(0)\dot{\boldsymbol{x}}^T(0)\boldsymbol{S}_c\right] && \text{(2.39a)}\\
&\quad - E\left[\boldsymbol{S}_c^T\dot{\boldsymbol{x}}(n)\bar{\boldsymbol{x}}^T(n)\boldsymbol{S}\;\boldsymbol{v}^D(t)e_0(0)\dot{\boldsymbol{x}}^T(0)\boldsymbol{S}_c\right] && \text{(2.39b)}\\
&\quad - E\left[\boldsymbol{S}_c^T\dot{\boldsymbol{x}}(n)e_0(n)\boldsymbol{v}^T(0)\boldsymbol{S}^T\bar{\boldsymbol{x}}(0)\dot{\boldsymbol{x}}^T(0)\boldsymbol{S}_c\right] && \text{(2.39c)}\\
&\quad + E\left[e_0(n)\boldsymbol{S}_c^T\dot{\boldsymbol{x}}(n)\dot{\boldsymbol{x}}^T(0)\boldsymbol{S}_c e_0(0)\right] && \text{(2.39d)}\\
&\quad - E\left[\boldsymbol{S}_c^T\dot{\boldsymbol{x}}(n)\bar{\boldsymbol{x}}^T(n)\boldsymbol{S}\;\boldsymbol{v}^D(t)\right]E\left[\boldsymbol{v}^T(0)\boldsymbol{S}^T\bar{\boldsymbol{x}}(0)\dot{\boldsymbol{x}}^T(0)\boldsymbol{S}_c\right] && \text{(2.39e)}\\
&\quad + E\left[\boldsymbol{S}_c^T\dot{\boldsymbol{x}}(n)\bar{\boldsymbol{x}}^T(n)\boldsymbol{S}\;\boldsymbol{v}^D(t)\right]E\left[e_0(0)\dot{\boldsymbol{x}}^T(0)\boldsymbol{S}_c\right] && \text{(2.39f)}\\
&\quad + E\left[\boldsymbol{S}_c^T\dot{\boldsymbol{x}}(n)e_0(n)\right]E\left[\boldsymbol{v}^T(0)\boldsymbol{S}^T\bar{\boldsymbol{x}}(0)\dot{\boldsymbol{x}}^T(0)\boldsymbol{S}_c\right] && \text{(2.39g)}\\
&\quad - E\left[e_0(n)\boldsymbol{S}_c^T\dot{\boldsymbol{x}}(n)\right]E\left[\dot{\boldsymbol{x}}^T(0)\boldsymbol{S}_c e_0(0)\right]\Big\} && \text{(2.39h)}
\end{aligned}$$

Each of the terms of Eq. (2.39) needs to be approximated. In order to simplify the notation, $\boldsymbol{v}^D(t)$ will be written as $\boldsymbol{v}(t)$. Term (2.39a) then becomes:

$$\begin{aligned}
&E\left[\boldsymbol{S}_c^T\dot{\boldsymbol{x}}(t)\bar{\boldsymbol{x}}^T(t)\boldsymbol{S}\;\boldsymbol{v}(t)\boldsymbol{v}^T(0)\boldsymbol{S}^T\bar{\boldsymbol{x}}(0)\dot{\boldsymbol{x}}^T(0)\boldsymbol{S}_c\right]\\
&\approx E\left[\boldsymbol{S}_c^T\dot{\boldsymbol{x}}(t)\bar{\boldsymbol{x}}^T(t)\boldsymbol{S}\right]\boldsymbol{v}(t)\boldsymbol{v}^T(0)E\left[\boldsymbol{S}^T\bar{\boldsymbol{x}}(0)\dot{\boldsymbol{x}}^T(0)\boldsymbol{S}_c\right]
\end{aligned} \tag{2.40}$$

Term (2.39b) becomes:

$$
\begin{aligned}
&E\left[\boldsymbol{S}_c^T\dot{\boldsymbol{x}}(n)\bar{\boldsymbol{x}}^T(n)\boldsymbol{S}\ \boldsymbol{v}(t)e_0(0)\dot{\boldsymbol{x}}^T(0)\boldsymbol{S}_c\right]\\
&= E\Big[\boldsymbol{S}_c^T\dot{\boldsymbol{x}}(n)\bar{\boldsymbol{x}}^T(n)\boldsymbol{S}\ \boldsymbol{v}(t)(z(0)+\boldsymbol{w}_o^T\boldsymbol{x}(0)-\boldsymbol{w}_\infty^T\boldsymbol{S}^T\bar{\boldsymbol{x}}(0))\dot{\boldsymbol{x}}^T(0)\boldsymbol{S}_c\Big]\\
&= E\Big[\boldsymbol{S}_c^T\dot{\boldsymbol{x}}(n)\bar{\boldsymbol{x}}^T(n)\boldsymbol{S}\ \boldsymbol{v}(t)(\boldsymbol{w}_o^T\boldsymbol{x}(0)-\boldsymbol{w}_\infty^T\boldsymbol{S}^T\bar{\boldsymbol{x}}(0))\dot{\boldsymbol{x}}^T(0)\boldsymbol{S}_c\Big]\\
&\approx E\left[\boldsymbol{S}_c^T\dot{\boldsymbol{x}}(n)\bar{\boldsymbol{x}}^T(n)\boldsymbol{S}\right]\boldsymbol{v}(t)\boldsymbol{w}_o^T E\left[\boldsymbol{x}(0)\dot{\boldsymbol{x}}^T(0)\boldsymbol{S}_c\right]\\
&\quad -E\left[\boldsymbol{S}_c^T\dot{\boldsymbol{x}}(n)\bar{\boldsymbol{x}}^T(n)\boldsymbol{S}\right]\boldsymbol{v}(t)\boldsymbol{w}_\infty^T E\left[\boldsymbol{S}^T\bar{\boldsymbol{x}}^T(0))\dot{\boldsymbol{x}}(0)\boldsymbol{S}_c\right]
\end{aligned}
\tag{2.41}
$$

Term (2.39c) becomes:

$$
\begin{aligned}
&E[\boldsymbol{S}_c^T\dot{\boldsymbol{x}}(n)e_0(n)\boldsymbol{v}^T(0)\boldsymbol{S}^T\bar{\boldsymbol{x}}(0)\dot{\boldsymbol{x}}^T(0)\boldsymbol{S}_c]\\
&= E[\boldsymbol{S}_c^T\dot{\boldsymbol{x}}(n)(z(n)+\boldsymbol{w}_o^T\boldsymbol{x}(n)-\boldsymbol{w}_\infty^T\boldsymbol{S}^T\bar{\boldsymbol{x}}(n))\boldsymbol{v}^T(0)\boldsymbol{S}^T\bar{\boldsymbol{x}}(0)\dot{\boldsymbol{x}}^T(0)\boldsymbol{S}_c]\\
&= E[\boldsymbol{S}_c^T\dot{\boldsymbol{x}}(n)(\boldsymbol{w}_o^T\boldsymbol{x}(n)-\boldsymbol{w}_\infty^T\boldsymbol{S}^T\bar{\boldsymbol{x}}(n))\boldsymbol{v}^T(0)\boldsymbol{S}^T\bar{\boldsymbol{x}}(0)\dot{\boldsymbol{x}}^T(0)\boldsymbol{S}_c]\\
&\approx E\left[\boldsymbol{S}_c^T\dot{\boldsymbol{x}}(n)\boldsymbol{x}^T(n)\right]\boldsymbol{w}_o\boldsymbol{v}^T(0)E\left[\boldsymbol{S}^T\bar{\boldsymbol{x}}(0)\dot{\boldsymbol{x}}^T(0)\boldsymbol{S}_c\right]\\
&\quad -E[\boldsymbol{S}_c^T\dot{\boldsymbol{x}}(n)\bar{\boldsymbol{x}}^T(n)\boldsymbol{S}]\boldsymbol{w}_\infty\boldsymbol{v}^T(0)E[\boldsymbol{S}^T\bar{\boldsymbol{x}}(n))\dot{\boldsymbol{x}}^T(0)\boldsymbol{S}_c]
\end{aligned}
\tag{2.42}
$$

Term (2.39e) becomes:

$$
\begin{aligned}
&E[\boldsymbol{S}_c^T\dot{\boldsymbol{x}}(n)\bar{\boldsymbol{x}}^T(n)\boldsymbol{S}\ \boldsymbol{v}(t)]E[\boldsymbol{v}^T(0)\boldsymbol{S}^T\bar{\boldsymbol{x}}(0)\dot{\boldsymbol{x}}^T(0)\boldsymbol{S}_c]\\
&= E[\boldsymbol{S}_c^T\dot{\boldsymbol{x}}(n)\bar{\boldsymbol{x}}^T(n)\boldsymbol{S}]\boldsymbol{v}(t)\boldsymbol{v}^T(0)E[\boldsymbol{S}^T\bar{\boldsymbol{x}}(0)\dot{\boldsymbol{x}}^T(0)\boldsymbol{S}_c]
\end{aligned}
\tag{2.43}
$$

Term (2.39d) becomes:

$$
\begin{aligned}
&E[e_0(n)\boldsymbol{S}_c^T\dot{\boldsymbol{x}}(n)\dot{\boldsymbol{x}}^T(0)\boldsymbol{S}_c e_0(0)] \\
&= E[(z(n)+\boldsymbol{w}_o^T\boldsymbol{x}(n)-\boldsymbol{w}_\infty^T\boldsymbol{S}^T\bar{\boldsymbol{x}}(n))\boldsymbol{S}_c^T\dot{\boldsymbol{x}}(n)\dot{\boldsymbol{x}}^T(0)\boldsymbol{S}_c \\
&\quad (z(0)+\boldsymbol{w}_o^T\boldsymbol{x}(0)-\boldsymbol{w}_\infty^T\boldsymbol{S}^T\bar{\boldsymbol{x}}(0))] \\
&= E[z(n)z(0)\boldsymbol{S}_c^T\dot{\boldsymbol{x}}(n)\bar{\boldsymbol{x}}^T(0)\boldsymbol{S}_c] \\
&+E[\boldsymbol{S}_c^T\dot{\boldsymbol{x}}(n)\boldsymbol{x}^T(n)\boldsymbol{w}_o\boldsymbol{w}_o^T\boldsymbol{x}(0)\dot{\boldsymbol{x}}^T(0)\boldsymbol{S}_c] \\
&-E[\boldsymbol{S}_c^T\dot{\boldsymbol{x}}(n)\boldsymbol{x}^T(n)\boldsymbol{w}_o\boldsymbol{w}_\infty^T\boldsymbol{S}^T\bar{\boldsymbol{x}}(0)\dot{\boldsymbol{x}}^T(0)\boldsymbol{S}_c] \\
&-E[\boldsymbol{S}_c^T\dot{\boldsymbol{x}}(n)\bar{\boldsymbol{x}}^T(n)\boldsymbol{S}\boldsymbol{w}_\infty\boldsymbol{w}_o^T\boldsymbol{x}(0)\dot{\boldsymbol{x}}^T(0)\boldsymbol{S}_c] \\
&+E[\boldsymbol{S}_c^T\dot{\boldsymbol{x}}(n)\bar{\boldsymbol{x}}^T(n)\boldsymbol{S}\boldsymbol{w}_\infty\boldsymbol{w}_\infty^T\boldsymbol{S}^T\bar{\boldsymbol{x}}(0)\dot{\boldsymbol{x}}^T(0)\boldsymbol{S}_c] \\
&\approx E[z(n)z(0)]E[\boldsymbol{S}_c^T\dot{\boldsymbol{x}}(n)\dot{\boldsymbol{x}}^T(0)\boldsymbol{S}_c] \\
&+E[\boldsymbol{S}_c^T\dot{\boldsymbol{x}}(n)\boldsymbol{x}^T(n)]\boldsymbol{w}_o\boldsymbol{w}_o^TE[\boldsymbol{x}(0)\dot{\boldsymbol{x}}^T(0)\boldsymbol{S}_c] \\
&-E[\boldsymbol{S}_c^T\dot{\boldsymbol{x}}(n)\boldsymbol{x}^T(n)]\boldsymbol{w}_o\boldsymbol{w}_\infty^TE[\boldsymbol{S}^T\bar{\boldsymbol{x}}(0)\dot{\boldsymbol{x}}^T(0)\boldsymbol{S}_c] \\
&-E[\boldsymbol{S}_c^T\dot{\boldsymbol{x}}(n)\bar{\boldsymbol{x}}^T(n)\boldsymbol{S}]\boldsymbol{w}_\infty\boldsymbol{w}_o^TE[\boldsymbol{x}(0)\dot{\boldsymbol{x}}^T(0)\boldsymbol{S}_c] \\
&+E[\boldsymbol{S}_c^T\dot{\boldsymbol{x}}(n)\bar{\boldsymbol{x}}^T(n)\boldsymbol{S}]\boldsymbol{w}_\infty\boldsymbol{w}_\infty^TE[\boldsymbol{S}^T\bar{\boldsymbol{x}}(0)\dot{\boldsymbol{x}}^T(0)\boldsymbol{S}_c]
\end{aligned}
\tag{2.44}
$$

Term (2.39f) becomes:

$$
\begin{aligned}
&E[\boldsymbol{S}_c^T\dot{\boldsymbol{x}}(n)\bar{\boldsymbol{x}}^T(n)\boldsymbol{S}\ \boldsymbol{v}(t)]E[e_0(0)\dot{\boldsymbol{x}}^T(0)\boldsymbol{S}_c] \\
&= E[\boldsymbol{S}_c^T\dot{\boldsymbol{x}}(n)\bar{\boldsymbol{x}}^T(n)\boldsymbol{S}\boldsymbol{v}(t)]E[(z(0)+\boldsymbol{w}_o^T\boldsymbol{x}(0)-\boldsymbol{w}_\infty^T\boldsymbol{S}^T\bar{\boldsymbol{x}}(0))\dot{\boldsymbol{x}}^T(0)\boldsymbol{S}_c] \\
&= E[\boldsymbol{S}_c^T\dot{\boldsymbol{x}}(n)\bar{\boldsymbol{x}}^T(n)\boldsymbol{S}\boldsymbol{v}(t)]E[(\boldsymbol{w}_o^T\boldsymbol{x}(0)-\boldsymbol{w}_\infty^T\boldsymbol{S}^T\bar{\boldsymbol{x}}(0))\dot{\boldsymbol{x}}^T(0)\boldsymbol{S}_c] \\
&= E[\boldsymbol{S}_c^T\dot{\boldsymbol{x}}(n)\bar{\boldsymbol{x}}^T(n)\boldsymbol{S}\boldsymbol{v}(t)]E[\boldsymbol{w}_o^T\boldsymbol{x}(0)\dot{\boldsymbol{x}}^T(0)\boldsymbol{S}_c] \\
&-E[\boldsymbol{S}_c^T\dot{\boldsymbol{x}}(n)\bar{\boldsymbol{x}}^T(n)\boldsymbol{S}\boldsymbol{v}(t)]E[\boldsymbol{w}_\infty^T\boldsymbol{S}^T\bar{\boldsymbol{x}}(0)\dot{\boldsymbol{x}}^T(0)\boldsymbol{S}_c] \\
&= E[\boldsymbol{S}_c^T\dot{\boldsymbol{x}}(n)\bar{\boldsymbol{x}}^T(n)\boldsymbol{S}]\boldsymbol{v}(t)\boldsymbol{w}_o^TE[\boldsymbol{x}(0)\dot{\boldsymbol{x}}^T(0)\boldsymbol{S}_c] \\
&-E[\boldsymbol{S}_c^T\dot{\boldsymbol{x}}(n)\bar{\boldsymbol{x}}^T(n)\boldsymbol{S}]\boldsymbol{v}(t)\boldsymbol{w}_\infty^TE[\boldsymbol{S}^T\bar{\boldsymbol{x}}(0)\dot{\boldsymbol{x}}^T(0)\boldsymbol{S}_c]
\end{aligned}
\tag{2.45}
$$

Term (2.39g) becomes:

$$
\begin{aligned}
&E[\boldsymbol{S}_c^T\dot{\boldsymbol{x}}(n)e_0(n)]E[\boldsymbol{v}^T(0)\boldsymbol{S}^T\bar{\boldsymbol{x}}(0)\dot{\boldsymbol{x}}^T(0)\boldsymbol{S}_c] \\
&= E[\boldsymbol{S}_c^T\dot{\boldsymbol{x}}(n)(z(n)+\boldsymbol{w}_o^T\boldsymbol{x}(n)-\boldsymbol{w}_\infty^T\boldsymbol{S}^T\bar{\boldsymbol{x}}(n))]E[\boldsymbol{v}^T(0)\boldsymbol{S}^T\bar{\boldsymbol{x}}(0)\dot{\boldsymbol{x}}^T(0)\boldsymbol{S}_c] \\
&= E[\boldsymbol{S}_c^T\dot{\boldsymbol{x}}(n)(\boldsymbol{w}_o^T\boldsymbol{x}(n)-\boldsymbol{w}_\infty^T\boldsymbol{S}^T\bar{\boldsymbol{x}}(n))] \\
&E[\boldsymbol{v}^T(0)\boldsymbol{S}^T\bar{\boldsymbol{x}}(0)\dot{\boldsymbol{x}}^T(0)\boldsymbol{S}_c] = E[\boldsymbol{S}_c^T\dot{\boldsymbol{x}}(n)\boldsymbol{x}^T(n)\boldsymbol{w}_o]E[\boldsymbol{v}^T(0)\boldsymbol{S}^T\bar{\boldsymbol{x}}(0)\dot{\boldsymbol{x}}^T(0)\boldsymbol{S}_c] \\
&-E[\boldsymbol{S}_c^T\dot{\boldsymbol{x}}(n)\bar{\boldsymbol{x}}^T(n)\boldsymbol{S}\boldsymbol{w}_\infty]E[\boldsymbol{v}^T(0)\boldsymbol{S}^T\bar{\boldsymbol{x}}(0)\dot{\boldsymbol{x}}^T(0)\boldsymbol{S}_c] \\
&= E[\boldsymbol{S}_c^T\dot{\boldsymbol{x}}(n)\boldsymbol{x}^T(n)]\boldsymbol{w}_o\boldsymbol{v}^T(0)E[\boldsymbol{S}^T\bar{\boldsymbol{x}}(0)\dot{\boldsymbol{x}}^T(0)\boldsymbol{S}_c] \\
&-E[\boldsymbol{S}_c^T\dot{\boldsymbol{x}}(n)\bar{\boldsymbol{x}}^T(n)\boldsymbol{S}]\boldsymbol{w}_\infty\boldsymbol{v}^T(0)E[\boldsymbol{S}^T\bar{\boldsymbol{x}}(0)\dot{\boldsymbol{x}}^T(0)\boldsymbol{S}_c]
\end{aligned}
\tag{2.46}
$$

And term (2.39h) becomes:

$$
\begin{aligned}
&E[e_0(n)\boldsymbol{S}_c^T\dot{\boldsymbol{x}}(n)]E[\dot{\boldsymbol{x}}^T(0)\boldsymbol{S}_c e_0(0)] \\
&= E[\boldsymbol{S}_c^T\dot{\boldsymbol{x}}(n)(z(n)+\boldsymbol{w}_o^T\boldsymbol{x}(n)-\boldsymbol{w}_\infty^T\boldsymbol{S}^T\bar{\boldsymbol{x}}(n))] \\
&E[\dot{\boldsymbol{x}}^T(0)\boldsymbol{S}_c(z(0)+\boldsymbol{w}_o^T\boldsymbol{x}(0)-\boldsymbol{w}_\infty^T\boldsymbol{S}^T\bar{\boldsymbol{x}}(0))] \\
&= E[\boldsymbol{S}_c^T\dot{\boldsymbol{x}}(n)(\boldsymbol{w}_o^T\boldsymbol{x}(n)-\boldsymbol{w}_\infty^T\boldsymbol{S}^T\bar{\boldsymbol{x}}(n))] \\
&E[\dot{\boldsymbol{x}}^T(0)\boldsymbol{S}_c(\boldsymbol{w}_o^T\boldsymbol{x}(0)-\boldsymbol{w}_\infty^T\boldsymbol{S}^T\bar{\boldsymbol{x}}(0))] \\
&= E[\boldsymbol{S}_c^T\dot{\boldsymbol{x}}(n)\boldsymbol{x}^T(n)\boldsymbol{w}_o]E[\boldsymbol{w}_o^T\boldsymbol{x}(0)\dot{\boldsymbol{x}}^T(0)\boldsymbol{S}_c] \\
&-E[\boldsymbol{S}_c^T\dot{\boldsymbol{x}}(n)\boldsymbol{x}^T(n)\boldsymbol{w}_o]E[\boldsymbol{w}_\infty^T\boldsymbol{S}^T\bar{\boldsymbol{x}}(0)\dot{\boldsymbol{x}}^T(0)\boldsymbol{S}_c] \\
&-E[\boldsymbol{S}_c^T\dot{\boldsymbol{x}}(n)\boldsymbol{x}^T(n)\boldsymbol{S}\boldsymbol{w}_\infty)]E[\boldsymbol{w}_o^T\boldsymbol{x}(0)\dot{\boldsymbol{x}}^T(0)\boldsymbol{S}_c] \\
&+E[\boldsymbol{S}_c^T\dot{\boldsymbol{x}}(n)\boldsymbol{x}^T(n)\boldsymbol{S}\boldsymbol{w}_\infty)]E[\boldsymbol{w}_\infty^T\boldsymbol{S}^T\bar{\boldsymbol{x}}(0)\dot{\boldsymbol{x}}^T(0)\boldsymbol{S}_c] \\
&= E[\boldsymbol{S}_c^T\dot{\boldsymbol{x}}(n)\boldsymbol{x}^T(n)]\boldsymbol{w}_o\boldsymbol{w}_o^TE[\boldsymbol{x}(0)\dot{\boldsymbol{x}}^T(0)\boldsymbol{S}_c] \\
&-E[\boldsymbol{S}_c^T\dot{\boldsymbol{x}}(n)\boldsymbol{x}^T(n)]\boldsymbol{w}_o\boldsymbol{w}_\infty^TE[\boldsymbol{S}^T\bar{\boldsymbol{x}}(0)\dot{\boldsymbol{x}}^T(0)\boldsymbol{S}_c] \\
&-E[\boldsymbol{S}_c^T\dot{\boldsymbol{x}}(n)\boldsymbol{x}^T(n)\boldsymbol{S}]\boldsymbol{w}_\infty\boldsymbol{w}_o^TE[\boldsymbol{x}(0)\dot{\boldsymbol{x}}^T(0)\boldsymbol{S}_c] \\
&+E[\boldsymbol{S}_c^T\dot{\boldsymbol{x}}(n)\boldsymbol{x}^T(n)\boldsymbol{S}]\boldsymbol{w}_\infty\boldsymbol{w}_\infty^TE[\boldsymbol{S}^T\bar{\boldsymbol{x}}(0)\dot{\boldsymbol{x}}^T(0)\boldsymbol{S}_c]
\end{aligned}
\tag{2.47}
$$

After developing or approximating each term, one notices that term (2.39a) can be cancelled by term (2.39e), term (2.39b) cancelled by term (2.39f), term (2.39c) cancelled by term (2.39g) and four of the five terms of (2.39d) can be cancelled by term (2.39h). The only term left is the first term of Eq. (2.44). $\boldsymbol{P}$ can then be

approximated by:

$$\begin{aligned}\boldsymbol{P}(\boldsymbol{v}(t)) &\approx \sum_{n\,\in\,\mathbb{Z}} E[z(n)z(0)]E[\boldsymbol{S}_c^T\dot{\boldsymbol{x}}(n)\dot{\boldsymbol{x}}^T(0)\boldsymbol{S}_c] \\ &= E[z^2(0)]E[\boldsymbol{S}_c^T\dot{\boldsymbol{x}}(0)\dot{\boldsymbol{x}}^T(0)\boldsymbol{S}_c] = \sigma_z^2\boldsymbol{R}_{cc} \end{aligned} \tag{2.48}$$

with $\boldsymbol{R}_{cc} = E\left[\boldsymbol{S}_c^T\dot{\boldsymbol{x}}(n)\dot{\boldsymbol{x}}^T(n)\boldsymbol{S}_c\right]$. The summation in Eq. (2.48) disappears because $E[z(n)z(0)] = 0$ when $n \neq 0$, which is the case here because the noise is white.

2.3.2 Case when $\boldsymbol{S}_c = \boldsymbol{S}$ (perfect secondary path estimation)

When $\boldsymbol{S}_c = \boldsymbol{S}$, the matrix $\boldsymbol{R}_{ss_c}$ is equal to $\boldsymbol{R}_{ss}$ and then Eq. (2.36) becomes equal to $-\boldsymbol{R}_{ss}$. Using the definition of $\tilde{\boldsymbol{K}}$, $\tilde{\boldsymbol{K}}(n) = \boldsymbol{Q}^T\boldsymbol{K}(n)\boldsymbol{Q}$, Eq. (2.34) can be simplified greatly to:

$$\begin{aligned}\frac{d}{dt}\boldsymbol{Q}^T\boldsymbol{K}(t)\boldsymbol{Q} &= \mu\boldsymbol{Q}^T\boldsymbol{F}(\boldsymbol{v}^*)\boldsymbol{K}(t)\boldsymbol{Q} + \mu\boldsymbol{Q}^T\boldsymbol{K}(t)\boldsymbol{F}^T(\boldsymbol{v}^*)\boldsymbol{Q} + \mu^2\boldsymbol{Q}^T\boldsymbol{P}(\boldsymbol{v}^*)\boldsymbol{Q} \\ \frac{d}{dt}\tilde{\boldsymbol{K}}(t) &= -\mu\boldsymbol{Q}^T\boldsymbol{R}_{ss}\boldsymbol{K}(t)\boldsymbol{Q} - \mu\boldsymbol{Q}^T\boldsymbol{K}(t)\boldsymbol{R}_{ss}\boldsymbol{Q} + \mu^2\boldsymbol{Q}^T\boldsymbol{P}(\boldsymbol{v}^*)\boldsymbol{Q} \\ &= -\mu\left(\boldsymbol{\Lambda}\tilde{\boldsymbol{K}}(t) + \tilde{\boldsymbol{K}}(t)\boldsymbol{\Lambda}\right) + \mu^2\tilde{\boldsymbol{P}} \\ &\Rightarrow \frac{d}{dt}\tilde{k}_i(t) = -2\mu\lambda_i\tilde{k}_i(t) + \mu^2\tilde{\pi}_i \end{aligned} \tag{2.49}$$

with $\boldsymbol{R}_{ss} = \boldsymbol{Q}\boldsymbol{\Lambda}\boldsymbol{Q}^T$, $\boldsymbol{\lambda} = diag(\boldsymbol{\Lambda})$, $\tilde{\boldsymbol{k}}(t) = diag(\tilde{\boldsymbol{K}}(t)) = [\tilde{k}_0(t)\cdots\tilde{k}_i(t)\cdots\tilde{k}_N(t)]^T$, $\tilde{\boldsymbol{P}} = \boldsymbol{Q}^T\boldsymbol{P}(\boldsymbol{v}^*)\boldsymbol{Q}$ and $\tilde{\boldsymbol{\pi}} = diag(\tilde{\boldsymbol{P}})$. Note that Eq. (2.49) is now a set of N independent equations. Its solution is given by:

$$\tilde{k}_i(t) = e^{-2\mu\lambda_i\ t}\left[\tilde{k}_i(0) - \tilde{k}_i(\infty)\right] + \tilde{k}_i(\infty) \tag{2.50}$$

with $\tilde{\boldsymbol{k}}(\infty) = [\tilde{k}_0(\infty)\cdots\tilde{k}_i(\infty)\cdots\tilde{k}_N(\infty)]^T$ given by (assuming nonzero eigenvalues):

$$\tilde{k}_i(\infty) = \frac{\mu}{2\lambda_i}\tilde{\pi}_i \tag{2.51}$$

The next step is then to calculate $\boldsymbol{P}$ to obtain $\tilde{\pi}_i$ in Eq. (2.51). As the case $\boldsymbol{S}_c = \boldsymbol{S}$ is considered in this section, Eq. (2.51) can be simplified, since $\boldsymbol{P} \approx \sigma_z^2 \boldsymbol{R}_{ss}$:

$$\tilde{k}_i(\infty) = \frac{\mu}{2}\sigma_z^2 \tag{2.52}$$

Eq. (2.50) becomes:

$$\tilde{k}_i(t) = e^{-2\mu\lambda_i\ t}\left[\tilde{k}_i(0) - \frac{\mu}{2}\sigma_z^2\right] + \frac{\mu}{2}\sigma_z^2 \tag{2.53}$$

Eq. (2.21) can be rewritten as a function of the eigen matrix $\boldsymbol{Q}$ and the eigenvalue matrix $\boldsymbol{\Lambda}$:

$$E\left[e^2(t)\right] \approx e_0^2 - 2H^T\boldsymbol{v}(t) + \boldsymbol{\lambda}^T\tilde{\boldsymbol{k}}(t) \tag{2.54}$$

2.3.3 General case when $\boldsymbol{S}_c \neq \boldsymbol{S}$

In this case the solution cannot be simplified, and so the matrices found for the general case are substituted; with $\boldsymbol{F} = \boldsymbol{R}_{ss_c}$ and $\boldsymbol{P} = \sigma_z^2\boldsymbol{R}_{cc}$, Eq. (2.37) becomes:

$$\boldsymbol{K}(t) = e^{-\mu\boldsymbol{R}_{ss_c}t}\left[\boldsymbol{K}(0) - \boldsymbol{K}(\infty)\right]e^{-\mu\boldsymbol{R}_{ss_c}^T t} + \boldsymbol{K}(\infty) \tag{2.55}$$

and Eq. (2.38)

$$\boldsymbol{R}_{ss_c}\boldsymbol{K}(\infty) + \boldsymbol{K}(\infty)\boldsymbol{R}_{ss_c}^T = -\mu\sigma_z^2\boldsymbol{R}_{cc} \tag{2.56}$$

The Lyapunov equation is solved through [53] verifying that the new eigenvalues $\lambda_0, \ldots, \lambda_{N-1}$ of $\boldsymbol{R}_{ss_c}$ satisfy $\lambda_i + \lambda_j \neq 0$ for $i, j = 0, \ldots, N-1$.

The MSE (see Eq. (2.21)) can be rewritten as:

$$\begin{aligned} E\left[e^2(n)\right] &\approx e_0^2 - 2H^T e^{-\mu\boldsymbol{R}_{ss_c}t}\boldsymbol{v}(0) \\ &+\mathrm{tr}\left\{\boldsymbol{R}_{ss}\left(e^{-\mu\boldsymbol{R}_{ss_c}t}\left[\boldsymbol{K}(0) - \boldsymbol{K}(\infty)\right]e^{-\mu\boldsymbol{R}_{ss_c}^T t} + \boldsymbol{K}(\infty)\right)\right\} \end{aligned} \tag{2.57}$$

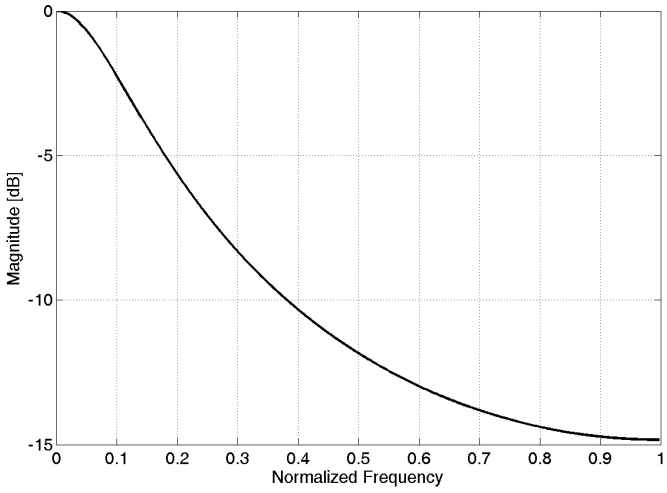

Figure 2.7: The IIR filter generating the correlated input $x(n)$.

2.3.4 Simulations

The main objective of this section is to confirm, through simulation results, the performance of this new model with correlated signal inputs.

simulation 1

The objective of the simulation is to show the accuracy of the model for a number of $\boldsymbol{w}_o$ taps N equals to 100, $\boldsymbol{s}$ taps L equals to 10 and 100, and for $\mu = 0.005, 0.0001$. In the simulation it was not possible to compare the performance of this model with the best existing model [18], because it would have been too much time-consuming in terms of computing [18]'s model for the number of taps L used.

Two curves are plotted: simulations (1000 runs) and the new model. The simulation specifications are: to obtain correlated signal input $x(n)$, the input signal is generated by a second-order auto-regressive filter with the parameters $a_0 = 1$, a_1, a_2 and a Gaussian white, zero mean excitation. The coefficients a_1 and a_2 have values $a_1 = -0.7$ and $a_2 = 0.01$ giving the Fig. 2.8. To be able to generate an input signal with dispersions $\chi = 30$.

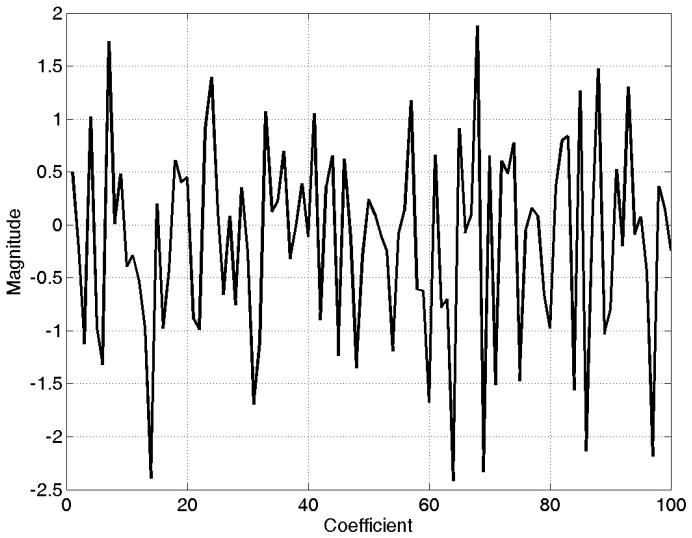

Figure 2.8: $\boldsymbol{w}_0$, the plant filter used for the simulation with 100 coefficients.

To the generated signal $x(n)$ a Gaussian, zero mean noise with variance $\sigma_z^2 = 1e^{-6}$ is added. The auto-correlation matrix of the system is given by [16]. The plant shape is an N random coefficients vector with $\|\boldsymbol{v}(0)\|^2 = 88$. Fig. 2.8 shows the plant vector. The $\boldsymbol{s}$ filter shape is an L random coefficients vector. Figs. 2.9 and 2.10 show the two $\boldsymbol{s}$ vectors used.

Figs. 2.11, 2.12 give the results obtained in this simulation.

simulation 2

This simulation represents a more realistic case where the plant $\boldsymbol{w}_o$ is a low-pass filter with number of coefficients N equals to 100 as shown in Fig. 2.13; $\boldsymbol{s}$ is also a low-pass filter, including the plant frequency range with taps L equal to 10 with the characteristic shown in Fig. 2.14, and 100 with the characteristic shown in Fig. 2.15, and for $\mu = 0.002, 0.001$ which are in Fig. 2.16 and Fig. 2.17 respectively. The input specification is the same as simulation 1. Figs. 2.16 and 2.17 give the results obtained in simulation 2.

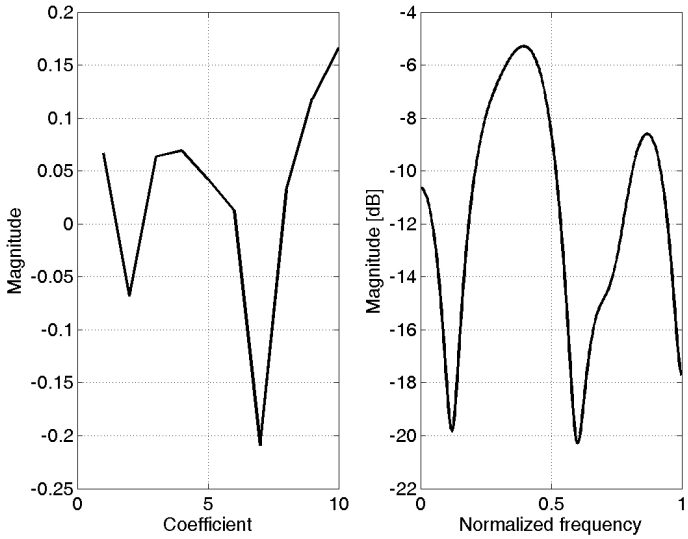

Figure 2.9: The 10 $\boldsymbol{s}$ coefficients used.

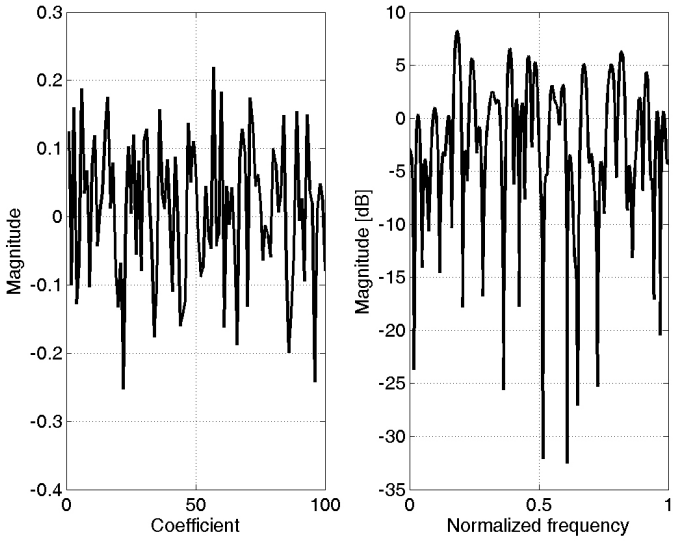

Figure 2.10: The 100 $\boldsymbol{s}$ coefficients used.

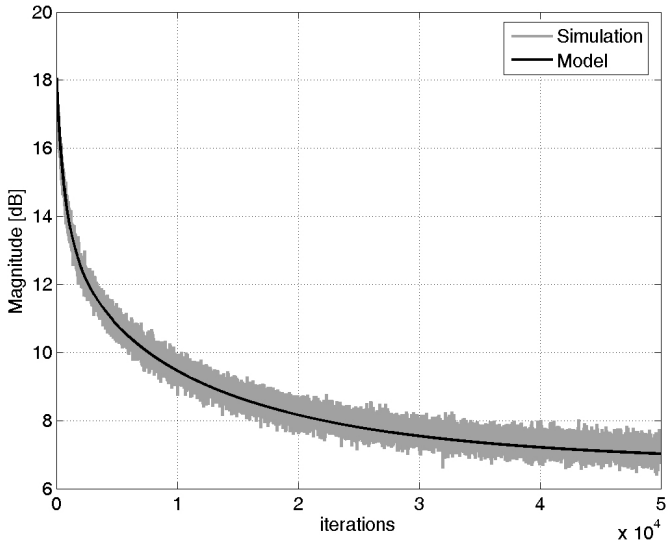

Figure 2.11: MSE comparisons between simulations and new model for $L = 10$.

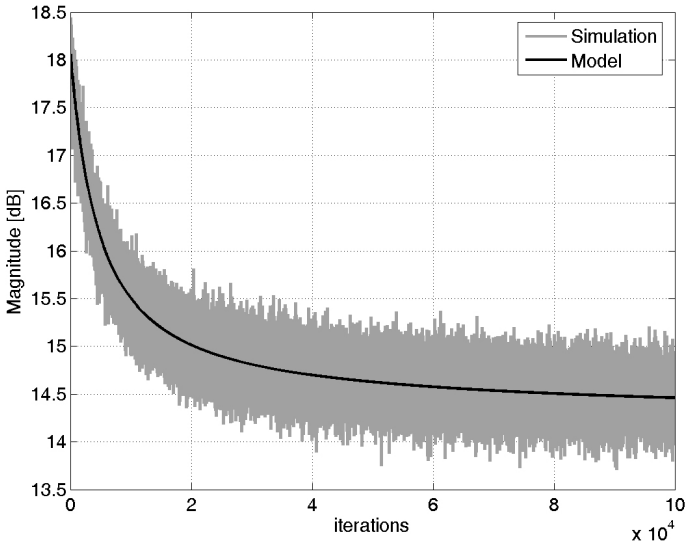

Figure 2.12: MSE comparisons between simulations and new model for $L = 100$.

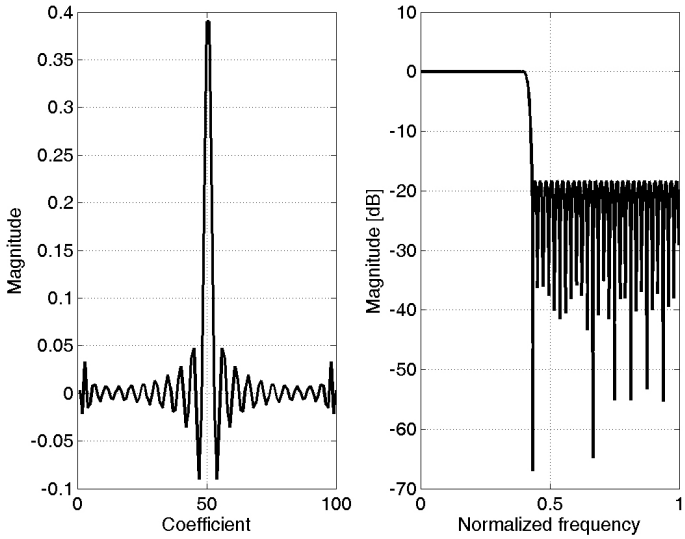

Figure 2.13: $\boldsymbol{w}_0$, the plant filter used for the simulation with 100 coefficients.

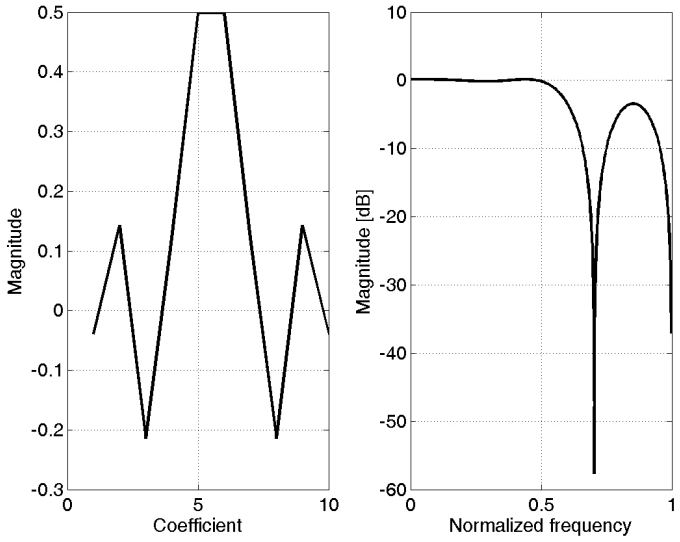

Figure 2.14: The 10 coefficients $\boldsymbol{s}$ low-pass filter.

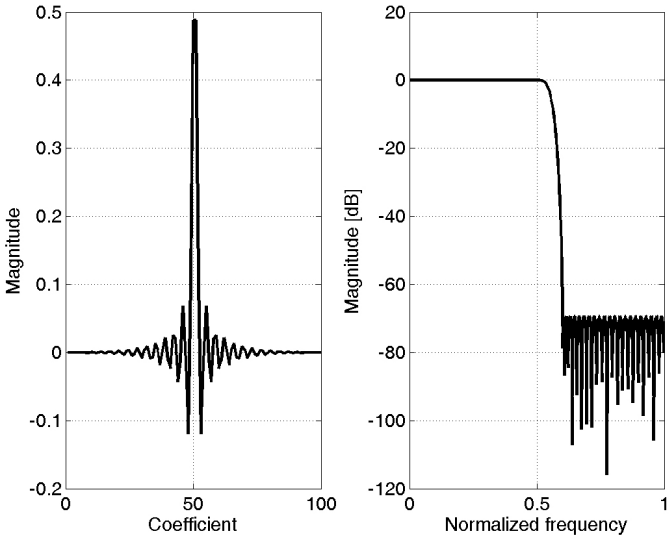

Figure 2.15: The 100 coefficients $\boldsymbol{s}$ low-pass filter.

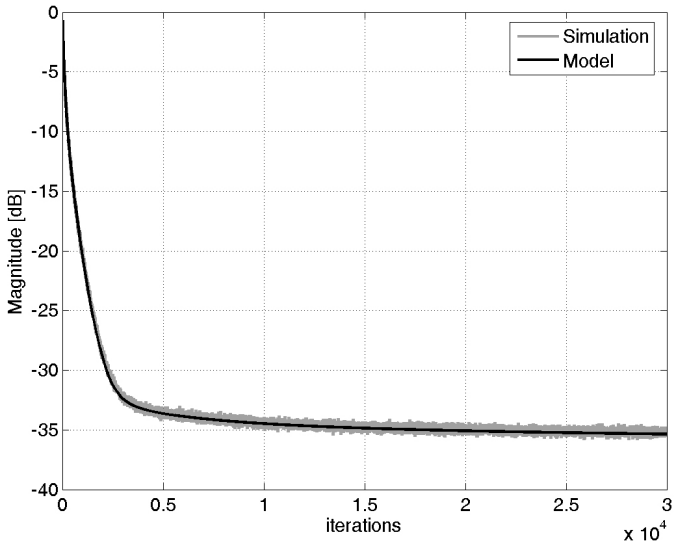

Figure 2.16: MSE comparisons between simulations and new model for $L = 10$.

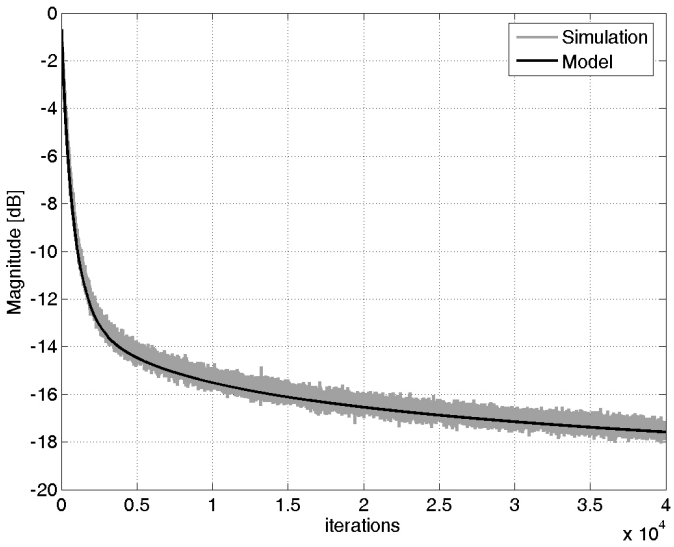

Figure 2.17: MSE comparisons between simulations and new model for $L = 100$.

simulation 3

This simulation represents a case where $\boldsymbol{s}$ is a band-pass filter in the plant frequency range with taps L equal to 100 and for $\mu = 0.005$ (see Fig. 2.18). The input simulation specification was the same as in simulations 1 and 2. The plant $\boldsymbol{w}_0$ is the same as in simulation 2.

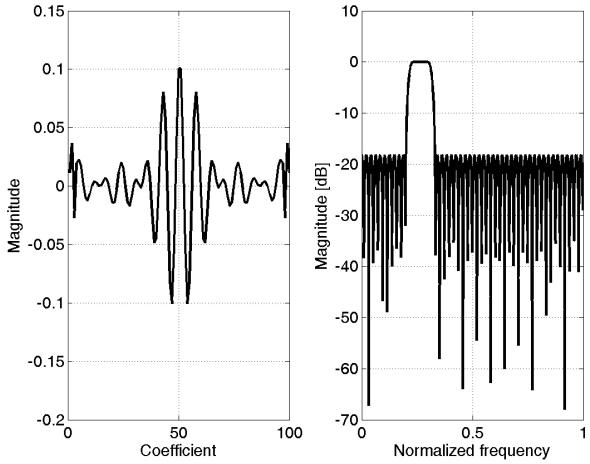

Figure 2.18: The 100 coefficients $\boldsymbol{s}$ band-pass filter.

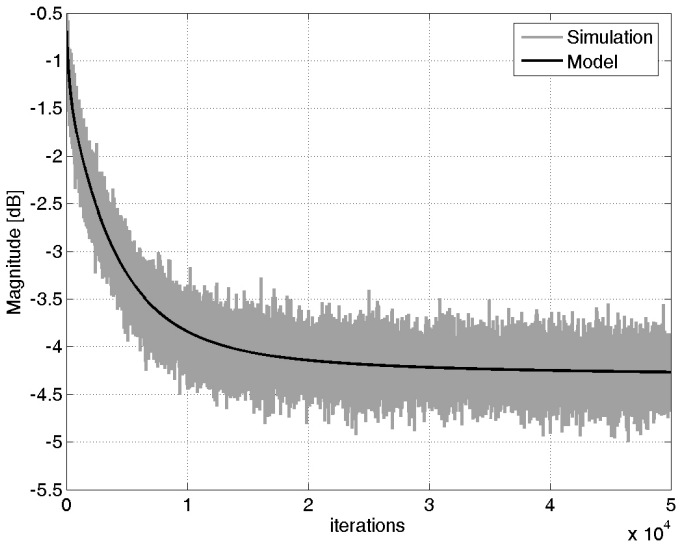

Figure 2.19: MSE comparisons between simulations and new model for $L = 100$.

Fig. 2.19 gives the results obtained for the simulation 3.

2.4 Real-time tools

In the past, real-time experiments were reserved for applications that had large budgets (army and aerospace applications, for example). In 1978, Texas Instruments launched a toy able to deal with a numerical signal in real-time. But it was not until 1985 that the first DSP (Digital Signal Processor) card, which could be used in industrial systems, became available. The DSP card allows complex numerical operations, such as the Fourier transform, to be carried out at very high speed. Hardware that allows the implementation and use of a control system in real-time is of growing interest in the industrial world, as the cost of these tools progressively drops.

Two viable approaches may be differentiated according to the factor of cost and ease of implementation. The first approach involves using a DSP card, which is the most commonly used tool. The effective use of a DSP card alone requires a knowledge of relatively low-level machine language so that the control system can

be programmed into the card. There are some software programs that allow one to overcome this knowledge requirement, but the choice of hardware is restricted by the software and the software provider. The most well-known software is dSpace, provided by the MathWorks company [54].

The second approach does not use a DSP card but, instead, a standard input, and output card and is based on the principle that the DSP typically imposes both financial and practical constraints on the user. This alternative approach uses an Operational System (OS) and Freeware (QNX or Linux), is dedicated to real-time processing, and can be installed on any general purpose computer. The advantage of this approach is that it allows the design of embedded systems for direct application of the type FPGA (Field Programmable Gate Array), without requiring the designer to have knowledge of machine language (VHDL). This technology is currently rarely used because it is still new, but the interest from industry has been growing considerably in the past seven years as its viability increases with dropping costs. The most well-known software engines are XPcTarget [55] and RT-LAB [56] provided by MathWorks and Opal-rt respectively. The idea underlying these software packages, dSpace, xPcTarget and RT-LAB is to cater to the restrictions of real-time operation using other softwares that are already well developed from the theoretical point of view in the areas of mathematical calculations, signal processing, automation, and the generation of the codes C, FORTRAN such as Matlab/Simulink or LabVIEW.

One of the original aspects of RT-LAB is the use of a cross-platform, open-source scripting language called Python, whose use is growing in popularity, particularly for technical applications. Its syntax is very close to m-script, which has become very popular among Matlab users. It is object-oriented and allows users to automate applications on any platform. The RT-LAB API allows users to configure models and automate test runs using the Python language. Also, because Python is multi-threaded, it is possible to interface to multiple concurrent models, running on several target processors. This means that it is possible to program several different tests, and even have data flowing from one test platform to another from a single operator station. In other words, this functionality allows the

generation of a statistical representation of an experiment or process behaviour, which is a valuable tool for industrial applications.

2.5 Model adaptation

The new theoretical model gives very good results compared with the simulation data (see section 2.3). A new step is provided in this section, comparing between the new theoretical model with results from an experiment implementing narrow-band ANC in a finite duct. To be able to compare real data with the theoretical model, the theoretical model cannot be used as it is because the real block diagram of an ANC system must be used (Fig. 2.21), and not the simplified one, Eq. (2.6), that can be used in theoretical study.

Diagram 2.20 presents the experiment setup. Some details on the real-time software used are provided to explain how the results were generated. The digital feedforward control system depicted previously in Fig. 2.6 models active attenuation of the discrete tones in the finite duct. The reference signal is electronically provided by the generator source that controls the first speaker. In this process, the reference signal does not suffer any interference. The reference signal is passed through an adaptive digital filter to generate the resulting control signal which is fed to a control source that introduces the control disturbance into the duct [22]. One of the biggest difficulties in comparing experimental with theoretical results is to obtain a statistical representation of an experiment. In other words, the real-time model needs to be run many times in a test cycle in order to conduct Monte Carlo analysis. In order to achieve this, the software RT-LAB supports API which is based on the scripting language; Python, which has been detailed in section 2.6.

In order to evaluate $\boldsymbol{s}$ of the ANC system (which includes the D/A converter, reconstruction filter, power amplifier, loudspeaker, acoustic path from loudspeaker to error microphone, error microphone, preamplifier, anti-aliasing filter and A/D converter), an experimental setup for the off-line secondary-path is evaluated (for more details on this technique see [11]). However, in our case, as the duct is finite, $\boldsymbol{s}$ is not only the acoustic path from the loudspeaker to the error microphone but

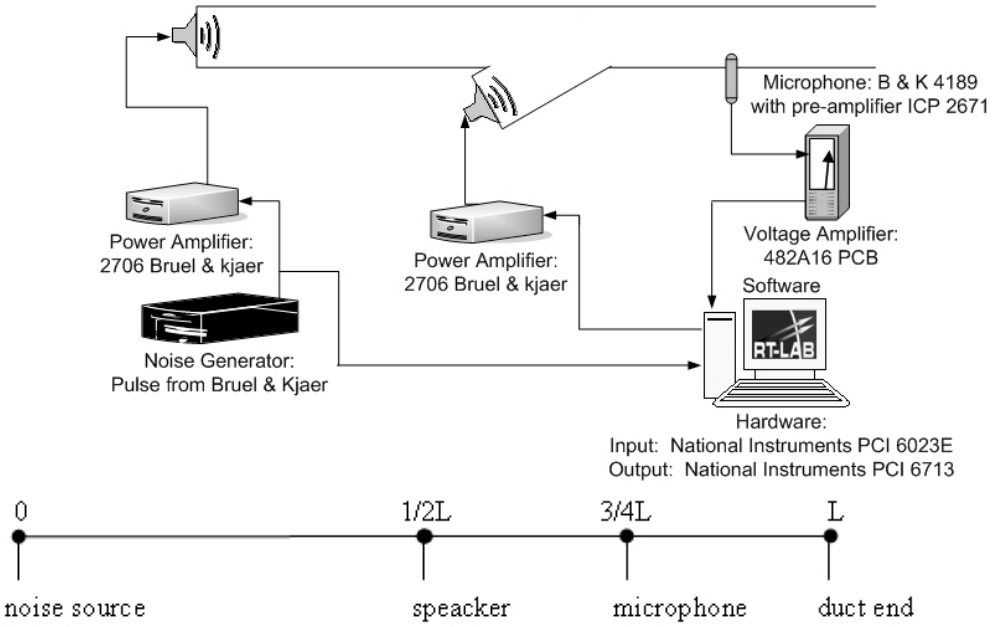

Figure 2.20: Configuration of narrowband ANC system used, L=3.30m.

also includes the reflection effect from both sides of the duct. Thus, the evaluated $\boldsymbol{s}$ is in fact $\boldsymbol{s} = \boldsymbol{s}' + \boldsymbol{r}$ of diagram 2.21. Diagram 2.21 can be redrawn to allow the evaluated $\boldsymbol{s}$ to be processed by the theoretical model as shown in diagram 2.22.

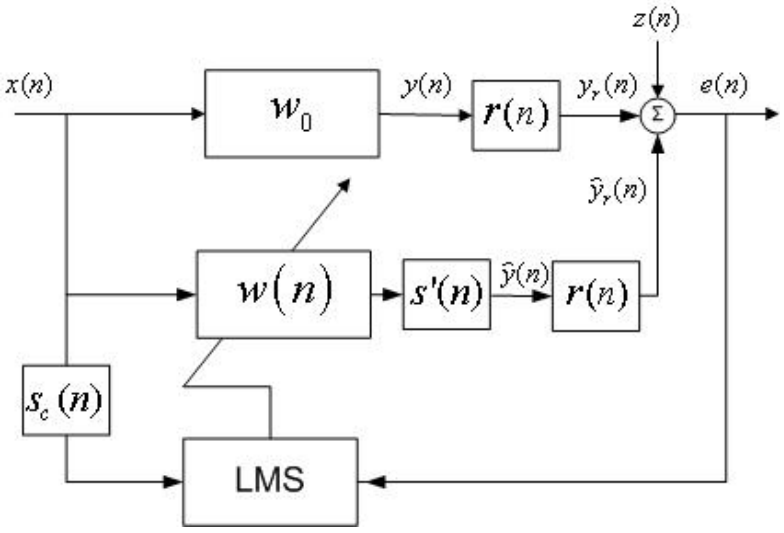

Figure 2.22: redrawn block diagram of an ANC system.

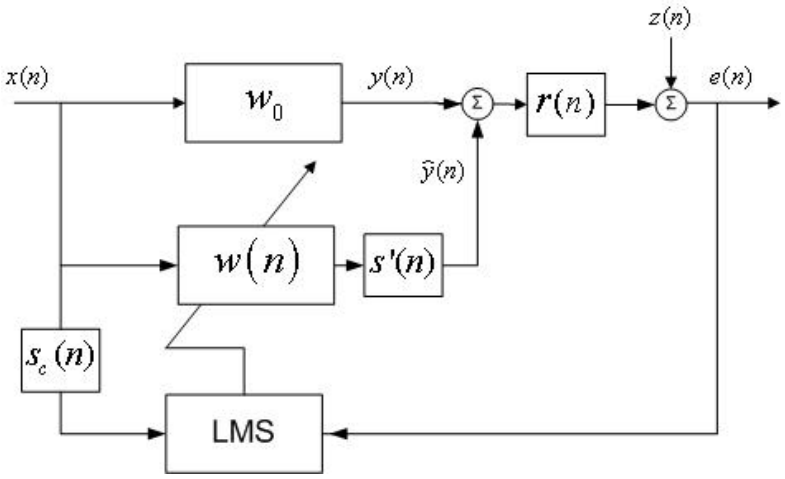

Figure 2.21: Block diagram of an ANC system.

The filter s' due to the electronic devices can be assumed almost perfect, as the acoustics signal is monotone; it is then simply a two time delay filter. The plant can also be approximated by a time delay filter (the length of the duct up to the second speaker) with attenuation. The evaluated s is hence r without two time delays.

2.6 ANC real-time experiment and specifications

The first unique feature of this experiment is the fact that no DSP card has been used but only I/O cards (see diagram 2.20). RT-LAB, the software used, provides tools for running and monitoring simulations or controls on various runtime targets. An open architecture allows RT-LAB to work with the popular diagramming tools Matlab/Simulink which is used in this work, and MATRIXx/SystemBuild. The real-time processing is carried out by freeware operating systems (QNX or Linux) allowing real-time observation and manipulation. The second unique feature is the use of Python to validate the statistical representation of the experiments.

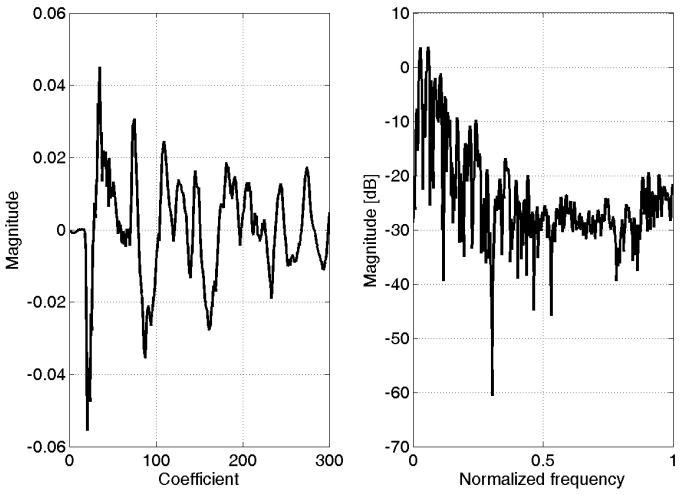

Figure 2.23: The $\boldsymbol{s}_c$ filter with 300 coefficients.

2.6.1 Experiment 1

In this work 1000 runs have been processed, providing enough results for a reliable Monte Carlo analysis, furnishing the same evaluating conditions as the simulations mentioned in section 2.6.

Regarding the first experiment, the FxLMS algorithm was operated at a 10kHz sampling frequency, with step size $\mu = 0.00005$. $\boldsymbol{w}$ and $\boldsymbol{s}_c$ had 400 and 300 coefficients respectively. The response $\boldsymbol{s}_c$ is shown in Fig. 2.23. The reference signal $x(n)$ was a 200Hz tone with electric dynamic range of 0.5V. $z(n)$ was assumed to be zero-mean, stationary, white Gaussian noise with variance $\sigma_z^2 = 3.54e^{-4}$. The duct was 3.4m long. The secondary speaker was installed at 1.7m and the error microphone at 2.55m. In the theoretical model, $\boldsymbol{s} = \boldsymbol{s}_c$ was assumed. $\boldsymbol{w}_0$ was assumed to correspond to 52 unit delays and an attenuation coefficient. Fig. 2.24 shows MSE behaviour obtained from the resulting curve from the ANC experiment (average of 1000 runs) and the theoretical prediction by the analytical model (smooth curve). These curves show that the proposed model was able to accurately predict the algorithm behaviour.

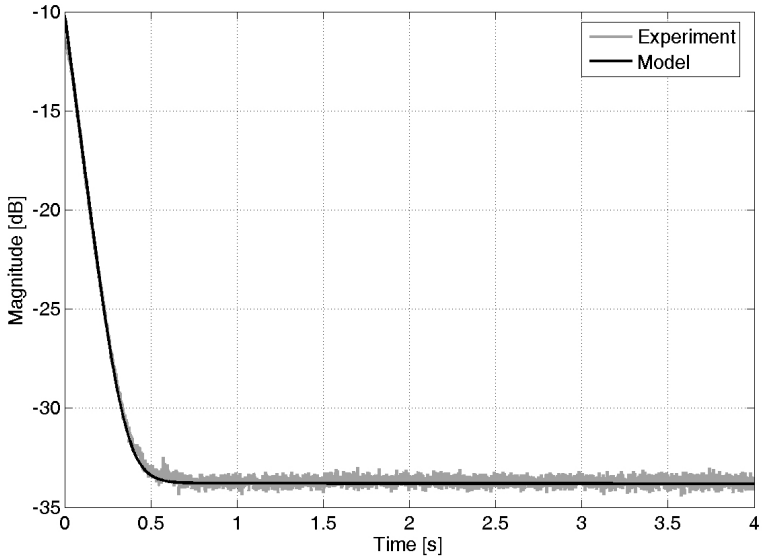

Figure 2.24: Comparisons between theoretical and experimental MSE over 1000 runs for monotone input frequency 200Hz.

2.6.2 Experiment 2

The same experiment was carried out for monotone frequency 600Hz.

2.6.3 Experiment 3

A third experiment was carried out with a input signal composed of 8 sinusoids with values: 200Hz, 220Hz, 240Hz, 250Hz, 260Hz, 270Hz, 280Hz and 300Hz, under the same conditions as the previous experiments but with $\mu = 0.005$. It can be seen that the theoretical model does not match as well as the two first experiments, which is mainly due to the assumption made that $\boldsymbol{s} = \boldsymbol{s}_c$ and the fact that the duct cannot be only represented by a time delay with attenuation for a non-monotone signal but also acts as a filter weighting differently on each frequency. In order to better evaluate the algorithm convergence of the duct, the duct model should be better approximated.

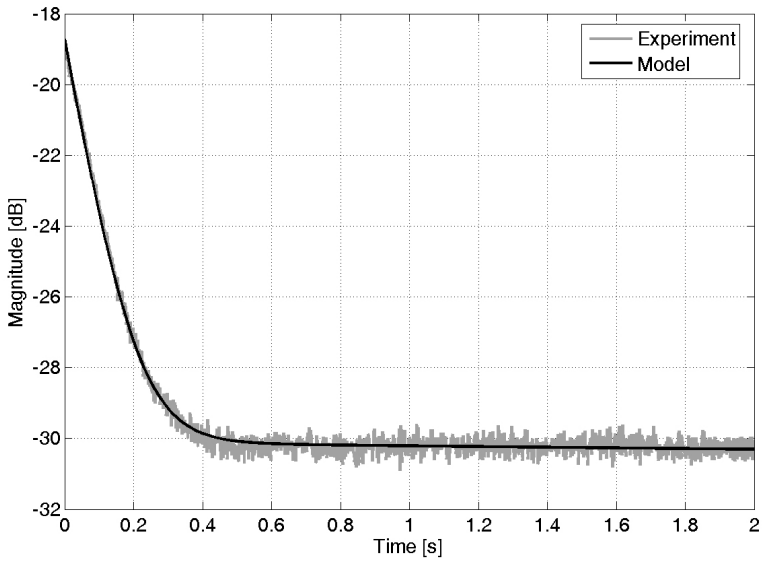

Figure 2.25: Comparisons between theoretical and experimental MSE over 1000 runs for monotone input frequency 600Hz.

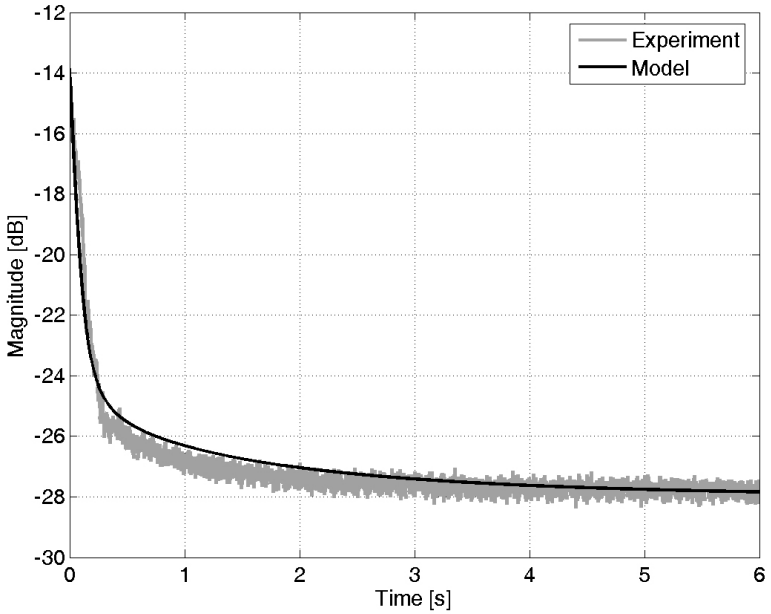

Figure 2.26: Comparisons between theoretical and experimental MSE over 1000 runs for multi-tone input frequency.

2.6.4 Experiment 4

The last experiment was carried out with white noise, low-pass filtered up to 800Hz signal input under the same conditions as before with the convergence step $\mu = 0.00005$. The objective of this experiment was to show the efficiency of the feedforward approach when the unwanted noise is broadband. Fig. 2.27 shows the spectral density function results.

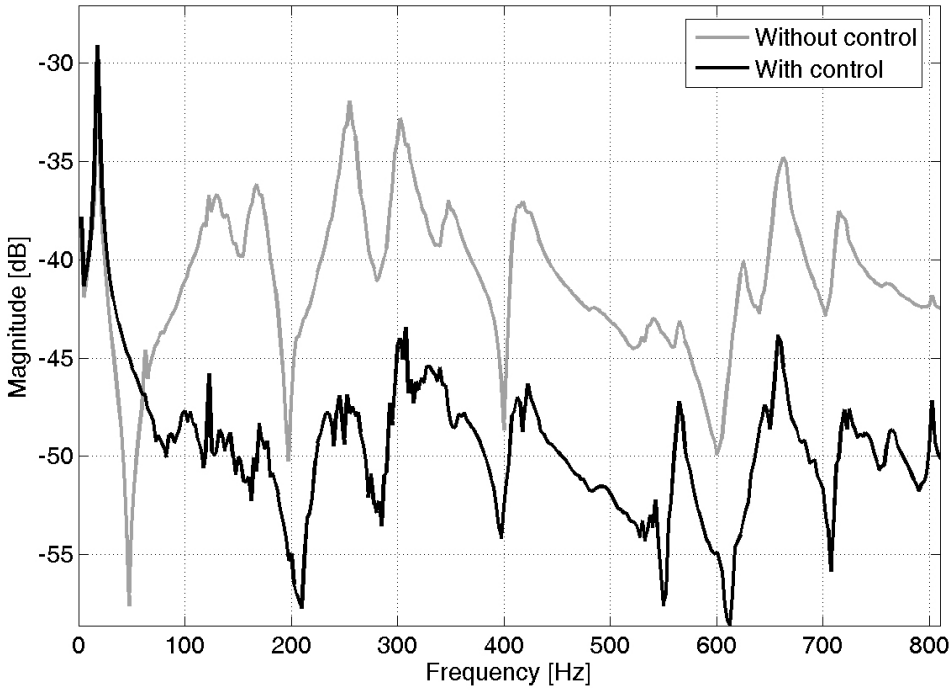

Figure 2.27: Error spectral density function.

2.7 Summary

This chapter summarised the basic idea of active and adaptive control, and presented a full resolution of an ANC system from the theoretical part of the control up to the statistical behaviour analysis of one of the most popular adaptive control algorithms, the FxLMS. A new analytical model for the behaviour of the FxLMS

adaptive algorithm has be provided; the model was derived using a stochastic differential equation approach. The real-time ANC system was implemented using I/O cards and a general purpose computer only. The experiments validated the new analytical model and also provide better understanding of active noise control as it was the first time this type of experiments have been realised in the UFSC.

Chapter 3

NOISE RADIATION

This chapter sets out an unconventional ANC approach using structural sensors and actuators, and examines the effectiveness of this approach in actively attenuating the sound radiation from an irregular enclosure excited by an internal sound field. The aim was to minimise the radiated sound field by controlling vibration of the enclosure.

The design of a suitable control system was made more complicated by the fact that most of the energy of the interior noise spectrum fell below the first enclosure structural resonance frequency. There will be a description of how this problem was overcome showing how a simple robust active noise control system can be used to attenuate noise radiating from the irregular enclosure in question. Two properties make the control system particularly robust: the use of only structural sensors/actuators and the choice of an adaptive feedforward controller using a simple FxLMS control algorithm.

Following will be a discussion on the type and reliability of the equipment which is most appropriate, and then a presentation of experimental results illustrating the performance of this unconventional ANC approach. The experimental data show a direct correlation between the attenuation of enclosure surface vibration and the reduction in noise radiation. This promising result, combined with the control system's robustness, simplicity and small size, suggest great appeal for in-

dustrial applications.

This chapter will discuss two main issues in the design of this ANC approach: the use of structural sensors and actuators to control noise radiation and the type of control approach needed to drive the ANC system.

3.1 Structural actuators/sensors to control acoustic radiation

To actively attenuate the noise radiated by a structure, a set of actuators and sensors must first be chosen. Acoustic actuators such as loudspeakers are typically difficult and impractical to implement, because of their size and the need for them to completely surround the sound source in order to achieve global noise attenuation. If the goal is to use the noise control system in an embedded way, the logical choice is to use piezoelectric patches as structural sensors/actuators, because they are small, light-weight and low-cost. Choosing the size and location of the piezo patches becomes particularly important when the first structural modes have resonances that are quite high in frequency, as the wavelengths begin to get smaller than the piezo size. Selecting a smaller piezo patch is not a solution to this, as the piezo may then be unable to provide enough strength as an actuator. The size and location of the piezo patch(es) have a direct influence on the observability and controllability of the vibrating system in question. The piezo sensor is able to determine the response at most of the disturbance frequencies that may be applied to the structure but it is only able to excite structural modes to which it is strongly coupled. In addition, when the piezo patch is sometimes driven at relatively high voltage levels in order to produce the required output, it generates harmonics of the applied frequency which may compromise the overall controller performance.

The shaker is the most effective type of structural actuator, as it is capable of producing a wide range of vibrations of different frequencies and amplitudes. The classic electro-dynamic shaker, however, has a number of major drawbacks: it is typically heavy and cumbersome, requires a support structure and is difficult

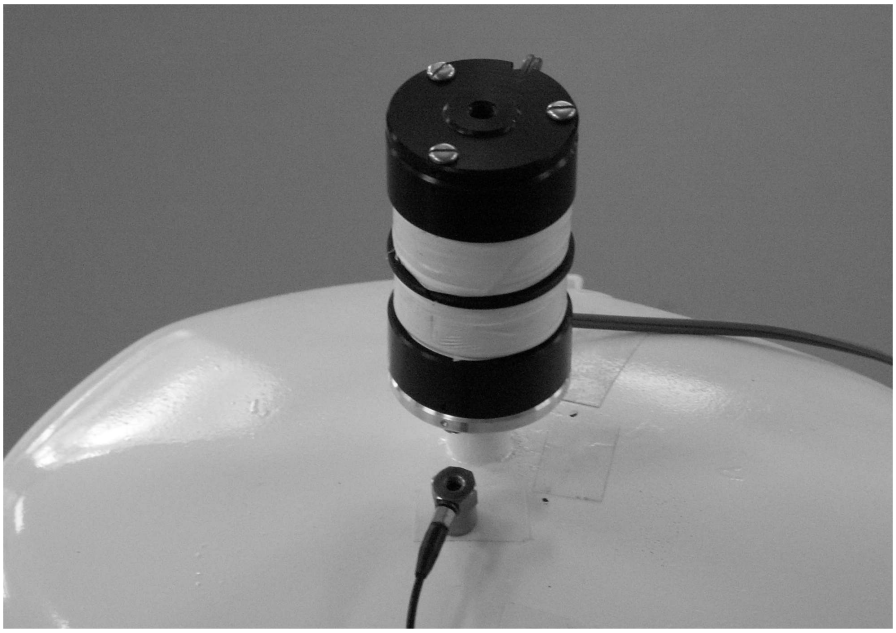

Figure 3.1: Inertial shaker used in the experiment.

to attach, and the shaker body itself radiates noise. An inertial shaker, on the other hand, is less problematic. The weight of an inertial shaker can be adjusted depending on the control force that is required. The shaker is mounted directly on the structure, so it does not suffer the mis-alignment that can easily occur with the classic electro-dynamic shaker, should its external support structure be shifted. And the inertial shaker resonance frequency can be tuned to closely match the frequency range to be controlled, thereby optimising the excitation efficiency. For the work described in this chapter, an inertial shaker was specially developed and optimised for the required dynamic range and force input requirements; the result was a compact device of 4cm diameter and 7cm height, shown in Fig. 3.1.

In order to set up a control system to attenuate structurally radiated noise, either a structural sensor (such as an accelerometer) or an acoustic sensor (such as a microphone) can be used. The most appropriate sensor would depend on the application and the surrounding environment. When the signal to noise (S/N) ratio is high (that is, when the background noise does not greatly interfere with the signal of interest), acoustic sensors are the most intuitive to implement. How-

ever, under typical workplace circumstances it would be difficult to consistently prevent background noise that could interfere with the sensors, and the sensors themselves, along with any attached wiring, would be likely to get in the way of other necessary activities. Structural sensors thereby have two main advantages over acoustic sensors: they are less susceptible to acoustic interference and cause less inconvenience to activities that may need to be performed in the vicinity of the equipment or, in the case of consumer products, less inconvenience in the use and assembly of the product.

The choice of what particular structural sensors to use would depend on the frequency bandwidth of interest, giving that noise radiation is a function of the amplitude of excitation of radiation modes and not vibration modes [57, 58]. Thus, a radiation mode model must be incorporated into the control system design. However, it is well known that any radiation mode is a linear combination of vibration modes, and one radiation mode can be made up of a very large number of vibration modes, which makes it extremely difficult to achieve an accurate radiation model for a specified bandwidth that might include several radiation modes; the control design, therefore, may not be as robust as is desirable for industrial applications.

In the case considered here, the resonance frequency of the first structural mode is higher than the frequency spectrum of interest (that is, the first mode resonance frequency is higher than 1kHz). Therefore there are no vibration or radiation modes that must be incorporated into the control system design. In other words, the transfer function between the inside enclosure noise and the structural sensor is only a constant gain as a function of frequency.

As previously mentioned, another concern in the application of ANC to industrial or consumer products is that installing the ANC system does not cause excessive inconvenience in the assembly of the product. In this case, as the structure to be controlled is enclosed, it would not be an easy task to put a sensor or actuator inside. An internal microphone would be ideal for feedforward control, which requires a reference signal that is not greatly influenced by the control source and has a high S/N ratio. However, for the case considered here, an outside

structural sensor could be just as effective, as the transfer function between the structural vibration and the inside noise are constant as a function of frequency. Nonetheless, some compensation will be necessary to account for the feedback path from the control actuator to the reference sensor.

In conclusion, structural sensors and actuators have been chosen for the example considered here, in designing a control system to attenuate structurally radiated sound. It has been determined that no structural or radiation modes are involved, as the frequency range of interest is below the resonance frequency of the first mode. These system properties will improve the robustness and simplicity of the final control system. The next step in building the ANC system is to determine the optimum type of control system for this application: feedforward or feedback?

3.2 Feedback/Feedforward

To decide which control system is more suitable three factors must be considered: the system to be controlled, the surrounding environment and the inside disturbance type (for example white noise, periodic noise, etc.). Here, the system is an irregular enclosure with an average shell thickness of 3mm, giving a very high structural stiffness; as a result the structural resonance frequencies are relatively high. The surrounding environment in which the noise has to be cancelled is an open space. The inside noise is a periodic noise with a frequency spectrum ranging from 50Hz to 900 Hz. Spectral analysis indicates that the spectrum is composed mainly of harmonics of 50Hz. Given these circumstances, it can be determined that a feedback approach would not be suitable as it is based on damping the resonant modes of the structure. Although one means of implementing feedback control would be to create a model of the irregular enclosure with virtual modes at the frequencies of interest, this approach has not yet been realised on any practical system.

Thus, the noise periodicity and other factors indicate that the feedforward approach is likely to give the best results. The next step is to decide on the optimum number and locations of error sensors and control actuators which will

be discussed in section 3.3. Also to be considered is the type of real-time system that would be most suited to running the controller. Section 2.6 will address questions as to its reliability and how it may be applied in an industrial setting.

3.3 Experiment description

The experiment was performed on an irregular asymmetrical enclosure in the shape of an ellipsoid cylinder, with many irregular bumps, welded on a plinth which was placed on a table. Fig. 3.2 shows a very simplified schematic of the structure. A loud speaker was inserted inside the enclosure to simulate the pressure that a real inside disturbance might produce. As in a real-life situation the top lid and main enclosure body would be strongly coupled in the final assembly of the product, the top lid was then welded to the main body for the experiment.

The sensors were positioned according to the zones of highest noise radiation on the irregular enclosure, measured with a microphone that was moved around the outside of enclosure. Four sections were found to be significant noise radiators: the top, the left and right sides, and the bottom. It was noted that what surrounds the enclosure and what supports it may determine the optimum position of the sensors and actuators. For example, if the enclosure is in contact with another object such as a table, then that object could become a radiation noise amplifier. A trial set of experiments showed that the best compromise was reached between efficiency and the number of sensors/actuators used when there was just one actuator on the enclosure top in combination with 3 error sensors (on the top, left and on the bottom) as shown in Fig. 3.2 (in this figure, the bottom sensor does not appear for obvious perspective reasons). As the feedforward approach was used, a reference sensor was needed, which was placed on the plinth. The transfer function between the accelerometer output and the disturbance was, as previously mentioned, only a constant complex gain. The enclosure was made of steel; its general features are described in Table 3.1.

The sensors and accelerometers were amplified and the resulting signal passed through low-pass filters that were directly connected to the data acquisition card.

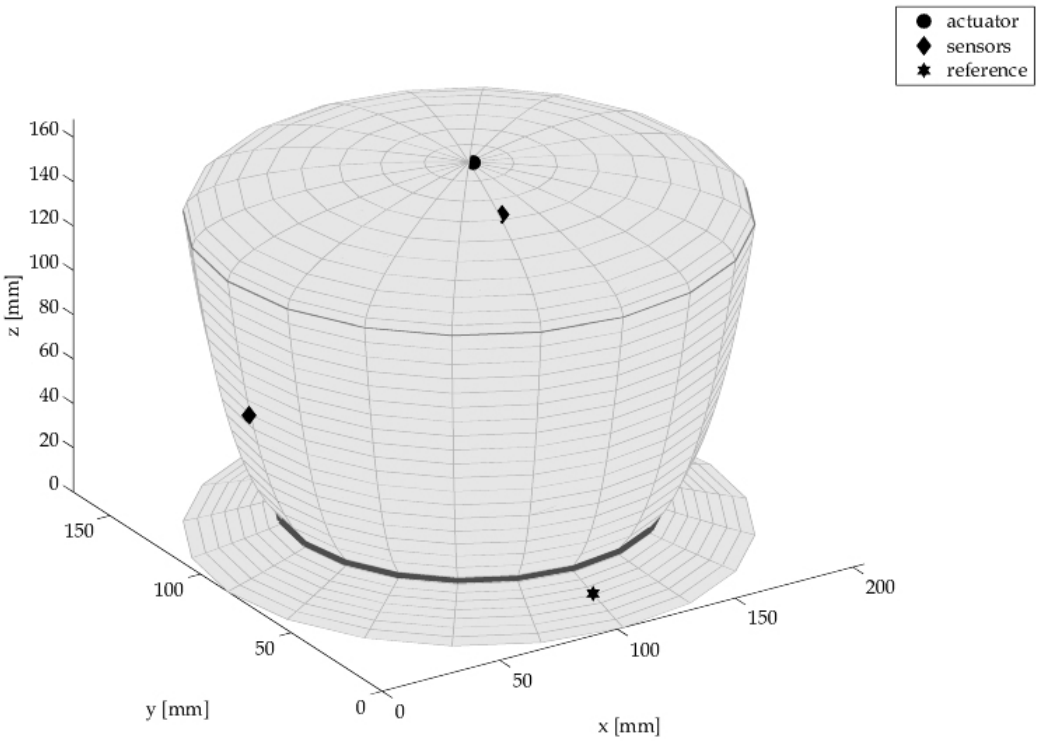

Figure 3.2: Simplified diagram of the structure showing the position of the error sensors, the reference sensor and the actuator.

Table 3.1: Enclosure features

x radius[a]	102 mm
y radius[a]	85 mm
Height[a] (h)	170 mm
Thickness[a] (t)	3 mm
Young's modulus (E)	209×10^9 N/m^2
Density (ρ)	8000 kg/m^3

[a]as the shell is irregular, it just an order of magnitude.

For the output, a standard power amplifier was used to drive the shaker. Vibration velocities were measured at 200 discrete points along the top of the enclosure, using a Polytech PSV 400 scanning laser vibrometer, to show the direct relationship between the vibration reduction and the noise radiation reduction. The sound radiation before and after implementation of the controller was measured using a set of 16 microphones surrounding the enclosure.

3.4 Control design

The objective of this control system is to attenuate noise radiation from the enclosure, and it has been explained how a feedforward, single-reference/single-input /multiple-output (SIMO) FxLMS adaptive control algorithm was selected as the optimum approach to achieve this objective. That an adaptive algorithm is used enhances the robustness of the control system; if any features of the enclosure change over time due to material fatigue or minor damage, or if the environment changes thereby changing the wavelength of the sound, the algorithm will adapt itself. Fig. 3.3 shows the details of the $[1 \times 1 \times 3]$ SIMO vibration control system used for the experiment.

x is the reference signal, which in this case is the equivalent of the enclosure interior noise. The algorithm design for the experiment takes into account the feedback effects $\boldsymbol{F}(n)$ of the actuator on the reference sensor [11, 59, 60]. An estimator of $\boldsymbol{F}(n)$, $\widehat{\boldsymbol{F}}(n)$, is modelled to account for interference with the reference signal from the actuator signal. $\widehat{\boldsymbol{F}}(n)$ is estimated simultaneously with the secondary paths ($\hat{\boldsymbol{s}}_{11}, \hat{\boldsymbol{s}}_{12}$ and $\hat{\boldsymbol{s}}_{13}$), which are estimated off-line using a standard LMS algorithm. Plant_1, Plant_2 and Plant_3 are the different paths of the primary source disturbance to the sensors. The weight update equation for the control filter weights is given by:

$$\boldsymbol{w}(n+1) = \boldsymbol{w}(n) + \mu \left\{ e_1(n)\widehat{\boldsymbol{S}}_{11}^T + e_2(n)\widehat{\boldsymbol{S}}_{12}^T + e_3(n)\widehat{\boldsymbol{S}}_{13}^T \right\} \dot{\boldsymbol{x}} \tag{3.1}$$

where $\boldsymbol{w}(n) = [w_0(n) \cdots w_N(n)]^T$ is the adaptive weight vector of length N, $\dot{\boldsymbol{x}} = [x(n) \cdots x(n-N-L+1)]^T$ is the input data vector, L is the estimated filter

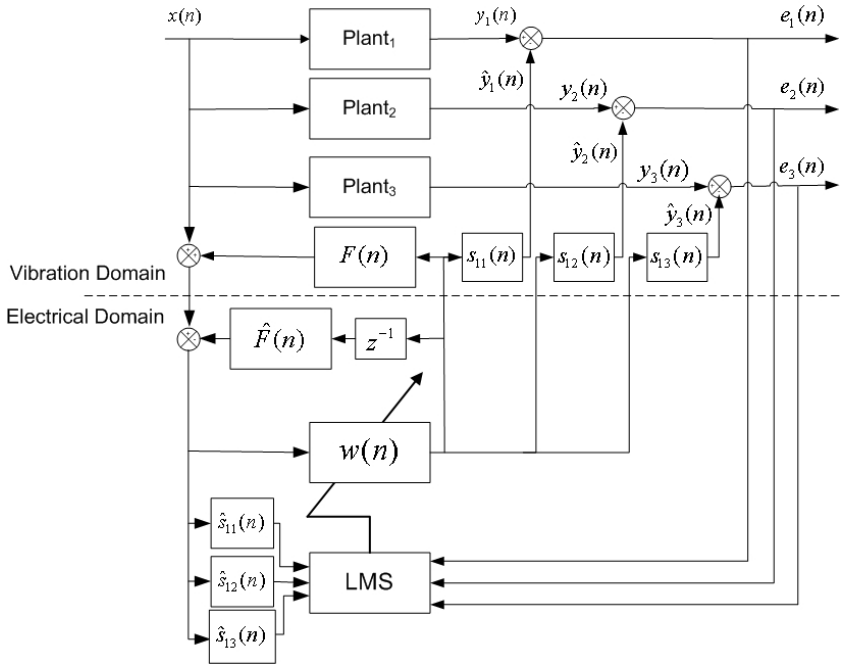

Figure 3.3: Detailed diagram of the $[1 \times 1 \times 3]$ SIMO system showing the electronic part and the vibration/acoustic part.

length of the $\hat{\boldsymbol{s}}_{11}, \hat{\boldsymbol{s}}_{12}$ and $\hat{\boldsymbol{s}}_{13}$ secondary paths, and μ is the step-size. $\widehat{\boldsymbol{S}}_{1\alpha}$ is given by the following matrix with $\alpha = 1, 2$ or 3:

$$\underset{[N+L-1,N]}{\widehat{\boldsymbol{S}}_{1\alpha}} = \begin{bmatrix} \hat{\boldsymbol{s}}_{1\alpha}(0) & 0 & \cdots & 0 \\ \vdots & \hat{\boldsymbol{s}}_{1\alpha}(0) & \ddots & \vdots \\ \vdots & \vdots & & 0 \\ \vdots & \vdots & & \hat{\boldsymbol{s}}_{1\alpha}(0) \\ \hat{\boldsymbol{s}}_{1\alpha}(L-1) & \vdots & & \vdots \\ 0 & \hat{\boldsymbol{s}}_{1\alpha}(L-1) & & \vdots \\ \vdots & \ddots & \ddots & \vdots \\ 0 & \cdots & 0 & \hat{\boldsymbol{s}}_{1\alpha}(L-1) \end{bmatrix}$$

The experiment focused on the vibration control over the bandwidth from 0Hz to 900Hz; hence all the output and input signals of the control system were low-pass filtered using a filter with a cut off frequency of 900Hz. The SIMO algorithm was

implemented in Matlab/Simulink using RT-LAB software to provide the real-time system. The FxLMS algorithm was operating at a sampling frequency of 8kHz, with a step size $\mu = 0.0001$. $\boldsymbol{w}$ and $\hat{\boldsymbol{s}}_{1\alpha}$ have 300 and 200 coefficients, respectively.

3.5 Experiment results

The laser vibrometer measured the vibration levels at 200 points across the enclosure top for the cases with control and without. Fig. 3.4 shows the velocity spectrum average of the 200 points.

From Fig. 3.4, it can be seen that the controller succeeded to heavily reduce the vibration of the enclosure in the scanned area. This general impression is confirmed by inspection of the Root Mean Square (RMS) of the scanned area; Fig. 3.5 shows the RMS calculated for the cases with control and without. No measurements were done on the inertial shaker actuator, which explains the large surface of interpolation in the middle of the scanned area of Fig. 3.5.

The result of the vibration attenuation was a significant reduction in noise radiation. Fig. 3.6 shows the noise radiation measured by the microphone (of an array of 16) that measured the worst-case noise attenuation. It can be seen from the frequency peaks in Figs. 3.4, 3.5 and 3.6 that the vibration attenuation is directly related to the noise radiation attenuation. Fig. 3.6 indicates quite a high background noise level, as the experiment was deliberately done in a standard room with a large amount of noisy equipment to simulate industrial conditions.

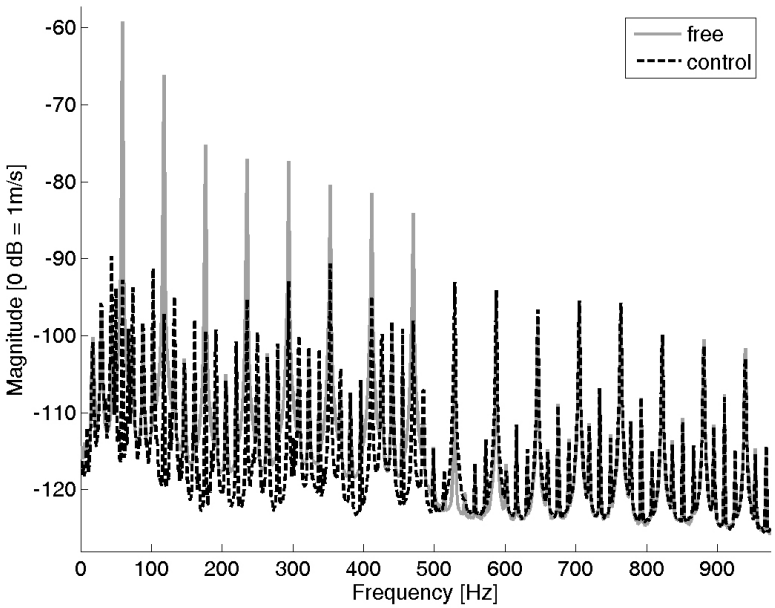

Figure 3.4: Average spectrum of velocity in the shell scanned area with control and without.

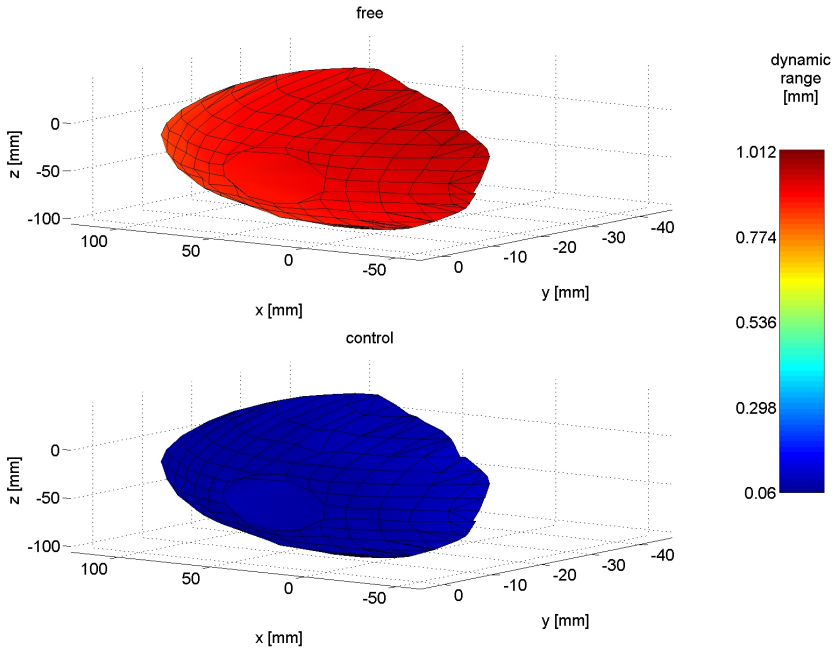

Figure 3.5: RMS of the scanned area.

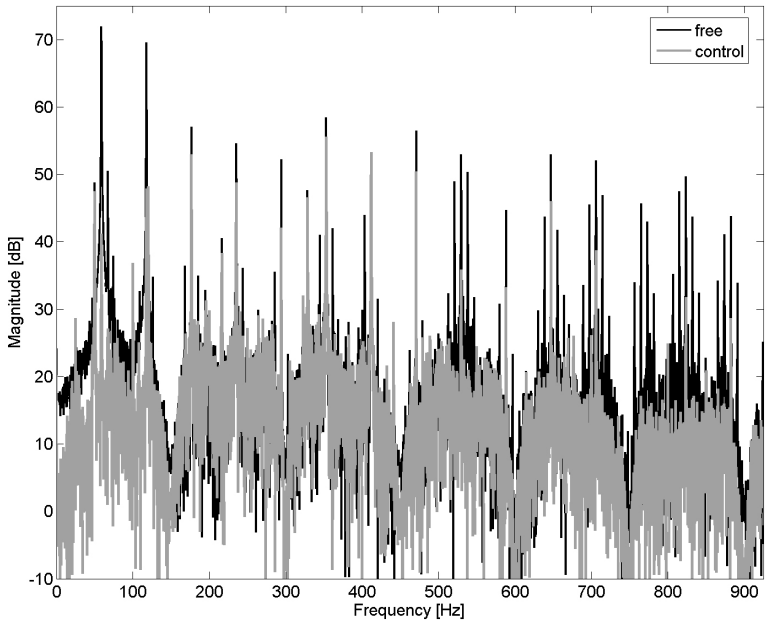

Figure 3.6: Microphone pressure power spectrum.

3.6 Summary

In describing the choices made for this unconventional ANC approach, this chapter has discussed some of the major issues that must be taken into account when designing an active noise control system for an industrial application. More specifically, for an enclosure radiating sound at frequencies below the first structural resonance, it has been shown how it is possible to design an effective, simple feedforward system to significantly attenuate the radiated sound without using any sound field sensors such as microphones. The process was illustrated with an experiment using a irregularly shaped enclosure radiating sound into an industrial type environment.

Chapter 4

ANALYTICAL VIBRATION MODELLING AND OPTIMISATION

There continue to be instability problems with feedback model-based control design that uses a nominal truncated model to attenuate vibration in a flexible structure. This is due to the inability of the truncated model to account for the infinite number of vibration modes in a real structure and to thereby incorporate the spillover of unmodelled vibration modes in the controller design. This has meant that the influence of unmodelled modes on the response in the frequency bandwidth of interest has had to be included through the use of an approximation term. The underlying theory describing this control approach has been well documented [4, 22]: the approach usually targets the first few structural resonances within a particular bandwidth, with zero Hz as the lower limiting frequency. However, in some practical cases, it may be necessary to target resonances occurring at higher frequencies and to ignore those occurring at low frequencies; for example when the objective is to reduce the sound radiation from a structure. In this case, it would be desirable to truncate the model at both the low and high frequencies so that the control effort is focused only on the modes of interest. As normal, an approximation term needs to be developed to minimise spillover and maximize stability, here, by taking into account the influence on the structural response of

lower order modes, resonant outside the frequency bandwidth of interest. The following sections will discuss what adjustment is needed to account for the effect on the system response of both low and high frequency unmodelled modes. The objective is for the truncated model to achieve a more accurate approximation of the real system.

4.1 Modelling of flexible structure systems

The analytical model for axial, torsional and flexural vibration is derived using standard partial derivative equation methods, which can be found in [61, 62]. For spatially distributed systems:

$$\mathcal{L}\left\{y(t,r)\right\} + \mathcal{C}\left\{\frac{\partial y(t,r)}{\partial t}\right\} + \mathcal{M}\left\{\frac{\partial^2 y(t,r)}{\partial t^2}\right\} = f(t,r) \tag{4.1}$$

where y is the structural displacement at the location r along the structure, $\mathcal{L}$ and $\mathcal{M}$ are linear homogeneous differential operators, and $\mathcal{C}$ is the damping operator. In this work it is assumed that the modes are not coupled through the damping and that the damping is proportional, as is commonly used in modal theory. $\mathcal{C}$ is then equal to $c_1\mathcal{L} + c_2\mathcal{M}$, where c_1 and c_2 are non-negative constants. Finally, a general excitation force is denoted by f. In modal analysis, the solution for $y(t,r)$ in Eq. (4.1) can be assumed to be in a separable form, consisting of contributions from an infinite number of modes:

$$y(t,r) = \sum_{i=1}^{\infty} \phi_i(r) q_i(t) \tag{4.2}$$

where $q_i(t)$ is the temporal function of the system, $\phi_i(r)$ is the structural eigenfunction obtained by solving the associated eigenvalue problem:

$$\mathcal{L}\{\phi_i(r)\} = \lambda_i \mathcal{M}\{\phi_i(r)\} \tag{4.3}$$

with λ_i related to the natural frequency ($\lambda_i = \omega_i^2$) of mode i.

The eigenfunction mode shapes are orthogonal and normalised through the

following orthogonality conditions:

$$\int_{\mathcal{R}} \phi_i(r)\mathcal{L}\{\phi_i(r)\}dr = \delta_{ij}\omega_i^2 \tag{4.4a}$$

$$\int_{\mathcal{R}} \phi_i(r)\mathcal{M}\{\phi_i(r)\}dr = \delta_{ij} \tag{4.4b}$$

$$\int_{\mathcal{R}} \phi_i(r)\mathcal{C}\{\phi_i(r)\}dr = 2\delta_{ij}\zeta_i\omega_i \tag{4.4c}$$

where δ_{ij} is the Kronecker delta function, ω_i is the i^{th} natural frequency, ζ_i is the i^{th} damping ratio ($\zeta_i = \frac{c_1\omega_i^2+c_2}{2\omega_i}$), and $\mathcal{R}$ is the domain of the structure where $r \in \mathcal{R}$. Substituting Eq. (4.2) into Eq. (4.1), the following is obtained:

$$\mathcal{L}\left\{\sum_{i=1}^{\infty}\phi_i(r)q_i(t)\right\} + \mathcal{C}\left\{\frac{\partial}{\partial t}\sum_{i=1}^{\infty}\phi_i(r)q_i(t)\right\} + \mathcal{M}\left\{\frac{\partial^2}{\partial t^2}\sum_{i=1}^{\infty}\phi_i(r)q_i(t)\right\} = f(t,r). \tag{4.5}$$

Multiplying Eq. (4.5) by $\phi_j(r)$, integrating over its domain ($\mathcal{R}$) and using the orthogonality conditions Eqs. (4.4a), (4.4b) and (4.4c) gives the following:

$$\ddot{q}_i(t) + 2\zeta_i\omega_i\dot{q}_i(t) + \omega_i^2 q_i(t) = F_i(t),\ i = 1, 2, ... \tag{4.6}$$

$$F_i(t) = \int_{\mathcal{R}} \phi_i(r)f(t,r)dr. \tag{4.7}$$

The transfer function between the applied force $f(t,r)$ and the displacement $y(t,r)$ can then be expressed by taking the Laplace transform of Eq. (4.6):

$$G(s,r) = \sum_{i=1}^{\infty}\frac{\phi_i(r)F_i}{s^2 + 2\zeta\omega_i s + \omega_i^2} \tag{4.8}$$

where F_i is the modal amplitude of the applied force.

Commonly used boundary conditions [61] at the location $r = r_o$ are:

▷ simply-supported:

$$\phi_i(r_o) = 0 \quad \text{and} \quad \left.\frac{\partial^2 \phi_i(r)}{\partial r^2}\right|_{r_o} = 0 \tag{4.9}$$

▷ clamped:

$$\phi_i(r_o) = 0 \quad \text{and} \quad \left.\frac{\partial \phi_i(r)}{\partial r}\right|_{r_o} = 0 \tag{4.10}$$

▷ free:

$$\left.\frac{\partial^2 \phi_i(r)}{\partial r^2}\right|_{r_o} = 0 \text{and} \quad \left.\frac{\partial^3 \phi_i(r)}{\partial r^3}\right|_{r_o} = 0 \tag{4.11}$$

For the flexural vibration of a Bernoulli-Euler beam or plate, $\mathcal{L} = \frac{\partial^2}{\partial r^2}\left(EI(r)\frac{\partial^2}{\partial r^2}\right)$ and $\mathcal{M} = \rho A$, with $I(r)$ representing the inertial moment, E the Young's modulus of the beam, ρ the beam density, and A the beam cross-sectional area. With Eq. (4.13) and the above equation, the natural frequency can be calculated:

$$\omega_i^2 = \lambda^4 \frac{EI}{\rho A} = \left(\frac{i\pi}{L}\right)^4 \frac{EI}{\rho A} \tag{4.12}$$

Next, as an example, the modes of a simply-supported beam and a cantilever beam are detailed. The $\phi_i(r)$ general solution can be written as follows:

$$\phi_i(r) = A_i \sin \lambda_i r + B_i \cos \lambda_i r + C_i \sinh \lambda_i r + D_i \cosh \lambda_i r \tag{4.13}$$

For the case of a simply-supported beam, the above boundary conditions allow to determine that B_i ,C_i and D_i are equal to zero, and $\sin \lambda_i r$ is also equal to zero which indicates an infinity of discrete natural periods for the system and natural mode shape.

$$\phi_i(r) = A_i \sin \lambda_i r \tag{4.14}$$

Using Eq. (4.4a), A_i is obtained: $A_i = \sqrt{\frac{2}{\rho A L}}$ where L is the length of the beam.

For the case of a cantilever beam, the boundary conditions give $B_i + D_i = 0$ and $A_i + C_i = 0$ leading to the transcendental Eq. (4.15).

$$\cos \lambda_i r \cosh \lambda_i r = -1 \tag{4.15}$$

There are an infinite number of solutions to this equation, and thus an infinite number of natural mode shapes as follows, if A_i is assumed to be equal to one [61].

$$\phi_i(r) = (\sin \lambda_i r - \sinh \lambda_i r) + \alpha_i (\cos \lambda_i r - \cosh \lambda_i r) \tag{4.16}$$

with

$$\alpha_i = \frac{\sin \lambda_i r + \sinh \lambda_i r}{\cos \lambda_i r + \cosh \lambda_i r} \tag{4.17}$$

If the force is point-wise at $r = r_f$, then $f(t, r_f) = f(t)\delta(r_f)$, and $F_i(t) = f(t)\phi_i(r_f)$. Using Laplace transform $\mathtt{L}[\ddot{q}_i(t)] = s^2 q_i(s)$, Eq. (4.6) becomes: $q_i(s) = \phi_i(r_f)\frac{f(s)}{s^2+2\zeta\omega_i s+\omega^2}$. Based on Eq. (4.2), the transfer function between the applied point force $f(s)$ at $r = r_f$, and the transverse deflection of the beam at $y(s, r)$ is ($\mathtt{L}[y(t, r)] = y(s, r)$):

$$\begin{aligned} y(s,r) &= \sum_{i=1}^{\infty} \frac{\phi_i(r)\phi_i(r_f)f(s)}{s^2 + 2\zeta\omega_i s + \omega_i^2} \\ \Leftrightarrow \frac{y(s,r)}{f(s)} &= \sum_{i=1}^{\infty} \frac{\phi_i(r)\phi_i(r_f)}{s^2 + 2\zeta\omega_i s + \omega_i^2} \end{aligned} \tag{4.18}$$

4.2 Piezoelectric modelling

In order to design a control design using an analytical model of piezoelectric sensors/actuators, there must first be an understanding and successful modelling of the piezoelectric phenomena over the structure to be controlled. This section gives just a brief summary of the piezoelectric model for the unidirectional dimension, as this has already been extensively covered in the existing literature [9, 33, 34, 63].

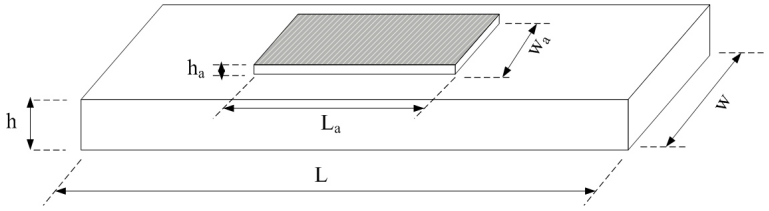

Figure 4.1: Beam with piezo patch attached [4].

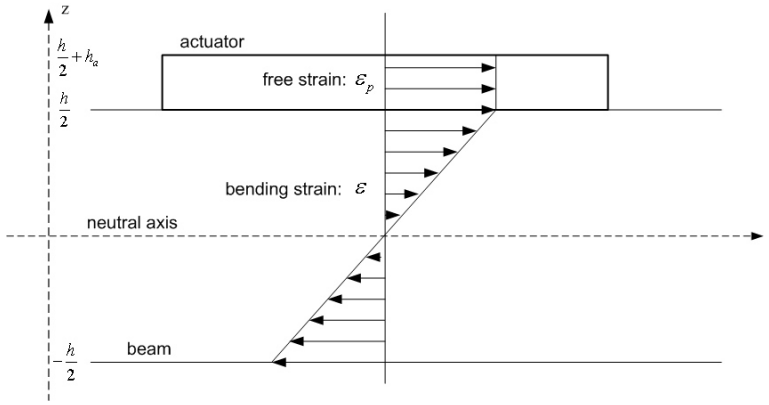

Figure 4.2: Assumed piezo substructure strain distribution [5].

4.2.1 Piezoelectric actuator laminate beam

Considering the beam model Fig. 4.2, a piezoelectric actuator is added and used as an external force to the beam structure. The constraint due to the piezo actuator can be considered as a moment applied between the two extremities of the piezo patch [5]. The force is expressed in Eq. (4.19), with M_a representing the bending moment. The subscript a denotes the piezoelectric actuator.

$$f(t,r) = \frac{\partial^2}{\partial r^2} M_a(t,r) \tag{4.19}$$

For simplicity's sake, the contribution to the beam features of the piezo patch in terms of mass and stiffness is considered as negligible. The overall longitudinal strain inside the actuator consists of the induced longitudinal strain due to the beam bending ϵ and the unconstrained strain ϵ_a. The unconstrained strain is that generated in the patch due to the applied voltage only [20, 22]. The unconstrained

strain of the actuator in the z-direction is given by Eq. (4.20).

$$\epsilon_a(t) = \frac{d_{31}}{h_a} v_a(t) \tag{4.20}$$

where $v_a(t)$ is the applied voltage in the direction of polarisation, h_a is the actuator thickness, and d_{31} is the piezo material strain constant.

Based on Kirchhoff's hypothesis of laminate plate theory, $\epsilon(z) = \alpha z$, the beam stress distribution can be written as follows, by using Hooke's law:

$$\sigma(z) = E\epsilon(z) = E\alpha z \tag{4.21}$$

where E is the Young's elastic modulus of the beam. The piezo actuator's stress distribution can be written:

$$\sigma_a(z, v_a) = E\big(\epsilon(z) - \epsilon_a(v_a)\big) \tag{4.22}$$

The strain gradient α is determined from the moment equilibrium equation on the neutral axis of the beam:

$$\int_{-\frac{h}{2}}^{\frac{h}{2}} z\sigma(z)dz + \int_{\frac{h}{2}}^{\frac{h}{2}+h_a} z\sigma_a(z)dz = 0 \tag{4.23}$$

$$\Leftrightarrow \alpha = k\epsilon_a = \frac{12E_a h_a(h_a + h)}{2Eh^3 + E_a\left[(h + 2h_a)^3 - h^3\right]}\epsilon_a \tag{4.24}$$

with E_a representing the piezoelectric Young modulus, d_{31} the charge constant, h the beam height, h_a the piezoelectric height, and w_a the piezoelectric width. The bending moment of the actuator patch on the beam is [5]:

$$M_a(t) = K\left[H(r - r_b) - H(r - r_e)\right] v_a(t) \tag{4.25}$$

where r_b is the location of one end of the piezoelectric patch, r_e is the location of the other end, the subscript i indicates the mode and the subscript j indicates the

actuator,

$$H(z) = \begin{cases} 0 & \text{if } z < 0 \\ 1 & \text{if } 0 \geq z \end{cases} \tag{4.26}$$

and $K = \frac{kEd_{31}h^3w_a}{12h_a}$.

Using Eq. (4.7) the applied force can be expressed as:

$$F_{ij}(t) = \int_0^L \phi_i(r) \frac{\partial^2 M_a(r_j)}{\partial r^2} dr = K_j \Psi_{ij} v_a(t) \tag{4.27}$$

where

$$\Psi_{ij} = \int_0^L \phi_i(r) \left[\frac{\partial \delta(r - r_{b_j})}{\partial r} - \frac{\partial \delta(r - r_{e_j})}{\partial r} \right] dz = \frac{\partial \phi_i(r_{e_j})}{\partial r} - \frac{\partial \phi_i(r_{b_j})}{\partial r} \tag{4.28}$$

knowing that:

$$\int_{-\infty}^{\infty} \frac{\partial^n \delta(r - \theta)}{\partial r^n} \phi(r) dr = (-1)^n \frac{\partial^n \phi(\theta)}{\partial r^n} \tag{4.29}$$

j is the attribute to the actuator number if there is more than one. Thus, Eq. (4.6) is rewritten, adding an attenuation parameter:

$$\ddot{q}_i(t) + 2\zeta\omega_i \dot{q}_i(t) + \omega_i^2 q_i(t) = \sum_{j=1}^{J} K_j \Psi_{ij} v_{a_j}(t), \quad i = 1, 2, ... \tag{4.30}$$

with

$$\Psi_{ij} = \frac{\partial \phi_i(r_{e_j})}{\partial r} - \frac{\partial \phi_i(r_{b_j})}{\partial r} \tag{4.31}$$

The MIMO transfer function between the actuator tensions $\boldsymbol{v}_a = [v_{a_1} \cdots v_{a_j}]^T$ and

the beam deflection $y(s,r)$ is:

$$y(s,r) = \sum_{i=1}^{\infty} \frac{\phi_i(r)}{s^2 + 2\zeta\omega_i s + \omega_i^2} \sum_{j=1}^{\infty} K_i \Psi_{ij} v_{a_j}(t)$$
$$\Leftrightarrow \frac{y(s,r)}{\boldsymbol{v}_a^T(s)} = \sum_{i=1}^{\infty} \frac{\phi_i(r)\mathbf{P}_i}{s^2 + 2\zeta\omega_i s + \omega^2} \tag{4.32}$$

where

$$\mathbf{P}_i = \frac{1}{\rho A}[K_i\Psi_{i1} \cdots K_J\Psi_{iJ}] \tag{4.33}$$

4.2.2 Piezoelectric sensor laminate beam modelling

This model begins with the same assumptions as in the previous model. From [64], it is known that the electric charges distribution q_s for the piezo sensor due to the strain is given by:

$$q_s(t) = \frac{k_{31}^2 w_s}{g_{31}} \epsilon_s(t) \tag{4.34}$$

with k_{31} being the electromechanical coupling factor and g_{31} the piezoelectric voltage constant. The sensor strain is

$$\epsilon_s(t) = \frac{(h + h_s)}{2} \frac{\partial^2 y(t)}{\partial z^2} \tag{4.35}$$

with h_s the sensor height . The overall electric charge generated can be obtained by integrating the charge q_s (see Eq. (4.34)) over the length of the k^{th} sensor.

$$v_{s_k}(t) = \Omega_k \sum_{i=1}^{\infty} \int_{r_{b_k}}^{r_{e_k}} \frac{\partial^2 \phi_i(r)}{\partial r^2} dr.q_i(t)$$
$$= \Omega_k \sum_{i=1}^{\infty} \left[\frac{\partial \phi_i(r_{e_k})}{\partial r} - \frac{\partial \phi_i(r_{b_k})}{\partial r} \right] q_i(t) = \Omega_k \sum_{i=1}^{\infty} \Psi_{ik} q_i(t) \tag{4.36}$$

where $\Omega_k = \frac{k_{31}^2 w_s}{C_k g_{31}} \frac{(h+h_s)}{2}$, w_s is the piezoelectric patch width, C_k the capacitance of the k^{th} sensor, g_{31} the voltage constant and h_s the piezoelectric actuator thickness.

Adding ω_k and summing $q_i(t)$, Eq. (4.6), is rewritten with the addition of an attenuation parameter for a point force:

$$\begin{aligned} v_{sk}(s)\sum_{i=1}^{\infty}\left[s^2+2\zeta\omega_i s+\omega_i^2\right] &= \Omega_k\sum_{i=1}^{\infty}\Psi_{ik}f(t)\phi_i(r_f) \\ \Leftrightarrow \frac{v_{sk}(s)}{f(s)} &= \Omega_k\sum_{i=1}^{\infty}\frac{\Psi_{ik}\phi_i(r_f)}{s^2+2\zeta\omega_i s+\omega_i^2} \\ \Leftrightarrow \frac{\boldsymbol{v}_s(s)}{f(s)} &= \sum_{i=1}^{\infty}\frac{\boldsymbol{\Upsilon}_i\phi_i(r_f)}{s^2+2\zeta\omega_i s+\omega_i^2} \end{aligned} \tag{4.37}$$

where $\boldsymbol{\Upsilon}_i = [\Omega_i\Psi_{i1}\cdots\Omega_J\Psi_{iJ}]^T$ and $\boldsymbol{v}_s = [v_{s_1}\cdots v_{s_j}]^T$.

4.2.3 Transfer function between the piezo actuators and sensors

Manipulating Eqs. (4.32) and (4.36), it is possible to get the transfer function between the j^{th} actuator and the k^{th} sensor.

$$\begin{aligned} G_{s_k,a_j}(s) = \frac{v_{s_k}(s)}{v_{a_j}(s)} &= \Omega_k K_j\sum_{\iota=1}^{\infty}\frac{\Psi_{\iota k}\Psi_{\iota j}}{s^2+2\zeta\omega_\iota s+\omega_\iota^2} \\ \Leftrightarrow \frac{\boldsymbol{v}_s(s)}{\boldsymbol{v}_a(s)} &= \sum_{i=1}^{\infty}\frac{\boldsymbol{\Upsilon}_i\mathbf{P}_i}{s^2+2\zeta\omega_i s+\omega_i^2} \end{aligned} \tag{4.38}$$

4.3 State-space representation

Most contemporary control designs are represented in the state-space for the sake of convenience in terms of modelling and to optimise the chances of finding the most suitable controller. Thus, the previous analytical equations will now be expressed in the terms of this space.

A state-space representation can be made using $\boldsymbol{x}(s) = [\boldsymbol{q}(s)\ \ \dot{\boldsymbol{q}}(s)]^T$ as the state variable, with $\boldsymbol{q}(s) = [q_1(s)\cdots q_N(s)]$, combined with the transfer functions Eqs. (4.32), (4.2.2) and (4.2.3) [45]. For the state-space domain, Eqs. (4.39) show how it is possible to obtain: the system matrix $\boldsymbol{A}$, the actuator input matrix

$\boldsymbol{B}_a$, with N_a the number of actuators; the sensor output matrix $\boldsymbol{C}_s$, with N_s the number of sensors; and the feedthrough matrix $\boldsymbol{D}_{as}$ relating the actuators to the sensors.

$$\dot{\boldsymbol{x}}(s) = \boldsymbol{A}\boldsymbol{x}(s) + \boldsymbol{B}_f\boldsymbol{f}(s) + \boldsymbol{B}_a\boldsymbol{v}_a(s) \tag{4.39a}$$

$$\boldsymbol{y}(s) = \boldsymbol{C}_y\boldsymbol{x}(s) \tag{4.39b}$$

$$\boldsymbol{v}_s(s) = \boldsymbol{C}_s\boldsymbol{x}(s) + \boldsymbol{D}_{as}\boldsymbol{v}_a(s) \tag{4.39c}$$

where $\boldsymbol{f}$ are the disturbances, $\boldsymbol{y}$ are the displacement output at particular locations, $\boldsymbol{v}_s$ are the sensor measurements, and $\boldsymbol{v}_a$ are the actuators. In the case of a cantilever beam with piezoelectric sensor/actuator patches as modelled in section 4.2, to which a point-wise disturbance is applied, the state-space matrices can be written as follows:

$$\boldsymbol{A}_{[2N\times 2N]} = \begin{bmatrix} \boldsymbol{0}_{[N\times N]} & \boldsymbol{I}_{[N\times N]} \\ -\operatorname{diag}(\omega_1^2,\ldots,\omega_N^2) & -2\operatorname{diag}(\zeta_1\omega_1,\ldots,\zeta_N\omega_N) \end{bmatrix}$$

$$\boldsymbol{B}_{f\,[2N\times N_f]} = \begin{bmatrix} & \boldsymbol{0}_{[N\times N_f]} & \\ \phi_1(r_{f_1}) & \cdots & \phi_1(r_{f_{N_f}}) \\ \vdots & \ddots & \vdots \\ \phi_N(r_{f_1}) & \cdots & \phi_N(r_{f_{N_f}}) \end{bmatrix}$$

$$\boldsymbol{B}_{a\,[2N\times N_a]} = \frac{1}{\rho A}\begin{bmatrix} & \boldsymbol{0}_{[N\times N_a]} & \\ \kappa_1\Psi_{11} & \cdots & \kappa_1\Psi_{1N_a} \\ \vdots & \ddots & \vdots \\ \kappa_N\Psi_{N1} & \cdots & \kappa_N\Psi_{NN_a} \end{bmatrix}$$

$$\boldsymbol{C}_{y\,[N_y\times 2N]} = \begin{bmatrix} \phi_1(r_{y_1}) & \cdots & \phi_N(r_{y_1}) & \\ \vdots & \ddots & \vdots & \boldsymbol{0}_{[N_y\times N]} \\ \phi_1(r_{y_{N_y}}) & \cdots & \phi_N(r_{y_{N_y}}) & \end{bmatrix}$$

$$\boldsymbol{C}_{s\,[N_s\times 2N]} = \begin{bmatrix} \Omega_1\Psi_{11} & \cdots & \Omega_N\Psi_{N1} & \\ \vdots & \ddots & \vdots & \boldsymbol{0}_{[N_s\times N]} \\ \Omega_{N_s}\Psi_{1N_s} & \cdots & \Omega_N\Psi_{NN_s} & \end{bmatrix}$$

This state-space representation then enables a vibration control system to be designed for a given structure.

4.4 Analytical optimal truncated model

Developing a feedback controller for flexible structures is usually done by first developing a modal model of the structural response, as detailed in the preceding sections of this chapter. Because it is not possible to model the infinite number of modes which make up the total structural response, the approach uses a truncated model which ignores the influence of all modes resonant above a certain frequency. The effect of these unmodelled modes is then usually taken into account using approximation terms, in order to compensate for spillover and improve the controller stability. In some cases, it is desirable to control a structure over a finite bandwidth which excludes some low frequency modes. In this case, it was found that the optimal model is one that excludes both low and high frequency modes.

The following section first looks at how approximation terms were developed for the model to include the effect of high frequency unmodelled vibration modes on the structural response. This is called classical optimal truncation, and is well documented in the literature for being highly effective in controlling low frequencies. Secondly, this section describes the development of approximation terms for the model to include the effect of both low and high frequency unmodelled vibration modes on the structural response. This will be called new optimal truncation. There will be an outlining of procedures for calculating the optimal correction terms that include the lower and higher order mode contributions. The new control approach has a lower order compared to the standard approach that usually includes all the lowest vibration modes up to the highest frequency of interest.

4.4.1 Classical optimal truncation

It is not viable to use a full representation of the system $\boldsymbol{G}(s)$, in the controller design because of the excessive time required to compute it and also restrictions on the size of the controller. The system model must be truncated; this reduced

model $\boldsymbol{G}_r(s)$, has a direct influence on the controller's performance. Maintaining high controller performance requires the consideration of the residual dynamic $\boldsymbol{G}_d(s)$, of the full system $\boldsymbol{G}(s)$. This phenomena was studied by [65] who shows the alteration in the location of the poles and zeros due to the model truncation.

$$\begin{aligned}\boldsymbol{G}(s) &= \sum_{i=1}^{\infty} \frac{\boldsymbol{F}_i}{s^2 + 2\zeta\omega_i s + \omega_i^2} \\ &= \sum_{i=1}^{N} \frac{\boldsymbol{F}_i}{s^2 + 2\zeta\omega_i s + \omega_i^2} + \sum_{i=N+1}^{\infty} \frac{\boldsymbol{F}_i}{s^2 + 2\zeta\omega_i s + \omega_i^2} \qquad (4.40) \\ &= \boldsymbol{G}_r(s) + \boldsymbol{G}_d(s) \qquad (4.41)\end{aligned}$$

$\boldsymbol{G}(s)$ can be approximated by $\widetilde{\boldsymbol{G}}(s)$, a function containing $\boldsymbol{G}_r(s)$ and a zero-order parameter $\boldsymbol{K}_d$:

$$\widetilde{\boldsymbol{G}}(s) = \boldsymbol{G}_r(s) + \boldsymbol{K}_d \qquad (4.42)$$

The idea is to try to evaluate $\boldsymbol{K}_d$ minimising the cost function J using the $\mathcal{H}_2$ norm:

$$J = \left\| \boldsymbol{\mathcal{W}}(s) \left(\boldsymbol{G}(s) - \widetilde{\boldsymbol{G}}(s) \right) \right\|_2^2 \qquad (4.43)$$

with $\boldsymbol{\mathcal{W}}(s)$ a perfect low-pass filter applied between $\pm\omega_c$: $\omega_c = \frac{\omega_n + \omega_{n+1}}{2}$. Assuming that the damping is very small: $2\zeta\omega_i \to 0$

$$\begin{aligned}J &= \left\| \boldsymbol{\mathcal{W}}(s) \left(\boldsymbol{G}_r(s) + \boldsymbol{G}_d(s) - \boldsymbol{G}_r(s) - \boldsymbol{K}_d \right) \right\|_2^2 \\ &= \left\| \boldsymbol{\mathcal{W}}(s) \left(\sum_{i=N+1}^{\infty} \frac{\boldsymbol{F}_i}{s^2 + \omega_i^2} - \boldsymbol{K}_d \right) \right\|_2^2 \\ &= \frac{1}{2\pi} \int_{-\omega_c}^{\omega_c} \left| \sum_{i=N+1}^{\infty} \frac{\boldsymbol{F}_i}{s^2 + \omega_i^2} - \boldsymbol{K}_d \right|^2 d\omega \\ &= \frac{1}{2\pi} \int_{-\omega_c}^{\omega_c} \left\{ \left| \sum_{i=N+1}^{\infty} \frac{\boldsymbol{F}_i}{s^2 + \omega_i^2} \right|^2 - 2 \sum_{i=N+1}^{\infty} \frac{\boldsymbol{F}_i}{s^2 + \omega_i^2} \boldsymbol{K}_d + \boldsymbol{K}_d^2 \right\} d\omega \qquad (4.44)\end{aligned}$$

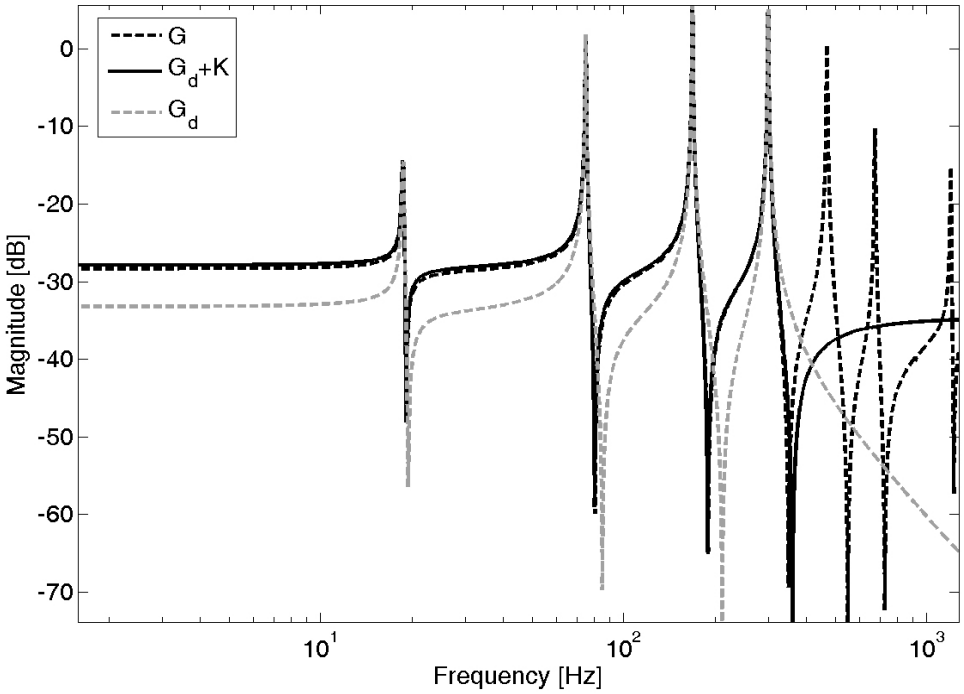

Figure 4.3: Dynamic effect of the model truncation: V_s/V_a.

Differentiating J with respect to $\boldsymbol{K}_d$, one obtains the optimum value of $\boldsymbol{K}_d$ when it is equal to 0:

$$\begin{aligned}
\frac{\partial J}{\partial \boldsymbol{K}_d} &= \frac{1}{2\pi} \int_{-\omega_c}^{\omega_c} \left\{ 2 \sum_{i=N+1}^{\infty} \frac{\boldsymbol{F}_i}{s^2 + \omega_i^2} + 2\boldsymbol{K}_d \right\} d\omega \\
\Leftrightarrow \boldsymbol{K}_d &= \frac{1}{2\omega_c} \int_{-\omega_c}^{\omega_c} \sum_{i=N+1}^{\infty} \frac{\boldsymbol{F}_i}{s^2 + \omega_i^2} \, d\omega \\
\boldsymbol{K}_d &= \frac{1}{2\omega_c} \sum_{i=N+1}^{\infty} \frac{\boldsymbol{F}_i}{\omega_i} \ln\left(\frac{\omega_i + \omega_c}{\omega_i - \omega_c} \right)
\end{aligned} \tag{4.45}$$

Fig. 4.3 shows the effect of the model truncation, with the residual dynamic coefficient $\boldsymbol{K}_d$ and without, for a simulated pinned-pinned beam with a piezoelectric sensor and actuator. As all the transfer functions of the model are truncated, the residual dynamic correction needs to be calculated for each term of the state-space

system of Eqs. (4.39) [45]:

$$\boldsymbol{K}_{as} = \frac{1}{2\omega_c} \sum_{i=N+1}^{\infty} \frac{\boldsymbol{\Upsilon}_i \mathbf{P}_i}{\omega_i} \ln\left(\frac{\omega_i + \omega_c}{\omega_i - \omega_c}\right) \tag{4.46a}$$

$$\boldsymbol{K}_{fy}(r) = \frac{1}{2\omega_c} \sum_{i=N+1}^{\infty} \frac{\phi_i(r)\phi_i(r_f)}{\omega_i} \ln\left(\frac{\omega_i + \omega_c}{\omega_i - \omega_c}\right) \tag{4.46b}$$

$$\boldsymbol{K}_{ay}(r) = \frac{1}{2\omega_c} \sum_{i=N+1}^{\infty} \frac{\phi_i(r)\mathbf{P}_i}{\omega_i} \ln\left(\frac{\omega_i + \omega_c}{\omega_i - \omega_c}\right) \tag{4.46c}$$

$$\boldsymbol{K}_{fs} = \frac{1}{2\omega_c} \sum_{i=N+1}^{\infty} \frac{\phi_i(r_f)\boldsymbol{\Upsilon}_i}{\omega_i} \ln\left(\frac{\omega_i + \omega_c}{\omega_i - \omega_c}\right) \tag{4.46d}$$

giving the following state-space expression:

$$\dot{\boldsymbol{x}}(s) = \boldsymbol{A}\boldsymbol{x}(s) + \boldsymbol{B}_f\boldsymbol{f}(s) + \boldsymbol{B}_a\boldsymbol{v}_a(s) \tag{4.47a}$$

$$\boldsymbol{y}(s) = \boldsymbol{C}_y\boldsymbol{x}(s) + \boldsymbol{K}_{fy}\boldsymbol{f}(s) + \boldsymbol{K}_{ay}\boldsymbol{v}_a(s) \tag{4.47b}$$

$$\boldsymbol{v}_s(s) = \boldsymbol{C}_s\boldsymbol{x}(s) + \boldsymbol{K}_{fs}\boldsymbol{f}(s) + \boldsymbol{K}_{as}\boldsymbol{v}_a(s) \tag{4.47c}$$

4.4.2 New optimal truncation for high frequency

There is usually a particular frequency bandwidth that is of interest for high frequency modal control, whereas standard controller design approaches usually include all lower frequency modes, even when their resonance frequencies are below the region of interest. This may complicate the control design, since the states representing the lower frequency modes also need to be included, resulting in a controller that unnecessarily attempts to control those lower frequency modes in addition to the higher frequency modes which are of interest.

Here, a control approach is presented that minimises the unnecessary control effort spent on those low frequency modes, which thereby gives a lower order controller. Because the model must be truncated for practical reasons, the performance of the controller is directly determined by the reduced model $\boldsymbol{G}_r(s)$, and the way in which it is reduced. To maintain high controller performance, the model must take into account the residual dynamic $\boldsymbol{G}_d(s)$, due to higher frequency

modes. This has been done by others [65] who show the required relocation of poles and zeros to account for the model truncation. However in the analysis of [65], all the lower modes are included in the model. As previously mentioned, when the focus is only on a specified frequency bandwidth, to maximise the control efficiency in the bandwidth of interest requires the truncation of the modes above and below that bandwidth. In this case, to account for the altered poles and zeros as a result of the truncation, it is necessary to account for the lower order modes using a low frequency residual dynamic $\boldsymbol{G}_l(s)$, as well as the higher modes using a high frequency residual dynamic $\boldsymbol{G}_d(s)$. This section looks at how $\boldsymbol{G}_d(s)$ is derived.

Consider a general transfer function, similar to the one shown in Eq. (4.8). Supposing that the objective is to control broadband vibration between the frequencies of the m_1^{th} and m_2^{th} vibration modes, the modal model may then be written as:

$$\begin{aligned}\boldsymbol{G}(s) &= \sum_{i=1}^{\infty} \frac{\boldsymbol{F}_i}{s^2 + 2\zeta_i\omega_i s + \omega_i^2} \\ &= \sum_{i=1}^{m_1-1} \frac{\boldsymbol{F}_i}{s^2 + 2\zeta_i\omega_i s + \omega_i^2} + \sum_{i=m_1}^{m_2} \frac{\boldsymbol{F}_i}{s^2 + 2\zeta_i\omega_i s + \omega_i^2} + \sum_{i=m_2+1}^{\infty} \frac{\boldsymbol{F}_i}{s^2 + 2\zeta_i\omega_i s + \omega_i^2} \\ &= \boldsymbol{G}_l(s) + \boldsymbol{G}_r(s) + \boldsymbol{G}_d(s) \end{aligned} \tag{4.48}$$

where m_1 is the mode number of the first vibration mode of interest, m_2 is that of the last one, and $\boldsymbol{F}_i$ is the matrix of the external forces. Using a similar approach to that used in modal analysis [6] as shown in Fig. 4.4, it can be seen that the contribution of the modes with resonance frequencies above and below the frequency bandwidth of interest can be approximated by a relatively simple function. Hence, the full model $\boldsymbol{G}(s)$ can be approximated by $\widetilde{\boldsymbol{G}}(s)$, which is a function containing $\boldsymbol{G}_r(s)$ that includes the modes in the frequency bandwidth of interest, along with a zero-order parameter $\boldsymbol{K}_d$ to represent the contribution of the higher frequency modes to that bandwidth of interest, and a second-order parameter $\boldsymbol{K}_l/\omega^2$ to represent the contribution of the lower frequency modes, where $s = j\omega$.

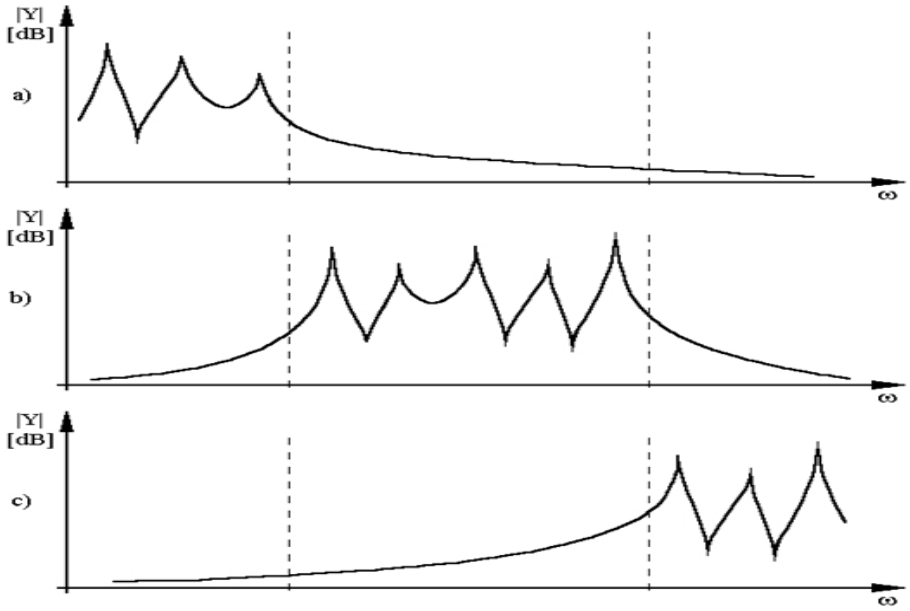

Figure 4.4: Mode contributions to energy inside and outside the frequency bandwidth of interest: a) low frequencies, b) frequencies of interest and c) high frequencies, from [6].

$$\widetilde{\boldsymbol{G}}(\omega) = \frac{\boldsymbol{K}_l}{\omega^2} + \boldsymbol{G}_r(\omega) + \boldsymbol{K}_d \tag{4.49}$$

The idea is to try to evaluate the optimal $\boldsymbol{K}_d$ and $\boldsymbol{K}_l$ by minimising the $\mathcal{H}_2$ norm of the following cost function J:

$$J = \left\| \boldsymbol{\mathcal{W}}(\omega) \left(\boldsymbol{G}(\omega) - \widetilde{\boldsymbol{G}}(\omega) \right) \right\|_2^2 \tag{4.50}$$

where $\boldsymbol{\mathcal{W}}(\omega)$ is a perfect band-pass filter that has a unit value in $[-\omega_c, -\omega_a]$ and $[\omega_a, \omega_c]$ where $\omega_c = \frac{\omega_{m_2} + \omega_{m_2+1}}{2}$ and $\omega_a = \frac{\omega_{m_1} + \omega_{m_1-1}}{2}$. The optimum values of $\boldsymbol{K}_d$ and $\boldsymbol{K}_l$ can be found by differentiating J with respect to $\boldsymbol{K}_d$ and $\boldsymbol{K}_l$. Since the damping is usually small for flexible structures, the following derivation assumes $\zeta_i \to 0$.

Using Eqs. (4.48) and (4.49) , Eq. (4.50) can be rewritten as:

$$J = \frac{1}{2\pi}\int_{-\infty}^{\infty} \mathrm{tr}\left\{\left(\boldsymbol{\mathcal{W}}(\omega)(\boldsymbol{G}(\omega)-\widetilde{\boldsymbol{G}}(\omega))\right)^{*}\left(\boldsymbol{\mathcal{W}}(\omega)(\boldsymbol{G}(\omega)-\widetilde{\boldsymbol{G}}(\omega))\right)\right\} d\omega$$

$$= \frac{1}{\pi}\int_{\omega_a}^{\omega_c}\left\{\mathrm{tr}\left\{\sum_{\substack{i=1\\ i\notin[m_1,m_2]}}^{\infty}\frac{\boldsymbol{F}_i^{*}}{\omega_i^2-\omega^2}\sum_{\substack{i=1\\ i\notin[m_1,m_2]}}^{\infty}\frac{\boldsymbol{F}_i}{\omega_i^2-\omega^2}\right\}\right.$$

$$\left.-2\,\mathrm{Re}\left\{\mathrm{tr}\left\{\sum_{\substack{i=1\\ i\notin[m_1,m_2]}}^{\infty}\frac{\boldsymbol{F}_i^{*}}{\omega_i^2-\omega^2}\boldsymbol{K}_d\right\}\right\}+\mathrm{tr}\left\{\boldsymbol{K}_d^{*}\boldsymbol{K}_d\right\}\right.$$

$$\left.-2\,\mathrm{Re}\left\{\mathrm{tr}\left\{\sum_{\substack{i=1\\ i\notin[m_1,m_2]}}^{\infty}\frac{\boldsymbol{F}_i^{*}}{\omega_i^2-\omega^2}\frac{\boldsymbol{K}_l}{\omega^2}\right\}\right\}+\mathrm{tr}\left\{\frac{\boldsymbol{K}_l^{*}\boldsymbol{K}_l}{\omega^4}\right\}+2\,\mathrm{tr}\left\{\frac{\boldsymbol{K}_l^{*}\boldsymbol{K}_d}{\omega^2}\right\}\right\} d\omega \quad (4.51)$$

where $\mathrm{tr}\{\boldsymbol{F}\}$ represents the trace of a matrix $\boldsymbol{F}$ and * represents the conjugate transposed. Differentiating J with respect to $\boldsymbol{K}_l$ and equating it to zero gives:

$$\frac{\partial J}{\partial \boldsymbol{K}_l} = \frac{2}{\pi}\int_{\omega_a}^{\omega_c}\left\{\frac{\boldsymbol{K}_l}{\omega^4}+\frac{\boldsymbol{K}_d}{\omega^2}-\frac{1}{\omega^2}\sum_{\substack{i=1\\ i\notin[m_1,m_2]}}^{\infty}\frac{\boldsymbol{F}_i}{\omega_i^2-\omega^2}\right\} d\omega = 0. \quad (4.52)$$

The first term of the above equation can be expressed as follows:

$$\int_{\omega_a}^{\omega_c}\frac{\boldsymbol{K}_l}{\omega^4}d\omega = \left(\frac{1}{3}\frac{\omega_c^3-\omega_a^3}{\omega_c^3\omega_a^3}\right)\boldsymbol{K}_l = \beta\boldsymbol{K}_l. \quad (4.53)$$

The second term can be expressed as:

$$\int_{\omega_a}^{\omega_c}\frac{-\boldsymbol{K}_d}{\omega^2}d\omega = -\left(\frac{\omega_c-\omega_a}{\omega_c\omega_a}\right)\boldsymbol{K}_d = -\varpi\boldsymbol{K}_d. \quad (4.54)$$

And the third term can be similarly expressed, where $\sum_{\substack{i=1\\ i\notin[m_1,m_2]}}^{\infty} = \sum_{\notin}$ is used to

simplify the notation:

$$\int_{\omega_a}^{\omega_c} \frac{1}{\omega^2} \sum_{\notin} \frac{\boldsymbol{F}_i}{\omega_i^2 - \omega^2} d\omega = \int_{\omega_a}^{\omega_c} \sum_{\notin} \frac{\boldsymbol{F}_i}{\omega_i^2} \left(\frac{1}{\omega_i^2 - \omega^2} + \frac{1}{\omega^2} \right) d\omega$$
$$= \sum_{\notin} \frac{\boldsymbol{\chi}_i}{\omega_i^2} + \varpi \sum_{\notin} \frac{\boldsymbol{F}_i}{\omega_i^2} \tag{4.55}$$

with $\boldsymbol{\chi}_i = \dfrac{\boldsymbol{F}_i}{\omega_i^2} \ln \left\{ \dfrac{(\omega_c + \omega_i)|\omega_a - \omega_i|}{|\omega_c - \omega_i|(\omega_a + \omega_i)} \right\}$.

Thus, the optimal $\boldsymbol{K}_l$ can be obtained using Eqs. (4.53) , (4.54) and (4.55) as follows:

$$\boldsymbol{K}_l = \frac{1}{\beta} \left(\sum_{\notin} \frac{\boldsymbol{\chi}_i}{\omega_i^2} + \varpi \sum_{\notin} \frac{\boldsymbol{F}_i}{\omega_i^2} - \varpi \boldsymbol{K}_d \right) = \frac{1}{\beta} \left(\boldsymbol{\Gamma}_i - \varpi \boldsymbol{K}_d \right) \tag{4.56}$$

with $\boldsymbol{\Gamma}_i = \sum_{\notin} \dfrac{\boldsymbol{\chi}_i}{\omega_i^2} + \varpi \sum_{\notin} \dfrac{\boldsymbol{F}_i}{\omega_i^2}$. Using a similar approach, the optimal $\boldsymbol{K}_d$ is found by differentiating J in Eq. (4.51) with respect to $\boldsymbol{K}_d$. Substituting Eq. (4.56) into Eq. (4.51) gives:

$$\frac{\partial J}{\partial \boldsymbol{K}_d} = \frac{2}{\pi} \int_{\omega_a}^{\omega_c} \left\{ - \sum_{\notin} \frac{\boldsymbol{F}_i}{\omega_i^2 - \omega^2} + \frac{\boldsymbol{K}_l}{\omega^2} + \boldsymbol{K}_d \right\} d\omega$$
$$= \frac{2}{\pi} \int_{\omega_a}^{\omega_c} \left\{ \boldsymbol{K}_d \left(1 - \frac{\varpi}{\beta \omega^2} \right) + \frac{\boldsymbol{\Gamma}_i}{\beta \omega^2} - \sum_{\notin} \frac{\boldsymbol{F}_i}{\omega_i^2 - \omega^2} \right\} d\omega = 0. \tag{4.57}$$

The first term of Eq. (4.57) is equal to:

$$\int_{\omega_a}^{\omega_c} \boldsymbol{K}_d \left(1 - \frac{\varpi}{\beta \omega^2} \right) d\omega = \left(\omega_c - \omega_a - \frac{\varpi^2}{\beta} \right) \boldsymbol{K}_d = \gamma \boldsymbol{K}_d, \tag{4.58}$$

while the second term is:

$$\int_{\omega_a}^{\omega_c} \frac{\boldsymbol{\Gamma}_i}{\beta\omega^2} d\omega = \frac{\varpi}{\beta}\boldsymbol{\Gamma}_i, \tag{4.59}$$

and the third term is:

$$-\int_{\omega_a}^{\omega_c} \sum_{\notin} \frac{\boldsymbol{F}_i}{\omega_i^2 - \omega^2} d\omega = -\sum_{\notin} \boldsymbol{\chi}_i. \tag{4.60}$$

Substituting Eq. (4.58), (4.59) and (4.60) into Eq. (4.57), the optimal $\boldsymbol{K}_d$ is found to be

$$\boldsymbol{K}_d = \frac{1}{\gamma}\left(\sum_{\notin} \boldsymbol{\chi}_i - \frac{\varpi}{\beta}\boldsymbol{\Gamma}_i\right). \tag{4.61}$$

The optimisation approximation function $\widetilde{\boldsymbol{G}}(\omega)$ now can be calculated using Eq. (4.61). The next step in building an accurate model of the vibration in a real structure is to improve the conventional state-space model by incorporating the required additional terms to account for the effect of modes outside the frequency bandwidth of interest.

The state-space representation of section 4.3 combined with the optimisation results from the previous section gives the following expressions:

$$\dot{\boldsymbol{x}}_c(s) = \boldsymbol{A}_c\boldsymbol{x}_c(s) + \boldsymbol{B}_{1c}(r)f(s) + \boldsymbol{B}_{2c}\boldsymbol{v}_a(s) \tag{4.62a}$$

$$y(s,r) = \boldsymbol{C}_{1c}(r)\boldsymbol{x}_c(s) + \boldsymbol{D}_{11c}(r)f(s) + \boldsymbol{D}_{12c}(r)\boldsymbol{v}_a(s) \tag{4.62b}$$

$$\boldsymbol{v}_s(s) = \boldsymbol{C}_{2c}\boldsymbol{x}_c(s) + \boldsymbol{D}_{21c}f(s) + \boldsymbol{D}_{22c}\boldsymbol{v}_a(s) \tag{4.62c}$$

where,

$$\underset{[2(N+Nf+Na)\times 2(N+Nf+Na)]}{\boldsymbol{A}_c} = \begin{bmatrix} \boldsymbol{A} & \boldsymbol{0}_{[2N\times 2(N_f+N_a)]} \\ \boldsymbol{0}_{[2(N_f+N_a)\times 2N]} & \boldsymbol{A}_l \end{bmatrix} \tag{4.63a}$$

$$\underset{[2(N_f+N_a)\times 2(N_f+N_a)]}{\boldsymbol{A}_l} = \begin{bmatrix} \boldsymbol{0}_{[(N_f+N_a)\times(N_f+N_a)]} & \boldsymbol{I}_{[(N_f+N_a)\times(N_f+N_a)]} \\ \boldsymbol{0}_{[(N_f+N_a)\times(N_f+N_a)]} & \boldsymbol{0}_{[(N_f+N_a)\times(N_f+N_a)]} \end{bmatrix} \tag{4.63b}$$

$$\underset{[2(N_f+N_a)\times N_f]}{\boldsymbol{B}_{1c}} = \begin{bmatrix} \underset{[2N\times N_f]}{\boldsymbol{B}_1} \\ \boldsymbol{0}_{[(N_f+N_a)\times N_f]} \\ \boldsymbol{I}_{[N_f\times N_f]} \\ \boldsymbol{0}_{[N_a\times N_a]} \end{bmatrix}, \underset{[2(N_f+N_a)\times N_a]}{\boldsymbol{B}_{2c}} = \begin{bmatrix} \underset{[2N\times N_a]}{\boldsymbol{B}_2} \\ \boldsymbol{0}_{[(N_f+N_a)\times N_a]} \\ \boldsymbol{0}_{[N_f\times N_a]} \\ \boldsymbol{I}_{[N_a\times N_a]} \end{bmatrix} \tag{4.63c}$$

and where $\boldsymbol{F}_{[r\times c]}$ denotes the number of rows r and columns c of matrix $\boldsymbol{F}$. The correction terms $\boldsymbol{K}_l$ and $\boldsymbol{K}_d$ are calculated for each transfer function considering a combination of any pair of sensors, actuators or disturbance force. The remaining matrices in Eqs. (4.62) are:

$$\underset{[N_y\times 2(N+N_f+N_a)]}{\boldsymbol{C}_{1c}} = \begin{bmatrix} \underset{[N_y\times 2N]}{\boldsymbol{C}_1} & \boldsymbol{K}_{l_{yf}} & \boldsymbol{K}_{l_{ya}} & \boldsymbol{0}_{[N_y\times(N_f+N_a)]} \end{bmatrix} \tag{4.64a}$$

$$\underset{[N_s\times 2(N_f+N_a)]}{\boldsymbol{C}_{2c}} = \begin{bmatrix} \underset{[N_y\times 2N]}{\boldsymbol{C}_2} & \boldsymbol{K}_{l_{sf}} & \boldsymbol{K}_{l_{sa}} & \boldsymbol{0}_{[N_y\times(N_f+N_a)]} \end{bmatrix} \tag{4.64b}$$

$$\underset{[N_y\times N_f]}{\boldsymbol{D}_{11c}} = \boldsymbol{K}_{dfy},\ \underset{[N_y\times N_a]}{\boldsymbol{D}_{12c}} = \boldsymbol{K}_{day},\ \underset{[N_s\times N_f]}{\boldsymbol{D}_{21c}} = \boldsymbol{K}_{dfs},\ \underset{[N_s\times N_a]}{\boldsymbol{D}_{22c}} = \boldsymbol{K}_{das}. \tag{4.64c}$$

Subscripts a, f, s and y denote the terms associated with the control actuator, the disturbance force, the sensor, and the displacement respectively. N is the number of vibration modes taken into account ($N = m_2 - m_1 + 1$), and N_f is the number of point-wise disturbance sources.

The general theory developed in this section was tested using the particular example of a cantilevered beam. Extensive details of this experiment will be given in Chapter 8. The objective of the cantilevered beam experiment was to control the 4^{th} to the 7^{th} order vibration modes over a frequency range from 342Hz to 1125Hz. The effectiveness of the new correction method derived from the general theory was observed by looking at the frequency response between the beam's tip

displacement $y(s)$ and the applied point force $f(s)$. The results of the experiment were found to validate the general theory.

Fig. 4.5 compares the transfer function results for a full model, $\boldsymbol{G}(s)$, (using the first 30 modes, sufficient for representing the full model) with the results for three different model truncations: $\boldsymbol{G}_r(s)$, which has no correction terms; $\boldsymbol{G}_r(s) + \boldsymbol{K}_{do}$ when the only term taken into account in the objective function J is the zeroth order term of $\boldsymbol{K}_d$ (in this case $\gamma = \omega_c - \omega_a$ and $\Gamma_i = 0$); and $\boldsymbol{G}_r(s) + \boldsymbol{K}_d + + \boldsymbol{K}_l$; when both terms $\boldsymbol{K}_l$ and $\boldsymbol{K}_d$ are included in the truncated model. As laid out in the introduction, the bandwidth of interest falls between 330Hz and 1150Hz shown in Fig. 4.5 as the area between the two vertical thick black lines. Fig. 4.6 magnifies the frequency response in this range to show it more clearly.

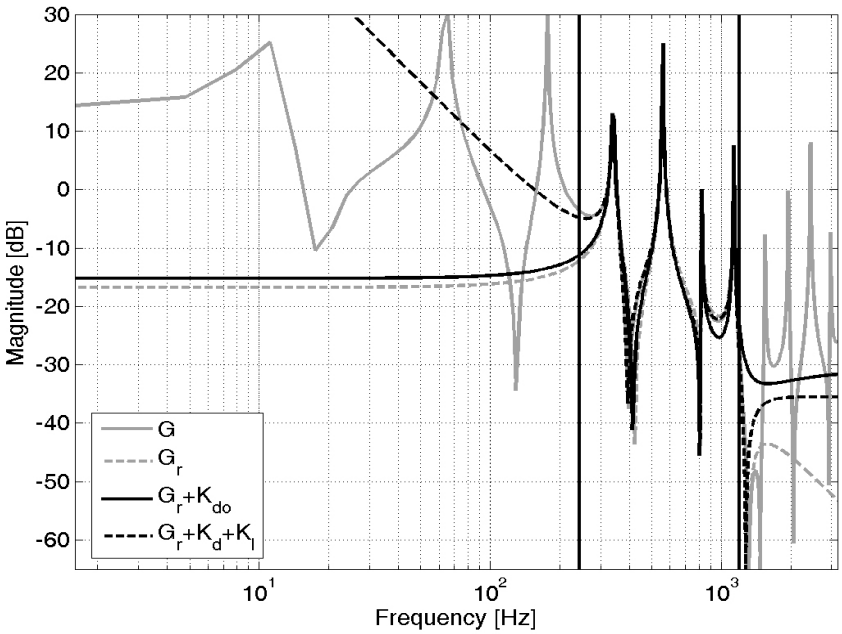

Figure 4.5: Frequency response $\frac{y(\omega)}{f(\omega)}$ due to model truncation and corrections. $\boldsymbol{G}(s)$ = the full model using 30 modes; $\boldsymbol{G}_r(s)$ = the truncated model without any correction terms, $\boldsymbol{G}_r(s) + \boldsymbol{K}_{do}$ = the truncated model with the optimal zero-order term of $\boldsymbol{K}_d$; and $\boldsymbol{G}_r(s) + \boldsymbol{K}_d + \boldsymbol{K}_l$ = the truncated model with both optimal terms $\boldsymbol{K}_l$ and $\boldsymbol{K}_d$.

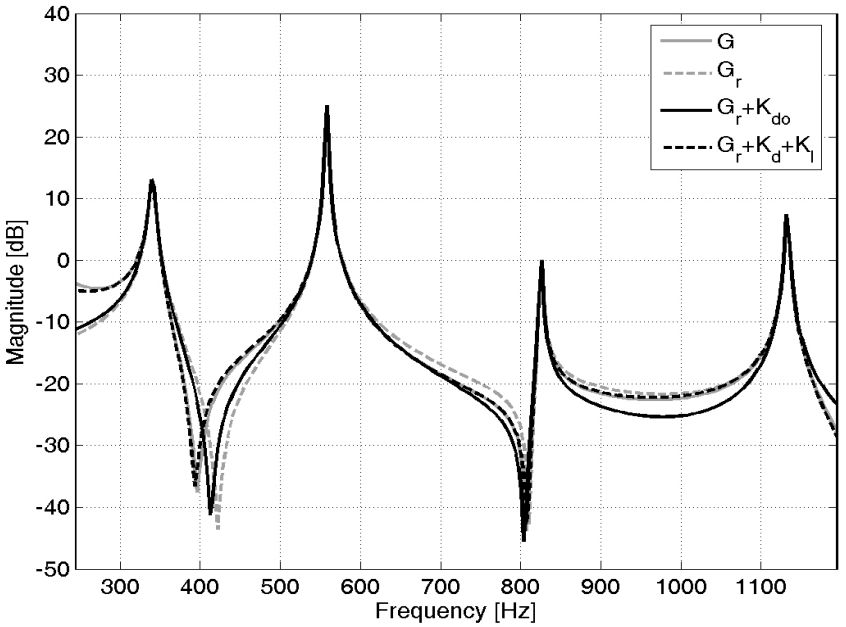

Figure 4.6: Dynamic effect of the model truncation and the corrections made within the frequency bandwidth of interest [330Hz, 1150Hz].

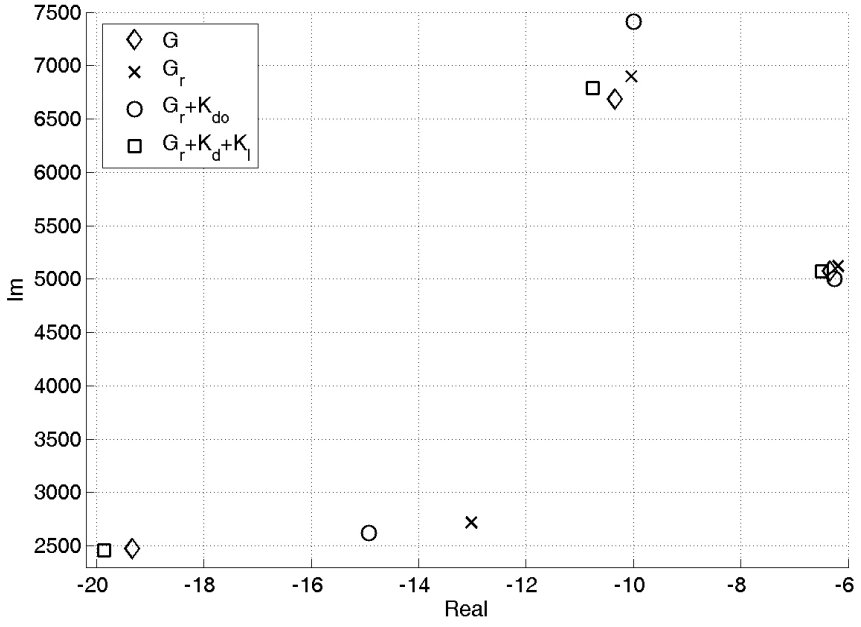

Figure 4.7: Location of zeros for various models.

The beneficial effect on the optimisation of using the two terms $\boldsymbol{K}_d$ and $\boldsymbol{K}_l$, as described above, can also be seen by comparing the zeros, or anti-resonance frequencies, of the full system with the truncated ones (knowing that the poles remain identical). This is shown in Fig. 4.7: for the zeros within the frequency bandwidth of interest, the reduced model with $\boldsymbol{K}_l$ and $\boldsymbol{K}_d$ (square symbols) can be seen to be the one that most closely matches the full model $\boldsymbol{G}(s)$ (diamond symbols).

4.4.3 Optimisation adaptation for robust control design purposes

For the design of optimal $\mathcal{H}_2$ or $\mathcal{H}_\infty$ controllers, it has been discussed in [66] that the next associated matrix $\boldsymbol{H}$ described in Eq. (4.65) must have full column rank:

$$\boldsymbol{H} = \begin{bmatrix} \boldsymbol{A}_c - j\omega \boldsymbol{I} & \boldsymbol{B}_{2c} \\ \boldsymbol{C}_{1c} & \boldsymbol{D}_{12} \end{bmatrix} \tag{4.65}$$

However, since $\boldsymbol{A}_c$ in Eq. (4.63a) depends on $\boldsymbol{A}_l$ in Eq. (4.63b), the associated matrix $\boldsymbol{H}$ will not have full column rank. One way of addressing this problem is to use the adjustment shown below in Eq. (4.66). The truncated model with this adjustment remains the best approximation compared to the conventional approach that uses only a zero-order term. This is shown in Fig. 4.6.

$$\boldsymbol{A}_c = \begin{bmatrix} \boldsymbol{A} & \boldsymbol{0}_{[2N \times 2(N_f+N_a)]} \\ \boldsymbol{0}_{[2(N_f+N_a)\times 2N]} & \boldsymbol{A}_{adj} \end{bmatrix} \tag{4.66}$$

where

$$\underset{[2(N_f+N_a)\times 2(N_f+N_a)]}{\boldsymbol{A}_{adj}} = \begin{bmatrix} \boldsymbol{0}_{[(N_f+N_a)\times(N_f+N_a)]} & \boldsymbol{I}_{[(N_f+N_a)\times(N_f+N_a)]} \\ -\omega_1^2 \boldsymbol{I}_{[(N_f+N_a)\times(N_f+N_a)]} & -2\zeta_1\omega_1 \boldsymbol{I}_{[(N_f+N_a)\times(N_f+N_a)]} \end{bmatrix}. \tag{4.67}$$

This adjustment comes from Eq. (4.6) for $i = 1$ and $F_i(t) = 0$, which is the contribution of the first mode to the truncated model. The transfer function $\frac{1}{s^2+2\zeta\omega_1 s+\omega_1^2}$ multiplied by $\boldsymbol{K}_l$ gives an approximate contribution of all the lowest modes to the truncated model, based on the first mode transfer function.

4.5 Summary

This chapter has set up a procedure for developing a new model-based feedback controller that excludes lower order modes as well as higher order modes that fall outside the bandwidth of interest. An approximation term was developed to take into account the effect of those lower order and higher order modes on the system response in the bandwidth of interest. The proposed approach has two main advantages over classical optimal truncation. Firstly, the proposed new method generates a lower order controller. This is because the order of the controller includes the order of the plant, and the order of the plant used ($2(N_f+N_a+N)$ states) is lower than that commonly used in control design ($2m_2$ states). Secondly, the proposed model saves unnecessary control effort by controlling only the specified frequency modes that are of interest within a particular bandwidth. In this sense the standard approach is not optimal, as it expends wasted effort on considering lower order modes which are not of interest in overall vibration attenuation.

Chapter 5

SPATIAL CONTROL DESIGN

When controlling the vibration of a flexible structure, the controller is conventionally designed to only minimise vibration at limited number of discrete locations in the system; as the result, the attenuation of vibration at other locations in the system may be less pronounced, or the vibration at these other locations may even be amplified. Moheimani et al. [45] developed a new approach, based on the spatial norm concept [67, 68], to spatially attenuate vibration in a given structure; in other words, to achieve global vibration attenuation for the structure, and not only control at discrete locations. The efficiency of this technique has already been demonstrated by others [4, 37, 69].

One of the required input parameters when designing a controller for a vibration control system is the location of the disturbance force, to assist in determining the effect of the disturbance force on the modelled system. Using the spatial norm concept together with the $\mathcal{H}_\infty$ and $\mathcal{H}_2$ methods, Halim [70] came up with a new controller design that made the structure control more robust by taking into account the spatial variation of the input disturbance. This spatial input control approach considers the contribution of external disturbance force(s) on the system as a whole, by mathematically distributing the force(s) over the entire structure. Spatial input/spatial output control theory is obtained by combining the spatial input control of Halim and the spatial output control of Moheimani et al.

This chapter will determine the relationship between the mathematically distributed force(s) and the actual external disturbance force(s), which would enable an external disturbance to be spatially controlled within a conventional control approach. Halim's design is that of a spatial input/output system without feedthrough terms, which leaves the user to make a subjective choice about those parameters given that they can be considered as negligible. By providing a means of obtaining exact feedthrough terms, this chapter extends Halim's theorem (see appendix A, theorem 4). In this chapter, the spatial control concept is applied to the example of vibration control of a flexible beam using piezoelectric actuators and sensors, as this example will also be used in the following chapters.

5.1 Point-wise input/spatial output control

The $\mathcal{H}_\infty$ norm of a MIMO transfer function $\boldsymbol{G}(s,r) = \frac{\boldsymbol{y}(s,r)}{f(s)}$ is defined as:

$$\begin{aligned} \|\boldsymbol{G}(s,r)\|_\infty &\triangleq \max_\omega \bar{\sigma}(\boldsymbol{G}(j\omega)) \\ &= \sup_\omega \left\{ \frac{\int_0^\infty \boldsymbol{y}(s,r)^T \boldsymbol{y}(s,r) ds}{\int_0^\infty f(s,r)^T f(s,r) ds} \right\} \end{aligned} \tag{5.1}$$

where $\bar{\sigma}$ is the system's maximum singular value.

It is possible to define a spatial weighting function $Q(s)$ to chose a region where the disturbance requires greater attenuation. In this case, the $\mathcal{H}_\infty$ norm of $\boldsymbol{G}(s)$ is defined as:

$$\|\boldsymbol{G}(s)\|_{\infty,Q} = \sup_\omega \left\{ \frac{\int_0^\infty \int_{\mathcal{R}} \boldsymbol{y}(s,r)^T Q(r) \boldsymbol{y}(s,r) dr ds}{\int_0^\infty f(s,r)^T f(s,r) ds} \right\} \tag{5.2}$$

For our case, a global vibration attenuation of the structure is desirable, so $Q(r) = 1$. Applying Eq. (5.2) to the conventional Eq. (4.62b), a new equation is defined that does not depend on the value of r:

$$\tilde{\boldsymbol{y}}(s) = \boldsymbol{\Pi} \boldsymbol{x}(s) + \boldsymbol{\Theta}_{11} f(s) + \boldsymbol{\Theta}_{12} \boldsymbol{v}_a(s) \tag{5.3}$$

Matrices $\mathbf{\Pi}$, $\mathbf{\Theta}_{11}$ and $\mathbf{\Theta}_{12}$ are determined from $\mathbf{\Gamma} = [\mathbf{\Pi}\ \mathbf{\Theta}_{11}\ \mathbf{\Theta}_{12}]$, which is:

$$\mathbf{\Gamma}^T\mathbf{\Gamma} = \int_{\mathcal{R}} \begin{bmatrix} \boldsymbol{C}_1^T(r) \\ \boldsymbol{D}_{11}^T(r) \\ \boldsymbol{D}_{12}^T(r) \end{bmatrix} \boldsymbol{Q}(r) \left[\boldsymbol{C}_1(r)\ \boldsymbol{D}_{11}(r)\ \boldsymbol{D}_{12}(r)\right] dr \tag{5.4}$$

The matrices $\boldsymbol{C}_1$, $\boldsymbol{D}_{11}$ and $\boldsymbol{D}_{12}$ are defined in the equation system (4.47). Hence

$$\mathbf{\Pi} = \begin{bmatrix} diag(\Phi_1, \ldots, \Phi_N, \boldsymbol{0}_{1\times N}) \\ \boldsymbol{0}_{[N_f\times 2N]} \\ \boldsymbol{0}_{[N_a\times 2N]} \end{bmatrix} \tag{5.5}$$

where

$$\int_0^L \phi_i(r)\phi_j(r)dr = \Phi_i^2\delta_{ij} \tag{5.6}$$

due to the modes' orthogonality and

$$\mathbf{\Theta}_{11} = \begin{bmatrix} \boldsymbol{0}_{[2N\times N_f]} \\ \dfrac{1}{2\omega_c}\left(\displaystyle\sum_{i=N+1}^{\infty} \frac{\Phi_i^2\boldsymbol{\phi}_i^2}{\omega_i^2} \ln^2\left(\frac{\omega_i+\omega_c}{\omega_i-\omega_c}\right)\right)^{\frac{1}{2}} \\ \boldsymbol{0}_{[2N\times N_f]} \end{bmatrix} \tag{5.7}$$

with the matrix $\boldsymbol{\phi}_i^2$ defined as:

$$\boldsymbol{\phi}_i^2 = [\phi_i(r_{f_1})\ \ldots\ \phi_i(r_{f_{N_f}})]^T[\phi_i(r_{f_1})\ \ldots\ \phi_i(r_{f_{N_f}})] \tag{5.8}$$

and finally

$$\mathbf{\Theta}_{12} = \begin{bmatrix} \boldsymbol{0}_{[2N\times N_a]} \\ \boldsymbol{0}_{[N_f\times N_a]} \\ \dfrac{1}{2\omega_c}\left(\displaystyle\sum_{i=N+1}^{\infty} \frac{\Phi_i^2\boldsymbol{P}_i^2}{\omega_i^2} \ln^2\left(\frac{\omega_i+\omega_c}{\omega_i-\omega_c}\right)\right)^{\frac{1}{2}} \end{bmatrix} \tag{5.9}$$

with the matrix $\boldsymbol{P}_i^2$ described as:

$$\boldsymbol{P}_i^2 = \mathbf{P}_i^T \mathbf{P}_i = \frac{1}{(\rho A)^2}[K_i\Psi_{i1} \cdots K_{N_a}\Psi_{iN_a}]^T[K_i\Psi_{i1} \cdots K_{N_a}\Psi_{iN_a}] \tag{5.10}$$

One ends up with equation system (5.11), which is the representation of the spatial control approach in the $\mathcal{H}_\infty$ sense.

$$\dot{\boldsymbol{x}}(t) = \boldsymbol{A}\boldsymbol{x}(t) + \boldsymbol{B}_1 f(t) + \boldsymbol{B}_2 \boldsymbol{v}_a(t) \tag{5.11a}$$

$$\tilde{\boldsymbol{y}}(t) = \boldsymbol{\Pi}\boldsymbol{x}(t) + \boldsymbol{\Theta}_{11} f(t) + \boldsymbol{\Theta}_{12} \boldsymbol{v}_a(t) \tag{5.11b}$$

$$\boldsymbol{v}_s(t) = \boldsymbol{C}_2 X(t) + \boldsymbol{D}_{21} f(t) + \boldsymbol{D}_{22} \boldsymbol{v}_a(t) \tag{5.11c}$$

The $\mathcal{H}_\infty$ controller $\boldsymbol{K}(s)$,

$$\dot{\boldsymbol{x}}_c(t) = \boldsymbol{A}_c \boldsymbol{x}_c(t) + \boldsymbol{B}_c \boldsymbol{v}_s(t) \tag{5.12a}$$

$$\boldsymbol{v}_a(t) = \boldsymbol{C}_c \boldsymbol{x}_c(t) + \boldsymbol{D}_c \boldsymbol{v}_s(t) \tag{5.12b}$$

is designed to stabilise the $\mathcal{H}_\infty$ norm of the augmented transfer function $\boldsymbol{G}(s)$ in closed-loop with $\boldsymbol{K}(s)$.

$$\min_\gamma \{\|\mathcal{F}(\boldsymbol{G}(s), \boldsymbol{K}(s))\|_\infty\} \leq \gamma \tag{5.13}$$

with $\mathcal{F}$ the feedback operator. The complete procedure for determining the optimal $\mathcal{H}_\infty$ controller is detailed in [66, 71–73].

5.2 Spatial input/spatial output control

As mentioned in the introduction to this chapter, Halim [70] designed a spatial input/output system that required the user to make a subjective choice about feedthrough parameters, which can usually be considered as negligible. However, even for those parameters that do not have significant function in the controller design, an appropriate order of magnitude must be chosen for each in order to mach the real system as closely as possible. This section sets out Halim's basic theorem and then extends it by objectively formulating the required feedback terms.

5.2.1 Relationship between real external force and conceptual spatial force

It was an original idea of Halim's to use a spatially-varied disturbance input in structural vibration control [70] and he determined the high potential of this new approach through several simulations but never through experiment; Chapter 8 will set out how, for the first time, a spatial input/output control experiment was performed. For the analysis in this chapter, a uni-dimensional system was used in the formulation of a methodology to determine the system's feedthrough terms. As this analysis uses the orthogonality between the modes, the derived methodology can be generalised for two- and three-dimensional systems.

Firstly, the classic state-space representation of a flexible structure with a piezoelectric sensor is described in Eqs. (5.14):

$$\dot{\boldsymbol{x}}(s) = \boldsymbol{A}\boldsymbol{x}(s) + \boldsymbol{B}_1(r_i)f(s) \tag{5.14a}$$

$$y(s, r_o) = \boldsymbol{C}_1(r_o)\boldsymbol{x}(s) \tag{5.14b}$$

$$\boldsymbol{v}_s(s) = \boldsymbol{C}_2\boldsymbol{x}(s) \tag{5.14c}$$

where r_i is the location of the point force, and r_o the location of the displacement, and $\boldsymbol{v}_s$ the tension in the piezoelectric sensor. The expression of the spatial input/point-wise output system defined by [70] can be written as follows:

$$\dot{\boldsymbol{x}}(s) = \boldsymbol{A}\boldsymbol{x}(s) + \boldsymbol{\Omega}\tilde{\boldsymbol{f}}(s) \tag{5.15a}$$

$$y(s, r_o) = \boldsymbol{C}_1(r_o)\boldsymbol{x}(s) \tag{5.15b}$$

$$\boldsymbol{v}_s(s) = \boldsymbol{C}_2\boldsymbol{x}(s) \tag{5.15c}$$

with

$$\boldsymbol{\Omega}\boldsymbol{\Omega}^T = \int_{\mathcal{R}_i} \boldsymbol{B}_1(r_i)Q_i(r_i)\boldsymbol{B}_1^T(r_i)dr_i$$

when $Q_i(r_i) = 1$ (in all the following $Q(r)$ is assumed to be unity):

$$\boldsymbol{\Omega}_{[2N\times 2N]} = \begin{bmatrix} \boldsymbol{0}_{[N\times N]} & \boldsymbol{0}_{[N\times N]} \\ \boldsymbol{0}_{[N\times N]} & diag\Big(\Phi_1, \ldots, \Phi_N\Big) \end{bmatrix} \tag{5.16}$$

with the modes' orthogonality property:

$$\int_0^L \phi_i(r)\phi_j(r)dr = \Phi_i^2\delta_{ij} \tag{5.17}$$

Spatial input control theory states that an external point-wise force applied on a structure can be interpreted as a distributed force over the entire structure. Such an interpretation means that the efficiency of the controller is less dependent on the extent of knowledge about the real disturbance force.

The spatial forces in Eq. (5.15a) can be expressed as a distributed force along the structure:

$$\int_0^L \boldsymbol{B}_1(r_i)dr_i f(s) = \boldsymbol{\Omega}\tilde{\boldsymbol{f}}(s) \tag{5.18}$$

Proof:

The classical state-space equation system with piezo actuators can be expressed as:

$$\dot{\boldsymbol{x}}(s) = \boldsymbol{A}\boldsymbol{x}(s) + \boldsymbol{B}_1(r_i)f(s) + \boldsymbol{B}_2\boldsymbol{v}_a(s) \tag{5.19a}$$

$$y(s, r_o) = \boldsymbol{C}_1(r_o)\boldsymbol{x}(s) + \boldsymbol{D}_{12}(r_o)\boldsymbol{v}_a(s) \tag{5.19b}$$

$$\boldsymbol{v}_s(s) = \boldsymbol{C}_2\boldsymbol{x}(s) + \boldsymbol{D}_{22}\boldsymbol{v}_a(s) \tag{5.19c}$$

And [70] spatial input/point-wise output control system with piezoelectric actua-

tors is expressed as:

$$\dot{\boldsymbol{x}}(s) = \boldsymbol{A}\boldsymbol{x}(s) + \boldsymbol{\Omega}\tilde{\boldsymbol{f}}(s) + \boldsymbol{B}_2\boldsymbol{v}_a(s) \tag{5.20a}$$

$$\tilde{y}(s, r_o) = \boldsymbol{C}_1(r_o)\boldsymbol{x}(s) + \boldsymbol{D}_{12}(r_o)\boldsymbol{v}_a(s) \tag{5.20b}$$

$$\boldsymbol{v}_s(s) = \boldsymbol{C}_2\boldsymbol{x}(s) + \boldsymbol{D}_{22}\boldsymbol{v}_a(s) \tag{5.20c}$$

Theorem 4 states that the two above systems are spatially equivalent; thus the spatial norm of the system in Eqs. (5.19) must be equal to the norm $\mathcal{H}_2$ of the system in Eqs. (5.20). The spatial norm of the classic control system is:

$$\ll y \gg_{2,i}^2 = \frac{1}{2\pi}\int_{-\infty}^{\infty}\int_{\mathcal{R}_i} [f(\omega) \quad \boldsymbol{v}_a^T(\omega)]\,\boldsymbol{G}_i^*(\omega, r_i, r_o)\,\boldsymbol{G}_i(\omega, r_i, r_o)[f(\omega) \quad \boldsymbol{v}_a^T(\omega)]^T dr_i d\omega \tag{5.21}$$

$$= \frac{1}{2\pi}\int_{-\infty}^{\infty}\int_{\mathcal{R}_i} \Big\{ f(\omega)\left[\boldsymbol{C}_1(r_o)\boldsymbol{N}\boldsymbol{B}_1(r_i)\right]^* \left[\boldsymbol{C}_1(r_o)\boldsymbol{N}\boldsymbol{B}_1(r_i)\right] f(\omega) \tag{5.21a}$$

$$+ f(\omega)\left[\boldsymbol{B}_1^T(r_i)\boldsymbol{N}^*\,\boldsymbol{C}_1^T(r_o)(\boldsymbol{C}_1(r_o)\boldsymbol{N}\boldsymbol{B}_2 + \boldsymbol{D}_{12}(r_o))\right]\boldsymbol{v}_a(\omega) \tag{5.21b}$$

$$+ \boldsymbol{v}_a^T(\omega)\left[(\boldsymbol{B}_2^T\boldsymbol{N}^*\,\boldsymbol{C}_1^T(r_o) + \boldsymbol{D}_{12}^T(r_o))\,\boldsymbol{C}_1(r_o)\boldsymbol{N}\boldsymbol{B}_1(r_i)\right] f(\omega) \tag{5.21c}$$

$$+ \boldsymbol{v}_a^T(\omega)\left[(\boldsymbol{C}_1(r_o)\boldsymbol{N}\boldsymbol{B}_2 + \boldsymbol{D}_{12}(r_o))^*(\boldsymbol{C}_1(r_o)\boldsymbol{N}\boldsymbol{B}_2 + \boldsymbol{D}_{12}(r_o))\right]\boldsymbol{v}_a(\omega)\Big\} dr_i d\omega \tag{5.21d}$$

with $\boldsymbol{G} = \boldsymbol{C}\boldsymbol{N}\boldsymbol{B}$, $\boldsymbol{N}(j\omega) = (j\omega\boldsymbol{I} - \boldsymbol{A})^{-1}$ simplified by $\boldsymbol{N}$ and $\bullet^*$ the transposed conjugate of $\bullet$. Now the norm $\mathcal{H}_2$ of the spatial control system is:

$$\|\tilde{y}\|_2^2 = \frac{1}{2\pi}\int_{-\infty}^{\infty} [\tilde{\boldsymbol{f}}^T(\omega) \quad \boldsymbol{v}_a^T(\omega)]\,\tilde{\boldsymbol{G}}_i^*(\omega, r_i, r_o)\,\tilde{\boldsymbol{G}}_i(\omega, r_i, r_o)[\tilde{\boldsymbol{f}}^T(\omega) \quad \boldsymbol{v}_a^T(\omega)]^T d\omega \tag{5.22}$$

$$= \frac{1}{2\pi}\int_{-\infty}^{\infty} \Big\{ \tilde{\boldsymbol{f}}^T(\omega)\,[\boldsymbol{C}_1(r_o)\boldsymbol{N}\boldsymbol{\Omega}]^*\,[\boldsymbol{C}_1(r_o)\boldsymbol{N}\boldsymbol{\Omega}]\,\tilde{\boldsymbol{f}}(\omega) \tag{5.22a}$$

$$+ \tilde{\boldsymbol{f}}^T(\omega)\left[\boldsymbol{\Omega}^T\boldsymbol{N}^*\boldsymbol{C}_1^T(r_o)(\boldsymbol{C}_1(r_o)\boldsymbol{N}\boldsymbol{B}_2 + \boldsymbol{D}_{12}(r_o))\right]\boldsymbol{v}_a(\omega) \tag{5.22b}$$

$$+ \boldsymbol{v}_a^T(\omega)\,[(\boldsymbol{C}_1(r_o)\boldsymbol{N}\boldsymbol{B}_2 + \boldsymbol{D}_{12}(r_o))^*\,\boldsymbol{C}_1(r_o)\boldsymbol{N}\boldsymbol{\Omega}]\,\tilde{\boldsymbol{f}}^T(\omega) \tag{5.22c}$$

$$+ \boldsymbol{v}_a^T(\omega)\,[(\boldsymbol{C}_1(r_o)\boldsymbol{N}\boldsymbol{B}_2 + \boldsymbol{D}_{12}(r_o))^*(\boldsymbol{C}_1(r_o)\boldsymbol{N}\boldsymbol{B}_2 + \boldsymbol{D}_{12}(r_o))]\,\boldsymbol{v}_a(\omega)\Big\} d\omega \tag{5.22d}$$

[70] proved that Eq. (5.21a) is equal to Eq. (5.22a). As Eq. (5.21d), independent of r_i, is effectively identical to Eq. (5.22d), a simple coefficient identification between Eq. (5.21b) and Eq. (5.22b) gives the following equality:

$$\int_0^L \boldsymbol{B}_1(r_i)dr_i f(s) = \boldsymbol{\Omega}\tilde{\boldsymbol{f}}(s) \tag{5.23}$$

This equality enables to the formulation of a new state-space system that can use the spatial input theory without having to use Halim's spatial input matrix, $\boldsymbol{\Omega}_{[2N\times 2N]}$.

$$\dot{\boldsymbol{x}}(s) = \boldsymbol{A}\boldsymbol{x}(s) + \boldsymbol{\beta} f(s) + \boldsymbol{B}_2\boldsymbol{v}_a(s) \tag{5.24a}$$

$$\tilde{y}(s, r_o) = \boldsymbol{C}_1(r_o)\boldsymbol{x}(s) + \boldsymbol{D}_{12}(r_o)\boldsymbol{v}_a(s) \tag{5.24b}$$

$$\boldsymbol{v}_s(s) = \boldsymbol{C}_2\boldsymbol{x}(s) + \boldsymbol{D}_{22}\boldsymbol{v}_a(s) \tag{5.24c}$$

where $\boldsymbol{\beta} = \int_0^L \boldsymbol{B}_1(r_i)dr_i$.

This new state-space system provides an alternative path for spatial input control, where the classical state-space system is used as per usual but in combination with a new input force matrix $\boldsymbol{\beta}$, and this provides the same performance as the spatial input method.

5.2.2 Theorem 4 extension: spatial input/spatial output systems with feedthrough term for the applied force

The section extends **theorem 4** by formulating a methodology for determining feedthrough terms for the second and third equations of the global system (5.25):

$$\dot{\boldsymbol{x}}(s) = \boldsymbol{A}\boldsymbol{x}(s) + \boldsymbol{B}_1(r_i)f(s) \tag{5.25a}$$

$$y(s, r_o) = \boldsymbol{C}_1(r_o)\boldsymbol{x}(s) + \boldsymbol{D}_{11}(r_o, r_i)f(s) \tag{5.25b}$$

$$\boldsymbol{v}_s(s) = \boldsymbol{C}_2\boldsymbol{x}(s) + \boldsymbol{D}_{21}(r_i)f(s) \tag{5.25c}$$

with r_o the position of the deformation on the beam and r_i the position of the applied force.

Theorem 4 ext: *Consider a spatial system (5.25a, 5.25b and 5.25c), where* $\boldsymbol{G}_{io}(s, r_i, r_o) = \boldsymbol{C}_1(r_o)(sI - \boldsymbol{A})^{-1}\boldsymbol{B}_1(r_i) + \boldsymbol{D}_{11}(r_o, r_i)$ *is the infinite-dimensional state-space system. Then*

$$\ll \boldsymbol{G}_{io} \gg_{\infty,i,o} = \|\boldsymbol{g}_{io}\|_\infty \tag{5.26}$$

where $\boldsymbol{g}_{io}(s) * \boldsymbol{g}_{io}(s) = \sum_k \lambda_k(\tilde{\boldsymbol{G}}_{io}(s) * \tilde{\boldsymbol{G}}_{io}(s))$, *and* $\tilde{\boldsymbol{G}}_{io}(s) = \boldsymbol{\Gamma}(sI - \boldsymbol{A})^{-1}\boldsymbol{\Omega} + \tilde{\boldsymbol{\Delta}}$ *is a finite-dimensional system.* $\boldsymbol{\Gamma}$, $\tilde{\boldsymbol{\Delta}}$ *and* $\boldsymbol{\Omega}$ *are matrices that satisfy*

$$\boldsymbol{\Omega}\boldsymbol{\Omega}^T = \int_{\mathcal{R}_i} \boldsymbol{B}_1(r_i)Q_i(r_i)\boldsymbol{B}_1^T(r_i)dr_i \tag{5.27a}$$

$$\boldsymbol{\Gamma}^T\boldsymbol{\Gamma} = \int_{\mathcal{R}_o} \boldsymbol{C}_1^T(r_o)Q_o(r_o)\boldsymbol{C}_1(r_o)dr_o \tag{5.27b}$$

$$\boldsymbol{\Delta}^T\boldsymbol{\Delta} = \int_{\mathcal{R}_o}\int_{\mathcal{R}_i} \boldsymbol{D}_{11}^T(r_o, r_i)Q_{oi}(r_o, r_i)\boldsymbol{D}_{11}(r_o, r_i)dr_i dr_o \tag{5.27c}$$

$$\tag{5.27d}$$

with

$$\tilde{\boldsymbol{\Delta}} = \begin{bmatrix} \boldsymbol{0}_{[N\times N]} & \boldsymbol{0}_{[N\times N_a]} & \boldsymbol{0}_{[N\times(N-N_a)]} \\ \boldsymbol{0}_{[N_a\times N]} & \frac{1}{\sqrt{N_a}}\text{diag}(\boldsymbol{\Delta},...,\boldsymbol{\Delta}) & \boldsymbol{0}_{[N_a\times(N-N_a)]} \\ \boldsymbol{0}_{[(N-N_a)\times N]} & \boldsymbol{0}_{[(N-N_a)\times N_a]} & \boldsymbol{0}_{[(N-N_a)\times(N-N_a)]} \end{bmatrix} \tag{5.28}$$

Proof of Theorem 4 extension:

Consider the case where $Q_o(r_o) = Q_i(r_i) = Q_{oi}(r_o, r_i) = 1$. Given that both $f(s)$ and $y(s)$ are scalars the spatial norm can be calculated as follows:

$$\begin{aligned} \ll y \gg^2_{2,i,o} &= \frac{1}{2\pi}\int_{-\infty}^{\infty}\int_{\mathcal{R}_o}\int_{\mathcal{R}_i} f(\omega)\,\boldsymbol{G}^*_{io}(\omega, r_i, r_o)\,\boldsymbol{G}_{io}(\omega, r_i, r_o) f(\omega) dr_i dr_o d\omega \qquad (5.29) \\ &= \frac{1}{2\pi}\int_{-\infty}^{\infty}\int_{\mathcal{R}_o}\int_{\mathcal{R}_i} f(\omega)\left[\boldsymbol{C}_1(r_o)\boldsymbol{N}\boldsymbol{B}_1(r_i) + \boldsymbol{D}_{11}(r_o, r_i)\right]^* \\ &\quad \left[\boldsymbol{C}_1(r_o)\boldsymbol{N}\boldsymbol{B}_1(r_i) + \boldsymbol{D}_{11}(r_o, r_i)\right] f(\omega) dr_i dr_o d\omega \\ &= \frac{1}{2\pi}\int_{-\infty}^{\infty}\int_{\mathcal{R}_o}\int_{\mathcal{R}_i} f(\omega)\Big[\boldsymbol{B}_1^T(r_i)\boldsymbol{N}^*\,\boldsymbol{C}_1^T(r_o)\boldsymbol{D}_{11}(r_o, r_i) \\ &\quad + \boldsymbol{B}_1^T(r_i)\boldsymbol{N}^*\,\boldsymbol{C}_1^T(r_o)\boldsymbol{C}_1(r_o)\boldsymbol{N}\boldsymbol{B}_1(r_i) \\ &\quad + \boldsymbol{D}_{11}^T(r_o, r_i)\,\boldsymbol{C}_1(r_o)\boldsymbol{N}\boldsymbol{B}_1(r_i) \\ &\quad + \boldsymbol{D}_{11}^T(r_o, r_i)\boldsymbol{D}_{11}(r_o, r_i)\Big] f(\omega) dr_i dr_o d\omega \\ \\ &= \frac{1}{2\pi}\int_{-\infty}^{\infty}\int_{\mathcal{R}_o}\int_{\mathcal{R}_i} f(\omega)\,tr\Big\{\boldsymbol{B}_1^T(r_i)\boldsymbol{N}^*\,\boldsymbol{C}_1^T(r_o)\boldsymbol{D}_{11}(r_o, r_i) \\ &\quad + \boldsymbol{B}_1^T(r_i)\boldsymbol{N}^*\,\boldsymbol{C}_1^T(r_o)\boldsymbol{C}_1(r_o)\boldsymbol{N}\boldsymbol{B}_1(r_i) \\ &\quad + \boldsymbol{D}_{11}^T(r_o, r_i)\,\boldsymbol{C}_1(r_o)\boldsymbol{N}\boldsymbol{B}_1(r_i) \\ &\quad + \boldsymbol{D}_{11}^T(r_o, r_i)\boldsymbol{D}_{11}(r_o, r_i)\Big\} f(\omega) dr_i dr_o d\omega \end{aligned}$$

$$
\begin{aligned}
&= \frac{1}{2\pi}\int_{-\infty}^{\infty} f(\omega)\Big[tr\Big\{\int_{\mathcal{R}_o}\int_{\mathcal{R}_i} \boldsymbol{B}_1^T(r_i)\boldsymbol{N}^*\boldsymbol{C}_1^T(r_o)\boldsymbol{D}_{11}(r_o,r_i)dr_i dr_o\Big\} \\
&\quad + tr\Big\{\int_{\mathcal{R}_o}\int_{\mathcal{R}_i} \boldsymbol{B}_1^T(r_i)\boldsymbol{N}^*\boldsymbol{C}_1^T(r_o)\boldsymbol{C}_1(r_o)\boldsymbol{N}\boldsymbol{B}_1(r_i)dr_i dr_o\Big\} \\
&\quad + tr\Big\{\int_{\mathcal{R}_o}\int_{\mathcal{R}_i} \boldsymbol{D}_{11}^T(r_o,r_i)\boldsymbol{C}_1(r_o)\boldsymbol{N}\boldsymbol{B}_1(r_i)dr_i dr_o\Big\} \\
&\quad + tr\Big\{\int_{\mathcal{R}_o}\int_{\mathcal{R}_i} \boldsymbol{D}_{11}^T(r_o,r_i)\boldsymbol{D}_{11}(r_o,r_i)dr_i dr_o\Big\}\Big] f(\omega)d\omega
\end{aligned}
$$

$$
\begin{aligned}
&= \frac{1}{2\pi}\int_{-\infty}^{\infty} f(\omega)\Big[tr\Big\{\int_{\mathcal{R}_i} \boldsymbol{B}_1^T(r_i)\boldsymbol{N}^*\Big(\int_{\mathcal{R}_o} \boldsymbol{C}_1^T(r_o)\boldsymbol{D}_{11}(r_o,r_i)dr_o\Big)dr_i\Big\} && \text{(5.30a)} \\
&\quad + tr\Big\{\int_{\mathcal{R}_o} \boldsymbol{N}^*\boldsymbol{C}_1^T(r_o)\boldsymbol{C}_1(r_o)\boldsymbol{N}\Big(\int_{\mathcal{R}_i} \boldsymbol{B}_1(r_i)\boldsymbol{B}_1^T(r_i)dr_i\Big)dr_o\Big\} && \text{(5.30b)} \\
&\quad + tr\Big\{\int_{\mathcal{R}_o} \Big(\int_{\mathcal{R}_i} \boldsymbol{D}_{11}^T(r_o,r_i)\boldsymbol{C}_1(r_o)dr_o\Big)\boldsymbol{N}\boldsymbol{B}_1(r_i)dr_i\Big\} && \text{(5.30c)} \\
&\quad + tr\Big\{\int_{\mathcal{R}_o}\int_{\mathcal{R}_i} \boldsymbol{D}_{11}^T(r_o,r_i)\boldsymbol{D}_{11}(r_o,r_i)dr_i dr_o\Big\}\Big] f(\omega)d\omega && \text{(5.30d)}
\end{aligned}
$$

Terms (5.30a) and (6.7) are equal to zero due to the modes' orthogonality:

$$
\begin{aligned}
&\int_{\mathcal{R}_o} \boldsymbol{C}_1^T(r_o)\boldsymbol{D}_{11}(r_o,r_i)dr_o \\
&= \frac{1}{2\omega_c}\int_{\mathcal{R}_o} \begin{bmatrix}\phi_1(r_o)\\ \vdots \\ \phi_N(r_o)\end{bmatrix} \sum_{i=N+1}^{\infty} \frac{\phi_i(r_o)\phi_i(r_i)}{\omega_i} \ln\left(\frac{\omega_i+\omega_c}{\omega_i-\omega_c}\right) dr_o = 0 && \text{(5.31)}
\end{aligned}
$$

The term (6.8) can be expressed as follows:

$$\begin{aligned} & tr\Big\{\int_{\mathcal{R}_o} \boldsymbol{N}^*\,\boldsymbol{C}_1^T(r_o)\,\boldsymbol{C}_1(r_o)\boldsymbol{N}\Big(\int_{\mathcal{R}_i} \boldsymbol{B}_1(r_i)\boldsymbol{B}_1^T(r_i)dr_i\Big)dr_o\Big\} \\ &= tr\Big\{\boldsymbol{N}^*\Big(\int_{\mathcal{R}_o} \boldsymbol{C}_1^T(r_o)\,\boldsymbol{C}_1(r_o)dr_o\Big)\boldsymbol{N}\boldsymbol{\Gamma}\boldsymbol{\Gamma}^T\Big\} \\ &= tr\Big\{\boldsymbol{N}^*\boldsymbol{\Gamma}^T\boldsymbol{\Gamma}\boldsymbol{N}\boldsymbol{\Omega}\boldsymbol{\Omega}^T\Big\} \\ &= tr\Big\{\left(\boldsymbol{\Omega}\boldsymbol{N}\boldsymbol{\Gamma}\right)^*\left(\boldsymbol{\Gamma}\boldsymbol{N}\boldsymbol{\Omega}\right)\Big\} \end{aligned} \tag{5.32}$$

And the term (5.30d) can be formulated using the modes' orthogonality as follows:

$$\begin{aligned} & tr\Big\{\int_{\mathcal{R}_o}\int_{\mathcal{R}_i} \boldsymbol{D}_{11}^T(r_o,r_i)\boldsymbol{D}_{11}(r_o,r_i)dr_i dr_o\Big\} \\ &= tr\Big\{\frac{1}{4\omega_c^2}\int_{\mathcal{R}_o}\int_{\mathcal{R}_i}\sum_{i=N+1}^{\infty}\frac{\phi_i^2(r_o)\phi_i^2(r_i)}{\omega_i^2}\ln^2\left(\frac{\omega_i+\omega_c}{\omega_i-\omega_c}\right)dr_i dr_o\Big\} \\ &= tr\Big\{\frac{1}{4\omega_c^2}\sum_{i=N+1}^{\infty}\frac{\Phi_i^2\Phi_i^2}{\omega_i^2}\ln^2\left(\frac{\omega_i+\omega_c}{\omega_i-\omega_c}\right)\Big\} \\ &= tr\Big\{\boldsymbol{\Delta}^T\boldsymbol{\Delta}\Big\} = tr\Big\{\tilde{\boldsymbol{\Delta}}^T\tilde{\boldsymbol{\Delta}}\Big\} \end{aligned} \tag{5.33}$$

with

$$\boldsymbol{\Delta} = \frac{1}{2\omega_c}\left(\sum_{i=N+1}^{\infty}\frac{\Phi_i^4}{\omega_i^2}\ln^2\left(\frac{\omega_i+\omega_c}{\omega_i-\omega_c}\right)\right)^{1/2} \tag{5.34}$$

Going back to Eq. (5.29), and using Eqs. (5.2.2), (5.32) and (5.33) gives:

$$\begin{aligned} \ll y \gg_{2,i,o}^2 &= \frac{1}{2\pi}\int_{-\infty}^{\infty} f(\omega)tr\Big\{\left(\boldsymbol{\Omega}\boldsymbol{N}\boldsymbol{\Gamma}+\tilde{\boldsymbol{\Delta}}\right)^*\left(\boldsymbol{\Gamma}\boldsymbol{N}\boldsymbol{\Omega}+\tilde{\boldsymbol{\Delta}}\right)\Big\}f(\omega)d\omega \\ &= \frac{1}{2\pi}\int_{-\infty}^{\infty} f(\omega)\bar{g}_{io}(\omega)g_{io}(\omega)f(\omega)d\omega \end{aligned} \tag{5.35}$$

A similar calculation can be done for $\boldsymbol{H}_i(s, r_i)$ where:

$$\boldsymbol{H}_i(s, r_i) = \boldsymbol{C}_2 \boldsymbol{N} \boldsymbol{B}_1(r_i) + \boldsymbol{D}_{21}(r_i) \tag{5.36}$$

giving,

$$\begin{aligned} \boldsymbol{\Pi}^T \boldsymbol{\Pi} &= \int_{\mathcal{R}_i} \boldsymbol{D}_{21}^T(r_i) Q_i(r_i) \boldsymbol{D}_{21}(r_i) dr_i \\ \Leftrightarrow \boldsymbol{\Pi} &= \frac{1}{2\omega_c} \left(\sum_{i=N+1}^{\infty} \frac{\Phi_i^2 \boldsymbol{\Upsilon}_i^T \boldsymbol{\Upsilon}_i}{\omega_i^2} \ln^2 \left(\frac{\omega_i + \omega_c}{\omega_i - \omega_c} \right) \right)^{1/2} \end{aligned} \tag{5.37}$$

The spatial input/spatial output control can be expressed using the following matrix system:

$$\dot{\boldsymbol{x}}(s) = \boldsymbol{A}\boldsymbol{x}(s) + \boldsymbol{\Omega}\tilde{\boldsymbol{f}}(s) \tag{5.38a}$$

$$\tilde{\boldsymbol{y}}(s) = \boldsymbol{\Gamma}\boldsymbol{x}(s) + \tilde{\Delta}\tilde{\boldsymbol{f}}(s) \tag{5.38b}$$

$$\boldsymbol{v}_s(s) = \boldsymbol{C}_2\boldsymbol{x}(s) + \tilde{\Pi}\tilde{\boldsymbol{f}}(s) \tag{5.38c}$$

with

$$\tilde{\boldsymbol{\Pi}} = \begin{bmatrix} \boldsymbol{0}_{[N_s \times (2N-1)]} & \frac{1}{\sqrt{N_s}} \boldsymbol{\Pi}. \, ones(N_s, 1) \end{bmatrix} \tag{5.39}$$

with matrix $\boldsymbol{\Omega}^\dagger$ as follows:

$$\boldsymbol{\Omega}^\dagger_{[2N \times 2N]} = \begin{bmatrix} \boldsymbol{0}_{[N \times N]} & \boldsymbol{0}_{[N \times N]} \\ \boldsymbol{0}_{[N \times N]} & \Big(diag\big(\Phi_1, \ldots, \Phi_N\big) \Big)^{-1} \end{bmatrix} \tag{5.40}$$

Using matrix $\boldsymbol{\Omega}^\dagger$ defined in Eq. (5.40), the spatial input/output control system

can be expressed as a function of the point-wise external disturbance force, $f(s)$:

$$\dot{\boldsymbol{x}}(s) = \boldsymbol{A}\boldsymbol{x}(s) + \boldsymbol{\beta} f(s) \tag{5.41a}$$
$$\tilde{\boldsymbol{y}}(s) = \boldsymbol{\Gamma}\boldsymbol{x}(s) + \tilde{\boldsymbol{\Delta}}\boldsymbol{\Omega}^{\dagger}\boldsymbol{\beta} f(s) \tag{5.41b}$$
$$\boldsymbol{v}_s(s) = \boldsymbol{C}_2\boldsymbol{x}(s) + \tilde{\boldsymbol{\Pi}}\boldsymbol{\Omega}^{\dagger}\boldsymbol{\beta} f(s) \tag{5.41c}$$

5.2.3 Spatial input/spatial output control system with feedthrough term for the actuator

Inserting the control actuator feedthrough term into a conventional system (see Eqs. (5.25)), adds to the equation system as follows:

$$\dot{\boldsymbol{x}}(s) = \boldsymbol{A}\boldsymbol{x}(s) + \boldsymbol{B}_1(r_i) f(s) + \boldsymbol{B}_2\boldsymbol{v}_a(s) \tag{5.42a}$$
$$y(s, r_o) = \boldsymbol{C}_1(r_o)\boldsymbol{x}(s) + \boldsymbol{D}_{11}(r_o, r_i) f(s) + \boldsymbol{D}_{12}(r_o)\boldsymbol{v}_a(s) \tag{5.42b}$$
$$\boldsymbol{v}_s(s) = \boldsymbol{C}_2\boldsymbol{x}(s) + \boldsymbol{D}_{21}(r_i) f(s) + \boldsymbol{D}_{22}\boldsymbol{v}_a(s) \tag{5.42c}$$

Using the method set out earlier for determining feedthrough terms, in combination with the matrices of section 4.3, the spatial norm of the new system can be calculated as follows:

$$\ll y \gg_{2,i,o}^{2}$$
$$= \frac{1}{2\pi} \int_{-\infty}^{\infty} \int_{\mathcal{R}_o} \int_{\mathcal{R}_i} [f(\omega) \quad \boldsymbol{v}_a^T(\omega)]\, \boldsymbol{G}_i^*(\omega, r_i, r_o)\, \boldsymbol{G}_i(\omega, r_i, r_o) [f(\omega) \quad \boldsymbol{v}_a^T(\omega)]^T dr_i dr_o d\omega \tag{5.43}$$
$$= \frac{1}{2\pi} \int_{-\infty}^{\infty} \int_{\mathcal{R}_o} \int_{\mathcal{R}_i} \Big(f(\omega) \left[\boldsymbol{C}_1(r_o)\boldsymbol{N}\boldsymbol{B}_1(r_i) + \boldsymbol{D}_{11}(r_o, r_i)\right]^* \left[\boldsymbol{C}_1(r_o)\boldsymbol{N}\boldsymbol{B}_1(r_i) + \boldsymbol{D}_{11}(r_o, r_i)\right] f(\omega) \tag{5.43a}$$
$$+ f(\omega) \left[\boldsymbol{C}_1(r_o)\boldsymbol{N}\boldsymbol{B}_1(r_i) + \boldsymbol{D}_{11}(r_o, r_i)\right)^* \left(\boldsymbol{C}_1(r_o)\boldsymbol{N}\boldsymbol{B}_2 + \boldsymbol{D}_{12}(r_o)\right)\right] \boldsymbol{v}_a(\omega) \tag{5.43b}$$
$$+ \boldsymbol{v}_a^T(\omega) \left[\left(\boldsymbol{C}_1(r_o)\boldsymbol{N}\boldsymbol{B}_2 + \boldsymbol{D}_{12}(r_o)\right)^* \left(\boldsymbol{C}_1(r_o) N B_1(r_i) + \boldsymbol{D}_{11}(r_o, r_i)\right)\right] f(\omega) \tag{5.43c}$$
$$+ \boldsymbol{v}_a^T(\omega) \left[\left(\boldsymbol{C}_1(r_o)\boldsymbol{N}\boldsymbol{B}_2 + \boldsymbol{D}_{12}(r_o)\right)^* \left(\boldsymbol{C}_1(r_o)\boldsymbol{N}\boldsymbol{B}_2 + \boldsymbol{D}_{12}(r_o)\right)\right] \boldsymbol{v}_a(\omega) \Big) dr_i dr_o d\omega \tag{5.43d}$$

The term (5.43a) has already been calculated (see Eq. (5.35)). Eq. (5.43d) is equal to:

$$\int_{\mathcal{R}_o}\int_{\mathcal{R}_i}(\boldsymbol{C}_1(r_o)\boldsymbol{N}\boldsymbol{B}_2+\boldsymbol{D}_{12}(r_o))^*(\boldsymbol{C}_1(r_o)\boldsymbol{N}\boldsymbol{B}_2+\boldsymbol{D}_{12}(r_o))dr_i dr_o$$
$$=(\boldsymbol{\Gamma}NB_2)^*(\boldsymbol{\Gamma}NB_2)+\boldsymbol{\Theta}^T\boldsymbol{\Theta} \tag{5.44}$$

because $\int_{\mathcal{R}_o}(\boldsymbol{C}_1(r_o)\boldsymbol{N})^*\boldsymbol{D}_{12}(r_o)dr_o=0$ due to the modes' orthogonality (see Eq. (4.46c)) and matrix shape of $\boldsymbol{C}_1$.

The matrix

$$\boldsymbol{\Theta}=\begin{bmatrix}\boldsymbol{0}_{[N\times N_a]}\\ \frac{1}{2\omega_c}\left(\sum_{i=N+1}^{\infty}\frac{\Phi_i^2\boldsymbol{P}_i^2}{\omega_i^2}\ln^2\left(\frac{\omega_i+\omega_c}{\omega_i-\omega_c}\right)\right)^{\frac{1}{2}}\\ \boldsymbol{0}_{[(N-N_a)\times N_a]}\end{bmatrix} \tag{5.45}$$

includes the matrix $\boldsymbol{P}_i^2$, as defined in Eq. (5.10). And finally term (5.43a) can be approximated using Eq. (5.23) as follows:

$$\int_{\mathcal{R}_o}\int_{\mathcal{R}_i}f(\omega)\left[(\boldsymbol{C}_1(r_o)\boldsymbol{N}\boldsymbol{B}_1(r_i)+\boldsymbol{D}_{11}(r_o,r_i))^*(\boldsymbol{C}_1(r_o)\boldsymbol{N}\boldsymbol{B}_2+\boldsymbol{D}_{12}(r_o))\right]\boldsymbol{v}_a(\omega)dr_i dr_o$$
$$=\tilde{\boldsymbol{f}}^T(\omega)(\boldsymbol{\Gamma}N\boldsymbol{\Omega})^*(\boldsymbol{\Gamma}NB_2)\boldsymbol{v}_a(\omega)+\int_{\mathcal{R}_o}\int_{\mathcal{R}_i}f(\omega)\left[D_{11}^T(r_o,r_i)D_{12}(r_o)\right]\boldsymbol{v}_a(\omega)dr_i dr_o$$
$$\approx\tilde{\boldsymbol{f}}^T(\omega)[(\boldsymbol{\Gamma}\boldsymbol{N}\boldsymbol{\Omega})^*(\boldsymbol{\Gamma}\boldsymbol{N}\boldsymbol{B}_2)+\tilde{\boldsymbol{\Delta}}^T\boldsymbol{\Theta}]\boldsymbol{v}_a(\omega) \tag{5.46}$$

The main equation, Eq. (5.43) can then be very closely approximated as:

$$\begin{aligned}
\ll y \gg_{2,i,o}^2 \approx \frac{1}{2\pi} \int_{-\infty}^{\infty} f(\omega) tr\Big\{ \left(\tilde{\boldsymbol{\Omega}} \boldsymbol{N} \boldsymbol{\Gamma} + \tilde{\boldsymbol{\Delta}}\right)^* \left(\tilde{\boldsymbol{\Gamma}} \boldsymbol{N} \boldsymbol{\Omega} + \tilde{\boldsymbol{\Delta}}\right) \Big\} f(\omega) \\
+ \tilde{\boldsymbol{f}}^T(\omega)[(\boldsymbol{\Gamma} \boldsymbol{N} \boldsymbol{\Omega})^* (\boldsymbol{\Gamma} \boldsymbol{N} \boldsymbol{B}_2) + \tilde{\boldsymbol{\Delta}}^T \boldsymbol{\Omega}] \boldsymbol{v}_a(\omega) \\
+ \boldsymbol{v}_a^T(\omega)[(\boldsymbol{\Gamma} \boldsymbol{N} \boldsymbol{B}_2)^T (\boldsymbol{\Gamma} \boldsymbol{N} \boldsymbol{\Omega}) + \boldsymbol{\Omega}^T \tilde{\boldsymbol{\Delta}}] \tilde{\boldsymbol{f}}(\omega) \\
+ \boldsymbol{v}_a^T(\omega)[(\boldsymbol{\Gamma} \boldsymbol{N} \boldsymbol{B}_2)^* (\boldsymbol{\Gamma} \boldsymbol{N} \boldsymbol{B}_2) + \boldsymbol{\Theta}^T \boldsymbol{\Theta}] \boldsymbol{v}_a(\omega) d\omega \\
\approx \|\tilde{\boldsymbol{y}}\|_2^2
\end{aligned}$$

which gives the following spatial input/spatial output system with all the feedthrough terms:

$$\dot{\boldsymbol{x}}(s) = \boldsymbol{A} \boldsymbol{x}(s) + \boldsymbol{\Omega} \tilde{\boldsymbol{f}}(s) + \boldsymbol{B}_2 \boldsymbol{v}_a(s) \tag{5.47a}$$

$$\tilde{\boldsymbol{y}}(s) = \boldsymbol{\Gamma} \boldsymbol{x}(s) + \tilde{\boldsymbol{\Delta}} \tilde{\boldsymbol{f}}(s) + \boldsymbol{\Theta} \boldsymbol{v}_a(s) \tag{5.47b}$$

$$\boldsymbol{v}_s(s) = \boldsymbol{C}_2 \boldsymbol{x}(s) + \tilde{\boldsymbol{\Pi}} \tilde{\boldsymbol{f}}(s) + \boldsymbol{D}_{22} \boldsymbol{v}_a(s) \tag{5.47c}$$

5.3 Summary

This chapter set out Halim's spatial input/spatial output control design, introducing some variants that improve the robustness of the conventional control approach by making it less dependent on the extent of knowledge about the real disturbance force. More specifically, this section has also developed a means of objectively deriving feedthrough terms of the spatial control system to increase its reliability when applied to a real system. It will be later shown in Chapter 7 how spatial input/spatial output is a key element for achieving high frequency control for complex structures.

Chapter 6

ROBUST CONTROL METHODS

As discussed in Chapters 1 and 4, vibration control design is generally model-based, and the model used is typically a truncation of either an analytical or experimental model. This means that the control design must then account for any unmodelled part of the system in question that could introduce instability into the system. Classical control theory [74, 75] rarely address this, or only in rudimentary ways. Modern control theory, on the other hand, and more specifically robust control theory, does account for the umodelled part of system in question by combining new functions, which represent unmodelled part(s) of the system, with the nominal truncated model to obtain an augmented-model that is equivalent to the real system. This work in this chapter and following chapters therefore use robust control theory, specifically the $\mathcal{H}_\infty$ control approach for vibration control. This chapter attempts to clear up some of the existing misunderstanding about the design, analysis and robustness of a $\mathcal{H}_\infty$ control design. A large part of this section is based on the work of [7, 9].

6.1 Control system design

In many control design applications, it can be a challenging task to successfully modify the behaviour and response of an unknown plant to meet certain perfor-

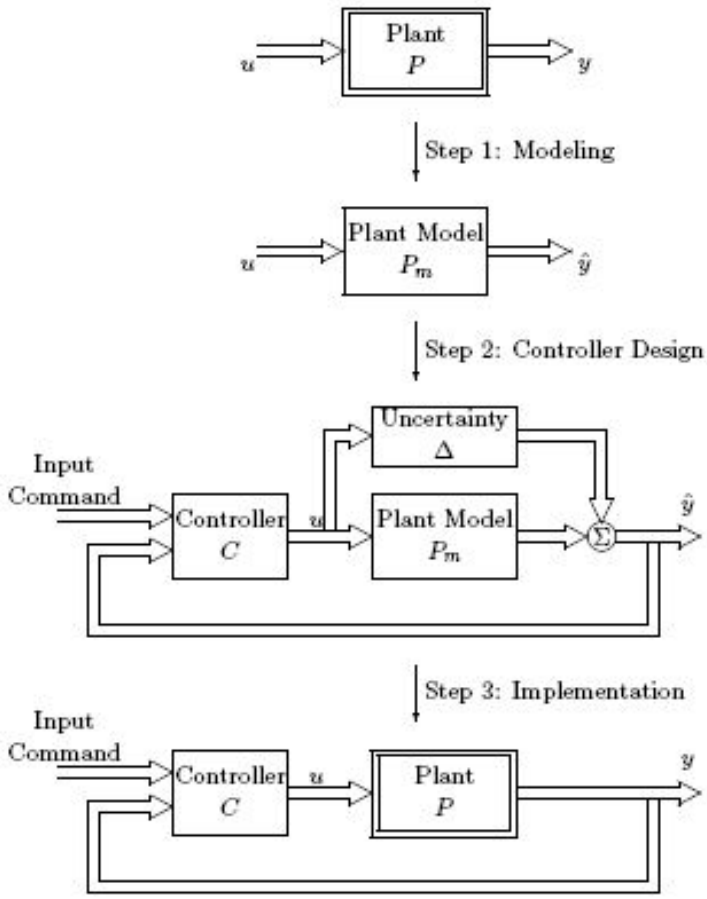

Figure 6.1: Control system design steps from [7].

mance requirements. By plant, it is meant any process characterised by a certain number of inputs $\boldsymbol{u}(s)$ and outputs $\boldsymbol{y}(s)$. The plant inputs $\boldsymbol{u}(s)$ are processed to produce several plant outputs $\boldsymbol{y}(s)$ that make up the overall output response of the plant. The control design task is to choose the input $\boldsymbol{u}(s)$ so that the output response $\boldsymbol{y}(s)$ satisfies certain defined performance requirements. In general, making an appropriate choice of $\boldsymbol{u}(s)$ is not a straightforward task, as the plant process is typically complex. Fig. 6.1 shows the control design steps that most control engineers would follow.

Control system engineers have three primary concerns when designing a control

system: observability, controllability and stability. Observability is the ability to observe all of the parameters or state variables in the system. Controllability is the ability to move a system from any given state to any desired state. Stability is often phrased as the bounded response of the system to any bounded input. A successful control system will exhibit and maintain all three of these properties. Achieving this is difficult for the control system engineer working with limited information; this lack of information about the system is known as uncertainty.

One way of dealing with uncertainty is to use stochastic control theory. This method deals with the expected value of control by modelling uncertainties in the system as probability distributions and then combining these distributions to yield a control law. However, there are isolated instances in which this may not deliver results that are close to the expected value, which is unlikely to be acceptable for embedded control systems that have safety implications.

Robust control on the other hand, unlike stochastic control, seeks to bound the uncertainty rather than only expressing it in the form of a distribution. Given a limit on the uncertainty, a control system can deliver results that meet the set requirements in all cases. Robust control theory could therefore be stated as a worst-case analysis method rather than a typical case method. It must be recognised that some performance efficiency is likely to be sacrificed in order to guarantee that the system will meet the set requirements. However, this is a recurring theme when dealing with embedded systems in which safety is critical.

Another technique for handling the model uncertainty that often occurs at high frequencies is to use gain scheduling to balance the performance and robustness of the system. Setting a high gain (near 1) means that the system will respond quickly to differences between the desired state and the actual state of the plant. When the plant has been accurately modelled, this high gain would typically result in high performance by the control system for low frequency. This region of operation is called the performance band. On the contrary, for high frequencies when the plant has not been modelled accurately, the gain should be set lower, as this would provide a larger error term between the measured output and the

reference signal. This region of operation is called the robustness band, where the feedback from the output is essentially ignored. To change the gain over different frequencies, a transfer function is employed. This involves setting the poles and zeros of the transfer function to achieve a filter. Between the two operation regions of performance and robustness, there is a transition region where the controller does not perform well on either performance or robustness. The transition region cannot arbitrarily be made small because its size is dependent on the number of poles and zeros in the transfer function. Adding terms in order to adjust the transfer function for this would only increase the complexity of the control system [76].

6.2 Robust control formulation

A classical SISO (Single Input Single Output) gain feedback controller is designed to be able to cope effectively with parameter changes, provided that those changes are within certain limits. In Fig. 6.2, $d(s)$ represents a perturbation, $r(s)$ a reference, $n(s)$ a noise, $G(s)$ a nominal system transfer function to be controlled, and $K(s)$ a controller transfer function. It gives the following equations:

$$\Rightarrow \text{for the output plant:} \quad y(s) = T(s)[r(s) - n(s)] + S(s)d(s) \tag{6.1a}$$

$$\Rightarrow \text{for the error signal:} \quad e(s) = S(s)[r(s) - d(s) - n(s)] \tag{6.1b}$$

$$\Rightarrow \text{for the control signal:} \quad u(s) = R(s)[r(s) - d(s) - n(s)] \tag{6.1c}$$

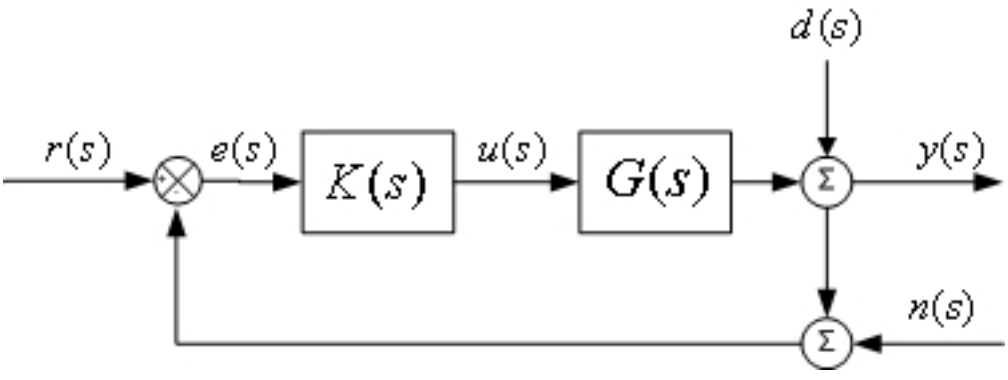

Figure 6.2: Model of SISO feedback control system.

with $S(s)$ being the sensitivity function of the output plant, $T(s)$ the sensitivity complementary function, and $R(s)$ the energy restriction function which represents the control strain measured.

$$S(s) = [I + G(s)K(s)]^{-1} \tag{6.2a}$$
$$T(s) = G(s)K(s)[I + G(s)K(s)]^{-1} \tag{6.2b}$$
$$R(s) = K(s)[I + G(s)K(s)]^{-1} \tag{6.2c}$$

For MIMO (Multiple Inputs Multiple Outputs) systems the above functions would be written in matrix form.

Since the purpose of the controller is to ensure that the error $e(s)$ is as close to zero as possible, S must be as small as possible (see Eq. (6.1b)); consequently T approximates identity because $S+T = I$. However, a small S results in an increase in R, and thereby an increase in control K. The requirements are conflicting and compromise must be established between the controller requirements and the bound pre-defined energy of the controller. One way of mathematically solving this problem of conflicting requirements expressed above is to calculate weight functions for each requirement using the $\mathcal{H}_\infty$ norm:

$$\|W_1(s)S(s)\|_\infty \leq 1 \tag{6.3a}$$
$$\|W_2(s)R(s)\|_\infty \leq 1 \tag{6.3b}$$
$$\|W_3(s)T(s)\|_\infty \leq 1 \tag{6.3c}$$

where $W_1(s)$, $W_2(s)$ and $W_3(s)$ need to be defined. The three coupled Eqs.6.3 can be considered as a global transfer function $T_{vp}(s)$:

$$\left\| \begin{array}{l} W_1(s)S(s) \\ W_2(s)R(s) \\ W_3(s)R(s) \end{array} \right\|_\infty = \|T_{vp}(s)\|_\infty \leq 1 \tag{6.4}$$

where p is the input vector $[d\ r\ n]^T$ and v is the output vector $[v_1\ v_2\ v_3]^T$. It

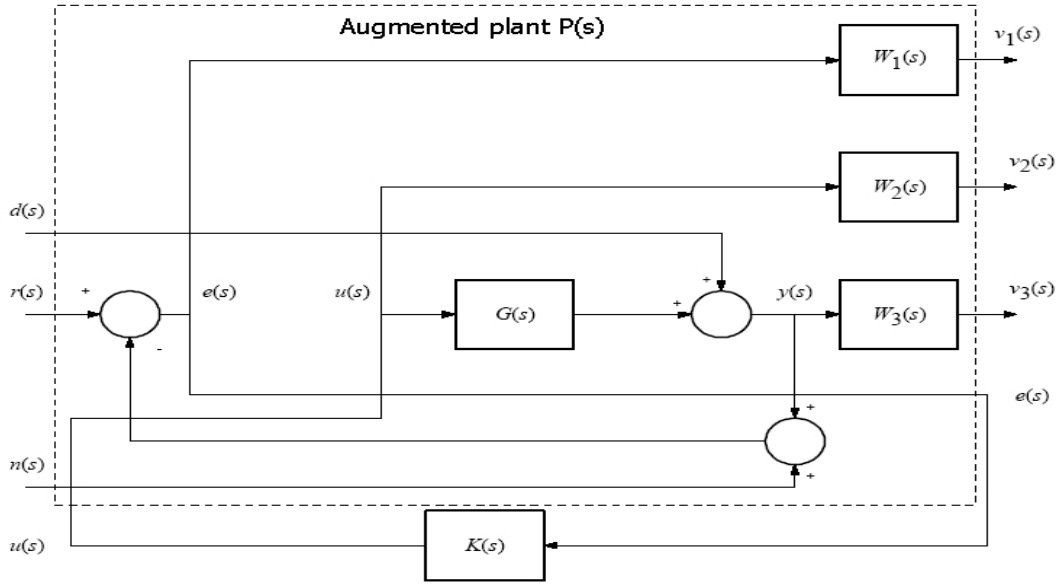

Figure 6.3: Augmented plant and controller for $\mathcal{H}_\infty$ control design from [8, 9].

is possible to describe this inequality with a convex representation as shown in Fig. 6.4.

Inevitably, there will be some discrepancies between the mathematical representation of the dynamics of a system and the system's actual behaviour. When expressed within an uncertainty model, the representation of this unavoidable error must reflect an understanding of the mechanisms which cause it and present a mathematical structure suitable for manipulations [10]. A single plant may present uncertainties of various orders, mainly due to the impossibility of perfectly modelling the dynamic system in question. The theory of robust control defines those uncertainties as either structured or non-structured.

The structured uncertainty model is associated with a class of uncertainty which is a function of a specific parameter of the nominal model G. This is the case, for example, for the uncertainty of the damping (ζ) of vibration modes in a structure. The damping values are not known precisely, but the range of their variation is known ($0 < \zeta < 1$). One way to deal with structural uncertainty

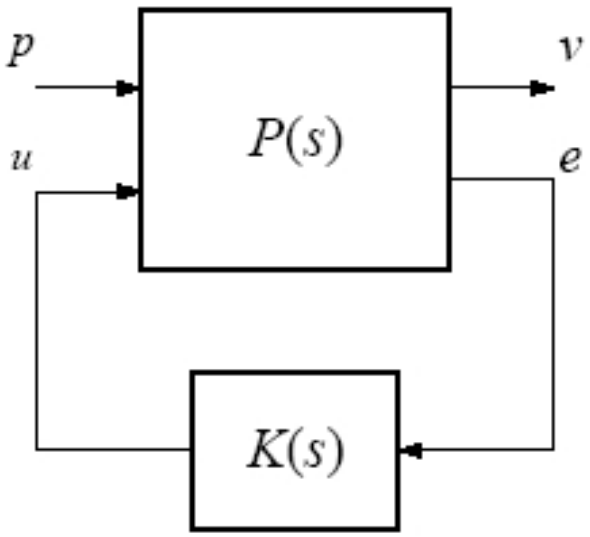

Figure 6.4: Augmented plant convex representation.

is to model it, according to convex description (such as an additional external feedback loop, along with the control loop), which allows it to be isolated from the nominal model P. Fig. (6.5) illustrates the configuration used for this type of representation.

Another way to deal with the errors is to allow them to be non-structured; that is, the errors are not visualised in the model structure. In practice, high frequency errors (dynamics not modelled due to truncated modes) are better represented in the form of non-structured uncertainties, while low frequency errors (dynamics of the nominal model) are better represented by highly parameterised structures. Thus, the non-structured uncertainties may be represented in the way shown in Fig. (6.6), where the nominal plant G and the disturbed plant G_p are inserted into a limited region. The extent of this region is given by the form (the profile accepted by the uncertainties as a function of frequency) together with the uncertainties norm (the extent of the uncertainties). It is assumed that the disturbed plant G_p represents exactly the real physical system under study. There is, therefore, a difference between the two representations (G and G_p), a difference

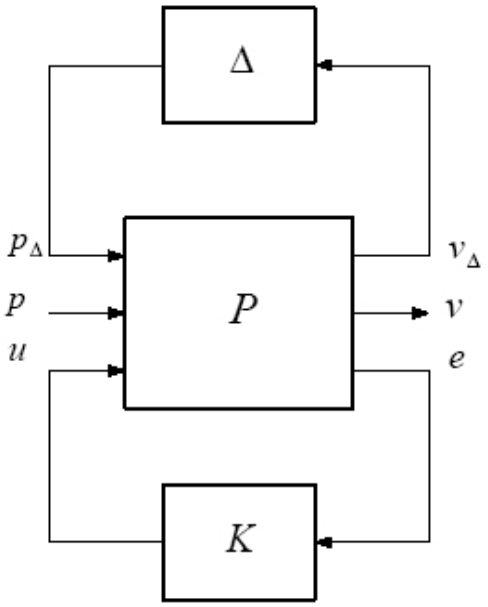

Figure 6.5: Augmented plant convex representation with uncertainties.

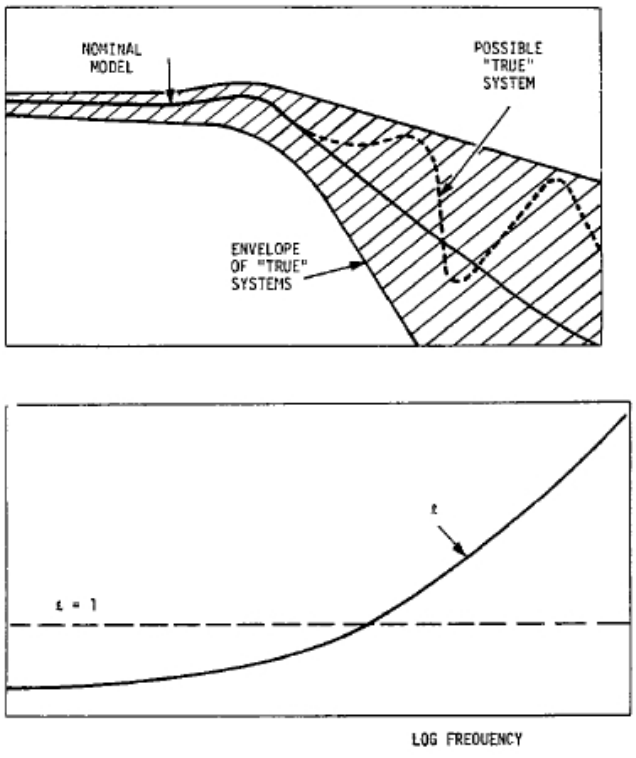

Figure 6.6: Typical behaviour of multiplicative perturbations from [10].

which is henceforth called the modelling error or residual uncertainty $E(s)$. It is useful for the project concerned in this thesis that this modelling error $E(s)$ can be mathematically represented. The non-structured uncertainties admit two predominant types of representation: the multiplicative uncertainty and the additive uncertainty. The stability conditions of the disturbed model G_p can be encompassed in a strict mathematical formalism based on combining weight functions with the nominal plant G. Depending on the type of uncertainties of concern for the control designer, the function can weight $R(s)$ if the uncertainty is considered as additive, or $T(s)$ if the uncertainty is considered as multiplicative or both.

6.3 Controller design taking into account the parametric and unmodelled dynamic model uncertainty

The designed controller $K(s)$ works perfectly within the nominal system but would be unable to accurately control the actual full system because unconsidered modes would interfere with the controller input and output. In order to control the full system, both the unmodelled dynamics uncertainty (due to the model truncation or some lack of understanding of the overall physical process) and the parametric uncertainty (where the structure of the model is known but some of its parameters are uncertain) must be taken into account.

6.3.1 Unmodelled dynamics

The unmodelled dynamics uncertainty can be analysed mathematically as an additive uncertainty (see [9] for more details):

$$G_d(s) = G_n(s) + E_a(s) \tag{6.5}$$

where $G_d(s)$ is the disturbed transfer function, G_n the nominal transfer function, and $E_a(s)$ the additive uncertainty. The disturbed closed-loop system $G_d(s)K(s)[I+$

$G_d(s)K(s)]^{-1}$ is stable if the matrix of $I+G_d(s)K(s)$ is not singular for any $s \in \mathbb{C}^+$.

$$I + G_d(s)K(s) = I + G_n(s)K(s) + E_a(s)K(s) \tag{6.6}$$

As the nominal system is, by definition, stable, Eq. (6.6) can be multiplied by $[I+G_n(s)K(s)]^{-1}$; and using the results from [42], assuming that A is not singular and $A+B$ is also not singular if $\underline{\sigma}(A) > \bar{\sigma}(B)$, gives:

$$\underline{\sigma}(I) > \bar{\sigma}\left(\frac{E_a(s)K(s)}{I+G_n(s)K(s)}\right) \Leftrightarrow I > \bar{\sigma}(E_a(s)R(s)) \tag{6.7}$$

Knowing that

$$\bar{\sigma}(E_a(s)R(s)) < \bar{\sigma}(E_a(s))\bar{\sigma}(R(s)) \tag{6.8}$$

Eq. (6.8) gives the inequality (6.13).

$$\begin{aligned} \bar{\sigma}(R(s)) &< \frac{1}{\bar{\sigma}(E_a(s))} \\ \Leftrightarrow \|R(s)\|_\infty &< \frac{1}{\|E_a(s)\|_\infty} \end{aligned} \tag{6.9}$$

with $R(s) = K(s)[I + G_n(s)K(s)]^{-1}$. This gives a weight function that encompasses the unmodelled dynamics $W_a(s) = \|E_a(s)\|_\infty$ to be accounted for in the $\mathcal{H}_\infty$ controller design.

6.3.2 Parametric uncertainty

The parametric uncertainty can be analysed mathematically as either an additive or multiplicative uncertainty; most often it assumes the form of a multiplicative uncertainty, as expressed by Eq. (6.10).

$$G_d(s) = G_n(s)[I + E_m(s)] \tag{6.10}$$

where $E_m(s)$ is the multiplicative uncertainty. As mentioned in the unmodelled dynamics case, the disturbed closed-loop system is stable if the matrix of $I + G_d(s)K(s)$ is not singular for any $s \in \mathbb{C}^+$.

$$\begin{aligned} I + G_d(s)K(s) &= I + G_n(s)[I + E_m(s)]K(s) \\ &= I + G_n(s)K(s) + G_n(s)E_m(s)K(s) \end{aligned} \tag{6.11}$$

Using the same approach as in the preceding section 6.3.1, an inequality can be set up:

$$\underline{\sigma}(I) > \bar{\sigma}\left(\frac{E_m(s)G_n(s)K(s)}{I + G_n(s)K(s)}\right) \Leftrightarrow I > \bar{\sigma}(E_a(s)T(s)) \tag{6.12}$$

then

$$\begin{aligned} \bar{\sigma}(T(s)) &< \frac{1}{\bar{\sigma}(E_m(s))} \\ \Leftrightarrow \|T(s)\|_\infty &< \frac{1}{\|E_m(s)\|_\infty} \end{aligned} \tag{6.13}$$

with $T(s) = G_n(s)K(s)[I + G_n(s)K(s)]^{-1}$. In this case, this gives a weight function that encompasses the parametric uncertainty $W_m(s) = \|E_m(s)\|_\infty$ to also be accounted for in the $\mathcal{H}_\infty$ controller design. The two approaches in sections 6.3.1 and 6.3.2 can be combined to produce a fully augmented plant that includes both the unmodelled dynamics and the parametric uncertainty as weight functions. This gives a complete representation of the real system, despite the fact that the model was truncated, allowing a more robust design to be produced for the $\mathcal{H}_\infty$ controller.

To demonstrate how an unmodelled dynamics weight function can be defined in order to encompass unmodelled modes, Chapter 8 will conduct an experiment, based on the modelling set out in Chapter 4, on the example of a cantilever beam (see Fig. 8.5 to view the weight function results). The control objective can be broken down into three specifications:

- Attenuation of the desired modes;
- Controller design that will work for both the nominal case and the full sys-

tem;

- Minimisation of any non-considered modes, or spillover.

6.3.3 Robust stability and performance

All of the controller designs for the experiments conducted in this thesis prioritise the fulfillment of the robust performance criterium; for this reason, it is important to give a summary of the notions of Robust Stability (RS) and Robust Performance (RP) which have been comprehensively covered by Skogestad [42]. The notions (from [42]) have been defined as follows:

- RS analysis: for a given controller K, it is determined whether the system can remain stable for all plants in the uncertainty set.
- RP analysis: if RS is satisfied, it is then determined how *large* the transfer function, from exogenous inputs w to output z, can be for all plants in the uncertainty set.

The RS and RP analyses are aimed at attaining the most robust controller for vibration attenuation using a truncated model. The remainder of this section sets out how these analyses are conducted. The augmented plant P is usually divided up as:

$$P = \begin{bmatrix} P_{11} & P_{12} \\ P_{21} & P_{22} \end{bmatrix} \tag{6.14}$$

Assuming that both weight functions and uncertainties have been defined, the problem can be expressed in a convex form as seen earlier in Fig. 6.5. In order to analyse the closed-loop performance, P and K are related together in a plant N, denoting a lower Linear Fractional Transformation (LFT) of P, with K as the parameter (see Fig. 6.7), giving $N = P_{11} + P_{12}K(I - P_{22}K)^{-1}P_{21}$.

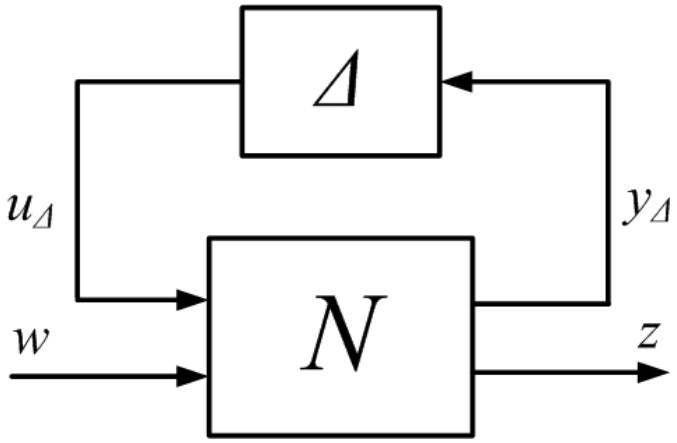

Figure 6.7: $N\Delta$-structure for robust performance analysis.

In a similar way, for the uncertainty closed-loop transfer function from w to z, $z = Fw$ is related to N and Δ by an upper LFT, with F given as follows:

$$F = N_{22} + N_{21}\Delta(I - N_{11}\Delta)^{-1}N_{12} \tag{6.15}$$

It is known that both N and Δ are stable. F is also stable if and only if the Nyquist plot of the $det(I - N_{11}\Delta)$ does not encircle the origin for all Δ [42], which can be mathematically expressed as follows:

$$\begin{aligned} det(I - M\Delta(j\omega)) \neq 0, \qquad & \forall\omega, \forall\Delta \qquad \text{with } M = N_{11} \\ \Leftrightarrow \lambda_i(M\Delta) \neq 1, \qquad & \forall i, \forall\omega, \forall\Delta \end{aligned} \tag{6.16}$$

The concept of the structured singular value denoted μ is used to analyse the robust performance of a given control system and takes the form of a function that gives a generalisation of the singular value, $\bar{\sigma}$. Mathematically, μ is defined as:

$$\mu(M)^{-1} \triangleq \min_{\Delta}\{\bar{\sigma}(\Delta) \,|\, (I - M\Delta) = 0 \quad \text{for} \quad \text{structured } \Delta\}$$

From [42] and assuming that both M and Δ are stable, the $M\Delta$-system is stable for the allowed perturbation with $\bar{\sigma}(\Delta) \leqslant 1$, $\forall w$ if and only if

$$\mu(M(jw)) < 1, \forall w \tag{6.17}$$

[42] analyses the RP and sets Eq. (6.18), using $N\Delta$.

$$\begin{aligned} &\|F\|_\infty < 1, \quad \forall \|\Delta\|_\infty \leqslant 1 \\ &\Leftrightarrow \mu_{\hat{\Delta}}(N(jw)) < 1, \quad \forall\omega \qquad \text{where } \hat{\Delta} = \begin{bmatrix} \Delta & 0 \\ 0 & \Delta_p \end{bmatrix} \end{aligned} \tag{6.18}$$

and Δ_p is a full complex matrix. The respective μ conditions for analysing Nominal Stability (NS), Nominal Performance (NP), RS and RP can be summarised as follows:

$$\text{NS} \quad \Leftrightarrow \quad N \text{ (internally) stable} \tag{6.19}$$

$$\text{NP} \quad \Leftrightarrow \quad \mu_{\Delta_p}(N_{22}) < 1, \forall\omega, \text{ and NS} \tag{6.20}$$

$$\text{RS} \quad \Leftrightarrow \quad \mu_{\Delta}(N_{11}) < 1, \forall\omega, \text{ and NS} \tag{6.21}$$

$$\text{RP} \quad \Leftrightarrow \quad \mu_{\hat{\Delta}}(N) < 1, \quad \forall\omega, \hat{\Delta} = \begin{bmatrix} \Delta & 0 \\ 0 & \Delta_p \end{bmatrix} \text{ and NS} \tag{6.22}$$

μ-synthesis and DK iteration can help in obtaining a higher order and/or a more suitable $\mathcal{H}_\infty$ controller. As $\mu(N)$ can be reformulated in the form of the matrix system $DN(K)D^{-1}$, the idea is to adjust K and D to find a more suitable K. In this way, the most suitable controller may be found for achieving vibration attenuation using a truncated model of a given structure.

6.4 Summary

This chapter provided a summary of the $\mathcal{H}_\infty$ control concept, which comes from robust control theory. The modelling problem was divided into two parts to be solved: the part of the system that is known and that forms a nominal model, and the part that is unknown that is not included in the model, by choice (in the case of truncation) or due to a lack of information (about the noise or some features of the structure in question). It was shown how the unknown part of the system can be quantified through the use of transfer functions, which can be added to a nominal model to form an augmented model that encompasses all of the real system features to be controlled. This augmented model would be used to assist

in designing a controller that is much more stable than any of those found using other design.

Chapter 7

EXPERIMENTAL VIBRATION MODELLING AND OPTIMISATION FOR ACTIVE VIBRATION CONTROL

When attempting to actively control the vibration of a complex structure subjected to unknown complex disturbance forces, how well the controller performs is primary determined by four factors: the frequency bandwidth to be controlled, the accuracy of the structure modelling, the robustness of the controller, and the extent to which the disturbance can be quantified. Each consideration can be separately addressed through the application of appropriate techniques or approaches that are not part of the original control system design. The difficulty confronting the control system designer is to find a way of combining all of these separate techniques into a unified approach.

The chapter outlines the techniques that can be used to address each consideration and how the techniques can be combined to produce a robust, fixed bandwidth controller for which the lower frequency limit for control can be any frequencies larger than 0Hz. It will be shown how Subspace Model Identification (SMI) can be used to obtain the system dynamics through experiment. There will

also be a description of the spatial input/output control approach, which provides a conceptualisation of the structure's global displacement and the contribution of the global disturbance on the structure. It will be shown how combining these two theories will enable an experimental model to be defined that could be used in achieving global vibration attenuation for the system in question. Finally the chapter sets out optimisation approaches that may be used to obtain the optimum experimental truncated model for vibration control purposes.

7.1 Overview of theory used to obtain an experimental model

Existing techniques generally permit the achievement of model-based global vibration control of a given system for a specified frequency bandwidth, provided that an analytical model [20, 75, 77] or a sufficiently accurate simulation of the full system is available [4, 9, 78]. The typical complexity of real-world systems generally makes the development of analytical models virtually impossible, and even if it were possible in some cases the time required to develop such a model would likely be excessive to the point of impracticability. There are also problems that occur with the use of simulation models, which are often grossly simplified in order to be practicable, the consequence being simulation models that may be less-than-accurate representations of their actual systems, with such problems as the mismatching of resonance frequencies and damping.

However, it is also possible to achieve a mathematical model of a given complex dynamic system by processing data that is obtained from the real system. This is the approach used in this chapter, employing an experimental model of the system to be controlled, which is a more viable way of determining the correct dynamic features of a complex system within a specified level of uncertainty. However, as Van Overschee wrote [79], *Model uncertainty is allowed as long as the robustness of the overall system is ensured.* It will be shown here using subspace model identification (SMI) theory [79–81], combined with spatial input/spatial output control theory [45, 70, 77] and robust control theory [42, 43, 66], how global vibration

attenuation of a system can be ensured when using a mathematical model derived from experimental data of a system.

There are four key ideas when building a conceptual experimental model of a complex structure (to be used in designing the desired global vibration controller): first, to build an equivalent experimental model of the system in order to control it without requiring any knowledge of where and how the disturbance forces are applied to the system; second, to combine a conceptualisation of the global vibration attenuation with the experimental model; third, to be able to use the resulting truncated model to control any combination of resonance frequencies, low and/or high, for those frequencies that are observable and controllable by the sensors and actuators; and finally, to achieve global vibration attenuation of a specific part of an unknown system.

The first step towards fulfilling these ideas is to use SMI theory and associated tools to extract information from the unique data generated by the actuators and received by the sensors in the absence of any control effort. Using the SMI technique in the state-space domain gives the matrices used in Eqs. (7.1): the system matrix $\boldsymbol{A}$; the actuator input matrix $\boldsymbol{B}_a$, with N_a the number of actuators; the sensor output matrix $\boldsymbol{C}_s$, with N_s the number of sensors; and the feedthrough matrix $\boldsymbol{D}_{as}$ relating the actuators to the sensors.

Spatial input/spatial output control theory then enables the modelling of the system's global displacement/velocity and of the contribution of the disturbances on the response of the entire structure, represented by the matrices $\boldsymbol{B}_f$ and $\boldsymbol{C}_y$ in Eqs. (7.1). Given that the SMI technique provides the state-space representation of the system up to a similarity transformation, the final step in the process of building an experimental model is to use a similarity transformation to transform the matrices $\boldsymbol{A}$, $\boldsymbol{B}_a$, $\boldsymbol{D}_{as}$ and $\boldsymbol{C}_s$ to the same orthogonal subspace as $\boldsymbol{B}_f$, $\boldsymbol{C}_y$. The equation system for representing the system in question can therefore be written

as:

$$\dot{\boldsymbol{x}}(s) = \boldsymbol{A}\boldsymbol{x}(s) + \boldsymbol{B}_f\boldsymbol{f}(s) + \boldsymbol{B}_a\boldsymbol{v}_a(s) \tag{7.1a}$$

$$\boldsymbol{y}(s) = \boldsymbol{C}_y\boldsymbol{x}(s) \tag{7.1b}$$

$$\boldsymbol{v}_s(s) = \boldsymbol{C}_s\boldsymbol{x}(s) + \boldsymbol{D}_{as}\boldsymbol{v}_a(s) \tag{7.1c}$$

where $\boldsymbol{x}$ is the state of the system, $\boldsymbol{f}$ is the disturbance, $\boldsymbol{y}$ is the displacement output at a particular location, $\boldsymbol{v}_s$ is the sensor measurements, and $\boldsymbol{v}_a$ is the actuator measurements.

Once a full experimental model has been obtained, the model is truncated according to the frequency bandwidth of interest in order to maximise control efficiency in the bandwidth of interest without wasting energy on controlling frequencies outside of this bandwidth. However, it is then necessary, in the truncated model, to account for both lower order and higher order modes in order to minimise any errors in the poles and zeros of the system in question that could lead to instability [65]. This problem can be addressed using the convex optimisation proposed by Moheimani and Halim [82]. The above four key ideas process will be discussed in greater detail in the remainder of this chapter.

7.2 Experimental truncated model for global vibration control within a specified frequency bandwidth

7.2.1 Subspace Model Identification

Frequency response analysis undertaken using SMI theory provides essential information about the dynamic of the system: resonance frequencies, damping and coupling among actuators and sensors. This section is mainly based on research published by Haverkamp [81] and Van Overschee and De Moor [79]. The objective of using SMI is to estimate the $\boldsymbol{A}$, $\boldsymbol{B}_a$, $\boldsymbol{C}_s$ and $\boldsymbol{D}_{as}$ matrices of a given real system represented in the system of equations shown in Eqs. (7.1).

Several SMI algorithm families are summarised in [79, 81]. This work has chosen to use the Multivariable Output-Error state-space (MOESP) algorithm family for the amenability of these algorithms to being used with the combined deterministic/stochastic equation system. As this work assumes that the output error is a contribution of white noise and process noise, the Post Output MOESP (PO-MOESP) algorithm is known to be the most appropriate (for more details on this algorithm see [83–86]).

Each system can be represented in discrete state-space using a combination of deterministic and stochastic parts, as shown below:

$$\hat{\boldsymbol{x}}(k+1) = \boldsymbol{A}\hat{\boldsymbol{x}}(k) + \boldsymbol{B}_a\boldsymbol{v}_a(k) + \boldsymbol{K}\boldsymbol{e}(k) \tag{7.2a}$$

$$\hat{\boldsymbol{v}}_s(k) = \boldsymbol{C}_s\hat{\boldsymbol{x}}(k) + \boldsymbol{D}_{as}\boldsymbol{v}_a(k) \tag{7.2b}$$

$$\boldsymbol{v}_s(k) = \hat{\boldsymbol{v}}_s(k) + \boldsymbol{e}(k) \tag{7.2c}$$

where $\boldsymbol{K}$ is the Kalman matrix filter gain, $\boldsymbol{e}(k)$ the zero mean white noise, and $\hat{\boldsymbol{v}}_s(k)$ the minimum variance estimate of the output $\boldsymbol{v}_s(k)$. The order n of the unknown system needs to be determined. From measurements of the input $\boldsymbol{v}_a(k)$ and the output $\boldsymbol{v}_s(k)$, the system matrices $\boldsymbol{A}$, $\boldsymbol{B}_a$, $\boldsymbol{C}_s$ and $\boldsymbol{D}_{as}$ up to a similarity transformation and the matrix $\boldsymbol{K}$ can be determined. The controllable modes of $(\boldsymbol{A}, [\boldsymbol{B}_a\ \boldsymbol{K}])$ are assumed to be stable, the pair $(\boldsymbol{A}, \boldsymbol{C}_s)$ is assumed to be observable, and $\boldsymbol{v}_a(k)$ is assumed to be a *spectrally rich* persistent excitation of sufficient order. Given N_m measurements of the input $\boldsymbol{v}_a(k)$, the system equations can be rewritten as follows:

$$\boldsymbol{Y}_{i,j,N} = \boldsymbol{\Gamma}_j\boldsymbol{X}_{i,N} + \boldsymbol{H}_j\boldsymbol{U}_{i,j,N} + \boldsymbol{G}_j\boldsymbol{\mathcal{E}}_{i,j,N}, \tag{7.3}$$

where $\boldsymbol{\mathcal{E}}_{i,j,N}$, $\boldsymbol{Y}_{i,j,N}$ and $\boldsymbol{U}_{i,j,N}$ are the Hankel matrices of the error, output and input data respectively, and $\boldsymbol{\Gamma}_j$ the observability matrix of a standard state-space

system.

$$\boldsymbol{Y}_{i,j,N} = \begin{bmatrix} \boldsymbol{v}_s(i) & \cdots & \boldsymbol{v}_s(i+N-1) \\ \vdots & & \vdots \\ \boldsymbol{v}_s(i+j-1) & \cdots & \boldsymbol{v}_s(i+j+N-2) \end{bmatrix}, \tag{7.4}$$

$$\boldsymbol{U}_{i,j,N} = \begin{bmatrix} \boldsymbol{v}_a(i) & \cdots & \boldsymbol{v}_a(i+N-1) \\ \vdots & & \vdots \\ \boldsymbol{v}_a(i+j-1) & \cdots & \boldsymbol{v}_a(i+j+N-2) \end{bmatrix}, \tag{7.5}$$

$$\boldsymbol{X}_{i,N} = \begin{bmatrix} \boldsymbol{x}(i) & \cdots & \boldsymbol{x}(i+N-1) \end{bmatrix}, \tag{7.6}$$

$$\boldsymbol{\Gamma}_j = \begin{bmatrix} \boldsymbol{C} \\ \boldsymbol{CA} \\ \vdots \\ \boldsymbol{CA}^{j-1} \end{bmatrix}, \quad \boldsymbol{H}_j = \begin{bmatrix} \boldsymbol{D} & 0 & \cdots & 0 \\ \boldsymbol{CB} & \boldsymbol{D} & & \\ \vdots & & \ddots & \\ \boldsymbol{CA}^{j-2}\boldsymbol{B} & \boldsymbol{CA}^{j-3}\boldsymbol{B} & \cdots & \boldsymbol{D} \end{bmatrix}, \tag{7.7}$$

$$\boldsymbol{G}_j = \begin{bmatrix} \boldsymbol{I} & 0 & \cdots & 0 \\ \boldsymbol{CK} & \boldsymbol{I} & & \\ \boldsymbol{CAK} & \boldsymbol{CK} & \boldsymbol{I} & \\ \vdots & & \ddots & \\ \boldsymbol{CA}^{j-2}\boldsymbol{K} & \boldsymbol{CA}^{j-3}\boldsymbol{K} & \cdots & \boldsymbol{I} \end{bmatrix}, \tag{7.8}$$

$$\boldsymbol{\mathcal{E}}_{i,j,N} = \begin{bmatrix} \boldsymbol{e}(i) & \cdots & \boldsymbol{e}(i+N-1) \\ \vdots & & \vdots \\ \boldsymbol{e}(i+j-1) & \cdots & \boldsymbol{e}(i+j+N-2) \end{bmatrix}, \tag{7.9}$$

The subscript i describes the measurement of interest, and the subscript j denotes

the temporary order of the system that will allow n to be determined, which is why j is usually chosen to be greater than the estimated value of n. The subscript N is the number of columns in the Hankel matrices, typically equal to $N_m - 2j + 1$. The preceding equations are valid for any subspace provided that the required transformation matrix can be found. It is now possible to implement the PO-MOESP algorithm using the LQ factorisation of Eq. (7.10)

$$\begin{bmatrix} \boldsymbol{U}_{i,j,N} \\ \boldsymbol{U}_{0,j,N} \\ \boldsymbol{Y}_{0,j,N} \\ \boldsymbol{Y}_{i,j,N} \end{bmatrix} = \begin{bmatrix} \boldsymbol{\Lambda}_{11} & \boldsymbol{0} & \boldsymbol{0} & \boldsymbol{0} \\ \boldsymbol{\Lambda}_{21} & \boldsymbol{\Lambda}_{22} & \boldsymbol{0} & \boldsymbol{0} \\ \boldsymbol{\Lambda}_{31} & \boldsymbol{\Lambda}_{32} & \boldsymbol{\Lambda}_{33} & \boldsymbol{0} \\ \boldsymbol{\Lambda}_{41} & \boldsymbol{\Lambda}_{42} & \boldsymbol{\Lambda}_{43} & \boldsymbol{\Lambda}_{44} \end{bmatrix} \begin{bmatrix} \boldsymbol{Q}_1 \\ \boldsymbol{Q}_2 \\ \boldsymbol{Q}_3 \\ \boldsymbol{Q}_4 \end{bmatrix}. \tag{7.10}$$

The SVD of the matrix $[\boldsymbol{\Lambda}_{42} \quad \boldsymbol{\Lambda}_{43}]$ is computed as:

$$[\boldsymbol{\Lambda}_{42} \quad \boldsymbol{\Lambda}_{43}] = \mathbf{U}\boldsymbol{\Sigma}\,\boldsymbol{V}^T, \tag{7.11}$$

and the order n of the system is estimated from the gap in the singular values. Based on this order n, matrices $\boldsymbol{A}$ and $\boldsymbol{C}$ can be estimated. The quantity $\hat{\boldsymbol{C}}$ is equal to the upper n rows of $\mathbf{U}$: $\mathbf{U}(1 : N_s, 1 : n)$, and $\hat{\boldsymbol{A}}$ equals $\mathbf{U}_1^{\dagger}\mathbf{U}_2$ where $(\bullet)^{\dagger}$ denotes the Moore-Penrose pseudo-inverse, $\mathbf{U}_1$ is the $[(j-1)N_a \times n]$ upper matrix of $\mathbf{U}$: $\mathbf{U}(1 : (j-1)N_a, 1 : n)$ and $\mathbf{U}_2$ is the $[(j-1)N_a \times n]$ lower matrix of $\mathbf{U}$: $\mathbf{U}(N_a + 1 : jN_a, 1 : n)$.

The next step provides the estimation of the $\boldsymbol{B}_a$ and $\boldsymbol{D}_{as}$ matrices, based on the estimated $\boldsymbol{C}_s$ and $\boldsymbol{A}$ matrices. From Eq. (7.2a) and (7.2b), the output $\boldsymbol{v}_s(k)$ can be expressed as:

$$\boldsymbol{v}_s(k) = \boldsymbol{C}_s\boldsymbol{A}^k\boldsymbol{x}(0) + \sum_{\tau=0}^{k-1} \boldsymbol{C}_s\boldsymbol{A}^{k-1-\tau}[\boldsymbol{B}\boldsymbol{u}(\tau) + \boldsymbol{K}\boldsymbol{e}(\tau)] + \boldsymbol{D}\boldsymbol{u}(k) + \boldsymbol{e}(k) \tag{7.12}$$

Using the Kronecker product $\otimes$, Eq. (7.12) can be rewritten as follows:

$$\boldsymbol{v}_s(k) = \boldsymbol{C}\boldsymbol{A}^k\boldsymbol{x}(0) + \left[\sum_{\tau=0}^{k-1} \boldsymbol{u}(\tau)^T \otimes \boldsymbol{C}\boldsymbol{A}^{k-1-\tau}\right]\mathcal{B} + \left[\sum_{\tau=0}^{k-1} \boldsymbol{e}(\tau)^T \otimes \boldsymbol{C}\boldsymbol{A}^{k-1-\tau}\right]\mathcal{K} + \left[\boldsymbol{u}(k)^T \otimes \boldsymbol{I}_l\right]\mathcal{D} + \boldsymbol{e}(k) \tag{7.13}$$

with $\mathcal{B} = \mathrm{vec}(\boldsymbol{B})$, $\mathcal{K} = \mathrm{vec}(\boldsymbol{K})$, and $\mathcal{D} = \mathrm{vec}(\boldsymbol{D})$, where $\mathrm{vec}(\bullet)$ denotes the vector resulting from storing the columns of the matrix $(\bullet)$ on top of each other. From the above equation, the matrix $\boldsymbol{Y}_{0,N,1}$ can be expressed as:

$$\boldsymbol{Y}_{0,N,1} = \begin{bmatrix}\boldsymbol{\Gamma}_N & \mathcal{Y} & \mathcal{U}\end{bmatrix}\begin{bmatrix}\boldsymbol{x}(0)\\ \mathcal{B}\\ \mathcal{D}\end{bmatrix} + \boldsymbol{E} \tag{7.14}$$

with

$$\boldsymbol{E} = \begin{bmatrix} \boldsymbol{e}(0) \\ [\boldsymbol{e}(0)^T \otimes \boldsymbol{C}]\mathcal{K} + \boldsymbol{e}(1) \\ \vdots \\ \left[\sum_{\tau=0}^{N-2} \boldsymbol{e}(\tau)^T \otimes \boldsymbol{C}\boldsymbol{A}^{N-2-\tau}\right]\mathcal{K} + \boldsymbol{e}(N-1) \end{bmatrix}, \tag{7.15}$$

and

$$\mathcal{Y} = \begin{bmatrix} 0 \\ \boldsymbol{v}_s(0)^T \otimes \boldsymbol{C} \\ \vdots \\ \sum_{\tau=0}^{N-2} \boldsymbol{v}_s(\tau)^T \otimes \boldsymbol{C}\boldsymbol{A}^{N-2-\tau} \end{bmatrix}, \quad \mathcal{U} = \begin{bmatrix} \boldsymbol{v}_s(0)^T \otimes \boldsymbol{I}_l \\ \vdots \\ \boldsymbol{v}_s(N-1)^T \otimes \boldsymbol{I}_l \end{bmatrix}. \tag{7.16}$$

Because $\boldsymbol{x}(0)$ and $\boldsymbol{v}_s(k)$ are independent of the noise $\boldsymbol{e}(k)$, the coefficients of $\mathcal{B}$ and $\mathcal{D}$ can be retrieved, unbiased, by solving the above equation in a least squares

sense:

$$\begin{bmatrix} \boldsymbol{x}(0) \\ \mathcal{B} \\ \mathcal{D} \end{bmatrix} = \begin{bmatrix} \boldsymbol{\Gamma}_N & \mathcal{Y} & \mathcal{U} \end{bmatrix}^{\dagger} \boldsymbol{Y}_{0,N,1}, \tag{7.17}$$

with $\hat{\boldsymbol{B}}_a = \mathcal{B}$ and $\hat{\boldsymbol{D}}_{as} = \mathcal{D}$.

The above conclusion has been explained in further detail in [81], as previously mentioned. Estimations are now available of the matrices $\boldsymbol{A}$, $\boldsymbol{B}_a$, $\boldsymbol{C}_s$ and $\boldsymbol{D}_{as}$ of the desired system, represented by matrices $\hat{\boldsymbol{A}}$, $\hat{\boldsymbol{B}}_a$, $\hat{\boldsymbol{C}}_s$ and $\hat{\boldsymbol{D}}_{as}$.

7.2.2 Global vibration and global disturbance conceptualisation

The first main assumption for the next step is that all the modes of interest are observable and controllable through the sensors and actuators used. The second main assumption is that the modes are not coupled through the damping; or, if they are, the occurrence can be neglected. It will be shown that using these assumptions can lead to a very accurate approximation of the system in question.

The model dynamics for the SMI model can be obtained through the estimated $\boldsymbol{A}$ matrix, and the behaviour of the actuators and sensors can be described by the matrices $\boldsymbol{B}_a$ and $\boldsymbol{C}_s$ respectively. However, these matrices give no information about the system's displacement or velocity, nor any information about the effect of the disturbances on the system. But the question can be posed as to whether or not knowledge of the displacement $\boldsymbol{y}(n)$ and/or of the unknown disturbances $\boldsymbol{f}(n)$ are required to be able to efficiently control the entire structure. The answer comes from the spatial input/spatial output control theory [70] as it applies for several point-wise or distributed disturbances. Using this theory, new input $\boldsymbol{\Omega}$ and output $\boldsymbol{\Gamma}$ matrices are created in order to achieve global vibration reduction on the entire structure. These new matrices do not represent the actual displacement or the actual amplitude of the disturbances applied at a specific location; instead

they summarise, for each vibration mode and associated resonance frequency, the structure's global displacement/velocity, $\boldsymbol{\Gamma}$ (see Eq. (7.19b)) and the global contribution of the applied disturbances, $\boldsymbol{\Omega}$ (see Eq. (7.19b)). Further details on the application of these matrices were set out in Chapter 5. An interesting property of these matrices is that they depend only on knowledge of the system material characteristics. With this in mind, the spatial input/output control system equations can be written as follows:

$$\dot{\boldsymbol{x}}(s) = \boldsymbol{A}_{ss}\boldsymbol{x}(s) + \boldsymbol{\Omega}\tilde{\boldsymbol{f}}(s) + \boldsymbol{B}_2\boldsymbol{v}_a(s) \tag{7.18a}$$

$$\tilde{\boldsymbol{y}}(s) = \boldsymbol{\Gamma}\boldsymbol{x}(s) \tag{7.18b}$$

$$\boldsymbol{v}_s(s) = \boldsymbol{C}_2\boldsymbol{x}(s) + \boldsymbol{D}_{as}\boldsymbol{v}_a(s) \tag{7.18c}$$

where $\tilde{\boldsymbol{f}}(s)$ is a virtual disturbance force vector showing the contribution of the disturbance to each mode and $\tilde{\boldsymbol{y}}(s)$ is the spatial displacement for each mode. As seen in Chapter 5, $\boldsymbol{\Omega}$ and $\boldsymbol{\Gamma}$ can be expressed as follows:

$$\boldsymbol{\Omega}\boldsymbol{\Omega}^T = \int_{\mathcal{R}} \boldsymbol{B}_f(r)\boldsymbol{B}_f^T(r)dr \tag{7.19a}$$

$$\boldsymbol{\Gamma}^T\boldsymbol{\Gamma} = \int_{\mathcal{R}} \boldsymbol{C}_y^T(r)\,\boldsymbol{C}_y(r)dr \tag{7.19b}$$

Both previous studies of spatial input/output control [45, 70] and the theory explained in Chapter 5 have shown that $\boldsymbol{\Omega}$ and $\boldsymbol{\Gamma}$ have the following shape:

$$\boldsymbol{\Omega}_{[2n\times 2n]} = \text{diag}\Big(\boldsymbol{0}_{1\times n},\, \Phi_1, \ldots, \Phi_n\Big) \tag{7.20a}$$

$$\boldsymbol{\Gamma}_{[2n\times 2n]} = \text{diag}\Big(\Phi_1, \ldots, \Phi_n,\, \boldsymbol{0}_{1\times n}\Big) \tag{7.20b}$$

with

$$\int_{\mathcal{R}} \phi_i(r)\phi_j(r)dr = \Phi_i^2\delta_{ij} \tag{7.21}$$

The matrices of Eqs. (7.20) were obtained using the standard matrix shapes $\boldsymbol{B}_f$

and $\boldsymbol{C}_y$:

$$\underset{[2n\times N_f]}{\boldsymbol{B}_f} = \begin{bmatrix} & \boldsymbol{0}_{[n\times N_f]} & \\ \phi_1(r_{f_1}) & \cdots & \phi_1(r_{f_{N_f}}) \\ \vdots & \ddots & \vdots \\ \phi_n(r_{f_1}) & \cdots & \phi_n(r_{f_{N_f}}) \end{bmatrix}$$

$$\underset{[N_y\times 2n]}{\boldsymbol{C}_y} = \begin{bmatrix} \phi_1(r_{y_1}) & \cdots & \phi_n(r_{y_1}) & \\ \vdots & \ddots & \vdots & \boldsymbol{0}_{[N_y\times n]} \\ \phi_1(r_{y_{N_y}}) & \cdots & \phi_n(r_{y_{N_y}}) & \end{bmatrix}$$

Consequently the shape of the $\boldsymbol{A}_{ss}$ matrix is

$$\underset{[2n\times 2n]}{\boldsymbol{A}_{ss}} = \begin{bmatrix} \boldsymbol{0}_{[n\times n]} & \boldsymbol{I}_{[n\times n]} \\ -\mathrm{diag}(\omega_1^2,\ldots,\omega_n^2) & -2\mathrm{diag}(\zeta_1\omega_1,\ldots,\zeta_n\omega_n) \end{bmatrix} \tag{7.22}$$

where δ_{ij} is the Kronecker delta function, ω_i the i^{th} natural frequency, ζ_i the i^{th} damping ratio and $\mathcal{R}$ the domain of the structure where $r \in \mathcal{R}$. As previously mentioned, n is the order of the system, $r_{f\alpha}$ is the theoretical discrete location of the α^{th} disturbance ($\alpha = 1,\ldots,N_f$) and $r_{y\beta}$ is the theoretical discrete location of the β^{th} displacement point ($\beta = 1,\ldots,N_y$), if those locations were available.

The matrices $\boldsymbol{\Gamma}$ and $\boldsymbol{\Omega}$ represent the disturbance force contribution to the system for each mode, $\boldsymbol{I}$ is the identity matrix, and Φ_i^2 is equal to $\frac{1}{\rho S}$, assuming that both the density ρ and the cross-sectional area are constant through the structure. Referring back to Eqs. (7.1) of section 7.1, the unknown matrices $\boldsymbol{C}_y$ and $\boldsymbol{B}_f$ can be replaced by $\boldsymbol{\Gamma}$ and $\boldsymbol{\Omega}$ respectively to provide an equivalent experimental model of the global system displacement under any given disturbance forces.

7.2.3 Similarity transformation

Examining the block diagonal system matrix $\boldsymbol{A}_{ss}$ (see Eq. (7.22)) reveals that the states of the model derived using spatial input/output control theory are expressed in one modal subspace. The states of the model derived using SMI can also be

expressed in modal form, but not in the same modal subspace. Thus, the next step is to find the transformation that relates the SMI model subspace with that of the spatial input/output model. This transformation $\boldsymbol{T}$ allows the matrices ($[\boldsymbol{A},\ \boldsymbol{C}_s,\ \boldsymbol{B}_a,\ \boldsymbol{D}_{as}]$ and $[\boldsymbol{\Gamma},\ \boldsymbol{\Omega}]$) to be combined together in the same subspace, as shown below:

$$\boldsymbol{A} = \boldsymbol{T}^{-1}\boldsymbol{A}_{ss}\boldsymbol{T}, \quad \boldsymbol{B}_f = \boldsymbol{T}^{-1}\boldsymbol{\Omega}, \quad \boldsymbol{C}_y = \boldsymbol{\Gamma}\boldsymbol{T}. \tag{7.23}$$

SMI theory makes it possible to estimate the resonance frequencies and the damping ratios of the system in question, which then makes it possible to build an estimation of $\boldsymbol{A}_{ss}$, $\widetilde{\boldsymbol{A}}_{ss}$, based on this information. The two estimated matrices of $\boldsymbol{A}$ and $\boldsymbol{A}_{ss}$ are equivalent, and their eigenvectors must therefore be the same. Conducting an eigenvalue decomposition makes it possible to estimate the $\boldsymbol{T}$ transformation matrix $\widetilde{\boldsymbol{T}}$, assuming that no eigenvalue is equal to zero:

$$\begin{aligned} \widetilde{\boldsymbol{A}} &= \widetilde{\boldsymbol{T}}^{-1}\widetilde{\boldsymbol{A}}_{ss}\widetilde{\boldsymbol{T}} \\ \boldsymbol{V}\boldsymbol{D}\boldsymbol{V}^{-1} &= \widetilde{\boldsymbol{T}}^{-1}\acute{\boldsymbol{V}}\boldsymbol{D}\acute{\boldsymbol{V}}^{-1}\widetilde{\boldsymbol{T}} \\ \Leftrightarrow\ \boldsymbol{V}^{-1} &= \acute{\boldsymbol{V}}^{-1}\widetilde{\boldsymbol{T}} \\ \widetilde{\boldsymbol{T}} &= \acute{\boldsymbol{V}}\,\boldsymbol{V}^{-1}. \end{aligned} \tag{7.24}$$

With an estimation of the transformation $\boldsymbol{T}$ matrix now determined, as $\widetilde{\boldsymbol{T}}$ in Eq. (7.24), all the required matrices of the system in Eqs. (7.18) and (7.1) are now available.

7.3 Convex optimal truncated model

As the experimental model has a large number of states, it needs to be truncated for computational purposes and control design optimisation. The model is truncated simply by selecting the frequencies that need to be controlled. The methodology for accounting for the unmodelled modes $\boldsymbol{G}_l(s)$ has been set out in section 4.4.2 for the analytical case. The next two sections explain how the optimal truncation method can be used to calculate correcting terms when analytical information is not available. In order to easily manipulate the information contained inside the

matrices of the system, the matrices are put into modal canonical form. It is easy now to select any block diagonal corresponding to its eigenvalue. Each block in the diagonal is a 2×2 matrix containing an eigenvalue and its complex conjugate.

7.3.1 Classical optimal truncation

Moheimani and Halim [82] solve this optimisation problem using linear matrix inequality (LMI) techniques [87]. The idea is to calculate the optimal feedthrough term $\boldsymbol{D}_{opt}$ of the truncated transfer function $\widetilde{\boldsymbol{G}}(s)$ of the full experimental model $\boldsymbol{G}(s)$ by minimising the $\mathcal{H}_2$ norm of the following cost function J as set out in section 4.4:

$$J = \left\| \boldsymbol{\mathcal{W}}(s) \left(\boldsymbol{G}(s) - \widetilde{\boldsymbol{G}}(s) \right) \right\|_2^2 = \| \boldsymbol{E}_{\boldsymbol{\mathcal{W}}} \|_2^2 \tag{7.25}$$

where $\boldsymbol{\mathcal{W}}(s)$ is a band-pass filter that needs to be determined and must encompass the frequency bandwidth of interest. $\boldsymbol{G}(s)$, $\widetilde{\boldsymbol{G}}(s)$ and $\boldsymbol{\mathcal{W}}(s)$ can be written in the state-space form as:

$$\widetilde{\boldsymbol{G}}(s) = \left[\begin{array}{c|c} \boldsymbol{A} & \boldsymbol{B} \\ \hline \boldsymbol{C} & \boldsymbol{D}_{opt} \end{array}\right], \tag{7.26}$$

$$\boldsymbol{G}(s) = \left[\begin{array}{cc|c} \boldsymbol{A} & \boldsymbol{0} & \boldsymbol{B} \\ \boldsymbol{0} & \boldsymbol{A}_2 & \boldsymbol{B}_2 \\ \hline \boldsymbol{C} & \boldsymbol{C}_2 & \boldsymbol{D} \end{array}\right] \quad \text{and} \quad \boldsymbol{\mathcal{W}}(s) = \left[\begin{array}{c|c} \boldsymbol{A}_w & \boldsymbol{B}_w \\ \hline \boldsymbol{C}_w & 0 \end{array}\right] \tag{7.27}$$

The subscript 2 denotes to the states that are not taken into account in the truncated model. Using Eqs. (7.26) and (7.27), $\boldsymbol{E}_{\boldsymbol{\mathcal{W}}}$ can be simplified as follows:

$$\begin{aligned} \boldsymbol{E}_{\boldsymbol{\mathcal{W}}} &= \left[\begin{array}{c|c} \boldsymbol{A}_w & \boldsymbol{B}_w \\ \hline \boldsymbol{C}_w & 0 \end{array}\right] \times \left(\left[\begin{array}{cc|c} \boldsymbol{A} & \boldsymbol{0} & \boldsymbol{B} \\ \boldsymbol{0} & \boldsymbol{A}_2 & \boldsymbol{B}_2 \\ \hline \boldsymbol{C} & \boldsymbol{C}_2 & \boldsymbol{D} \end{array}\right] - \left[\begin{array}{c|c} \boldsymbol{A} & \boldsymbol{B} \\ \hline \boldsymbol{C} & \boldsymbol{D}_{opt} \end{array}\right] \right) \\ &= \left[\begin{array}{c|c} \boldsymbol{A}_w & \boldsymbol{B}_w \\ \hline \boldsymbol{C}_w & 0 \end{array}\right] \times \left[\begin{array}{c|c} \boldsymbol{A}_2 & \boldsymbol{B}_2 \\ \hline \boldsymbol{C}_2 & \boldsymbol{D} - \boldsymbol{D}_{opt} \end{array}\right] \end{aligned} \tag{7.28}$$

$$= \left[\begin{array}{cc|c} \boldsymbol{A}_w & \boldsymbol{B}_w\boldsymbol{C}_2 & \boldsymbol{B}_w(\boldsymbol{D}-\boldsymbol{D}_{opt}) \\ \boldsymbol{0} & \boldsymbol{A}_2 & \boldsymbol{B}_2 \\ \hline \boldsymbol{C}_w & \boldsymbol{0} & 0 \end{array}\right] = \left[\begin{array}{c|c} \bar{\boldsymbol{A}} & \bar{\boldsymbol{B}}_1\boldsymbol{D}_{opt}+\bar{\boldsymbol{B}}_2 \\ \hline \bar{\boldsymbol{C}} & 0 \end{array}\right] \tag{7.29}$$

with

$$\bar{\boldsymbol{A}} = \begin{bmatrix} \boldsymbol{A}_w & \boldsymbol{B}_w\boldsymbol{C}_2 \\ \boldsymbol{0} & \boldsymbol{A}_2 \end{bmatrix}, \bar{\boldsymbol{B}}_1 = \begin{bmatrix} -\boldsymbol{B}_w \\ 0 \end{bmatrix}, \bar{\boldsymbol{B}}_2 = \begin{bmatrix} \boldsymbol{B}_w\boldsymbol{D} \\ \boldsymbol{B}_2 \end{bmatrix} \text{ and } \quad \bar{\boldsymbol{C}} = [\boldsymbol{C}_w \ \boldsymbol{0}]$$

Using the LMI theory [87], the cost function J can be expressed as:
$J = \text{tr}\left\{\bar{\boldsymbol{C}}\boldsymbol{P}\bar{\boldsymbol{C}}^T\right\}$, where $\boldsymbol{P} = \boldsymbol{P}^T > 0$ is the solution to the Lyapunov inequality:

$$\bar{\boldsymbol{A}}\boldsymbol{P} + \boldsymbol{P}\bar{\boldsymbol{A}}^T + (\bar{\boldsymbol{B}}_1\boldsymbol{D}_{opt}+\bar{\boldsymbol{B}}_2)(\bar{\boldsymbol{B}}_1\boldsymbol{D}_{opt}+\bar{\boldsymbol{B}}_2)^T < 0 \tag{7.30}$$

According to [82], $\boldsymbol{D}_{opt}$ can be found using the following expression of the optimisation problem:

$$\min_{\boldsymbol{P},\boldsymbol{D}_{opt}} \left(\text{tr}\{\bar{\boldsymbol{C}}\boldsymbol{P}\bar{\boldsymbol{C}}^T\}\right) : \begin{cases} \boldsymbol{P} > 0, \\ \begin{bmatrix} \bar{\boldsymbol{A}}\boldsymbol{P}+\boldsymbol{P}\bar{\boldsymbol{A}}^T & \bar{\boldsymbol{B}}_1\boldsymbol{D}_{opt}+\bar{\boldsymbol{B}}_2 \\ (\bar{\boldsymbol{B}}_1\boldsymbol{D}_{opt}+\bar{\boldsymbol{B}}_2)^T & -\boldsymbol{I} \end{bmatrix} < 0 \end{cases} \tag{7.31}$$

The interesting point to note about this optimisation procedure is that it does not require an analytical solution of the system in question; it is sufficient to simply have a matricial representation.

7.3.2 New optimal truncation for high frequency

Classical optimal truncation is limited to use in systems where only low frequencies are to be controlled, while the proposed new optimal truncation can be employed for any specified bandwidth of frequencies by using the convex optimisation approach. With Eq. (4.48) and Fig. 4.4, the idea is to evaluate the optimal feedthrough term $\boldsymbol{K}_d$ and second-order term $\boldsymbol{K}_l$ of the truncated transfer function $\widetilde{\boldsymbol{G}}(s)$ of the full experimental model $\boldsymbol{G}(s)$ by minimising the $\mathcal{H}_2$ norm of the

following cost function J:

$$J = \left\| \boldsymbol{\mathcal{W}}(s) \left(\boldsymbol{G}(s) - \widetilde{\boldsymbol{G}}(s) \right) \right\|_2^2 = \| \boldsymbol{E}_{\boldsymbol{\mathcal{W}}} \|_2^2 \tag{7.32}$$

where $\boldsymbol{\mathcal{W}}(s)$ is a band-pass filter that has a unit value in $[\omega_a, \omega_c]$ with $\omega_c = \frac{\omega_{m_2} + \omega_{m_2+1}}{2}$ and $\omega_a = \frac{\omega_{m_1} + \omega_{m_1-1}}{2}$. With $\boldsymbol{G}(s)$ and $\boldsymbol{\mathcal{W}}(s)$ expressed as in Eqs. 7.27, $\widetilde{\boldsymbol{G}}(s)$ can be written in state-space form as:

$$\widetilde{\boldsymbol{G}}(s) = \left[\begin{array}{cc|c} \boldsymbol{A} & \boldsymbol{0} & \boldsymbol{B} \\ \boldsymbol{0} & \boldsymbol{A}_l & \boldsymbol{B}_l \\ \hline \boldsymbol{C} & \boldsymbol{C}_l & \boldsymbol{K}_d \end{array}\right] = \left[\begin{array}{c|c} \widetilde{\boldsymbol{A}} & \widetilde{\boldsymbol{B}} \\ \hline \widetilde{\boldsymbol{C}} & \boldsymbol{K}_d \end{array}\right] \tag{7.33}$$

As in section 7.3.1, the subscript 2 denotes the states that are not accounted for in the truncated model. For this method, the subscript l denotes the new states implied by the corrective term $\boldsymbol{K}_l$, and N_a is the number of actuators.

$$\underset{[2N_a \times 2N_a]}{\boldsymbol{A}_l} = \begin{bmatrix} \boldsymbol{0}_{[N_a \times N_a]} & \boldsymbol{I}_{[N_a \times N_a]} \\ \boldsymbol{0}_{[N_a \times N_a]} & \boldsymbol{0}_{[N_a \times N_a]} \end{bmatrix}, \underset{[2N_a \times N_a]}{\boldsymbol{B}_l} = \begin{bmatrix} \boldsymbol{0}_{[N_a \times N_a]} \\ \boldsymbol{I}_{[N_a \times N_a]} \end{bmatrix}, \tag{7.34}$$

$$\underset{[N_s \times 2N_a]}{\boldsymbol{C}_l} = \begin{bmatrix} \boldsymbol{K}_l & \boldsymbol{0}_{[N_s \times N_a]} \end{bmatrix} \tag{7.35}$$

Using Eqs. (7.27) and (7.33), $\boldsymbol{E}_{\boldsymbol{\mathcal{W}}}$ can be simplified as follows:

$$\begin{aligned} \boldsymbol{E}_{\boldsymbol{\mathcal{W}}} &= \left[\begin{array}{c|c} \boldsymbol{A}_w & \boldsymbol{B}_w \\ \hline \boldsymbol{C}_w & 0 \end{array}\right] \times \left(\left[\begin{array}{cc|c} \boldsymbol{A} & \boldsymbol{0} & \boldsymbol{B} \\ \boldsymbol{0} & \boldsymbol{A}_2 & \boldsymbol{B}_2 \\ \hline \boldsymbol{C} & \boldsymbol{C}_2 & \boldsymbol{D} \end{array}\right] - \left[\begin{array}{cc|c} \boldsymbol{A} & \boldsymbol{0} & \boldsymbol{B} \\ \boldsymbol{0} & \boldsymbol{A}_l & \boldsymbol{B}_l \\ \hline \boldsymbol{C} & \boldsymbol{C}_l & \boldsymbol{K}_d \end{array}\right] \right) \\ &= \left[\begin{array}{c|c} \boldsymbol{A}_w & \boldsymbol{B}_w \\ \hline \boldsymbol{C}_w & 0 \end{array}\right] \times \left[\begin{array}{cc|c} \boldsymbol{A}_2 & \boldsymbol{0} & \boldsymbol{B}_2 \\ \boldsymbol{0} & \boldsymbol{A}_l & \boldsymbol{B}_l \\ \hline \boldsymbol{C} & -\boldsymbol{C}_l & \boldsymbol{D} - \boldsymbol{K}_d \end{array}\right] \\ &= \left[\begin{array}{ccc|c} \boldsymbol{A}_w & \boldsymbol{B}_w \boldsymbol{C}_2 & -\boldsymbol{B}_w \boldsymbol{C}_l & \boldsymbol{B}_w(\boldsymbol{D} - \boldsymbol{K}_d) \\ \boldsymbol{0} & \boldsymbol{A}_2 & \boldsymbol{0} & \boldsymbol{B}_2 \\ \boldsymbol{0} & \boldsymbol{0} & \boldsymbol{A}_l & \boldsymbol{B}_l \\ \hline \boldsymbol{C}_w & \boldsymbol{0} & \boldsymbol{0} & 0 \end{array}\right] \end{aligned} \tag{7.36}$$

$$= \left[\begin{array}{c|c} \bar{\boldsymbol{A}} + \bar{\boldsymbol{B}}_1 \bar{\boldsymbol{C}}_l & \bar{\boldsymbol{B}}_1 \boldsymbol{K}_d + \bar{\boldsymbol{B}}_2 + \bar{\boldsymbol{B}}_l \\ \hline \bar{\boldsymbol{C}} & \boldsymbol{0} \end{array}\right] \tag{7.37}$$

with

$$\bar{\boldsymbol{A}} = \begin{bmatrix} \boldsymbol{A}_w & \boldsymbol{B}_w \boldsymbol{C}_2 & \boldsymbol{0} \\ \boldsymbol{0} & \boldsymbol{A}_2 & \boldsymbol{0} \\ \boldsymbol{0} & \boldsymbol{0} & \boldsymbol{A}_l \end{bmatrix}, \bar{\boldsymbol{B}}_1 = \begin{bmatrix} -\boldsymbol{B}_w \\ 0 \\ 0 \end{bmatrix}, \bar{\boldsymbol{B}}_2 = \begin{bmatrix} \boldsymbol{B}_w \boldsymbol{D} \\ \boldsymbol{B}_2 \\ \boldsymbol{0} \end{bmatrix}, \bar{\boldsymbol{B}}_l = \begin{bmatrix} \boldsymbol{0} \\ \boldsymbol{0} \\ \boldsymbol{B}_l \end{bmatrix}, \tag{7.38}$$

$$\bar{\boldsymbol{C}} = [\boldsymbol{C}_w \ \boldsymbol{0} \ \boldsymbol{0}] \quad \text{and} \quad \bar{\boldsymbol{C}}_l = [\boldsymbol{0} \ \boldsymbol{0} \ \boldsymbol{C}_l]$$

Using the LMI theory [87], the cost function J can be expressed as:
$J = \text{tr}\left\{\bar{\boldsymbol{C}}\boldsymbol{P}\bar{\boldsymbol{C}}^T\right\}$, where $\boldsymbol{P} = \boldsymbol{P}^T > 0$ is the solution to the Lyapunov inequality:

$$\bar{\boldsymbol{A}}\boldsymbol{P} + \boldsymbol{P}\bar{\boldsymbol{A}}^T + \bar{\boldsymbol{B}}_1\bar{\boldsymbol{C}}_l\boldsymbol{P} + \boldsymbol{P}(\bar{\boldsymbol{B}}_1\bar{\boldsymbol{C}}_l)^T + (\bar{\boldsymbol{B}}_1\boldsymbol{K}_d + \bar{\boldsymbol{B}}_2)(\bar{\boldsymbol{B}}_1\boldsymbol{K}_d + \bar{\boldsymbol{B}}_2)^T < 0 \tag{7.39}$$

According to [82], $\boldsymbol{K}_d$ and $\bar{\boldsymbol{C}}_l$ (which includes $\boldsymbol{K}_l$) can be found using the following expression of the optimisation problem:

$$\begin{gathered} \min_{\boldsymbol{P},\boldsymbol{K}_d,\bar{\boldsymbol{C}}_l} \left(\text{tr}\{\bar{\boldsymbol{C}}\boldsymbol{P}\bar{\boldsymbol{C}}^T\}\right) : \\ \boldsymbol{P} > 0, \\ \begin{bmatrix} \bar{\boldsymbol{A}}\boldsymbol{P} + \boldsymbol{P}\bar{\boldsymbol{A}}^T + \bar{\boldsymbol{B}}_1\bar{\boldsymbol{C}}_l\boldsymbol{P} + \boldsymbol{P}(\bar{\boldsymbol{B}}_1\bar{\boldsymbol{C}}_l)^T & \bar{\boldsymbol{B}}_1\boldsymbol{K}_d + \bar{\boldsymbol{B}}_2 + \bar{\boldsymbol{B}}_l \\ (\bar{\boldsymbol{B}}_1\boldsymbol{K}_d + \bar{\boldsymbol{B}}_2 + \bar{\boldsymbol{B}}_l)^T & -\boldsymbol{I} \end{bmatrix} < 0 \end{gathered} \tag{7.40}$$

The optimisation problem represented by Eqs. (7.40) is extremely difficult to compute due to the fact that the term $\bar{\boldsymbol{B}}_1\bar{\boldsymbol{C}}_l\boldsymbol{P}$ contains two objective variables, $\bar{\boldsymbol{C}}_l$ and $\boldsymbol{P}$, that are multiplied together. However, there is a simple alternative that can be used to solve this computational issue: a temporary decomposition of this MIMO system into several MISO systems; in other words, considering only one sensor at the time. In the MISO case, the transfer function $\boldsymbol{G}_{li}(s)$ can have two equivalent expressions using matrices $\boldsymbol{B}_l$ and $\boldsymbol{C}_l$ of Eqs. (7.35), where the subscript i refers

Table 7.1: Optimisation process

for $i = 1 \rightarrow N_s$

$$\min_{\boldsymbol{P},\boldsymbol{K}_{di},\bar{\mathcal{B}}_{li}} \left(\text{tr}\{\bar{\boldsymbol{C}}\boldsymbol{P}\bar{\boldsymbol{C}}^T\}\right) : \begin{cases} \boldsymbol{P} > 0, \\ \begin{bmatrix} \bar{\mathcal{A}}\boldsymbol{P} + \boldsymbol{P}\bar{\mathcal{A}}^T & \bar{\boldsymbol{B}}_1\boldsymbol{K}_{di} + \bar{\boldsymbol{B}}_2 + \bar{\mathcal{B}}_{li} \\ (\bar{\boldsymbol{B}}_1\boldsymbol{K}_{di} + \bar{\boldsymbol{B}}_2 + \bar{\mathcal{B}}_{li})^T & -\boldsymbol{I} \end{bmatrix} < 0 \end{cases}$$

end.

$\boldsymbol{K}_d = \left[K_{d1}^T \cdots K_{dN_s}^T\right]^T$

$\boldsymbol{K}_l = \left[K_{l1}^T \cdots K_{lN_s}^T\right] \Longrightarrow \boldsymbol{C}_l = [\boldsymbol{K}_l \ \boldsymbol{0}]$ and $\boldsymbol{B}_l = [\boldsymbol{0} \ \boldsymbol{I}]^T$

to the i^{th} of N_s sensors, as follows:

$$\boldsymbol{G}_{li}(s) = \boldsymbol{C}_{li}(s\boldsymbol{I} - \boldsymbol{A})\boldsymbol{B}_l = \mathcal{C}_l(s\boldsymbol{I} - \boldsymbol{A})\mathcal{B}_{li} \text{ with } \mathcal{B}_{li} = \begin{bmatrix} \boldsymbol{0} \\ \boldsymbol{K}_{li} \end{bmatrix}, \ \mathcal{C}_l = \begin{bmatrix} \boldsymbol{I} & \boldsymbol{0} \end{bmatrix}. \quad (7.41)$$

The correction term $\boldsymbol{K}_{li}$ can be placed in either the input or output matrices. For computational purposes $\boldsymbol{K}_{li}$ is initially placed in the input matrix, then relocated inside $\boldsymbol{C}_l$ to its original position once its value(s) have been calculated. The optimisation problem expressed in Eqs. (7.40) can be then reformulated, as shown in table 7.1, without the two-objective-variable multiplication problem, with

$$\bar{\mathcal{A}} = \begin{bmatrix} \boldsymbol{A}_w & \boldsymbol{B}_w\boldsymbol{C}_2 & \boldsymbol{B}_w\mathcal{C}_l \\ \boldsymbol{0} & \boldsymbol{A}_2 & \boldsymbol{0} \\ \boldsymbol{0} & \boldsymbol{0} & \boldsymbol{A}_l \end{bmatrix} \quad \text{and} \quad \bar{\mathcal{B}}_{li} = \begin{bmatrix} \boldsymbol{0} \\ \boldsymbol{0} \\ \mathcal{B}_{li} \end{bmatrix}. \quad (7.42)$$

7.3.3 Optimisation adaptation for robust control design purposes

For the design of optimal $\mathcal{H}_2$ or $\mathcal{H}_\infty$ controllers, the associated matrix $\boldsymbol{H}$, described in Eq. (7.43), needs to have full column rank, as discussed in Chapter 4:

$$\boldsymbol{H} = \begin{bmatrix} \widetilde{\boldsymbol{A}} - j\omega\boldsymbol{I} & \widetilde{\boldsymbol{B}} \\ \widetilde{\boldsymbol{C}} & \boldsymbol{K}_d \end{bmatrix} \quad (7.43)$$

However because $\widetilde{\boldsymbol{A}}$ depends on $\boldsymbol{A}_l$ in Eq. (7.33), the associated matrix $\boldsymbol{H}$ of $\widetilde{\boldsymbol{A}}$ does not have full column rank. Nonetheless, it is possible to simply replace matrix $\boldsymbol{A}_l$ with matrix $\boldsymbol{A}_{adj}$ (see Eq. (7.44)), which produces an equally accurate optimisation, as the matrix $\boldsymbol{A}_{adj}$ is included in the optimisation process.

$$\boldsymbol{A}_{adj} = \begin{bmatrix} \boldsymbol{0} & \boldsymbol{I} \\ -\omega_1^2 \boldsymbol{I} & -2\zeta_1\omega_1 \boldsymbol{I} \end{bmatrix}. \tag{7.44}$$

with ω_1 and ζ_1 representing the natural frequency and damping ratio, respectively, of the first mode. This adjustment was derived from the fact that the first mode transfer function multiplied by a gain gives an approximate contribution of all the modes with resonance frequencies below the frequency bandwidth of interest in the truncated model. This now gives the full, functional truncated experimental model for a given system, which can be used to design the optimal controller for the frequencies of interest.

The effectiveness of this correction method can be seen from the experimental data for a point sensor $\boldsymbol{v}_s(s)$ and a point actuator $\boldsymbol{v}_a(s)$ set on a cantilevered beam. The transfer function for the experimental model $\boldsymbol{G}(s)$ was determined using the SMI technique, and was then compared to the experimental transfer function $\boldsymbol{G}_{exp}(s)$, which was determined as the ratio of the cross-power spectral density P_{as} (which relates the actuator data $\boldsymbol{v}_a$ with the sensor corresponding data $\boldsymbol{v}_s$) to the power spectral density P_{aa} of actuator $\boldsymbol{v}_a$. The correctness of the transfer function $\boldsymbol{G}(s)$ occurs for 99.95% of the corresponding experimental transfer function $\boldsymbol{G}_{exp}(s)$. Fig. 7.1 shows the curves of those two functions. The next step is to truncate the full experimental model $\boldsymbol{G}(s)$ (which has 15 modes) to just the four modes of interest: from the 3^{rd} up to the 6^{th} mode. The full experimental model $\boldsymbol{G}(s)$ is compared with three truncated models: one without any correction terms $\boldsymbol{G}_r(s)$, one with only the zeroth order term of $\boldsymbol{K}_d$, and one with both terms $\boldsymbol{K}_l$ and $\boldsymbol{K}_d$. Fig. 7.2 shows the effect of the correction terms. The bandwidth of interest [100Hz to 900Hz] lies between the two vertical black lines in Fig. 7.2. The frequency response in this range is magnified to show it more clearly in Fig. 7.3.

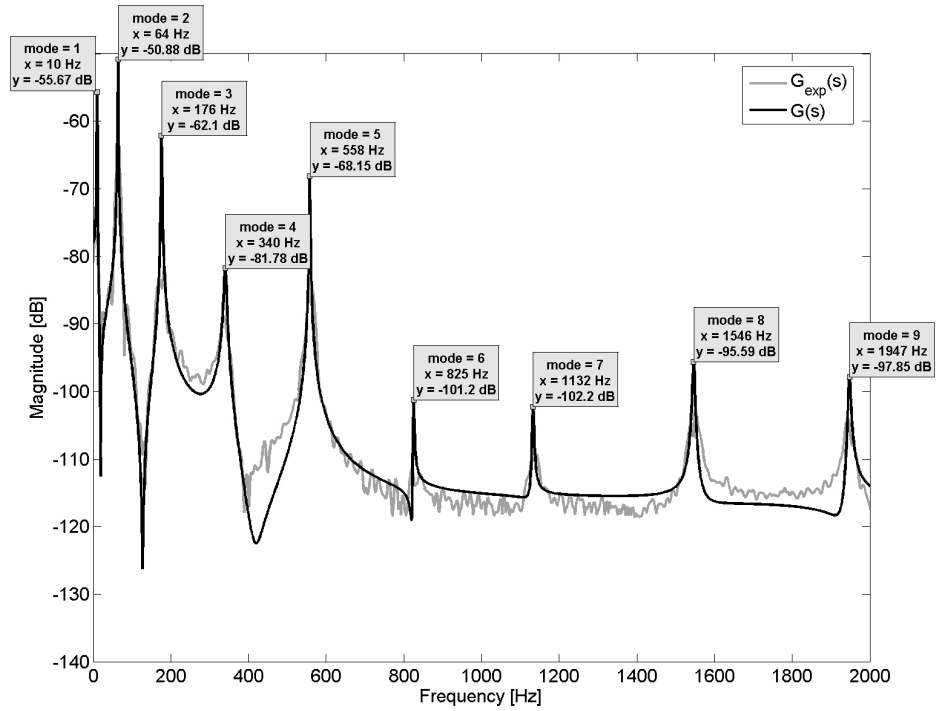

Figure 7.1: Cantilever beam sensor and actuator transfer function, $\boldsymbol{G}_{exp}(s)$: experimental transfer function, $\boldsymbol{G}_{(}s)$: experimental transfer function.

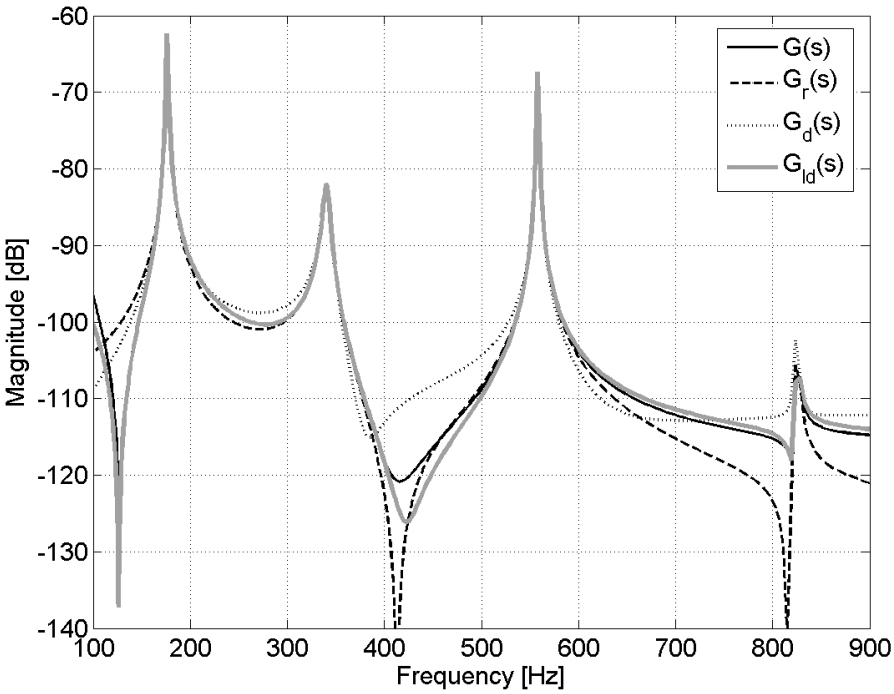

Figure 7.3: Dynamic effect of the model truncation and the corrections within the frequency bandwidth of interest [100Hz to 900Hz].

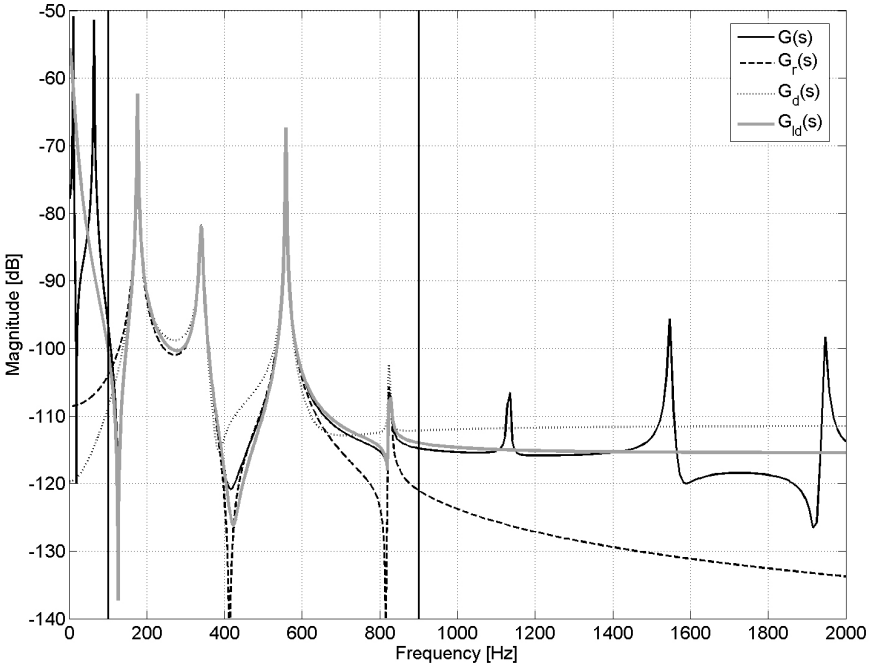

Figure 7.2: Frequency response $\frac{v_s(s)}{v_a(s)}$ due to model truncation and corrections. $\boldsymbol{G}(s)$ = the full experimental model, $\boldsymbol{G}_r(s)$ = the truncated model without any correction term, $\boldsymbol{G}_d(s)$ = the truncated model with the optimal zero-order term of $\boldsymbol{K}_d$ and $\boldsymbol{G}_{ld}(s)$ = the truncated model with both optimal terms $\boldsymbol{K}_l$ and $\boldsymbol{K}_d$.

The beneficial effect on the optimisation of using the two corrective terms described above can also be seen by comparing the zeros (or anti-resonance frequencies) of the full system with the truncated ones (knowing that the poles remain identical) as shown in Fig. 7.4: For the zeros within the frequency bandwidth of interest, the reduced model, with both the $\boldsymbol{K}_l$ and $\boldsymbol{K}_d$ terms included (square symbols), is the closest to the full experimental model $\boldsymbol{G}(s)$ (diamond symbols).

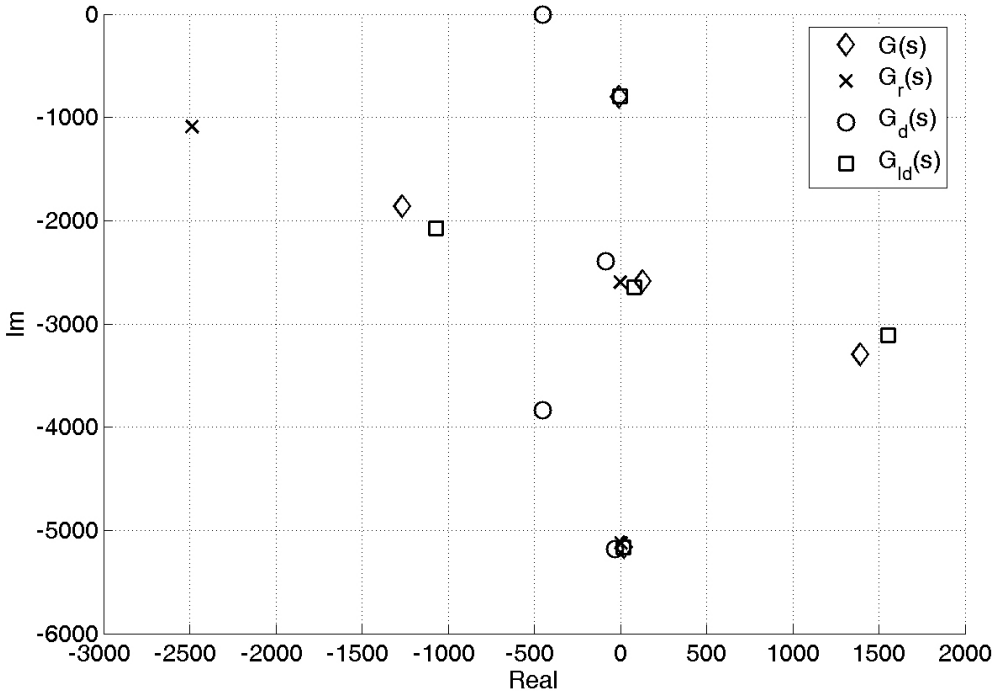

Figure 7.4: Location of zeros for various models.

7.4 Summary

A new procedure has been developed for designing a global vibration attenuation feedback controller based on a truncated experimental model that excludes both lower order and higher order modes outside the bandwidth of interest. An approximation term was developed in this chapter to account for the effect of these ummodelled modes. One advantage of the proposed approach is that obtaining the model does not require any simulation or deriving of analytical equations, but only a matricial representation of the system in question. Another advantage of the proposed approach is that the order of the plant used ($2(N_a + N)$ states) is lower than that of the plant most commonly used in control design ($2m_2$ states). Because the order of the plant partly determines the order of the controller, the proposed new method generates a lower order controller. A third advantage of the proposed approach is that the model allows control of specific modes within

a specified bandwidth without expending control effort on the lower order modes that are not of interest; something that cannot be achieved with the standard approach that includes lower order modes in the control model.

Chapter 8

VIBRATION CONTROL EXPERIMENTS FOR LOW AND HIGH FREQUENCY

This chapter seeks to validate all the new theories for vibration control set out in the previous chapters. Three experiments were conducted; the first experiment employed the spatial intput/spatial output control theory that has until now only been validated through simulations. The second experiment applied to a cantilever beam the developed global attenuate vibration methodology based on an analytical model. The final experiment applied the same methodology to a complex structure but based, this time, on experimental model.

8.1 Spatial input/output vibration control for low frequencies

This section summaries and demonstrates all the concepts, including modelling, weighting function, and $\mathcal{H}_\infty$ controller design, previously described for spatial input/output control using piezoelectric sensors and actuators. Spatial output control enables the control of global structure vibration for a given structure. The theory, developed only few years ago by Moheimani et al. [45], has already shown highly promising results. Halim [70] extended the theory by developing a way to

include the spatial input location disturbance of a system. As spatial input/output output control theory only came into existence even more recently, experimental validation is still needed to prove the theory's real-world usefulness. This first experiment, aimed at validating spatial input/output theory, was performed on a system commonly used for vibration control experiments: the cantilever beam.

8.1.1 Setup

The experimental setup for the cantilever beam is shown in Fig. 8.1. The aluminium beam possessed the following features:

Table 8.1: Properties of aluminium beam structure

Length (L)	500 mm
Width (w)	40 mm
Height (h)	3 mm
Young's modulus (E)	65×10^9 N/m^2
Density (ρ)	2650 kg/m^3

A piezoelectric actuator and a piezoelectric sensor were used on the beam, both having the characteristics and dimensions as shown in Table 8.2.

Table 8.2: Properties of piezoelectric ceramic patches

Length (L_p)	50 mm
Width (w_p)	25 mm
height (h_p)	0.25 mm
Young modulus (E_p)	$63e^9$ N/m^2
Poisson ratio (v_p)	0.3
Charge constant (d_{31})	$-1.66e^{-10}$ m/V
Voltage constant (g_{31})	$-1.15e^{-2}$ Vm/N
Capacitance (C)	$1.05e^{-7}$ F
Electromechanical coupling factor (k_{31})	0.34

It is common knowledge in the vibration control field that the optimal location for a piezoelectric actuator patch on a cantilever beam is close to the beam's clamped edge, as this is the region of highest strain [4, 9, 78]. The piezoelectric

Figure 8.1: Clamped beam.

actuator and sensor patches were therefore attached near the clamped edge on either side of the beam for this experiment.

The vibration signal from the piezoelectric sensor was processed using a National Instruments PCI 6023E acquisition card. For the piezoelectric actuator, a power amplifier with a gain set to 10 was specifically designed to provide a DC voltage of 100V, allowing the piezoelectric actuator to have a larger dynamic range without the risk of cracking. Suitable low-cost amplifiers are not commercially available, and the design of such an amplifier was no trivial exercise; as such the circuit diagram for the amplifier, based on information provided by [88], has been included in Appendix 8.3.5 for the benefit of the reader. The custom-designed power amplifier was fed by a National Instruments PCI 6713 output card.

A hand-made magnetic shaker was coupled with weightless magnet, as shown in Fig. 8.2, in order to be able to apply a point-wise disturbance on discrete locations of the beam without changing the boundary conditions. This can be contrasted with the classical shaker, which causes a clamped-free system to become more of

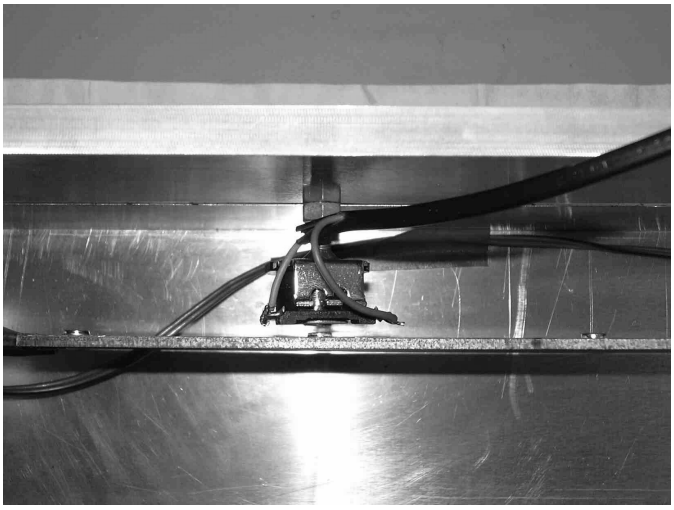

Figure 8.2: Electromagnetic shaker setup.

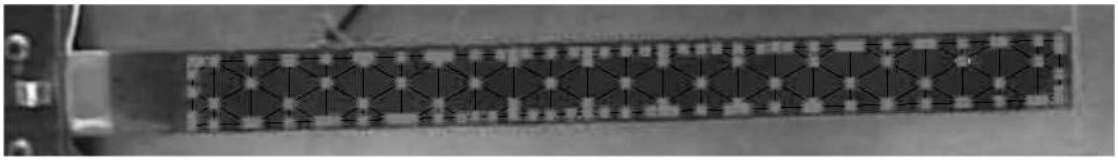

Figure 8.3: Beam meshing.

a clamped-pinned system the closer the shaker moves towards the free end of the beam.

A laser scan measured 110 points displacements on the beam. These discrete point measurements enable an analysis of the global vibration behaviour of the beam (see Fig. 8.3).

8.1.2 Controller design

The objective was to attenuate the first four modes of the system, and avoid increasing the others in the process. A state-space model was implemented under the specifications set out above and using the state-space matrices set out in chapter 4.

The model needed to be tuned to fit the particular cantilever beam in this experiment. The first four experimental and theoretical resonance frequencies are

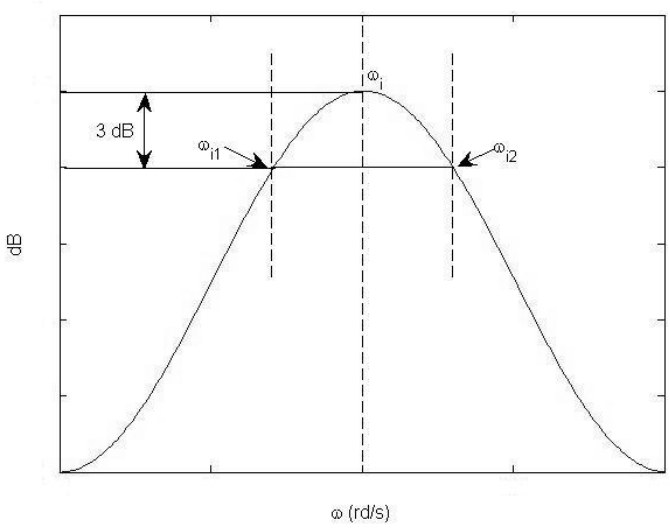

Figure 8.4: Damping ratio determination.

shown in Table 8.3.

Table 8.3: Resonance frequencies (Hz)

Mode	Theoretical	Experimental
1	9.60	10.345
2	60.16	63.375
3	168.46	175.375
4	330.12	339.75

The damping ratios (ζ_i)were determined using the following equation:

$$\zeta_i = \frac{\omega_{i1} - \omega_{i2}}{2\omega_i} \tag{8.1}$$

with ω_{i2} and ω_{i1} measured as shown in Fig. 8.4, based on [6], giving the following experimental results:

Table 8.4: Damping ratios

Mode	1	2	3	4	[5,∞[
$\zeta\,(1e^{-3})$	6	6.46	2.71	1.76	1.42

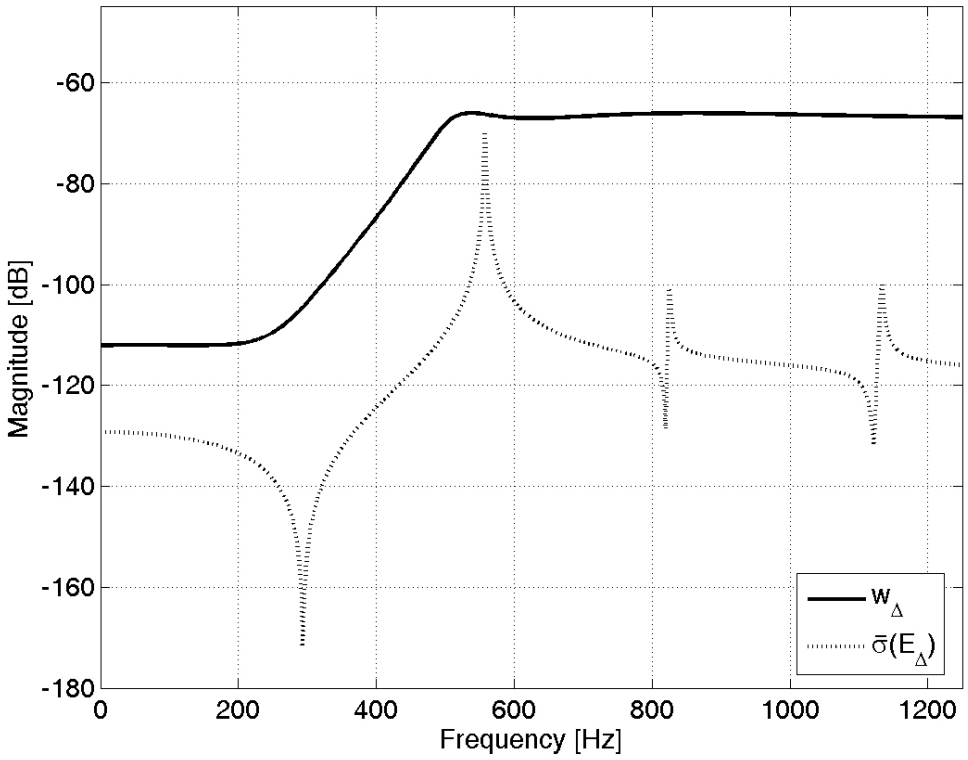

Figure 8.5: Weight functions: W_Δ weight function encompassing the spillover and $\bar{\sigma}(E_\Delta)$ norm of the error.

These experimental results were taken into account in the design of an appropriate controller. A high-pass filter after the 4^{th} frequency mode (339.75 Hz) was used to account for unmodelled modes due to truncation of the analytical model as shown in Fig 8.5. For this experiment, this high-pass filter was generated using Matlab signal processing toolbox. The Matlab elliptic filter was chosen to shape the weight function.

The $\mathcal{H}_\infty$ controller K was found using the Matlab Robust Control toolbox or, more specifically, the function *hinfsyn*. This function gives a continuous $\mathcal{H}_\infty$ controller, which was discretised, again using a Matlab function *c2d*. It was verified that the resulting controller met the Robust Stability and Robust Performance criteria. Because the real-time system had a high sample frequency (10kHz) com-

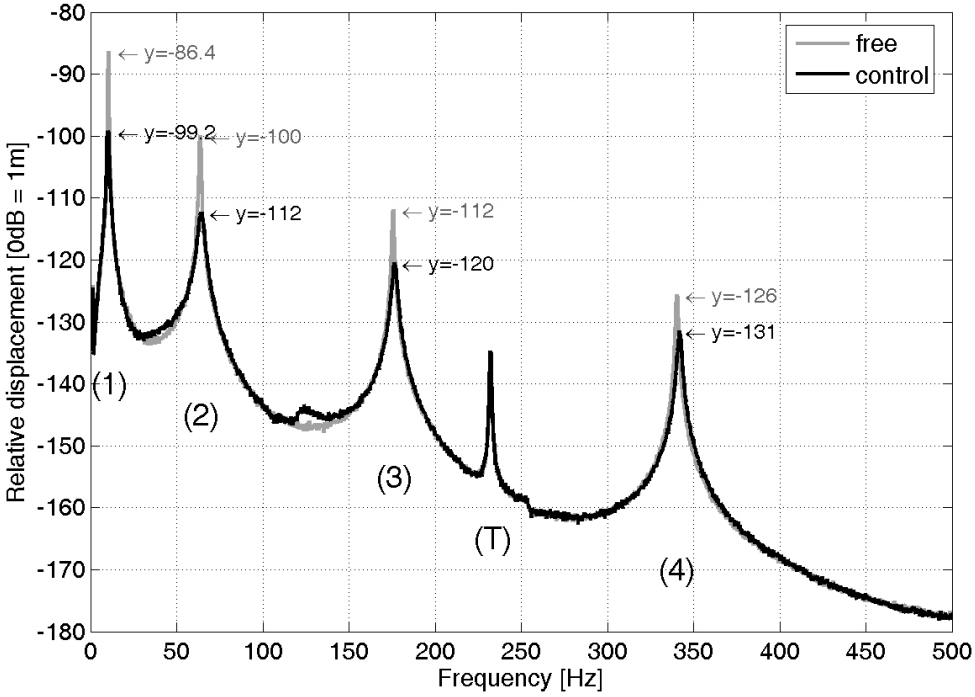

Figure 8.6: Average spectrum of the beam displacement.

pared to the frequencies of interest (0 to 400Hz), the small time delay between data acquisition and process output data was not considered. Consequently, the performance of all controllers was slightly degraded.

8.1.3 Experimental results

The displacement of each point along the beam (see Fig. 8.3) was acquired, and an average spectrum of all the points was built to evaluate the spatial vibration attenuation of the beam. The spectral curve is not shown after 500Hz because the two curves remain the same beyond this frequency. Table 8.5 summaries the key results illustrated in Fig. 8.6. It should be noted that each of the targeted modes has been attenuated.

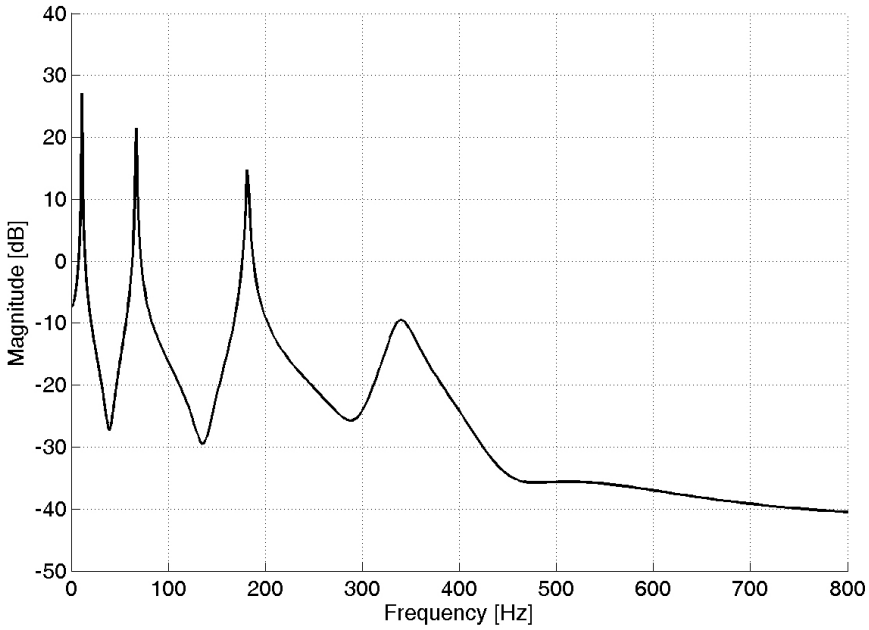

Figure 8.7: Controller gain.

Table 8.5: Attenuation, in dB

Mode	1	2	3	Torsional	4
Attenuation [dB]	12.6	12	8	0	5

As the clamping of the beam was not perfect, torsional modes (denoted by (T)) appeared in the transfer function of the system. The torsional mode located between the 3^{th} and 4^{th} mode did not create any undesirable interferences in the controlled system as it did not fall close to any frequencies of interest. Looking at the controller gain design, Fig. 8.7, it was expected that the two first modes would be more attenuated than the 3^{th} and the 4^{th}.

8.1.4 Experiment 1 - summary

The first experiment achieved its objective: to demonstrate, for the first time, spatial input/output in a real-world experiment. Results from the experiment showed promise for the viability of spatial input/output control outside of simula-

tion applications. Future research efforts could seek to validate the efficiency and robustness of spatial input/output control for when the location of the disturbance point varies along the beam.

8.2 Analytical model-based spatial output vibration control for high frequencies

The purpose of the following section is twofold: first, to set out a generalisable procedure for the design of a viable robust control system for high frequency, spatial vibration control; and second, to apply the control system procedure to spatially attenuate the vibration of a cantilever beam, subjected to a point-wise, broadband disturbance, for frequencies between the 4^{th} resonance frequency (342Hz) and the 7^{th} resonance frequency (1125Hz), using one piezoelectric sensor and one piezoelectric actuator. The uni-dimensionality of this example is ideal for its simplicity while still being a complete application. The performance of the spatial control system was measured using a scanning laser vibrometer, which measures vibration velocities at discrete points according to a predefined structural mesh. Each step in the procedure for designing the control system has been illustrated in being applied to the cantilever beam.

8.2.1 Setup

The experiment was performed on a cantilever beam as shown in Fig. 8.8. The truncated model is based on Chapter 4 and its transfer function is shown in the figures of section 4.4.2. The aluminium beam possessed the features described in Table 8.1 and was used in the same setup as section 8.1; however, because the position of the beam was not exactly the same for both experiments, the resonance frequencies of the cantilever beam system in experiment 8.1 are not identical to those in this experiment.

An active controller was designed to control the 4^{th}, 5^{th}, 6^{th} and 7^{th} bending modes within a bandwidth of [330Hz to 1.15kHz]. It is important to note that

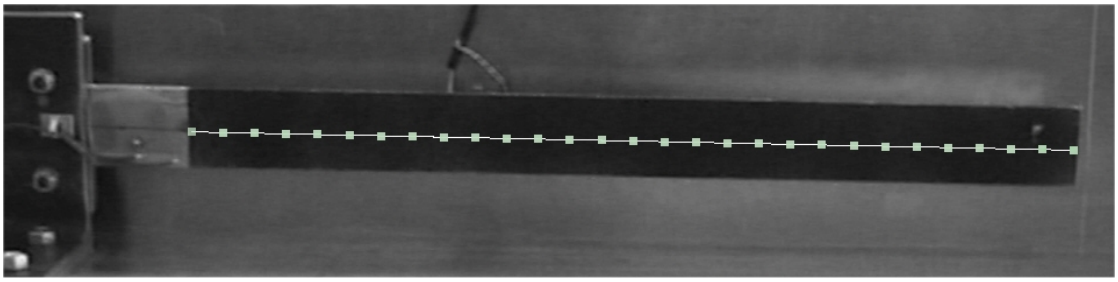

Figure 8.8: A clamped beam with the mesh used by the scanning laser vibrometer.

experiment did not set out with the goal of controlling the highest frequency possible with the available equipment. The properties of the piezoelectric sensor and the actuator used for the controller input and output are described in Table 8.2.

The real-time process for implementing the controller was the same as in the first experiment. A point-wise disturbance was applied at a discrete location of the beam (0.2m from the clamp) using an electromagnetic shaker coupled with a magnet of negligible weight attached to the beam. This electromagnetic shaker was used so that a non-contact disturbance excitation could be generated on the structure.

Vibration velocities were measured, using a Polytech PSV 400 scanning laser vibrometer, at 29 discrete points along the beam as shown in Fig. 8.8. Because vibration control is always more efficient at the location of the sensor/actuator, this region of the beam was deliberately omitted in the determination of global vibration attenuation. Had this part of the beam included, it could be argued that the displacement average would have been biased by the vibration attenuation result from the sensor location.

8.2.2 Controller design

In this experiment, the spatial output concept is extended for application to specified high frequency bandwidth. The objective of spatial $\mathcal{H}_\infty$ output control is to

achieve a controller that minimises the following cost function [45]:

$$\mathcal{J}_\infty = \frac{\int_0^\infty \int_{\mathcal{R}} y(t,r)^T Q(r) y(t,r) dr dt}{\int_0^\infty \int_{\mathcal{R}} f(t)^T f(t) dr dt}. \tag{8.2}$$

where $\mathcal{R}$ is the structural domain of interest, which in this case is the length of the beam L, and $Q(r)$ is the spatial weighting function describing the structural region of interest (for more details on spatial output control see chapter 5).

Thus, the cost function, in this case, represents the spatial output energy over the entire structure. It can be shown that spatial $\mathcal{H}_\infty$ output control requires the modification described by Eq. (8.3), which makes the controller independent of the location of the displacement r.

$$\tilde{\boldsymbol{y}}(s) = \boldsymbol{\Pi}_c \boldsymbol{x}_c(s) + \boldsymbol{\Theta}_{11c} f(s) + \boldsymbol{\Theta}_{12c} \boldsymbol{v}_a(s) \tag{8.3}$$

with matrices $\boldsymbol{\Pi}_c$, $\boldsymbol{\Theta}_{11c}$ and $\boldsymbol{\Theta}_{12c}$ determined from $\boldsymbol{\Gamma} = [\boldsymbol{\Pi}_c \; \boldsymbol{\Theta}_{11c} \, \boldsymbol{\Theta}_{12c}]$ detailed in Eq. (8.4).

$$\boldsymbol{\Gamma}^T \boldsymbol{\Gamma} = \int_{\mathcal{R}} \begin{bmatrix} \boldsymbol{C}_{1c}^T(r) \\ \boldsymbol{D}_{11}^T(r) \\ \boldsymbol{D}_{12}^T(r) \end{bmatrix} Q(r) \left[\boldsymbol{C}_{1c}(r) \; \boldsymbol{D}_{11}(r) \; \boldsymbol{D}_{12}(r) \right] dr. \tag{8.4}$$

In this experiment, the aim was to achieve global vibration attenuation of the entire structure, so a uniform spatial weighting $Q(r)$ is chosen equal to one, based on the new analytical optimised model (see section 4.4.2). Using $\boldsymbol{C}_{1c}(r)$, $\boldsymbol{D}_{11}(r)$ and $\boldsymbol{D}_{12}(r)$ described in Chapter 4 and using the modes' orthogonality properties of the beam: $\int_0^L \phi_i(r)\phi_j(r)dr = \Phi_i^2 \delta_{ij}$ with $\phi_i(r)$ is the i^{th} eigenfunction of the

structure, and the following matrices were obtained:

$$\mathbf{\Pi}_c = \begin{bmatrix} \mathbf{\Pi} & \boldsymbol{O}_{[2N\times(N_f+Na)]} & \boldsymbol{O}_{[2N\times(N_f+Na)]} \\ \boldsymbol{O}_{[(N_f+Na)\times 2N]} & \mathbf{\Xi} & \boldsymbol{O}_{[(N_f+Na)\times(N_f+Na)]} \\ \boldsymbol{O}_{[(N_f+Na)\times 2N]} & \boldsymbol{O}_{[(N_f+Na)\times(N_f+N_a)]} & \boldsymbol{O}_{[(N_f+Na)\times(N_f+N_a)]} \end{bmatrix}, \tag{8.5}$$

$$\mathbf{\Pi} = \mathrm{diag}(\Phi_1, \ldots, \Phi_N, \boldsymbol{O}_{1\times N}) \quad , \quad \mathbf{\Xi}^T\mathbf{\Xi} = \begin{bmatrix} \boldsymbol{K}_{dfy}^T\boldsymbol{K}_{dfy} & \boldsymbol{K}_{dfy}^T\boldsymbol{K}_{day} \\ \boldsymbol{K}_{day}^T\boldsymbol{K}_{dfy} & \boldsymbol{K}_{day}^T\boldsymbol{K}_{day} \end{bmatrix} \tag{8.6}$$

and

$$\mathbf{\Theta}_{11c} = \begin{bmatrix} \boldsymbol{O}_{[(2N+N_f+N_a)\times N_f]} \\ \mathbf{\Theta}_f \\ \boldsymbol{O}_{[N_a\times N_f]} \end{bmatrix} \tag{8.7}$$

with

$$\mathbf{\Theta}_f = \frac{1}{\gamma}\left\{\sum_{\notin} \boldsymbol{F}_i^2\left[\frac{1}{\omega_i^2}\ln\left\{\frac{(\omega_c+\omega_i)|\omega_a-\omega_i|}{|\omega_c-\omega_i|(\omega_a+\omega_i)}\right\}\left(1-\frac{\varpi}{\beta\omega_i^2}\right)-\frac{\varpi^2}{\beta\omega_i^2}\right]^2\right\}^{1/2} \tag{8.8}$$

$$\tag{8.9}$$

and here $\underset{[N_f\times N_f]}{\boldsymbol{F}_i^2} = \Phi_i^2[\phi_i(r_{f_1}) \ \ldots \ \phi_i(r_{f_{N_f}})]^T[\phi_i(r_{f_1}) \ \ldots \ \phi_i(r_{f_{N_f}})] = \Phi_i^2\phi_i^2(r_{f_1})$. The matrices $\mathbf{\Pi}_c$, $\mathbf{\Theta}_{11c}$ and $\mathbf{\Theta}_{12c}$ have to be modified from section 5.2.3 to fit the new optimised analytical model. In this experiment, $N_f = 1$ as only a single point-wise disturbance source was considered.

$$\mathbf{\Theta}_{12c} = \begin{bmatrix} \boldsymbol{O}_{[(2N+N_f+N_a)\times N_f]} \\ \boldsymbol{O}_{[N_f\times N_a]} \\ \mathbf{\Theta}_a \end{bmatrix} \tag{8.10}$$

where $\mathbf{\Theta}_a$ is the same expression as $\mathbf{\Theta}_f$ with the following substitution: $\underset{[N_a\times N_a]}{\boldsymbol{F}_i^2} = \Phi_i^2\mathbf{P}_i^T\mathbf{P}_i$. In this way, spatial control can be performed for a specified bandwidth, but it should be noted that matrix $\mathbf{\Xi}$ is not easy to determine, even though it is

symmetrical. However, it will be shown later in this section why it may not be necessary to include $\boldsymbol{\Xi}$, $\boldsymbol{\Theta}_{12c}$ or $\boldsymbol{\Theta}_{11c}$ in the control design.

One advantage of the proposed control approach is that the order of the plant used ($2(N_f + N_a + N)$ states) is lower than that of control design most commonly used plant ($2m_2$ states). For example, if one wants to control, using a single actuator, the vibration of the 5^{th} and 6^{th} modes due to a single disturbance input, then $N_f = 1$, $N = 2$, $N_a = 1$ and $m_2 = 6$. Thus, the standard model would require 12 states, and the proposed model only 8. Since the order of the controller is given by the sum of the order of the plant and the order of the weighting function used, the proposed method would generate a lower order controller.

Another advantage of the proposed approach is that it enables the control of specific modes within a bandwidth without exerting unnecessary control effort on lower order modes which are not of interest. In this sense, the standard approach is less efficient as it includes those lower order modes in the controller design. Although an order reduction procedure could be performed on the higher order controller produced by the standard approach, the stability of the closed-loop system would be negatively affected as a result.

It can be seen that the first N terms of the output $\tilde{\boldsymbol{y}}$ in Eq. (8.3) represent the modal contribution of each mode in the spatial input/output state-space representation. In the experiment under consideration, weight coefficients (as illustrated in Fig. 8.9 (b)) could be placed on these outputs in order to distribute the controller energy in the most efficient way. This was made possible using the spatial output control approach. The other outputs from the $(N + 1)^{th}$ term to the $(2N + N_a + N_f)^{th}$ term of the output $\tilde{\boldsymbol{y}}$ are the residual outputs, whose contribution to the overall control design is less significant than that of the previous outputs (that is, of the first N terms of $\tilde{\boldsymbol{y}}$). This means that $\boldsymbol{\Xi}$, $\boldsymbol{\Theta}_{11c}$ and $\boldsymbol{\Theta}_{12c}$ can be ignored in this control design without sacrificing the control performance. Because it was desirable to have a homogenous distribution of controller energy across the four modes of interest is desired, the weight functions at the output of the spatial system were set to unity: $w_1 = w_2 = w_3 = w_4 = 1$.

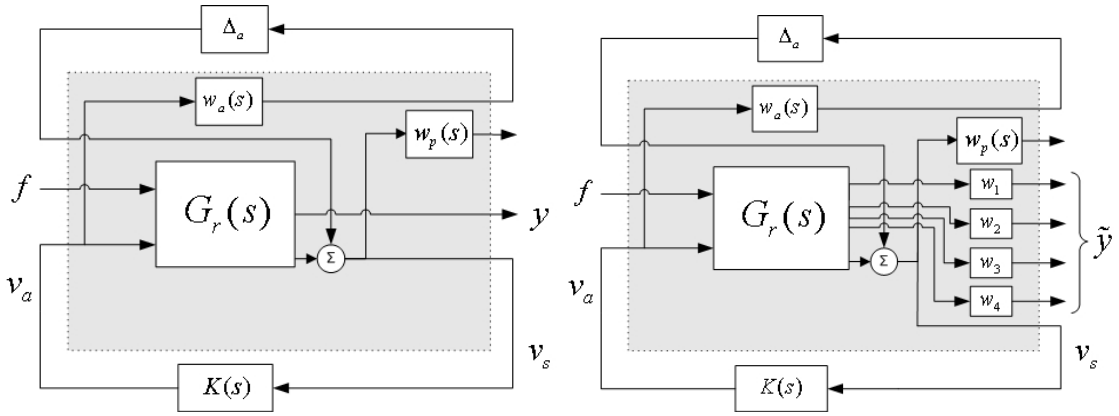

(a) Standard approach (b) Spatial approach with frequency weight

Figure 8.9: Control diagram for high frequency $\mathcal{H}_\infty$ control.

An analytical model was deliberately truncated to produce the model used for the control design, which resulted in the exclusion of some dynamic effects that can be represented using uncertainty functions. In the experiment being considered, the unmodelled dynamic is represented in the form of additional uncertainty, which can be expressed as $\boldsymbol{G}(s) \simeq \boldsymbol{G}_r(s) + \boldsymbol{\Delta}_a \boldsymbol{W}_a(s)$, where $\boldsymbol{G}_r(s)$ is the truncated plant, $\|\boldsymbol{\Delta}_a\|_\infty \leq 1$, $\boldsymbol{G}(s)$ the full model, and $\boldsymbol{W}_a(s) = \text{diag}(W_{a_1}, ..., W_{a_{N_a}})$ as previously detailed (see section 6.3).

For a MIMO system, the objective of $W_{a_i}(s)$ is to encompass the unmodelled dynamics $\boldsymbol{E}_{a_i}(s) = \boldsymbol{G}_i(s) - \boldsymbol{G}_{r_i}(s)$ due to the truncation between the i^{th} actuator and the outputs as shown in Fig. 8.10. The largest singular value of $\boldsymbol{E}_{a_i}(s)$ is measured to determined the shape of $W_{a_i}(s)$, $|W_{a_i}(\omega)| \geq \bar{\sigma}(\boldsymbol{E}_{a_i}(\omega))$. In this experiment, as $N_a = 1$ and $N_s = 1$, then $\boldsymbol{W}_a(s) = W_{a_1}(s) = W_a(s)$ and $\boldsymbol{E}_a(s) = \boldsymbol{E}_{a_1}(s)$. The unmodelled uncertainty function $W_a(s)$ was introduced in order to account for the spillover. $W_a(s)$ describes a band-stop filter encompassing the lowest and highest order modes of interest; that is, the 4^{th} to the 7^{th} (between 342 Hz and 1125 Hz). For this experiment, a band-stop filter was not taken directly from the Matlab functions available because the Matlab filters are not very adjustable in terms of magnitude of the gain over the band-stop. Instead, a minimum-phase

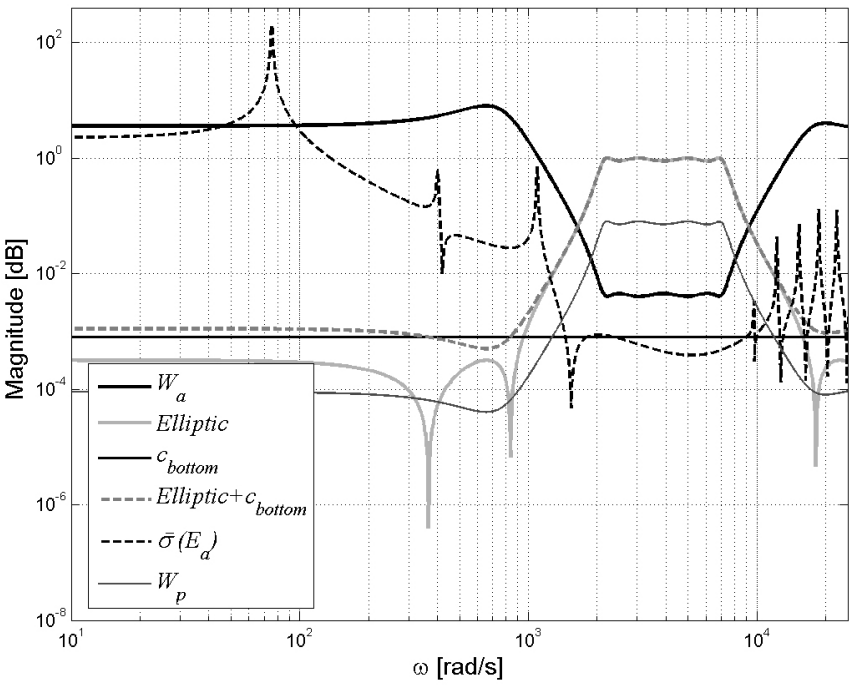

Figure 8.10: Weight functions: (1) W_a weight function encompassing the spillover, (2) *Elliptic* first step of the band-pass filter construction, (3) c_{bottom} constant to flatten the ripples, (4) $Elliptic + c_{bottom}$ minimum-phase band-pass filter, (5) $\bar{\sigma}(\boldsymbol{E}_a(s))$, (6) $\mathcal{H}_\infty$ norm of the error and (7) W_p performance weight function equal at $c_p(Elliptic + c_{bottom})$.

band-pass filter was generated, smoothed and then inverted to produce a band-stop filter.

The following describes in greater detail how the band-stop filter used in this experiment was derived. The order of the filter defines the sharpness of the band-pass and a 4^{th} order filter was chosen as the highest possible to produce a good compromise between the sharpness of the band-pass and the required shape required for encompassing the error shape. The band-pass corner frequencies were set at the 4^{th} and the 7^{th} resonance frequencies of 342Hz and 1125Hz respectively. The band-stop corner frequencies were set at 332Hz and 1325Hz. It was chosen to have a 1dB ripple in both the band-pass and band-stop and it was decided that the

band-stop would be 70dB lower than the peak value in the band-pass (see curve *Elliptic* in Fig. 8.10). The resulting band-pass filter had ripples in the band-stop part, and so a constant c_{bottom} (see Fig. 8.10) was introduced to flatten them; this constant was determined by trial and error to be 8×10^{-4}. From the resulting band-pass filter, a minimum-phase filter was extracted (see curve $Elliptic + c_{bottom}$ in Fig. 8.10) and this filter was then inverted to produce the desired band-stop. A gain $c_{tune} = 2 \times 10^{-3}$ was determined by trial and error so that the final filter W_a would encompass the error shape $\bar{\sigma}(\boldsymbol{E}_a(s))$ (see W_a in Fig. 8.10). It should be noted that a compromise was made so that the filter W_a did not cover for $\bar{\sigma}(\boldsymbol{E}_a(s))$ at the first resonance frequency, as can be seen in Fig 8.10. This allowed W_a to be shaped for achieving good spillover performance at most frequencies without an unnecessary use of higher order filtering.

The impact of the first resonance on the spillover is minimised by the inclusion of the performance filter W_p, which minimises the control energy expended at low frequencies. It will be shown in the experiment that this control design approach produced efficient control performance without significant spillover. The inverse of the minimum-phase band-pass filter (see curve $Elliptic + c_{bottom}$) was multiplied by a gain c_p to define the weight function $W_p(s)$ which determines the controller performance. Trial and error gave the optimum $c_p = 8 \times 10^{-2}$ (see curve W_p in Fig. 8.10).

8.2.3 Experimental results

The vibration levels at 29 points across the beam were measured using the laser vibrometer for the cases with control and without. Fig. 8.12 and 8.13 show the average spectrum of the displacements at those 29 points. From these figures, it can be seen that the proposed controller succeeded in attenuating the beam's vibration occurring at the 4^{th}, 5^{th}, 6^{th} and 7^{th} bending modes. By contrast, the controller did not have any significant effect on any other bending modes. Several torsional modes were also observed, identified as (T) in Fig. 8.13; however, these were not affected by the controller except for a slight effect on the one inside the frequency bandwidth to be controlled. Table 8.6 describes the vibration attenua-

Table 8.6: Attenuations for each mode

Mode	1	2	3	T	4	5	T	6	7	8
Attenuation [dB]	0.0	0.5	0.0	0.5	9.0	9.0	1.0	5.0	3.0	0.5

tion achieved at each resonance frequency mode, rounded to the nearest 0.5 dB. It was expected that the vibration attenuation of the 6^{th} and 7^{th} modes would not be as high as that of the 4^{th} and 5^{th} modes, as 6^{th} and 7^{th} modes were known to be less controllable and observable from simulations conducted outside this thesis.

Fig. 8.11 shows the effect of the controller on the maximum displacement amplitude of the beam for the four modes resonant in the frequency bandwidth of interest. For the remainder of the modes, there was no significant differences between the controlled and un-controlled beam.

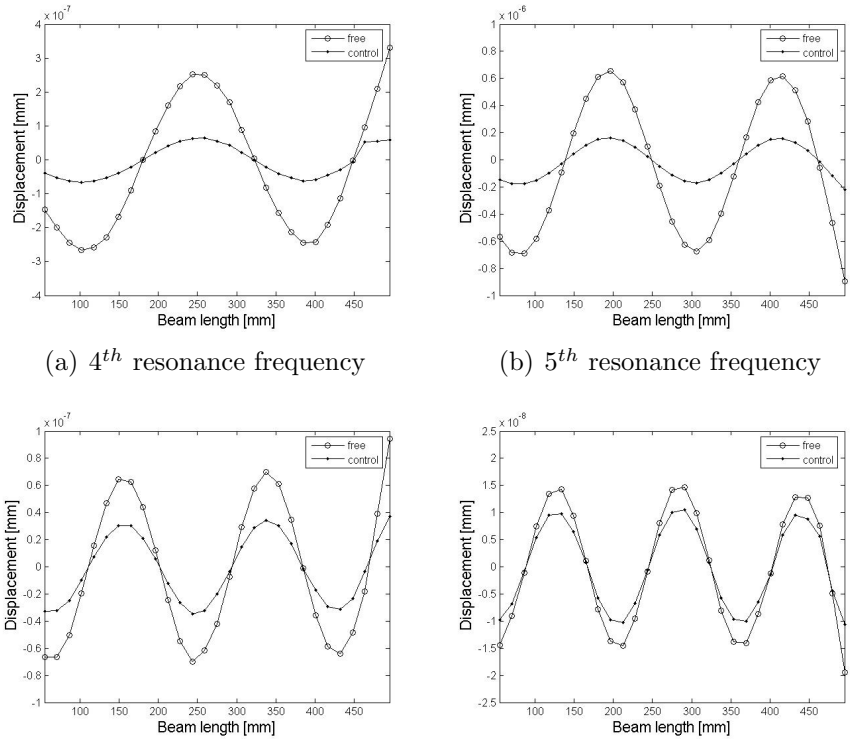

(a) 4^{th} resonance frequency (b) 5^{th} resonance frequency

(c) 6^{th} resonance frequency (d) 7^{th} resonance frequency

Figure 8.11: Displacement of the beam at the 4 controlled frequencies, with control and without.

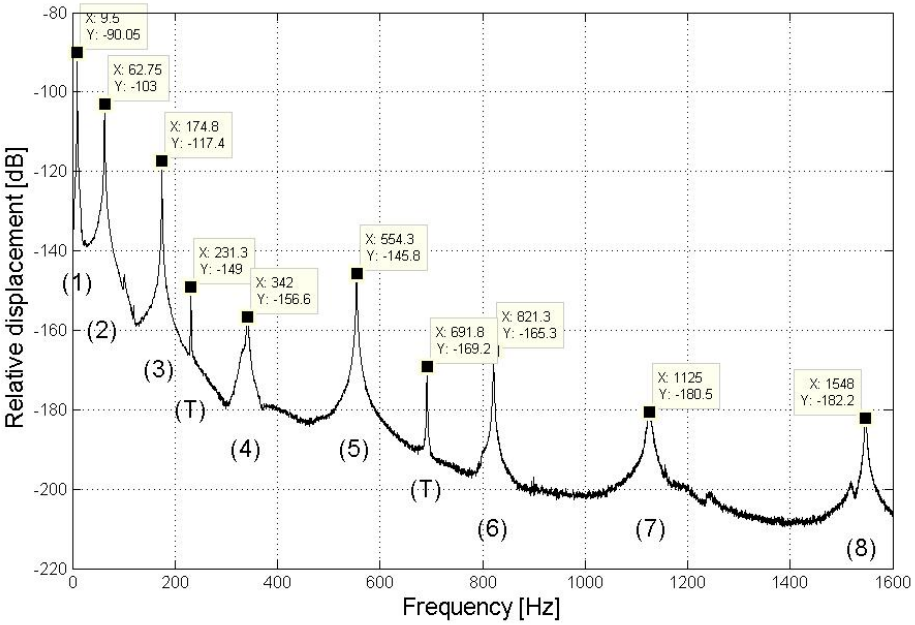

Figure 8.12: Average spectrum of the beam displacement without control.

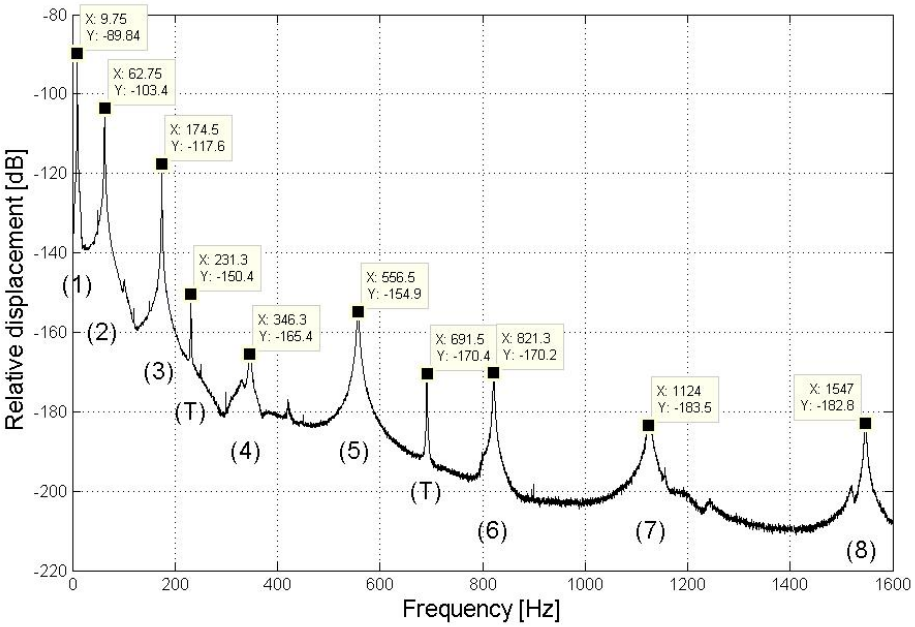

Figure 8.13: Average spectrum of the beam displacement with control.

8.2.4 Experiment 2 - summary

This section has presented new control design for high frequency control over a specified bandwidth using a lower order plant with corrective terms. The proposed method has enabled a lower order plant to be used, which consequently lowers the order of the obtained optimal controller. This new control design also enables the controller energy to be concentrated inside a specified frequency bandwidth. Experiments on a cantilever beam demonstrated the effectiveness of the proposed approach in controlling vibration due to vibration modes within the high frequency bandwidth of interest. The final experiment attempts to implement the same control method on a more complex structure.

8.3 Experimental model-based vibration control for high frequencies

The following section provides results from a high frequency (all above 800Hz) vibration control experiment on an irregularly shaped shell to demonstrate the effectiveness of the global vibration attenuation control approach proposed in Chapter 7.

8.3.1 Setup

The experiment was performed on a shell with a general shape similar to a half loaf of bread. One sensor (accelerometer) and one actuator (inertial shaker) were used for this experiment, with the disturbance being generated by a standard shaker. Fig. 8.14 shows a simplified diagram of the shell (represented by an ellipsoid), as well as the location of the sensor, actuator, disturbance and the control area of interest. The shell was made of steel, and its general features are described in Table 8.7.

The performance of the global vibration attenuation of the system was measured using a scanning laser vibrometer, which measures vibration displacement/velocity at discrete points according to a predefined structural mesh. Vibration velocities

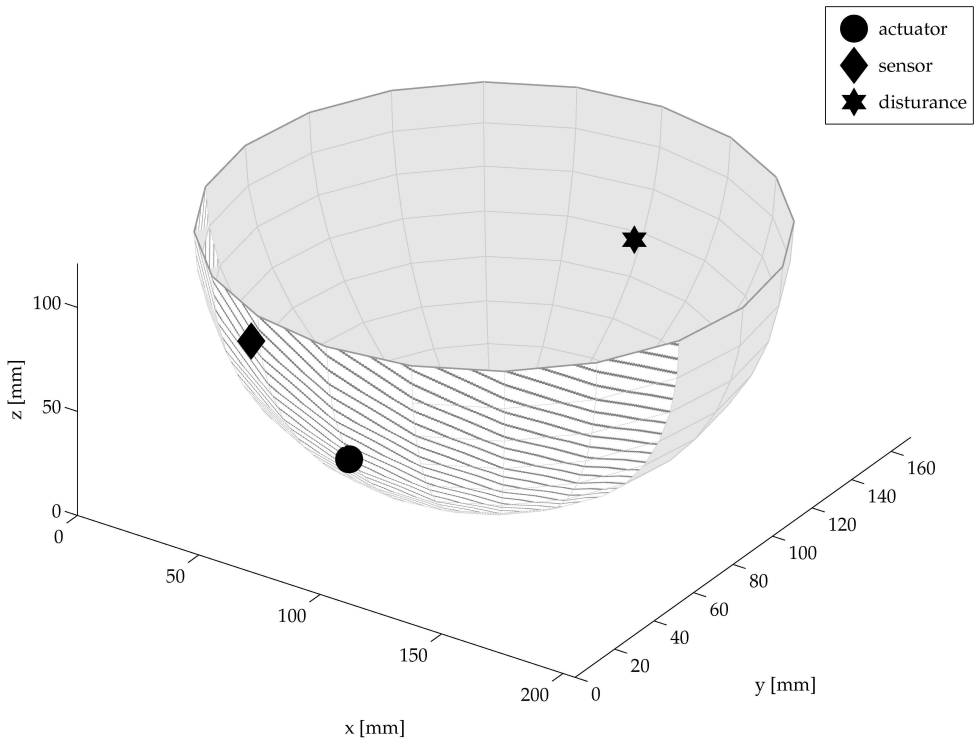

Figure 8.14: Simplified diagram of the structure showing the position of the sensor, actuator and disturbance and the zone scanned by the laser (hatched part of the shell).

were measured at 210 discrete points along the shell segment as shown in Fig. 8.15, using the same scanning laser vibrometer as in the previous experiments. The diagram shows the connection between each mesh point and the interpolated surface created by each set of points, much like a finite element model of the structure. The diagram also shows the locations of the sensor and actuator in the meshing. No measurements were taken from the area covered by shaker actuator, which is the reason for the large surface of interpolation in the region of the shaker (see point • in Fig. 8.15). The positions of the actuator and sensor were intuitively chosen, which meant that not all the important vibration modes were controllable and observable with this configuration, as will later be shown.

Table 8.7: Properties of Shell structure

x radius[1]	102 mm
y radius[1]	85 mm
Height[1] (h)	120 mm
Thickness[2] (t)	3 mm
Young's modulus (E)	209×10^9 N/m^2
Density (ρ)	8000 kg/m^3

[1] as the shell is irregular, this is just an order of magnitude
[2] on average

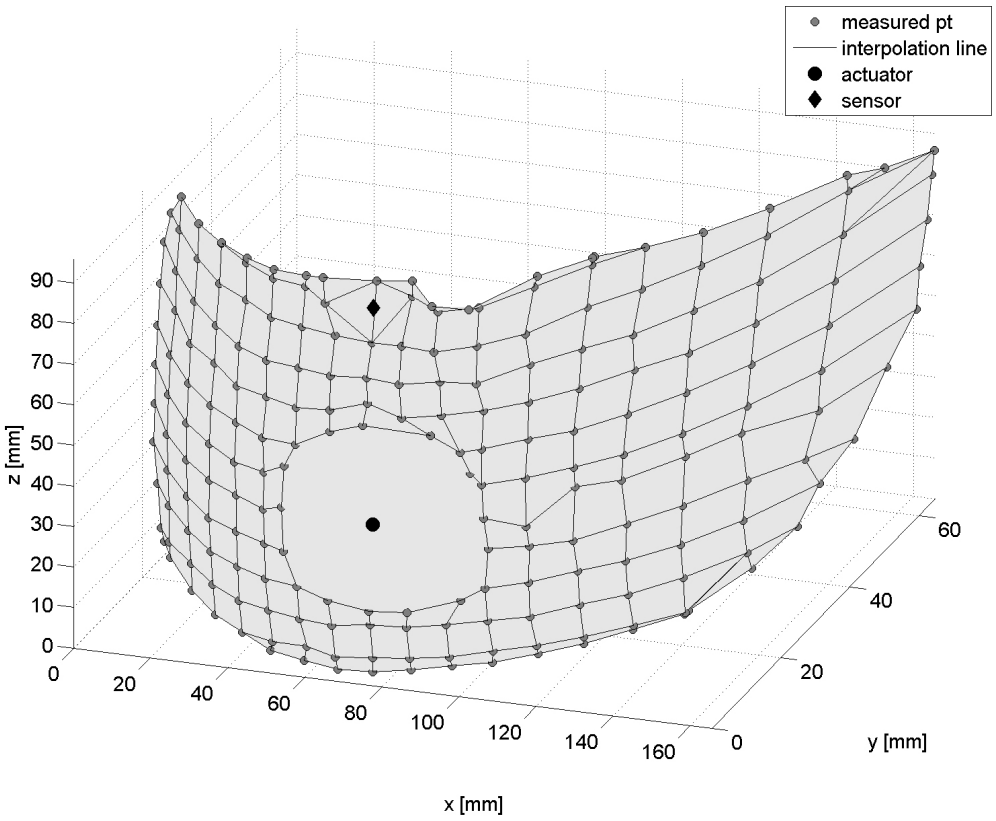

Figure 8.15: Laser scan meshing.

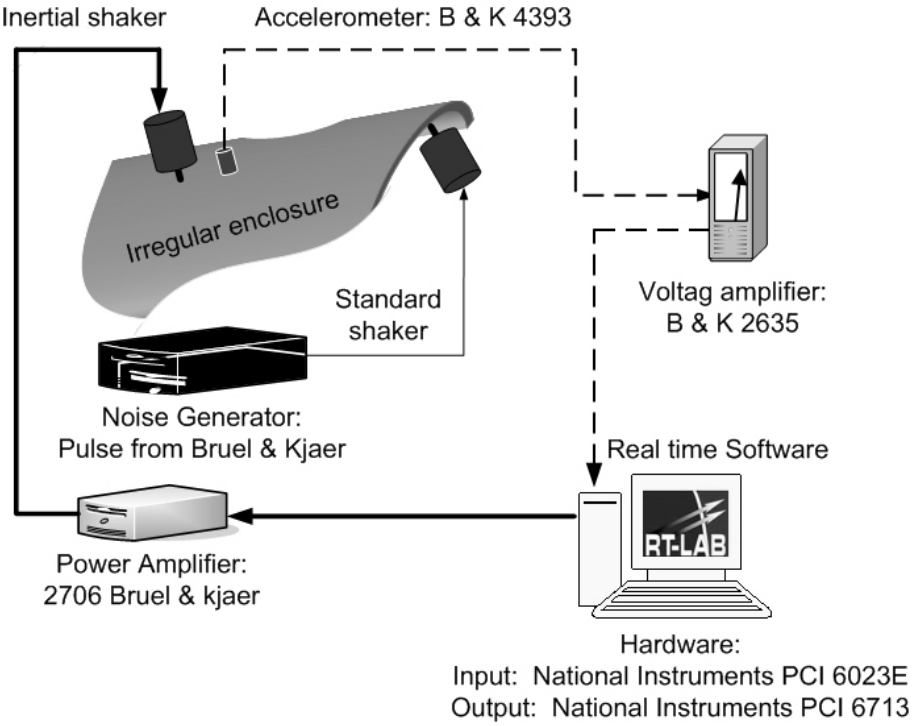

Figure 8.16: Experiment setup diagram.

The vibration signal from the accelerometer sensor was processed using a National Instruments PCI 6023E acquisition card. A power amplifier was connected to the inertial shaker actuator. This power amplifier was fed by a National Instruments PCI 6713 output card. The real-time process for implementing the controller was driven by RT-LAB, as in the previous two experiments. Fig. 8.16 illustrates the experiment setup. As it was not physically possible to scan the entire structure, the efficiency of the controller is only evaluated inside the laser mesh.

8.3.2 Experimental model

The truncated model to be used in this experiment was constructed based on the analysis set up in Chapter 7. Considering the state-space representation of the

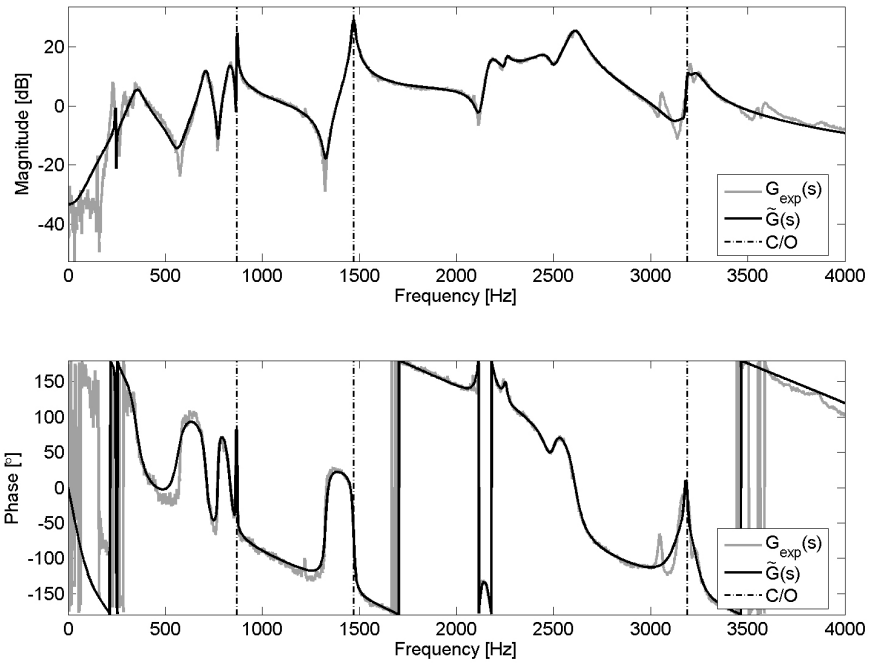

Figure 8.17: System transfer function, $G_{exp}(s)$: experimental transfer function, $\widetilde{G}_(s)$: estimated transfer function and C/O: controllable and observable modes.

system in question:

$$\boldsymbol{x}(k+1) = \boldsymbol{A}\boldsymbol{x}(k) + \boldsymbol{B}\boldsymbol{v}_a(k) \tag{8.11a}$$

$$\boldsymbol{v}_s(k) = \boldsymbol{C}\boldsymbol{x}(k) + \boldsymbol{D}\boldsymbol{v}_a(k) \tag{8.11b}$$

The SMI technique was used to estimate the system matrices $\boldsymbol{A}$, $\boldsymbol{B}$, $\boldsymbol{C}$ and $\boldsymbol{D}$ up to a similarity transformation based on measurements taken from the sensor output $\boldsymbol{v}_s(k)$ and the actuator input $\boldsymbol{v}_a(k)$. This technique was also used to evaluate the order n of the system. In the experiment, the output error was assumed to be a combination of white noise and process noise; for reasons given earlier, it was chosen therefore chosen to use the PO-MOESP algorithm. The controllable modes of $(\boldsymbol{A}, \boldsymbol{B})$ were assumed to be stable, the pair $(\boldsymbol{A}, \boldsymbol{C})$ assumed to be observable, and $\boldsymbol{v}_a(k)$ assumed to have persistent excitation of sufficient order. The observability matrix (see Eq. (7.7)) and controllability matrix, $\boldsymbol{\Gamma}_c = \begin{bmatrix}\boldsymbol{B} & \boldsymbol{A}\boldsymbol{B} \dots \boldsymbol{A}^{n-1}\boldsymbol{B}\end{bmatrix}$, of

the experimental model $\widetilde{\boldsymbol{G}}_(s)$ were computed, and they indicated that only three modes (874Hz, 1472Hz and 3.2kHz - see dashed lines in Fig. 8.17) are fully observable and controllable for the sensor/actuator locations that were chosen. These conditions provided an excellent opportunity to demonstrate how it is possible to control modes that are not necessarily adjacent to each other. However, if the objective were to control modes other than the three above, the sensor and/or actuator locations would need to be changed. Sensor and actuator data were collected, and the experimental transfer function $\boldsymbol{G}_{exp}(s)$ was determined as the ratio of the cross-power spectral density P_{xy} (with the actuator x, and sensor y) to the power spectral density P_{xx}. The SMI algorithm was used to construct $\widetilde{\boldsymbol{G}}(s)$, the experimental model transfer function of the system as shown in Fig. 8.17, and the performance of $\widetilde{\boldsymbol{G}}(s)$ was then compared to that of the experimental transfer function $\boldsymbol{G}_{exp}(s)$. The correctness of $\widetilde{\boldsymbol{G}}(s)$ was 98% compared to $\boldsymbol{G}_{exp}(s)$.

As the objective was to attenuate the vibration at those 3 resonance frequencies, a truncated model of the full experimental model $\widetilde{\boldsymbol{G}}(s)$ was made which included only those 3 modes. This model was then optimised based on the full experimental model (see section 7.3.2). The band-pass filter $\boldsymbol{\mathcal{W}}(s)$ used to encompass the frequencies of interest is shown in Fig. 8.18. Fig. 8.19 shows the result of the optimisation, comparing $\widetilde{\boldsymbol{G}}(s)$ (plain curve) with the truncated model without optimisation (dotted curve) and the model with optimisation (dash dot curve). In this particular case, the optimisation did not significantly improve the accuracy of the truncated model, due to the fact that energy exists only at a single frequency for each bandwidth to be controlled. This gave the matrices $\boldsymbol{A}$, $\boldsymbol{B}_a$, $\boldsymbol{C}_s$ and $\boldsymbol{D}_{as}$ of the desired system (see section 7.2.1). Using the data in table 8.7, Φ_{ij} (see Eq. (7.21)), which can be approximated by $\frac{1}{\rho t\, h}$, could be calculated and used to determine the $\boldsymbol{\Omega}$ and $\boldsymbol{\Gamma}$ matrices of Eqs. (7.20). The estimation of the transformation $\boldsymbol{T}$ matrix (see section 7.2.3) was then computed in order to put all the matrices in the same subspace and obtain the final model $\boldsymbol{G}_f(s)$ for conceptualisation of the disturbance force contribution and displacement, which was then used to design a suitable controller.

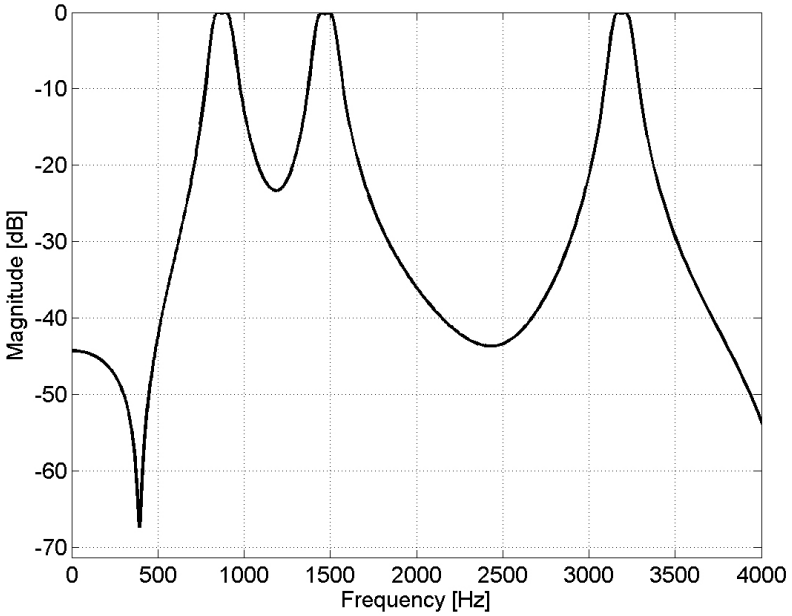

Figure 8.18: Band-pass filter $\boldsymbol{\mathcal{W}}(s)$.

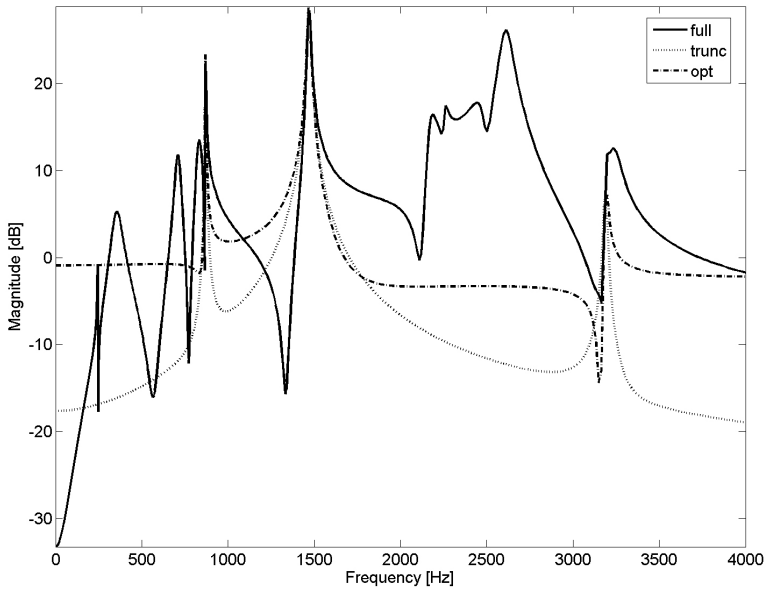

Figure 8.19: Full estimated, truncated and optimised model frequency responses.

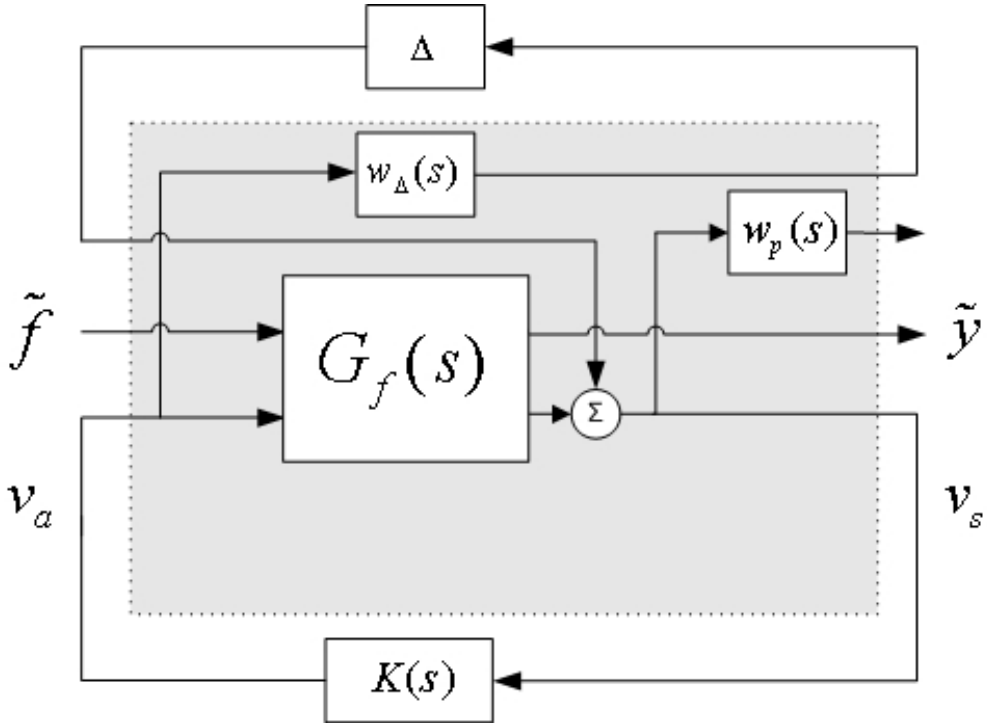

Figure 8.20: $\mathcal{H}_\infty$ control diagram.

8.3.3 Controller design

The objective of the controller design was to achieve global structural vibration control within a specified bandwidth. It was possible to achieve this using robust control theory, or more specifically the $\mathcal{H}_\infty$ optimal approach, as already discussed. The control design was similar to that for any other $\mathcal{H}_\infty$ optimal controller [42], as shown in Fig. 8.20, but the weight functions were different (that is, band-pass filters instead of low-pass filters) and were set according to the frequency bandwidth of interest.

The model used in the control design came from deliberate truncation of the full experimental model $\widetilde{\boldsymbol{G}}(s)$, which resulted in the exclusion of some dynamic effects that were then represented by uncertainty functions. For this experiment, the unmodelled dynamics were represented in the form of additional uncertainty, which can be expressed as $\boldsymbol{G}(s) \simeq \boldsymbol{G}_f(s) + \boldsymbol{\Delta}\,\boldsymbol{W}_\Delta(s)$, where $\boldsymbol{G}(s)$ is the full model, $\boldsymbol{G}_f(s)$ the final truncated plant, $\|\boldsymbol{\Delta}\|_\infty \leq 1$, and $\boldsymbol{W}_\Delta(s) = \mathrm{diag}(W_{\Delta_1}, ..., W_{\Delta_{N_a}})$.

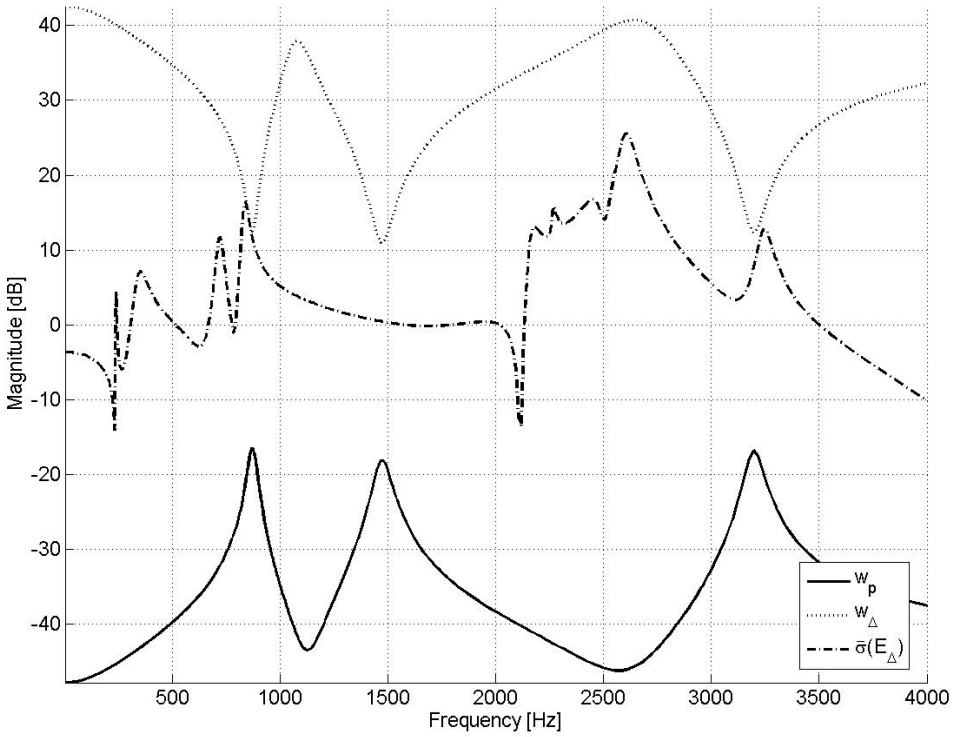

Figure 8.21: Weight functions: W_Δ weight function encompassing the spillover, W_p performance weight function, $\bar{\sigma}(E_\Delta)$ norm of the error.

The truncated experimental model required an unmodelled uncertainty function $W_\Delta(s)$ in order to account for spillover. To ensure system stability, it was chosen for $W_\Delta(s)$ to be minimum-phase. As each of the modes of interest were represented by a single discrete frequency, $W_\Delta(s)$ described a multi-band-stop filter which encompassed each mode of interest. In this experiment, the band-stop filter was generated using the Matlab signal processing toolbox, as in previous experiments.

A second weight function $W_p(s)$ was introduced into the plant design to determine the controller performance, as shown in Fig. 8.21. $W_p(s)$ was the inverse of $W_\Delta(s)$, and as $W_\Delta(s)$ was minimum-phase, so was $W_p(s)$. $W_p(s) = C_p W_\Delta^{-1}(s)$, with C_p a multiplicative gain found by trial and error in order to optimise the controller performance. The weight function $W_p(s)$ allowed the controller energy

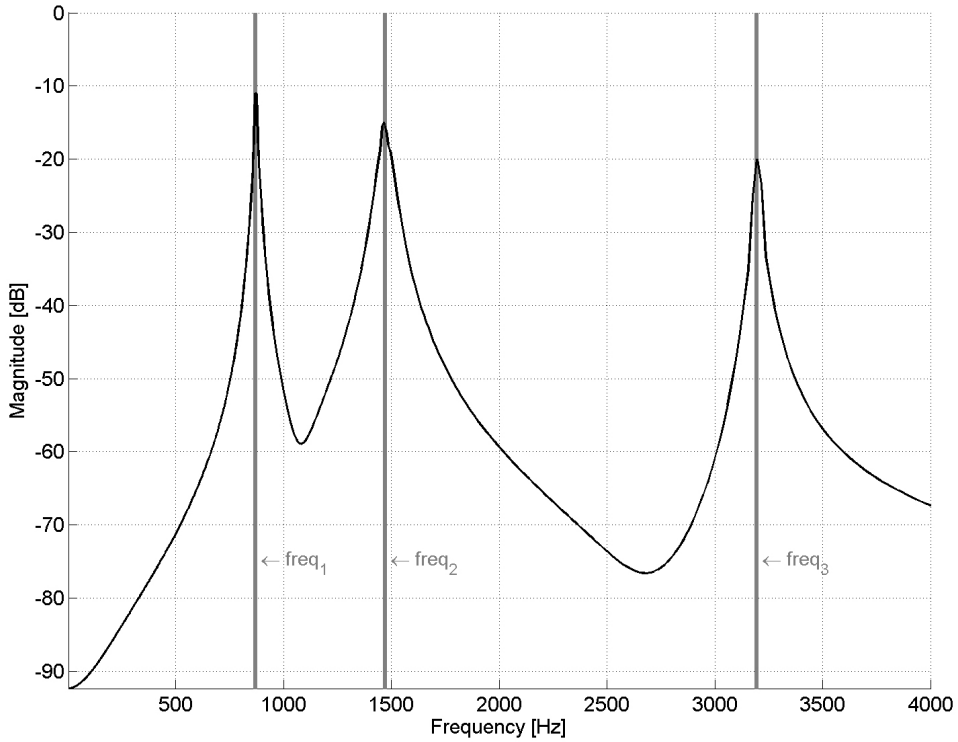

Figure 8.22: Controller transfer function magnitude [V/V].

to be concentrated only on the frequencies of interest. The Matlab robust control toolbox was again used to compute an $\mathcal{H}_\infty$ optimal controller. The magnitude of the control effort is shown in Fig. 8.22, where it can be seen that the three peaks of energy correspond to the three resonances frequencies of interest (freq_1=874Hz, freq_2=1472Hz and freq_3=3.2kHz).

8.3.4 Experiment results

A laser vibrometer was used to measure the vibration level at 210 points across the irregularly shaped shell for the cases with control and without. Figs. 8.23 and 8.24 show the average spectrum of the velocities of those 210 points.

Data taken from the laser vibrometer revealed many more modes than were

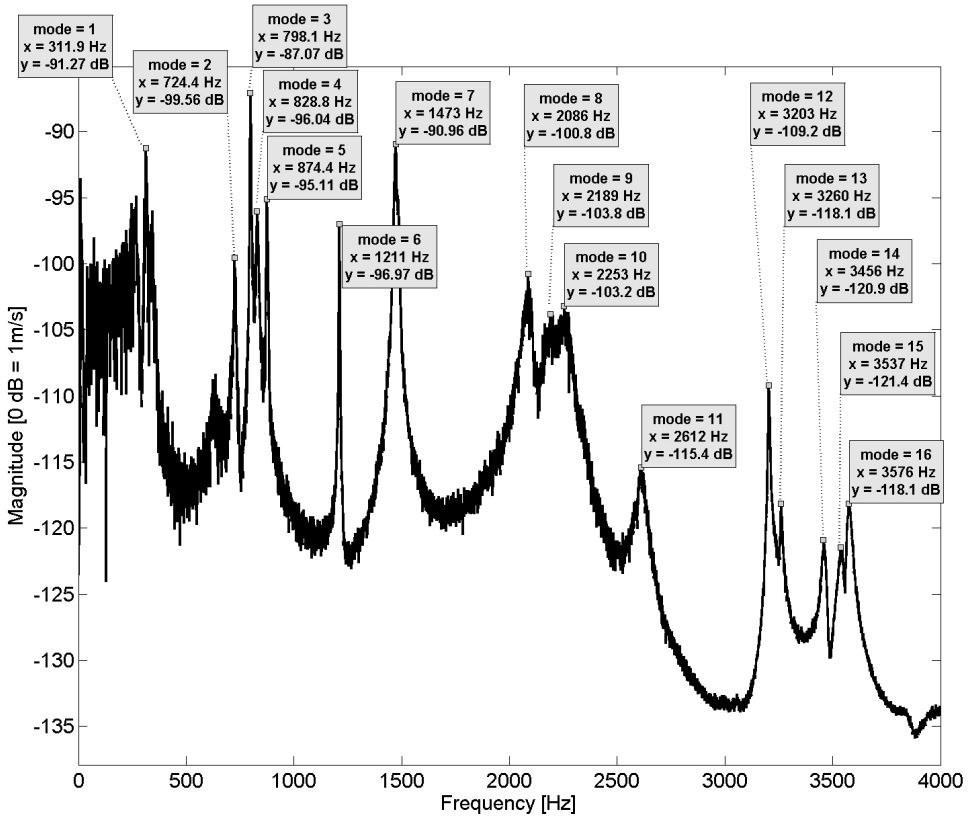

Figure 8.23: Average spectrum of velocity in the shell scanned area without control.

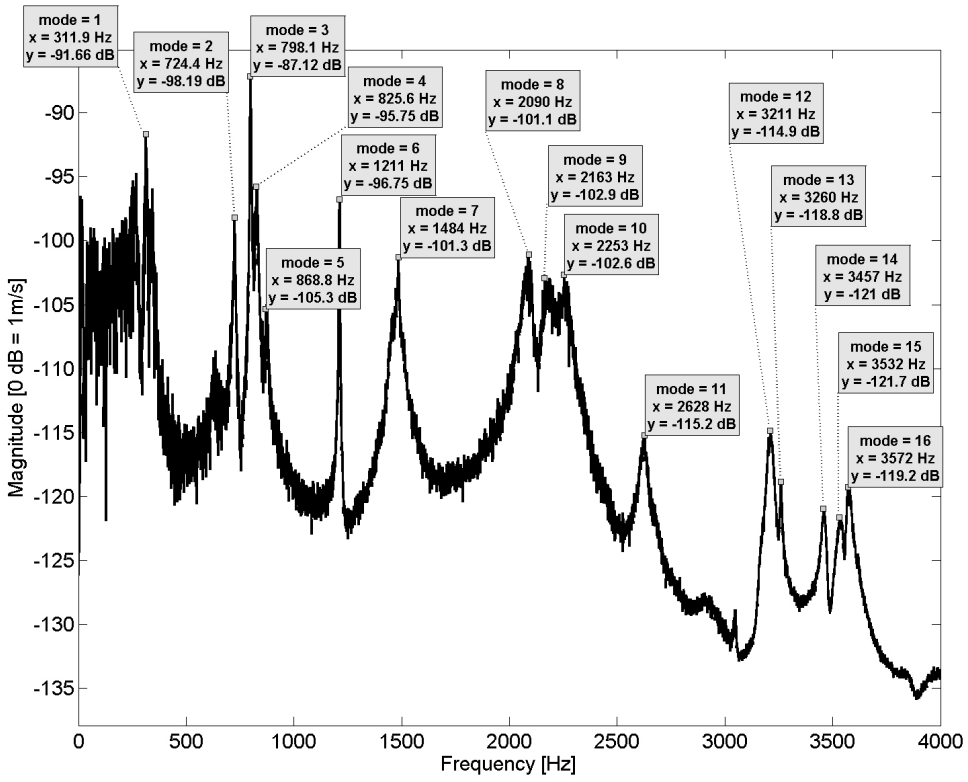

Figure 8.24: Average spectrum of velocity in the shell scanned area with control.

Table 8.8: Attenuations for each mode measured by the laser vibrometer

Mode	Attenuation [dB]	Mode	Attenuation [dB]
1	0.5	9	-1.0
2	-1.5[a]	10	-0.5
3	0.0	11	0.0
4	0.0	12	5.5
5	10.0	13	0.5
6	0.0	14	0.0
7	10.5	15	0.0
8	0.5	16	1.0

[a] the minus sign means the mode has been augmented
The shaded values represent those frequencies targeted by the controller.

found using SMI analysis. This is because only the modes sensed by the sensor and/or excited by the actuator are picked up in SMI analysis, whereas scanning the system in question with a laser vibrometer reveals all vibration modes occurring in the actual structure. As, for some of the modes, the sensor or actuator was located on their nodes, it was not possible to either detect or excite these modes. Results from the SMI analysis were thereby limited by the locations of the sensor and actuator.

Clearly, the sensor would not be able to measure displacement of the structure occurring on the other side of the shell (where, in this case, the disturbance was); a second sensor and actuator pair would therefore be required to make that area controllable and observable.

Figs. 8.23 and 8.24 show that the proposed control system succeeded in reducing the shell's three vibration modes of interest in the scanned area. By contrast, the controller did not significantly affect (maximum of ± 1.5 dB) the other bending modes. Table 8.8 summarises the vibration attenuation achieved at each modal resonance frequency, rounded to the nearest 0.5 dB. As anticipated, the vibration attenuation of the 12^{th} mode was not as high as that of the 5^{th} and 7^{th} modes, as the 12^{th} mode was known to be less controllable and observable. Figs. 8.25, 8.26 and 8.27 show how the controller affected the maximum velocity amplitude of the

shell for the three modes of interest. For the remainder of the modes, it was found there was no significant difference between the controlled and un-controlled shell vibration velocity amplitude.

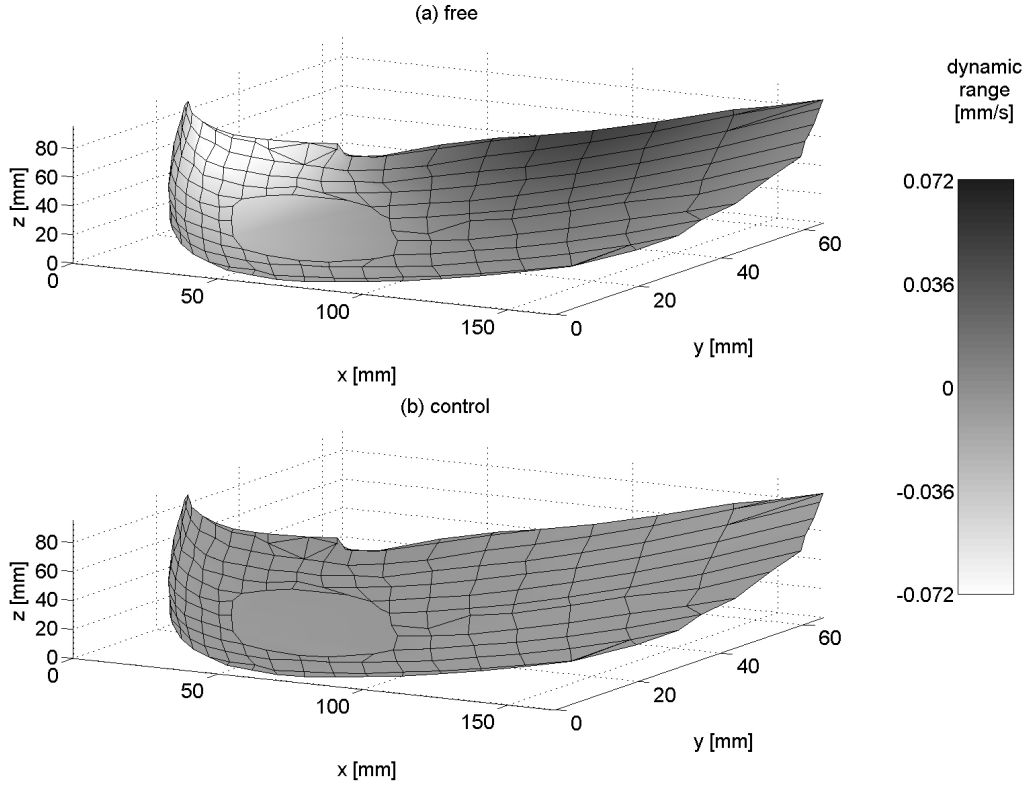

Figure 8.25: Velocity of the shell for mode 5, free (a) and controlled (b).

One advantage of the proposed control approach is that the order of the plant ($2N_c$ states, where N_c is the number of frequencies or modes to be controlled) is lower than that of control design's most commonly used plant ($2N_{max}$ states, where N_{max} is the mode number corresponding to the highest frequency to be controlled). For example, in the above experiment where the aim was to control the vibration of the 5^{th}, 6^{th} and 12^{th} modes, $N_c = 3$ and $N_{max} = 12$. Thus, the standard model would require 24 states, and the proposed model only 6. Since the order of the controller is given by the sum of the order of the plant and the order of the weighting function used, the proposed method would generate a much lower

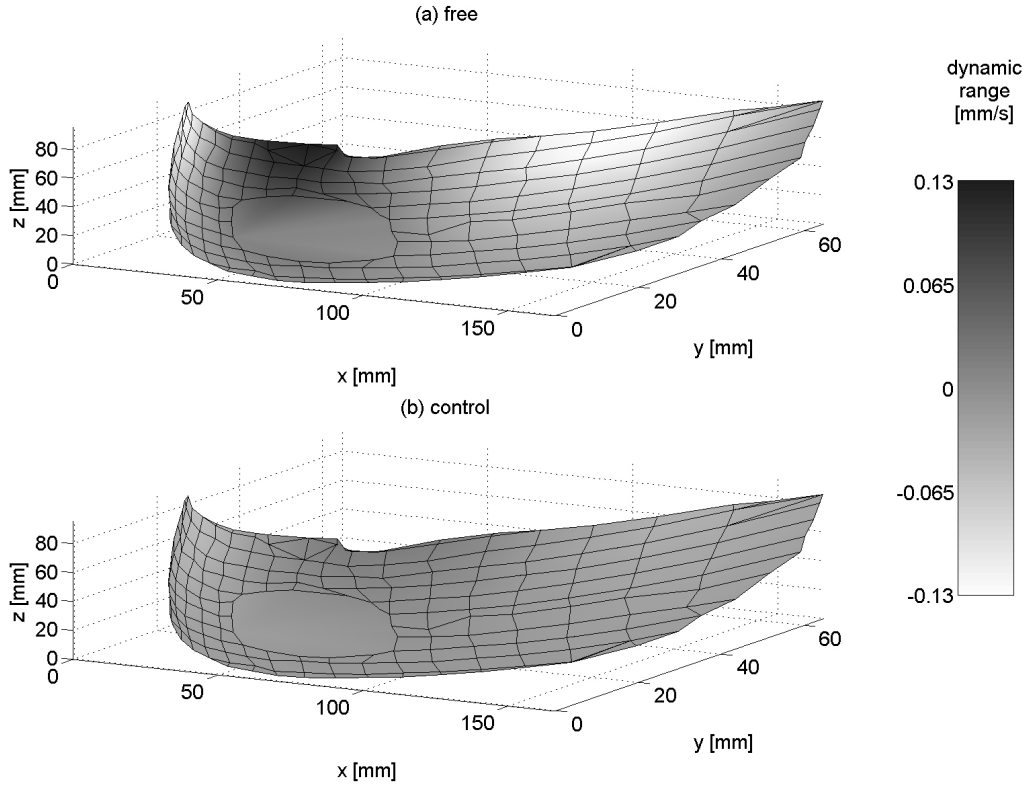

Figure 8.26: Velocity of the shell for mode 7, free (a) and controlled (b).

order controller.

Another advantage of the proposed approach is that it enables the control of specific modes within a bandwidth without exerting unnecessary control effort on lower order modes that are not of interest. As mentioned before, in this sense the standard approach is less efficient because it includes those lower order modes in the controller design.

8.3.5 Experiment 3 - summary

This control design works by combining the strengths of three techniques that would normally be employed separately: SMI, spatial input/output control, and $\mathcal{H}_\infty$ control. This section has demonstrated a new control design for achieving

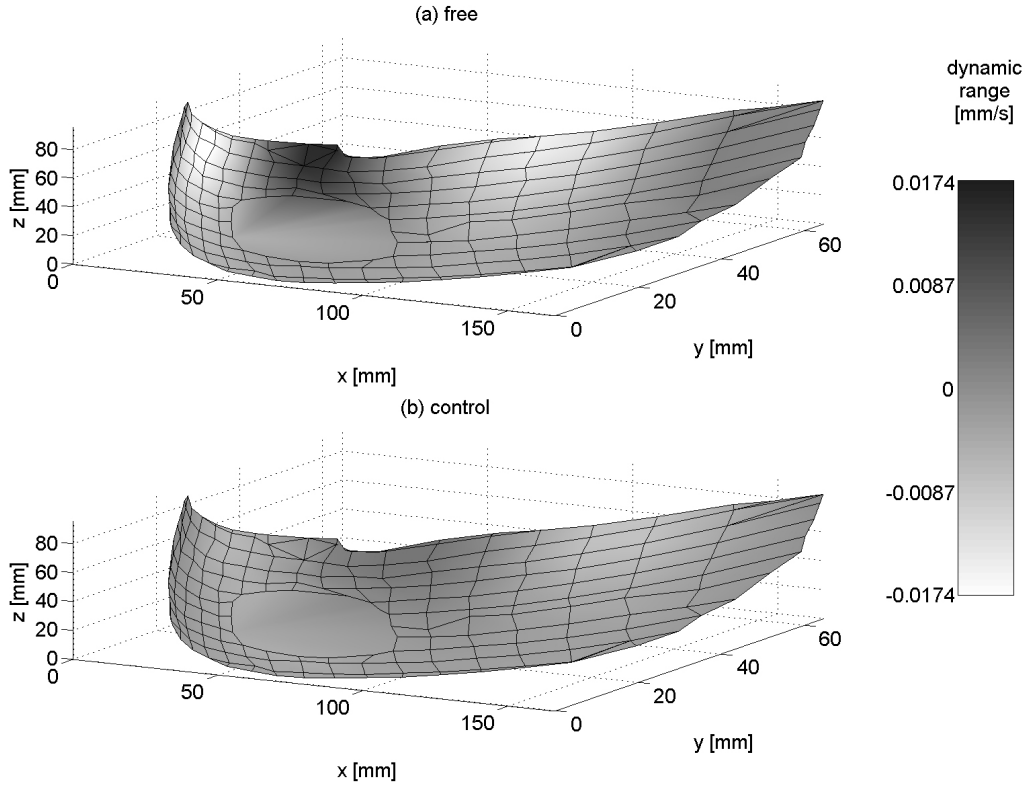

Figure 8.27: Velocity of the shell for mode 12, free (a) and controlled (b).

global vibration control for a complex structure over a specified bandwidth using an experimental model that does not require any knowledge about the nature of the disturbances and associated system displacement. The new control design also enabled the concentration of control energy into any specified frequency bandwidth, while maintaining the robustness of the control system. An experiment carried out on an irregularly shaped shell demonstrated the effectiveness of the proposed approach in controlling high frequency vibration modes of a complex structure.

CONCLUSIONS

This thesis has investigated several issues in signal processing and active vibration and noise radiation control. The main contributions of this thesis are listed below:

- The full realisation of an ANC system has been presented, from the control theory upon which it was based up to an analysis of the statistical behaviour of one of the most commonly used adaptive control algorithms, the FxLMS. A new analytical model for the FxLMS algorithm's behaviour has been provided, using stochastic differential equation theory.

- The real-time ANC system was implemented in such a way to enable stochastic analysis of an experiment to be performed, under the same conditions as in simulation where Monte Carlo analysis is conducted.

- Another ANC system example was presented, and indicated that active noise radiation control for complex structures could be viably achieved for industrial purposes using well-known control techniques and being able to ensure a robust controller even when minor incidental variations occur in the structure. The originality of the ANC control design lay in the fact that it uses structural sensors and actuators to actively attenuate the noise radiation of the enclosure. The design was possible because the first structure resonance frequency was well above the frequency range of the disturbance noise to be attenuated.

- A new procedure for the optimisation of a truncated analytical model of a given system to be controlled has been developed, to enable the building of a feedback controller that can exclude both lower order and higher order modes outside the control bandwidth of interest. This optimisation consists

of inserting a second-order term into the truncated model, on top of the classic zero-order term, to account for the effect of the lower order as well as higher order modes on the system response in the frequency bandwidth of interest.

- It has been shown how the optimisation procedure can be generalised for building suitable truncated experimental models. In this way, the procedure could be used for model optimisation problems in other fields.

- The theory of spatial input/output control was explained, and it has been shown how introducing some variants to the theory could improve the robustness of the conventional control approach by making it less dependent on the extent of knowledge about the real disturbance force. Exact analytical feedthrough terms for the resulting spatial state-space representation were also developed, permitting even greater precision when applied to a real system.

- It has been set out how the first spatial input/output control experiment was performed. Results from the experiment showed a promising performance by the applied control theory in terms of its efficiency. The model of the system used in this experiment used the exact feedthrough terms developed for the spatial control theory.

- A methodology has been proposed for designing an analytical model-based controller for global vibration attenuation of given structure's resonance frequencies over a specified bandwidth. An experiment was carried out on a cantilever beam to demonstrate the effectiveness of this methodology.

- A similar methodology has been proposed for designing an experimental model-based controller with the same objective. The methodology combines three main techniques that are normally used separately: subspace model identification (SMI), spatial input/output control, and $\mathcal{H}_\infty$ robust control. The key innovation in the methodology is the ability to obtain a conceptualisation of the structure's global displacement and the contribution of unknown external disturbance(s) on the system, using spatial input/output

control theory. An experiment was conducted on a complex structure to demonstrate the effectiveness of the proposed approach.

- The two methodologies have one key advantage in that they produce lower order plants than those commonly used in control design. Given that the order of the controller is derived from the order of the plant, the methodologies also generate lower order controllers. Another advantage is that they enable specific modes within a specified frequency bandwidth to be controlled without unnecessary effort being expended on controlling modes outside of that bandwidth.

Throughout this work, it has been indicated what unresolved issues could be investigated in future research efforts:

- How to use experimental data to optimise the location of sensors and actuators on complex structures to be controlled;
- The performance of spatial input control compared with classical control in instances when the location of the disturbance force varies;
- What other piezoelectric actuator designs could be used (for example, stacking several piezoelectric crystals in a "u" shape to generate greater bending force) and how effective they could be in achieving broadband vibration control; and
- How SMI could be used to gain more comprehensive knowledge of a disturbance, and how this knowledge could be used to design more efficient controllers.

APPENDIX A

Theorem 4 of [70]: *Consider a spatial system (5.14a, 5.14b and 5.14c), where* $\boldsymbol{G}_{io}(s, r_i, r_o) = \boldsymbol{C}_1(r_o)(sI - \boldsymbol{A})^{-1}\boldsymbol{B}_1(r_i)$ *is the infinite-dimensional state-space system. Then*

$$\ll \boldsymbol{G}_{io} \gg_{\infty,i,o} = \|\boldsymbol{g}_{io}\|_\infty \tag{12}$$

where $\boldsymbol{g}_{io}(s) * \boldsymbol{g}_{io}(s) = \sum_k \lambda_k(\tilde{\boldsymbol{G}}_{io}(s) * \tilde{\boldsymbol{G}}_{io}(s))$ *and* $\tilde{\boldsymbol{G}}_{io}(s) = \boldsymbol{\Gamma}\boldsymbol{N}\boldsymbol{\Omega}$ *is a finite-dimensional system, with* $\boldsymbol{N} = (sI - \boldsymbol{A})^{-1}$.

$$\boldsymbol{\Omega}\boldsymbol{\Omega}^T = \int_{\mathcal{R}_i} \boldsymbol{B}_1(r_i) Q_i(r_i) \boldsymbol{B}_1^T(r_i) dr_i \tag{13a}$$

$$\boldsymbol{\Gamma}\boldsymbol{\Gamma}^T = \int_{\mathcal{R}_o} \boldsymbol{C}_1(r_o) Q_o(r_o) \boldsymbol{C}_1^T(r_o) dr_o \tag{13b}$$

APPENDIX B

The circuit design of the power amplifier used to drive the piezoelectric actuator in the experiment is shown below.

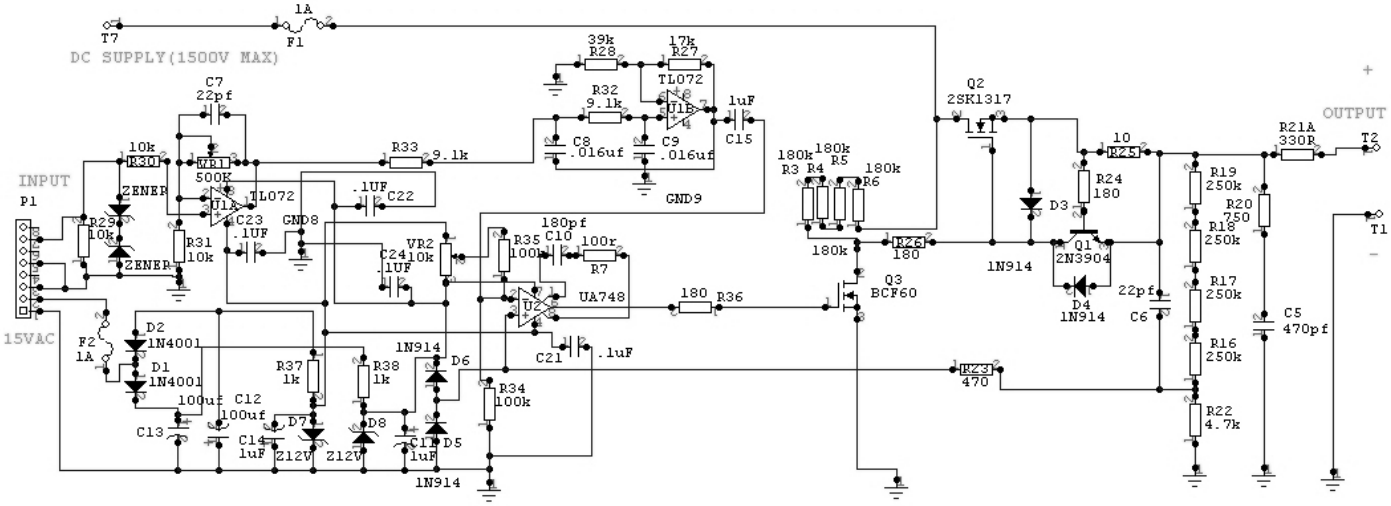

Figure 28: Piezoelectric power amplifier design.

BIBLIOGRAFIA

[1] J Yuang S. Liu and K. Y. Fung, "Robust active control of broadband noise in finite ducts," *JASA*, vol. 111, no. 6, July 2002. *(Cited on pages x, 8, and 9)*

[2] B. K. Wada, J. L. Fanson, and E. F. Crawley, "Adaptive Structures," *Journal of Intelligent Material Systems and Structures*, vol. 1, no. 2, 1990. *(Cited on pages x and 13)*

[3] R. C. Dorf, *Modern Control Systems*, Addison-Wesley publishing company, 1970. *(Cited on pages x and 17)*

[4] D. Halim, *Vibration analysis and control of smart Structures*, PhD thesis, School of Electrical Engineering and Computer Science, University of Newcastle, Australia, 2002. *(Cited on pages xi, 65, 70, 90, 122, and 144)*

[5] E. F. Crawley and J. de Luis, "Use of piezoelectric actuators as elements of intelligent structures," *AIAA Journal*, vol. 25, no. 10, pp. 1373–1385, 1987. *(Cited on pages xi, 70, and 71)*

[6] R. Jordan, *Análise modal experimental*, Programa de Pós-graduação em Engenharia Mecânica, 2004. *(Cited on pages xi, 80, 81, and 147)*

[7] P. A. Ioannou and J. Sun, *Robust Adaptive Control*, Prentice Hall, Inc., 1996. *(Cited on pages xi, 5, 106, and 107)*

[8] A. M. Sadri, R. J. Wayne, and J. R Wright, "Robust Strategies for Active vibration Control of Strain Actuated Plate Like Structures," *IEEE UKACC International Conference on Control 98*, september 1998. *(Cited on pages xi and 111)*

[9] G. L. C. M. de Abreu, *Projeto robusto H_∞ aplicado no controle de vibrações em estruturas flexiveis com materiais piezoeletricos incorporados*, Universidade Federal de Uberlândia departamento de Engenharia Mecanica, 2003. *(Cited on pages xi, 69, 106, 111, 114, 122, and 144)*

[10] J. C. Doyle and G. Stein, "Multivariable Feedback Design: Concepts for a Classica/Modern Synthesis," *IEEE Trans. on Automatic Control*, vol. 26, no. 1, February 1981. *(Cited on pages xi, 111, and 113)*

[11] S. M. Kuo and D. R. Morgan, *Active Noise Systems, Algorthms and DSP Implementations*, John Wiley and sons, inc., 1996. *(Cited on pages 5, 8, 22, 45, and 60)*

[12] K. Kido, "Reduction of noise by use of additional sound sources," *Proc. Inter-Noise*, 1975. *(Cited on page 5)*

[13] C. F. Ross, "A demonstration of active control of broadband sound," *J. Sound and Vibration*, 1981. *(Cited on page 5)*

[14] A. Duprez, *Design and Implementation of an Adaptive Control System for Active Noise Control*, Master thesis in Florida Atlantic University, 2001. *(Cited on page 6)*

[15] A. P. Tzes and S. Yurkovich, "Application and comparison of on-line identification methods for exible manipulator control," *The International Journal of robotics Research*, vol. 10, no. 5, October 1991. *(Cited on page 6)*

[16] S. Haykin, *Adaptive Filter Theory*, Prentice-Hall, fourth edition, 2002. *(Cited on pages 6, 22, and 37)*

[17] E. Bjarnason, "Analysis of the filtered-x lms algorithm," *IEEE Trans. on Acoustics, Speech and Signal Processing*, vol. 3, pp. 6, November 1995. *(Cited on page 7)*

[18] O. J. Tobias, *Analise Estatistica do Comportamento do Algoritmo LMS Filtrado*, PhD. thesis of the Federal University of Santa Catarina in eletrical engineering, 1999. *(Cited on pages 7, 23, and 36)*

[19] B. Widrow and S. D. Stearns, *Adaptive Signal Processing*, Prentice-Hall, Inc., 1985. *(Cited on page 7)*

[20] C.R. Fuller and A.H. Von Flotow, "Active control of sound and vibration," *IEEE Control systems*, December 1995. *(Cited on pages 7, 70, and 122)*

[21] S.J. Elliott and T.J. Sutton, "Performance of feedforward and feedback systems for active control," *IEEE Transactions on Speech and Audio signal processing*, vol. 4, no. 3, May 1996. *(Cited on page 7)*

[22] C. H. Hansen and S. D. Snyder, *Active Control of Noise and Vibration*, E and FN Spon, 1997. *(Cited on pages 8, 14, 45, 65, and 70)*

[23] P. A. Nelson and S. J. Elliott, *Active Control of Sound*, Academic press inc., 1993. *(Cited on page 8)*

[24] J. Yuang, "Improving robustness of active noise control in ducts," *JASA*, vol. 114, no. 1, July 2003. *(Cited on page 8)*

[25] J. Yuang, "A hybrid active noise controller for finite ducts," *Applied Acoustics*, vol. 65, 2004. *(Cited on page 8)*

[26] J. Yuang, "Improving active noise control in resonant fields," *Journal of Sound and Vibration*, vol. 291, pp. 749–763, 2006. *(Cited on page 8)*

[27] T. W. Leishman and J. Tichy, "On the significance of reflection coefficients produced by active surfaces bounding one-dimensional sound field," *JASA*, vol. 113, no. 3, March 2003. *(Cited on page 9)*

[28] K. R. Holland and P. O. A. L. Davies, "The measurement of sound power flux in flow ducts," *Journal of sound and vibration*, vol. 230, no. 4, 2000. *(Cited on page 9)*

[29] Seung-Ho Jang and Jeong-Guon Ih, "On the multiple microphone method for measuring in-duct acoustic properties in the presence of mean flow," *JASA*, vol. 103, no. 3, March 1998. *(Cited on page 9)*

[30] A. Boudreau and A. L'Esperance, "Actuators positioning for multichannel active control system in cicurlar ducts," *Applied Acoustics*, vol. 59, 2000. *(Cited on page 9)*

[31] D. C. Swanson, S. M. Hirsch, K. M. Reichard, and J. Tichy, "Development of a frequency-domain filtered-x intensity ANC algorithm," *Applied Acoustics*, vol. 57, 1999. *(Cited on page 9)*

[32] C. Bacon, "Separation of waves propagating in an elastic or viscoelastic Hopkinson pressure bar with three-dimensional effects," *International journal of Impact Engineering*, vol. 22, 1999. *(Cited on page 9)*

[33] T. Ikeda, *Fundamentals of Piezoelectricity*, Oxford University Press, 1984. *(Cited on pages 10 and 69)*

[34] G. Gautschi, *Piezoeletric Sensorics: Force, Strain, Pressure, Acceleration and Acoutic Emission Sensors, Materials and Amplifier*, Springer, 2002. *(Cited on pages 10 and 69)*

[35] J. S. Bevan, "Piezoceramic Actuator Placement for Acoustic Control of Panels," *NASA/CR-2001-211265*, December 2001. *(Cited on page 11)*

[36] N. W. Hagood and von Flotow, "Damping of Structural Vibrations with Piezoelectric Materials and Passive Electrical Networks," *Journal of Sound and Vibration*, vol. 146, no. 2, 1991. *(Cited on page 11)*

[37] G. L. C. M. de Abreu, J. F. Ribeiro, and Jr. V. Steffen, "Finite Element Modeling of a Plate with Localized Piezoelectric Sensors and Actuators," *J. of the Braz. Soc. of Mech. Sci. and Eng.*, vol. 26, no. 2, April-June 2004. *(Cited on pages 11 and 90)*

[38] H. Sumali, *A New Adaptive Array of Vibration Sensors*, PhD. thesis of the Virginia Polytechnic Institute in Mechanical Engineering, 1997. *(Cited on pages 12 and 13)*

[39] L. Meirovitch, H. F. van Landingham, and H. Oz, "Distributed control of spinning flexible spacecraft," *J. of Guidance and Control*, vol. 2, 1979. *(Cited on page 13)*

[40] L. Meirovitch, H. Baruh, and H. Oz, "A comparison of control technique for large flexible system," *J. of Guidance and Control*, vol. 6, no. 4, 1981. *(Cited on page 14)*

[41] S. L. Xie, X. N. Zhang, J. H. Zhang, and L. Yu, "H_∞ Robust vibration control of a thin plate covered with a controllable constrained damping layer," *Journal of Vibration and Control*, vol. 10, 2004. *(Cited on page 15)*

[42] S. Skogestad and I. Postlethwaite, *Mutlivariable feedback control, Analysis and Design*, John Wiley and Sons, 1996. *(Cited on pages 15, 115, 117, 118, 119, 122, and 168)*

[43] K. Zhou, J. C. Doyle, and K. Glover, *Robust and Optimal Control,*, Prentice-Hall,Upper Saddle River, New Jersey, 1996. *(Cited on pages 15 and 122)*

[44] M. Green and D. Limebeer, *Linear Robust Control*, Prentice Hall, Englewoods Cliffs, New Jersey, 1995. *(Cited on page 15)*

[45] S. O. R. Moheimani, D. Halim, and A. J. Fleming, *Spatial control of vibration: Theory and experiments*, World Scientific Publishing, 2003. *(Cited on pages 15, 74, 79, 90, 122, 130, 143, and 153)*

[46] N.J Bershad, "Analysis of the Normalized LMS Algorithm with Gaussian inputs," *IEEE Trans. on Acoustics, Speech and Signal Processing*, vol. 34, August 1986. *(Cited on page 23)*

[47] A. Benveniste, "A Measure of the Tracking Capability of Recursive Stochastic Algorithms with Constant Gains," *IEEE Trans. on Automatic Control*, vol. 27, no. 3, 1982. *(Cited on pages 23, 27, 28, and 29)*

[48] L. Ljung and T. Soderström, *Theory and Practice of Recursive Identification*, The MIT Press, third edition, 1986. *(Cited on page 24)*

[49] H. Fan, " structural view of a asymptotic convergence speed of adapting IIR filtering algorithms-Part II finite precision," *IEEE Trans. on Signal Processing*, vol. 45, no. 6, June 1997. *(Cited on pages 24 and 28)*

[50] G. Barrault, M. H. Costa, J. C. M. Bermudez, and A. Lenzi, "New Model of N-LMS algorithms for correlated input signals," *ICASSP-2005*, 2005. *(Cited on page 24)*

[51] O. J. Tobias, J. C. M. Bermudez, and N. J. Bershad, "Mean weight behavior of the filtered-x lms algorithm," *IEEE Transactions on Signal Processing*, vol. 48, no. 4, pp. 1061–1075, April 2000. *(Cited on pages 25 and 26)*

[52] P. A. Regalia, *Adaptive IIR Filtering in Signal Processing and Control*, Marcel Dekker, Inc., 1995. *(Cited on page 27)*

[53] R. H. Bartels and G. W. Stewart, "Solution of the Matrix Equation AX+XB=C," *Center for Numerical Analysis, University of Texas at Austin, TX 78712.* *(Cited on page 35)*

[54] Dspace, *http://www.mathworks.com/products/connections/product_main.html?prod_id* = 59, 2006. *(Cited on page 44)*

[55] xPcTarget, *http://www.mathworks.com/products/xpctarget*, 2006. *(Cited on page 44)*

[56] Opal-rt, *http://www.opal-rt.com/catalog/products*, 2006. *(Cited on page 44)*

[57] B. S. Cazzolato and C. Hansen, "Active control of sound transmission using structural error sensing ," *Journal of the Acoustical Society of America*, vol. 104, pp. 2878–2889, 1998. *(Cited on page 56)*

[58] B. S. Cazzolato and C. Hansen, "Structural radiation mode sensing for active control of sound radiation into enclosed spaces ," *Journal of the Acoustical Society of America*, vol. 106, pp. 3732–3735, 1999. *(Cited on page 56)*

[59] S. M. Kuo and J. Chen, "Multiple-microphone acoustic echo cancellation system with partial adaptive process," *Digital Signal Processing*, vol. 3, no. 1, 1993. *(Cited on page 60)*

[60] S. M. Kuo and J. Tsai, "Acoustical mechanisms and performance of various active duct noise control systems," *Applied Acoustics*, vol. 41, no. 1, 1994. *(Cited on page 60)*

[61] L. Meirovitch, *Elements of vibration Analysis*, McGraw-Hill., 2nd ed., Sydney, 1986. *(Cited on pages 66, 67, and 69)*

[62] C. W. de Silva, *Vibration: Fundamentals and Practice*, CRC Press, Boca Raton, 2000. *(Cited on page 66)*

[63] N. Setter, *Piezoelectric Material in Devices*, N. Setter, Lausanne, Switzerland, 2002. *(Cited on page 69)*

[64] H. S Tzou, "Integrated distributed sensing and active vibration suppresion of flexible manipulators using distributed piezoelectrics," *Journal of robotics systems*, vol. 6, 1989. *(Cited on page 73)*

[65] A. Boudreau and A. L'Esperance, "Accounting for out-of-bandwidth modes in the assumed modes approach: implications on colocated output feeback control," *ASME Journal of Dynamic Systems, Measurement, and Control*, vol. 119, pp. 390–395, 1997. *(Cited on pages 77, 80, and 124)*

[66] J. C. Doyle, K. Glover, P. P. Khrgonekar, and B. A Francis, "State-space solution to standard H_2 and H_∞ control problems," *IEEE Trans. on Automatic Control*, vol. 34, no. 8, pp. 831–847, August 1989. *(Cited on pages 88, 93, and 122)*

[67] S. O. R. Moheimani, H. R. Pota, and I. R. Petersen, "Spatial control for active vibration control of piezoelectric laminates," *Porceeding of 37th IEEE Conference on Decision and Control*, pp. 4308–4313, December 1998. *(Cited on page 90)*

[68] S. O. R. Moheimani and M. Fu, "Spatial $\mathcal{H}_2$ norm of flexible structures and its application in model order selection," *Porceeding of 37th IEEE Conference on Decision and Control*, vol. 40, no. 5, pp. 3623–3624, December 1998. *(Cited on page 90)*

[69] D. Halim and S. O. R. Moheimani, "Spatial resonance control of flexible structures-application to a piezoelectric laminate beam," *IEEE Trans. on Control Systems technology*, vol. 9, no. 1, 2001. *(Cited on page 90)*

[70] D. Halim, "Structural vibration control with spatially-varied disturbance input using a spatial H_∞ method," *Journal of Mechanical Systems and Signal Processing*, under submission. *(Cited on pages 90, 93, 94, 95, 97, 122, 129, 130, 143, and 179)*

[71] J. C. Doyle, K. Zhou, K. Glover, and B. Bodenheimer, "Mixed H_2 and H_∞ Performance objectives II: optimal control," *IEEE Trans. on Automatic Control*, vol. 39, no. 8, August 1994. *(Cited on page 93)*

[72] K. Glover and J. Doyle, "State-space formulae for all stalilizing controllers that satisfy an H_∞-norm bound and relations to risk sensitivity," *Systems and control letters*, , no. 11, 167-172 1988. *(Cited on page 93)*

[73] K. Zhou, K. Glover, B. Bodenheimer, and J. Doyle, "Mixed H_2 and H_∞ Performance objectives I: performance analysis," *IEEE Trans. on Automatic Control*, vol. 39, no. 8, pp. 1564–1574, August 1994. *(Cited on page 93)*

[74] M. J. Balas, "Feedback control of flexible systems," *IEEE Trans. on Automatic Control*, vol. 23, no. 4, 1978. *(Cited on page 106)*

[75] M. J. Balas, "Active control of flexible systems," *Journal of Optimization theory and Applications*, vol. 25, no. 3, 1978. *(Cited on pages 106 and 122)*

[76] L. Rollins, "Robust Control Theory," *www.ece.cmu.edu/ ∼ koopman/des_s99/ control_theory*, Spring 1999. *(Cited on page 109)*

[77] G. Barrault, D. Halim, and C. Hansen, "High frequency spatial vibration control using H_∞ method," *Journal of Mechanical Systems and Signal Processing*, under submission. *(Cited on page 122)*

[78] S. Leleu, *Amortessiment actif des vibrations d'une structure flexible de type plaque á l'aide de transducteurs piézoelectriques*, Thesis de doctorat de l'école normale supérieur de Cachan, 2002. *(Cited on pages 122 and 144)*

[79] P. Van Overschee and B. De Moor, *Subspace identification for linear systems, theory - implementation - applications*, Kluwer academic publishers, 1996. *(Cited on pages 122, 124, and 125)*

[80] R. Fraanje, *Robust and fast schemes in broadband active noise and vibration control*, PhD. thesis of University of Twente, 2004. *(Cited on page 122)*

[81] B. Haverkamp, *State spcae identification, theory and practice*, PhD. thesis of Delf University of technology, 2001. *(Cited on pages 122, 124, 125, and 129)*

[82] S. O. R. Moheimani and D. Halim, "A convex optimization approach to the mode acceleration problem," *Automatica*, vol. 40, no. 5, May 2004. *(Cited on pages 124, 133, 134, and 136)*

[83] M. H. Verhaegen, "Identification of the deterministic part of MIMO state space models given in innovations form from input-output data," *Automatica*, vol. 30, no. 1, 1994. *(Cited on page 125)*

[84] M. H. Verhaegen and P. Dewilde, "Subspace model identification part 1. The output-error state space model identification class of algorithms," *International Journal of Control*, vol. 56, no. 5, 1992. *(Cited on page 125)*

[85] M. H. Verhaegen and P. Dewilde, "Subspace moedl identification part 2. Analysis of the elementary output-error state space model identification algorithm," *International Journal of Control*, vol. 56, no. 5, 1992. *(Cited on page 125)*

[86] M. H. Verhaegen, "A subspace model identification solution to the identification of mixed causal, anti-causal LTI system," *SIAM Journal on matrix analysis and applications*, 1994. *(Cited on page 125)*

[87] E. Feron S. Boyd, L. El Ghaoui and V. Balakrishnan, *Linear Matrix Inequalities in System and Control Theory*, Volume 15 of Studies in Applied Mathematics, SIAM, 1994. *(Cited on pages 133, 134, and 136)*

[88] P. Horowitz and W. Hill, *The art of electronics*, Cambridge University Press, 2nd ed, 1989. *(Cited on page 145)*